

INFORMATION TO USERS

This manuscript has been reproduced from the microfilm master. UMI films the text directly from the original or copy submitted. Thus, some thesis and dissertation copies are in typewriter face, while others may be from any type of computer printer.

The quality of this reproduction is dependent upon the quality of the copy submitted. Broken or indistinct print, colored or poor quality illustrations and photographs, print bleedthrough, substandard margins, and improper alignment can adversely affect reproduction.

In the unlikely event that the author did not send UMI a complete manuscript and there are missing pages, these will be noted. Also, if unauthorized copyright material had to be removed, a note will indicate the deletion.

Oversize materials (e.g., maps, drawings, charts) are reproduced by sectioning the original, beginning at the upper left-hand corner and continuing from left to right in equal sections with small overlaps.

Photographs included in the original manuscript have been reproduced xerographically in this copy. Higher quality 6" x 9" black and white photographic prints are available for any photographs or illustrations appearing in this copy for an additional charge. Contact UMI directly to order.

Bell & Howell Information and Learning
300 North Zeeb Road, Ann Arbor, MI 48106-1346 USA
800-521-0600



Real-time Measurement and Trapping of Single Atoms by Single Photons

Thesis by

Christina J. Hood

In Partial Fulfillment of the Requirements
for the Degree of
Doctor of Philosophy

California Institute of Technology
Pasadena, California

2000

(Submitted May 1, 2000)

UMI Number: 9972606



UMI Microform 9972606

Copyright 2000 by Bell & Howell Information and Learning Company.
All rights reserved. This microform edition is protected against
unauthorized copying under Title 17, United States Code.

Bell & Howell Information and Learning Company
300 North Zeeb Road
P.O. Box 1346
Ann Arbor, MI 48106-1346

© 2000
Christina J. Hood
All Rights Reserved

Acknowledgements

First and foremost, thanks are due to my research advisor Jeff Kimble. Over the last six years I have been continually impressed by both his skills as a scientist, and his caring attitude to members of the group. The outstanding professional caliber and warm atmosphere of the research group he has assembled are a tribute to this unique combination of qualities.

I have particularly benefited from working alongside two fellow graduate students: Quentin Turchette, who gave me much needed faith and encouragement while teaching me the cavity QED trade, and Theresa Lynn, who I worked with through the highs and lows of the research detailed in this thesis. Thanks also to Michael Chapman, Jun Ye, Wolfgang Lange, Nikos Georgiades, Hideo Mabuchi, David Vernooy and Andrew Doherty, for their important contributions to this work. I have learned from and enjoyed the company of everyone in the Kimble group.

Outside the lab, my life has been enriched by the presence of some wonderful friends. In particular, I am profoundly grateful for support, kindness and fun times from Arthur Street and Penny Kneebone, who helped me through some of the difficult periods of the last six years and have joined me in exploration of this strange phenomenon that we call Los Angeles. Special thanks to a fantastic set of friends and flatmates: Sam Roweis, Aaron Batista, Mike Levene, Erik Winfree, Alli Magidsohn, Alice Shapley, Ben Oppenheimer, Lou Madsen, David Hogg, Beth Orsini, Hannah Lee and Mary Beth Tegan. Thanks also to New Zealand friends who managed to stop by and visit.

Finally, I would like to thank my parents for their love and support, and for always encouraging me to follow my own path, even when it has taken me away to strange and distant lands.

Abstract

Cavity quantum electrodynamics (QED), the system of a single atom interacting with a single mode of a high finesse optical resonator, has tremendous potential for use in quantum logic, quantum information processing, and in enabling observation of quantum mechanical effects in the laboratory. The work of this thesis demonstrates a number of steps toward realizing these goals, by employing an experimental system with the strongest atom-field coupling achieved to date in optical cavity QED. The effects of strong coupling in cavity QED are studied for single cold atoms measured one at a time, in real time. The passage of single atoms through the cavity is employed to map out the frequency response of the system, and to demonstrate that quantum rather than semiclassical theory provides the correct theoretical model. The mechanical effects of strong coupling on single atoms are explored, these experiments demonstrating the first trapping of single atoms with single photons. Additionally, strong coupling enables high signal-to-noise ratio for monitoring atomic position at single photon field strengths; this capability is employed to investigate the motion of atoms trapped within the cavity. The transmitted cavity field is used to reconstruct the trajectories of single atoms, thereby realizing a new form of microscopy - the Atom-Cavity Microscope. Technical developments necessary to create the cavities used in this experiment are detailed. Ideas for future extensions to the experiment are proposed; a zero light-shift dipole force trap, and measurement of photon statistics of a single strongly coupled atom (which realizes a photon blockade device) are discussed.

Contents

Acknowledgements	iii
Abstract	iv
1 Introduction	1
1.1 Motivation	1
1.2 A history of my involvement in the Kimble group	3
1.3 The experimental system: Cavity QED with cold atoms	8
1.3.1 History of CQED with cold atoms	9
1.4 Observed single atom signals	12
1.5 Results	14
1.5.1 Mapping the system response with single atom transits (Chapter 3)	14
1.5.2 Trapping single atoms with single photons (Chapter 4)	14
1.5.3 Publications from graduate work	16
2 Tools for CQED with single, strongly coupled atoms	18
2.1 Theoretical treatment of the atom-cavity system	18
2.1.1 Semiclassical theoretical treatment of the atom-cavity system .	24
2.1.2 Quantum theoretical treatment of the atom-cavity system .	27
2.1.3 What's so special about a single atom?	30
2.1.4 What do we mean by a "single photon?"	32
2.1.5 Calculating mode volumes	34
2.1.6 Optical Information	35
2.1.7 Motivation for cold atoms in cavity QED	37
2.2 Overview of experimental procedures	38

2.2.1	Atom source - Cold atoms from a MOT	39
2.2.2	Optical layout: laser locking, frequency shifting.	44
2.2.3	Basic cavity design	46
2.2.4	Cavity stabilization	48
2.2.5	Heterodyne detection, data acquisition	52
2.2.6	Calibration of measured signals	54
3	Real-time cavity QED with single atoms	56
3.1	Introduction	56
3.2	Experimental apparatus	58
3.3	Single atom transit signals	59
3.4	Vacuum-Rabi splitting from single atom transits	62
3.4.1	Selection criteria for data points, generation of error-bars . . .	67
3.5	Nonlinear saturation behavior of the atom-cavity system	69
3.6	Conclusion	73
4	Experiment 2: Trapping single atoms with single-photon fields	76
4.1	Apparatus	77
4.1.1	Cavity	78
4.1.2	Optical pumping	79
4.1.3	Locking method	79
4.2	Triggering trapping, the basic idea:	80
4.3	Simulated transits	82
4.4	Effective potentials, heating rates	83
4.4.1	Comparison to a classical dipole-force trap	85
4.5	Initial results: Triggering on resonant transits	87
4.6	Triggering on upgoing transits to trap single atoms	88
4.7	Characterization of transmission oscillations	93
4.8	Experimental characterization of single-photon trapping	96
4.8.1	Histograms of transit lengths - triggered vs. untriggered . . .	96
4.8.2	Histograms of traptimes - experimental vs. simulated transits	99

4.8.3	Histograms of traptimes for different atom-cavity detunings	101
4.9	Reconstruction of atom trajectories - the ACM	103
4.10	Extensions:	107
4.10.1	Quantum servos	107
4.10.2	Measuring quantum/semiclassical distinctions	107
4.10.3	Two-atom events?	117
5	REO Mirrors	120
5.1	Fabrication, inspection and cleaning	120
5.1.1	Fabrication of cone-shaped mirrors by REO	120
5.1.2	Inspection of mirror surfaces	123
5.1.3	Cleaning 1mm tapered cone mirrors	126
5.1.4	Cleaning 7.75mm mirrors	131
5.2	Cavity construction and alignment	132
5.2.1	Basic design	132
5.2.2	Basic alignment	132
5.2.3	Gluing, baking and cavity birefringence	134
5.3	Coating measurements and modeling	138
5.3.1	Introduction	138
5.3.2	Direct transmission and loss measurements	140
5.3.3	Technical details of the model	142
5.3.4	FSR measurements	145
5.3.5	Limitations to mode volume	150
6	Ideas for future directions	155
6.1	Manipulation of AC Stark shifts in optical traps by utilizing multiple excited states	155
6.1.1	Multi-level dipole traps - the basic idea	156
6.1.2	Theory with polarizations and hyperfine sublevels	158
6.1.3	Cesium parameters	160

6.1.4 Results for a cesium trap in an optical resonator	163
6.2 Photon statistics of a single, strongly coupled atom.	170
Bibliography	184

List of Figures

1.1	Homodyne measurement of squeezed vacuum.	6
1.2	Basic components for experiments with cold atoms in cavity QED.	9
1.3	Change in the atom-cavity spectrum, and associated time-dependent probe transmission as a single atom transits the cavity mode.	13
1.4	A single atom trapped by a single photon field in cavity QED	15
2.1	Schematic: Single-atom cavity QED.	19
2.2	The presence of a single atom in the cavity leads to the double-peaked vacuum-Rabi transmission spectrum.	23
2.3	Relative transmission versus empty cavity photon number for the quantum and semiclassical theories.	29
2.4	Energy eigenvalues of the atom-cavity system as a function of number of excitations, n , and number of intracavity atoms, N	30
2.5	Saturation of the relative transmission of the atom-cavity system, in a regime where $ \hat{a} ^2$ and $\langle \hat{a}^\dagger \hat{a} \rangle$ are quite dissimilar.	33
2.6	When integrating mode function $ \psi $ to calculate the mode volume V_m , leakage of the mode into the mirror stack is a significant contribution.	36
2.7	Time-lapse series of images showing a cloud of cesium atoms falling to the cavity.	41
2.8	Switching sequence of optical and magnetic fields, for cooling and dropping the MOT.	43
2.9	Simplified layout of the optical paths used for the cavity QED interaction and detection.	45
2.10	Frequencies of the LO, lock and probe laser beams.	46
2.11	Photograph of the cavity and cavity mount.	47
2.12	Schematic of the cavity mirrors.	47

2.13	The cavity mount is isolated from vibrations by a series of copper blocks seperated by rubber spacers.	49
2.14	Noise variance $(\Delta\bar{n})^2$ versus mean intracavity photon number \bar{n} in the absence of atoms.	51
2.15	Block diagram of the electronics used in the cavity lock, data acquisition, and for triggering on single-atom events.	53
2.16	Over the frequency range 5-250MHz used in heterodyne detection, the sensitivity and gain of the detectors varies by several dB.	55
3.1	Schematic of the experimental apparatus.	59
3.2	$\bar{m}(\Delta) \equiv \langle a \rangle ^2$ as a function of probe detuning Δ and atomic positions \vec{r}_i . For an atom transiting the cavity, this <i>position dependent coupling</i> yields a <i>time dependent transmission</i>	60
3.3	Measured cavity transmission $T(t) = \bar{m}(t)/\bar{n}$ as a function of time for individual atom transits.	63
3.4	Maximum and minimum normalized transmission $T(\Delta)$ versus detuning Δ , measured via single atom events.	64
3.5	Maximum and minimum normalized transmission $T(\Delta)$ versus detuning Δ measured via single atom events, plotted on a logarithmic scale.	66
3.6	The spectrum of Figure 3.4 is generated from these individual data points. Each circle represents the height or depth of an individual atom transit.	68
3.7	Transmission T versus probe photon number \bar{n}_0 for maximally coupled atom transits for fixed $\Delta/2\pi = -20\text{MHz}$	71
3.8	Saturation of downgoing atom transits as a function of drive strength \bar{n}_0 , for probe detunings $\Delta/2\pi = \{-20\text{MHz}, -10\text{MHz}, 0\text{MHz}\}$	72
3.9	Saturation of downgoing atom transits as a function of drive strength \bar{n}_0 , for probe detunings $\Delta/2\pi = \{-20\text{MHz}, -10\text{MHz}, 0\text{MHz}\}$, and cavity detunings chosen such that $\omega_{cavity} = \omega_{probe}$	74
4.1	Schematic of the experimental apparatus.	78

4.2 An atom entering the cavity in the ground state $ a, 0\rangle$ can be pumped into the lower dressed state $ -\rangle$, causing it to become trapped.	81
4.3 Effective Potential $U(\vec{r})$ and heating rate, along the standing-wave direction, x	83
4.4 Effective Potential $U(\vec{r})$ and heating rate, along the radial direction, ρ	84
4.5 Triggered trapping with downgoing trigger signals [26].	87
4.6 Individual trapped atoms give rise to different transmission signals $\bar{m}(t)$, depending on their individual trajectories.	91
4.7 (a,b) Examples of atom transits, i.e., cavity transmission as a function of time as an atom passes through the cavity field. (c,d) Theoretical simulations of atom transits.	92
4.8 Oscillation period as a function of amplitude from experimental (a) and simulated (b) atom transits.	95
4.9 Oscillation period vs. depth of oscillations, for a series of empty cavity photon numbers $\bar{n}_t = \{0.08, 0.16, 0.31, 0.70\}$	97
4.10 Dwell time τ of single atoms in the cavity, with and without employing the triggered trapping strategy.	98
4.11 Comparison of Experimental Data and Simulated Transits - Atom dwell τ time in the cavity.	100
4.12 Trap lifetimes vary with atom-cavity detuning Δ_{ac}	102
4.13 Interchanging the atom and cavity frequencies ((a) and (b)) still results in a trapping potential, but with lower trap times.	104
4.14 Reconstructed atomic trajectories for the transits of Figure 4.7(a,b), and simulated transits of Figure 4.7(c,d).	105
4.15 Saturation of atom transit heights/depths as the empty cavity photon number \bar{n} is increased.	109
4.16 Saturation of atom transit heights/depths as a function of the mean intracavity photon number.	111
4.17 Saturation of transit heights for the detunings of the data of Figures 4.8 and 4.9.	113

4.18 At detunings $\Delta_{ac}/2\pi = -80\text{MHz}$, $\Delta_{probe}/2\pi = -115\text{MHz}$, the distinction between quantum and semiclassical theories is more pronounced than for the parameters of the data.	115
4.19 For parameters $\Delta_{ac}/2\pi = 0\text{MHz}$, $\Delta_{probe}/2\pi = -30\text{MHz}$, an even larger effect is seen at high drive strengths.	116
4.20 The best contrast between quantum and semiclassical theories is observed near resonance, here at detunings $\Delta_{ac} = 0$, $\Delta_{probe}/2\pi = -5\text{MHz}$	117
4.21 Signals (b) and (f) are suggestive of 2-atom events.	119
5.1 Two mirrors face one another to form an optical resonator.	121
5.2 Dust and scratches observed on 4 mirrors.	127
5.3 Folding lens tissue for cleaning 1mm mirrors.	129
5.4 (a) Calculated and (b) Measured transmission of coating as a function of wavelength, for a 35 layer $\lambda/4$ stack with $n_H=2.0411$, $n_L=1.455$, and center wavelength 850nm.	144
5.5 The cavity length L_{expt} measured from the Free-Spectral Range (FSR) varies about the design wavelength of the coating.	148
5.6 Mirror refractive index stack design, and resulting electric field distribution for a resonant $3\lambda/2$ cavity made from dielectric mirrors.	151
5.7 Comparison of cavity mode volume achieved with real mirrors and ideal mirrors.	152
6.1 By utilizing an additional level $ c\rangle$, the AC Stark shifts of ground state $ a\rangle$ and excited state $ b\rangle$ can be made the same.	157
6.2 Sisyphus cooling scheme.	158
6.3 Transitions in atom Cesium. We consider light shifts to the $6S_{1/2}$ and $6P_{3/2}$ levels, so only transitions involving these particular levels are shown.	161
6.4 Shifts of the Cs $6S_{1/2}$, $F = 4, M = 4$ (dotted) and $6P_{3/2}$, $F = 5, M = 5$ (solid) levels, as a function of wavelength of an applied σ^+ polarized laser field.	166

6.5 Shifts of the Cs $6S_{1/2}$, $F = 4, M = 4$ (dotted) and $6P_{3/2}$, $F = 5, M = 5$ (solid) levels, as a function of wavelength of an applied σ^+ polarized laser field (Expanded View).	166
6.6 Shifts of the Cs $6S_{1/2}$, $F = 4, M = 4$ (dotted) and $6P_{3/2}$, $F = 5, M = 5$ (solid) levels, as a function of wavelength of an applied σ^- polarized laser field.	167
6.7 Shifts of the Cs $6S_{1/2}$, $F = 4, M = 4$ (dotted) and $6P_{3/2}$, $F = 5, M = 5$ (solid) levels, as a function of wavelength of an applied σ^- polarized laser field (Expanded View).	168
6.8 Second order intensity correlation function $g^{(2)}(\tau)$, in the weak-field approximation with no detunings ($\omega_a = \omega_0 = \omega_c$).	173
6.9 Level diagram showing the lowest states of the Jaynes-Cummings ladder for the atom-cavity system, indicating detunings where photon bunching and antibunching are expected.	174
6.10 Second order intensity correlation function $g^{(2)}(\tau)$, calculated in the weak-field approximation, with the probe beam tuned to state $ -\rangle$, that is $\omega_c - \omega_0 = \omega_a - \omega_0 = g_0$	176
6.11 Second order intensity correlation function $g^{(2)}(\tau)$, calculated in the weak-field approximation, with the probe beam tuned to state $ -\rangle$, that is $\omega_c - \omega_0 = \omega_a - \omega_0 = g_0$. Ideal cavity parameters.	177
6.12 Second order intensity correlation function $g^{(2)}(\tau)$, calculated in the weak-field approximation, with the probe field tuned to be resonant with the two-photon transition to the state $ 2-\rangle$, that is, $\omega_c - \omega_0 = \omega_a - \omega_0 = g_0/\sqrt{2}$	179
6.13 Second order intensity correlation function $g^{(2)}(\tau)$, calculated in the weak-field approximation, shown by the color scale is plotted as a function of time delay τ (x axis) and probe detuning from the atom-cavity resonance (y axis).	180

6.14 Second order intensity correlation function $g^{(2)}(\tau)$, calculated in the weak-field approximation, for increasing atom number, but the same effective coupling strength $g = g_0/\sqrt{N}$	182
--	-----

List of Tables

5.1	Measured and predicted values for the cavity free spectral range (FSR).	150
6.1	Lifetimes of relevant atomic Cesium levels used in the dipole-trap calculations.	162
6.2	Summary of Matrix Elements used in the dipole-trap calculation.	163

Chapter 1 Introduction

1.1 Motivation

The principal motivation of many researchers in experimental quantum optics, and certainly my personal reason for entering the field, is a desire to observe the weird and wonderful effects of quantum mechanics in the laboratory. The experimental system of cavity quantum electrodynamics (cavity QED)[1], consisting of an atom strongly coupled to the electromagnetic mode of a nearly lossless optical resonator, is one of very few physically realizable systems in which such effects can be observed, and is the setting for the experiments described in this thesis.

To generate quantum behavior in a real physical system is more difficult than one might think, given a first theoretical introduction to quantum mechanics is typically a simple closed system, such as a single particle in a box, for which quantum weirdness is manifest. The real world, however, is not like a single particle in a box. Real particles exist in a web of connections and interactions with their neighbors, the sum of all these outweighing any particular simple interaction of interest. So if you try to ask a simple question, like looking for an entanglement between two particles, the collective effect of interactions with the outside environment usually makes the measurement result indistinguishable from that of a classical system, a process known as decoherence. This leads us to the rich study of “open” quantum systems [2], where couplings to the environment are explicitly taken into account in the formalism, and leads us to ask under what circumstances, then, can decoherence can be avoided (or at least controlled, as in the case of quantum error correction [3, 4]), allowing quantum behavior to still be observable?

The simplest solution is to create a system of single quanta, eliminating interactions which lead to decoherence, while preserving the coherent quantum dynamics of interest. This is in practice by no means a simple undertaking. We call this a regime of

strong coupling, for which the coherent quantum evolution rate of these single quanta dominates any dissipation in the system. That is, we require $g_0 > \beta \equiv \max[\Gamma, T^{-1}]$, where g_0 is the rate of coherent, reversible, evolution, T is the interaction time and Γ is the set of decoherence rates for the system. In such a strongly coupled system, the coherent quantum evolution g_0 can be exploited to create quantum superpositions and entanglements of particles, and enable measurement and processing of these quantum states before decoherence eventually washes away the quantum behavior.

Beyond merely being interesting from the laboratory perspective of being able to experimentally explore fundamental quantum mechanics, research into strong coupling with cavity QED has been fueled by the potential application of this system as a quantum device for quantum computing [5, 6], quantum state preparation [7, 8], and quantum communications [9, 10]. Cavity QED is not alone in trying to realize quantum computing. In the last few years, a handful of experimental systems have demonstrated at least some of the required quantum behavior; ranging from trapped ions [11], and trapped atoms in high-finesse cavities [6, 12] or optical lattices [13], to Josephson junctions [14] and NMR systems [15]. Promising proposals also exist for utilizing coupled quantum dots [16, 17], spins of donor atoms embedded in silicon [18], or single quantum dots coupled to microcavities [19, 20, 21]. This newfound ability to measure and manipulate the quantum states of individual quanta, one by one, is a revolutionary development in recent experimental physics. It heralds the beginning of a new era of “quantum engineering,” in which single quanta interacting by the rules of quantum mechanics are the fundamental building blocks.

The quest to create and explore interesting quantum states has been one of the primary driving forces in experimental efforts in cavity QED. A rich array of quantum effects have been predicted theoretically over the last 35 years, since the first work by Jaynes and Cummings [22], but conditions in which they can be experimentally observed have proved difficult to achieve: to realize the simple Jaynes-Cummings Hamiltonian we are required to be dealing with *single quanta*, and be in the regime of *strong coupling*. Strong coupling at the level of single atoms was first observed in 1992 [23], by an averaged measurement over a series of single atoms from a thermal

atomic beam. A significant advance in the field was made in 1996 [24], with the use of laser-cooled atoms instead of a thermal beam, allowing single atoms to be measured one at a time, in real-time.

The work of this thesis involves experiments studying the effects of strong coupling on single cold atoms, measured one at a time. In Chapter 3, the passage of single atoms through the cavity is employed to map out the frequency response of the system, and to demonstrate that quantum theory is the correct description of this system [25]. In Chapter 4 the mechanical effect of strong coupling on single atoms is explored, these experiments demonstrating the first trapping of single atoms with single photons, first reported in Ref. [26] and fully explored in Ref. [27]. In addition, being in a strong-coupling regime generates superb signal to noise for atom detection by single photon fields, enabling us to reconstruct the trajectories of single atoms inside the cavity and realize a new form of microscopy [27]. Chapter 5 details technical developments which were necessary to fabricate the optical cavities used for these measurements, and finally in Chapter 6 I present calculations of ideas which could be incorporated into the cavity QED experiment in the future; exploring a zero-shift dipole trap and the possibility for measuring photon statistics from a single strongly coupled atom.

With atoms now trapped in cavities, both via the single photon quantum fields employed here [27] and with classical dipole-force traps [28], the stage is now set for elusive measurements of quantum behavior to finally become a reality: from quantum feedback control [29, 30], to generation of single photons [8], to demonstration of quantum communications schemes [9, 10]. With these prospects, the next few years should be an exciting time for optical cavity QED.

1.2 A history of my involvement in the Kimble group

Arriving in the Kimble group in September 1994, I started work with Quentin Turchette in what was at the time the sole cavity QED lab; a somewhat daunting room full

of optical elements, vacuum parts and electronics. By late 1994 news of Shor's factorization algorithm, which essentially launched the field of quantum computation, was spreading through the experimental quantum physics community. Visits to the group by Artur Ekert and Seth Lloyd in summer and fall of 1994 helped flesh out potential applications of cavity QED to quantum computing, and catalyzed a change in our immediate experimental direction; we decided to use the existing cavity QED apparatus for a proof-of-principle demonstration that this system can provide the necessary single-quanta non-linear coupling required for quantum logic, the results published as Ref. [6].

The scheme explored was to use a Kerr-type nonlinearity generated by a single atom medium (provided by an atomic beam) in the cavity to couple together two laser fields (at the single photon level), inducing a nonlinear polarization-dependent phase shift to the transmitted photons. Decoherence could be minimized by detuning the two lasers far from the atomic resonance (to avoid spontaneous emission losses), while maintaining a significant phase shift. This experiment was an extension of the previous 1D atom [31] work of the lab, measuring phase (instead of amplitude) transmission through the atom-cavity, and measuring the conditional saturation behavior of the system using two laser fields. From these measurements we inferred the logical truth table for a "quantum phase gate." My contributions to this experiment were primarily in lab setup work and data taking, sometimes running the experiment solo, taking some of the published data while Quentin was traveling. Additionally, I proposed our novel method for measuring the phase shift of a circularly polarized beam; by probing with a linear polarization and measuring a rotation of polarization. This turned out to be an existing technique in chemistry, known as polarization interferometry. With Wolfgang Lange's invaluable computer-controlled rotating waveplate, measuring these polarization rotations was relatively simple.

In my second year, Quentin, Nikos Georgiades and I worked on an experiment to couple squeezed vacuum into the atom-cavity, in the hope of measuring an altered radiative lifetime for the atom [32]. This was a tough experiment that had already been an ongoing project for 2 years when I joined the group. It was decided that the

coupling efficiencies weren't as high as they should have been in the previous attempt, so it was worth giving it another try. The initial setup phase of this experiment involved me working with Nikos in the squeezing lab, where I learned to generate squeezed vacuum from the OPO [33] - my first example shown in Figure 1.1. Even having optimized experimental efficiencies, we still didn't see linewidth narrowing directly, something of a mystery since the simple theory predicted a measurable result. Scott Parkins, our theoretical collaborator from the University of Auckland proposed a new method: adding a coherent saturating beam, then looking for modulation in the transmission signal as the phase of the squeezed vacuum was rotated. Again, nothing was obvious, but a complicated chain of signal analysis revealed modulation peaks at the expected frequency, buried in the noise. We mapped out this modulation as a function of detuning, coherent driving strength, degree of squeezing, and atom number, but from these quantities were never able to confidently claim that we had observed linewidth narrowing.

Why were the effects so small? We are now fairly confident that this was due to using an atomic beam as an atom source, averaging over the passage of many atoms to obtain our signal. While completing the manuscript (eventually published as Ref. [34]), I did some work modeling intracavity losses arising from the atomic beam, these results in the end explained the large degradation of observed signals fairly well.

Right around this time (the squeezing experiment was wrapping up in Spring of 1996) Hideo Mabuchi, Mike Chapman and Quentin demonstrated that laser-cooled atoms from a magneto-optical trap (MOT) can be used as a source of single slow atoms for cavity QED [24], measurable one at a time, in real time. Having just spent a year plagued by the evils of atomic beams, it was very clear to all of us that cavity QED with cold atoms was the way of the future.

So, in the summer of 1996, I joined post-doc Mike Chapman to build up a new cavity QED apparatus with a cold atom source; to run in parallel with Hideo's experiment. Joined in the fall by Theresa Lynn, we started spending the QUIC (Quantum Information and Computation) grant on furnishing this new lab, the new features of this experimental setup described in Section 2.2. New smaller mirrors (described in

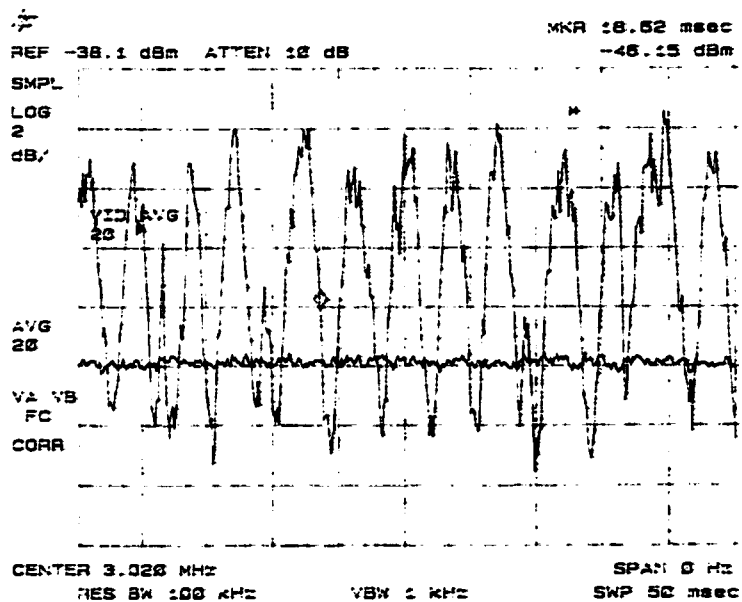


Figure 1.1: Homodyne measurement of squeezed vacuum. The horizontal line indicates the shot-noise level. The phase of the squeezing is rotated with respect to the detection beam, generating the observed oscillations. The squeezed quadrature here has noise 2dB below shot-noise; this was optimized to ~ 4 dB for use in the cavity QED experiment.

Chapter 5) allowed us to construct a shorter $10\mu\text{m}$ cavity with higher atom-cavity coupling ($g = 120\text{MHz}$) than previously achieved, and hence better signal-to-noise ratio for detecting single atoms. A year later, in the summer of 1997 the experiment was operational and we observed the first “upgoing transits” (probing on the Rabi sidebands), and were able to map out spectral response of the system using single atom events. We also measured the nonlinear saturation behavior of the atom transit signals, which due to being in a regime of strong coupling now showed a marked deviation from the predictions of semiclassical theory, and a corresponding agreement with quantum theory. These results were published as Ref. [25], and are described in detail in Chapter 3.

The next stage of this experiment was to try and trigger on these single-atom events to trap an atom in the cavity, via strong coupling to the cavity mode driven by single photon fields. Initial promising results were seen [26], but then a 12 month break occurred when our cavity failed and we spent time building new cavities, new mounts and battling vacuum problems. The main personal highlight of this period was somehow ending up in a Comedy Central spoof item on quantum teleportation, the experiment that Akira Furusawa, Jens Sorensen and Jeff had been working on in the squeezing lab [35].

Eventually we emerged from our technical nightmares with a next-generation cavity - with lower linewidth for even better signal-to-noise detection and better isolation from spontaneous emission heating. Almost immediately, in July of 1999, we saw single atoms trapped by single photons. Moreover, the exquisite signal-to-noise obtained from strong coupling allowed us to monitor the position of these trapped atoms as they moved within the cavity mode, realizing a new form of microscopy which we have called the atom-cavity microscope (ACM). These results were published as Ref. [27] in February 2000, and are described in detail in Chapter 4.

1.3 The experimental system: Cavity QED with cold atoms

The experiments described in this thesis take place in the setting of cavity quantum electrodynamics (cavity QED)[1], the system of a single atom strongly coupled to a single electromagnetic mode of a nearly lossless optical resonator (cavity). Here the quantum nature of the system stems from the fact that the rate g_0 that characterizes the coherent interaction of an atom with the cavity field for a single photon can dominate the dissipative rates for atomic spontaneous emission γ and cavity decay κ . The coherent interaction g_0 is made large by making the cavity volume small, as discussed in Chapter 2. Note that the value of g_0 is for an atom at a peak of the intracavity field mode; atoms at other positions \vec{r} see a reduced coupling strength $g(\vec{r}) \leq g_0$.

The basic components of the experiment are shown in Figure 1.2. Single atoms are provided by first laser cooling a cloud of $\sim 10^4$ cesium atoms in a magneto-optical trap (MOT)[36], then allowing this cloud to fall so that single atoms pass one at a time between the two mirrors which form the cavity, indicated by the arrows of Figure 1.2. The cavity length is locked such that only a single electromagnetic mode (TEM_{00}) is resonant in the cavity. The combined atom-cavity system is driven by a weak probe laser of strength $\lesssim 1$ intracavity photons; we measure transmission of this beam by balanced heterodyne detection to infer the intracavity field, and hence the atomic dynamics as single atoms pass through the cavity.

The light inside the cavity forms a standing-wave structure, shown in the inset to Figure 1.2. For certain choices of probe detuning and intensity, atoms can be channeled to pass through antinodes of these standing-waves (as in the experiments of Chapter 3), or even trapped in orbit at a single antinode of the field (the experiments of Chapter 4), as shown in the trajectory of the inset to Figure 1.2.

In addition to providing single-photon forces sufficient to trap a single atom, strong coupling ($g_0 > \kappa, \gamma$) means that the presence of a single atom in the cavity has a strong effect on the intracavity field. Moreover, the atom-cavity transmission changes as the

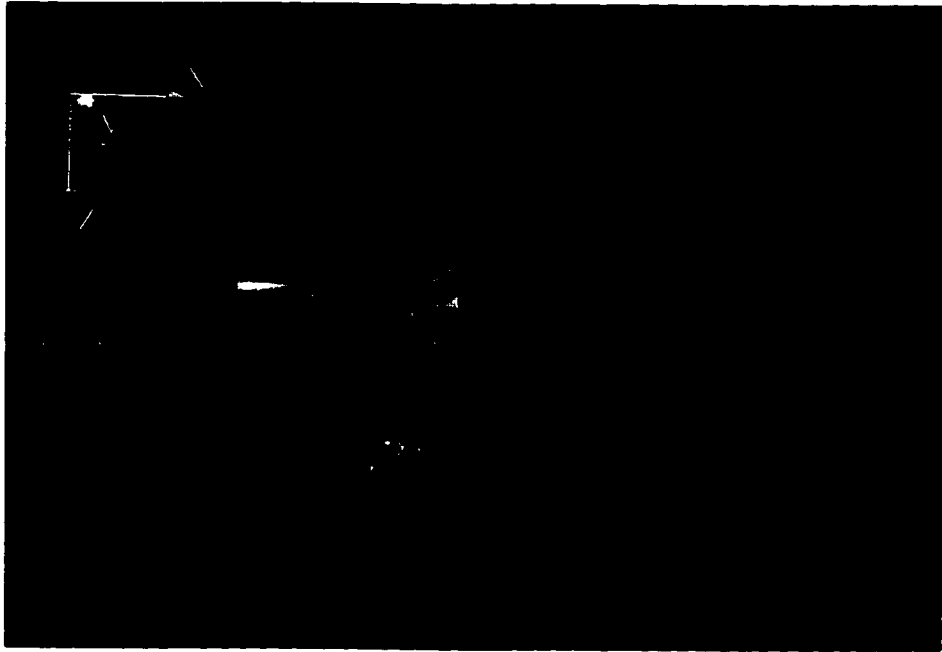


Figure 1.2: Basic components for experiments with cold atoms in cavity QED.

atom moves within the cavity mode and its coupling strength $g(\vec{r}) \leq g_0$ correspondingly varies. The position-dependent coupling strength $g(\vec{r})$ thereby gives rise to time-dependent transmission signals, with which we can track the motion of single atoms. This enhanced detection capability can be quantified by the “optical information” per atomic transit, discussed in Chapter 2.

1.3.1 History of CQED with cold atoms

Up until 1996, the quest to observe quantum effects in cavity QED experiments was plagued by difficulties caused by using thermal atomic beams as the source of atoms [34, 37], with losses due to many-atom effects described in Section 2.1.3, and Refs. [34, 37, 38]. One conceptually obvious, but practically difficult, solution was to try to combine the technology of laser cooling and trapping with that of cavity QED, to instead have a sample of cold, slow atoms as the source, or even a single trapped atom within the cavity mode. This was part of the “wish-list” of technologies in the Kimble group, mentioned by both Rob Thompson (who had been involved in

the atomic beam cavity QED experiments above) in 1994 [39], and Zhen Hu (who demonstrated a single atom trapped in a MOT) in 1995 [40] in their respective theses as a desirable next step.

Experimental efforts to integrate cold atoms with cavity QED began with microsphere (rather than Fabry-Perot) optical resonators. In 1994, Hideo Mabuchi was working on a project to couple atoms to the whispering-gallery modes of high-Q microspheres [41], which seemed most easily achieved by beginning with a very cold and dense sample of atoms. Hideo thus began work on an apparatus to form a MOT in close proximity to a microsphere. But before serious effort was put into coupling atoms from the MOT to a microsphere, it was decided to switch to a Fabry-Perot cavity; for two major reasons. Firstly, the larger mode volume of the Fabry-Perot would greatly increase the likelihood of observing passing atoms, then once the system was optimized a return to microspheres could be attempted. Secondly, in 1995 Scott Parkins visited, and told us about calculations he had carried out which showed that the mechanical forces from strong coupling would be enough to trap cold atoms dropped into a Fabry-Perot cavity [42]. Several iterations of the experiment later, Hideo and Quentin Turchette, joined by post-doc Michael Chapman, finally observed for the first time single atoms coupled one at a time to the cavity mode, in March of 1996 [24].

This new technology was so promising that a new lab was established, where myself, Michael Chapman and Theresa Lynn focused on trying to realize Scott Parkin's single-photon trapping scheme. Meanwhile, Hideo and Quentin pursued a program of trying to optimize and extend the earlier measurement to hopefully achieve atomic position measurement at the standard quantum limit. The new lab was observing atom signals by late 1997. These single-atom events were the basis for a series of experiments published in Ref. [25] in 1998. The most important of these was the mapping out of the frequency response of the atom-cavity system, and measuring its non-linear saturation behavior. Meanwhile, the microsphere experiment had been revived by David Vernooy who, working with Nikos Georgiades and Akira Furusawa, observed cavity QED coupling of cesium atoms in a vapor the mode of a microsphere

[43].

In January 1999, observation of single cold atoms in a cavity QED setting was also reported by Gerhard Rempe's group in Konstanz [44], followed up in May by an investigation of single atom dynamics by measuring photon statistics over an ensemble of single atom transits, to give information about atom dwell-time in the cavity [45].

Meanwhile, experiments in both Caltech labs were progressing nicely, with first evidence of atom trapping seen in the Hood/Lynn/Chapman lab, and the signal-to-noise improved in Hideo's experiment (now joined by post-doc Jun Ye) sufficient to demonstrate quantum-limited detection of atom transits, and a full measurement of both field quadratures in heterodyne. Both these results were published in Ref. [26] in April 1999, with a more detailed account of Hideo and Jun's experiment following in June 1999 [46].

After Hideo's graduation in early 1998, David Vernooy joined Jun Ye to work on a new experiment; to trap atoms via a classical standing-wave far off-resonant dipole-force trap (FORT), mutually resonant in the cavity with the cavity QED beam. This scheme holds tremendous promise for implementing quantum logic schemes, where ideally one would like the atom trapped independently of the cavity QED interactions. They demonstrated the remarkable achievement of a single-atom intracavity FORT lifetime of 28ms, published in December 1999 [28].

Also in 1999, in July Theresa and I finally realized Scott Parkin's trapping scheme, and saw clear signals of single atoms trapped by single photons fields. Additionally, the very high signal-to-noise generated by the large coupling in our experiment enabled us to track the trajectories of single atoms, and characterize the dynamics of single atom motion in the trap (oscillation frequencies, trap times). These results of trajectory reconstruction and oscillation frequency analysis were published in February 2000 [27]; the trap-time characterization manuscript is currently in preparation.

Shortly after our publication on single photon trapping, the Rempe group published a similarly titled manuscript in March 2000 [47] showing two examples of localized atoms and one simulated transit, but without the analysis of atom dynamics via large data sets presented in our work. From these few events an inference

was drawn that cooling of the atomic motion occurs as it hops between standing-wave well, a result which is currently under scrutiny [48], as part of a manuscript comparing characteristics of the two parameter regimes of these experiments.

1.4 Observed single atom signals

In the absence of an atom, the spectral response of the empty cavity is just its Lorentzian linewidth, shown by the dashed curve in Figure 1.3(c). However, in the presence of an atom, the strong atom-cavity coupling g_0 gives rise to a dressing of the system eigenstates and a corresponding splitting in the energy. For a single, optimally coupled atom the transmission spectrum is shown by the solid curve of Figure 1.3(c), the vacuum-Rabi spectrum. Optimal coupling is only achieved when the atom is at the point of maximum field strength (at the center of the Gaussian cavity mode). Thus as an atom falls through the cavity the coupling evolves from $g = 0$, with an empty-cavity Lorentzian transmission spectrum (dashed curve) to $g = g_0$ (solid curve) then back to $g = 0$. If the atom does not pass close to an antinode of the cavity standing-wave, a smaller $g_{max} < g_0$ will be achieved.

For an atom traversing the cavity mode (in $\simeq 75\mu s$), the position-dependent coupling gives rise to a time-dependent probe transmission [49, 50]. For two probe fields of fixed detuning (indicated by the arrows positions of Figure 1.3(c)) simultaneously illuminating the atom-cavity system and being detected in transmission with heterodyne detection, the real-time atom-cavity transmission is shown in Figure 1.3(a,b). Close to resonance (Figure 1.3(a)), transmission drops as an atom enters the cavity and the spectrum shifts from the empty-cavity Lorentzian response to the vacuum-Rabi spectrum. Transmission regularly drops by a factor of 100 at this detuning. For the same atom during the same transit but for a probe of detuning $-g_0$ (Figure 1.3(b)), the transmission correspondingly rises. For the data of Figure 1.3, the two probe fields are applied simultaneously, leading to a fundamental decrease in signal to noise over single-probe measurements due to the trade-off between reduction in shot noise and saturation of the atom-cavity response [25].

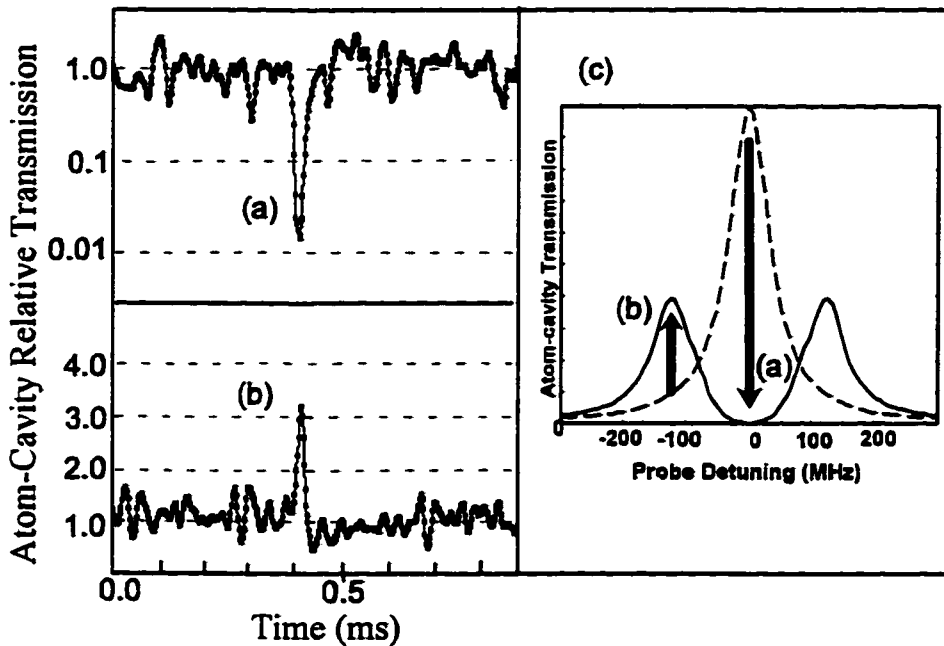


Figure 1.3: Transmission for each of two probe beams simultaneously illuminating the atom-cavity as a function of time for a single atom traversing the cavity mode. For (a) the probe detuning is -20 MHz, for (b) -100 MHz. The change in the atom-cavity spectrum which gives rise to these time traces is shown in (c). For these traces the atomic and cavity resonances are coincident, and the coupling strength $g_0/2\pi = 120\text{MHz}$.

1.5 Results

1.5.1 Mapping the system response with single atom transits (Chapter 3)

By recording atom transits such as those of Figure 1.3(a,b), the entire transmission spectrum (solid curve of Figure 1.3(c)) was mapped out [25]. This was the first time that the two-peaked spectrum had been seen via individual atom events, and served as independent confirmation of our geometrically calculated value for g_0 . Next, resonant transits (as in Figure 1.3(a)) were recorded as the intracavity photon number was increased, to map out the saturation behavior of the system. A quantum system respecting a Jaynes-Cummings ladder of states is predicted to saturate differently than the corresponding semiclassical system, due to the different structure for high-lying excitations. For our parameters the predictions differ by an order of magnitude, with the semiclassical case predicting bistability. The data of Chapter 3 shows strong agreement with the quantum master equation calculation, confirming the underlying quantum nature of the atom-field coupling and our ability to access it experimentally.

1.5.2 Trapping single atoms with single photons (Chapter 4)

Beyond simply measuring the spectral effects of strong coupling, the next phase of the experiment was to exploit it to trap single atoms using the vacuum-Rabi splitting [50, 51]. From Figure 1.3(c) it can be seen that the system has a resonance at a lower frequency (energy) with an atom present than the empty cavity resonance. That is, the lower dressed state of the atom-cavity system (the left peak of the solid curve of Figure 1.3(c)) has an energy *minimum* for an atom at the center of the cavity mode. The spatial dependence of the cavity mode (Gaussian transverse distribution, standing-wave along the cavity axis) therefore creates a series of trapping pseudo-potential wells for the atom, if a red-detuned probe field is applied to selectively populate this trapping state. For our parameters this gives a potential depth of $\simeq 5\text{mK}$, so with an initial atomic temperature of $15\mu\text{K}$ and a fall of only 2mm to the

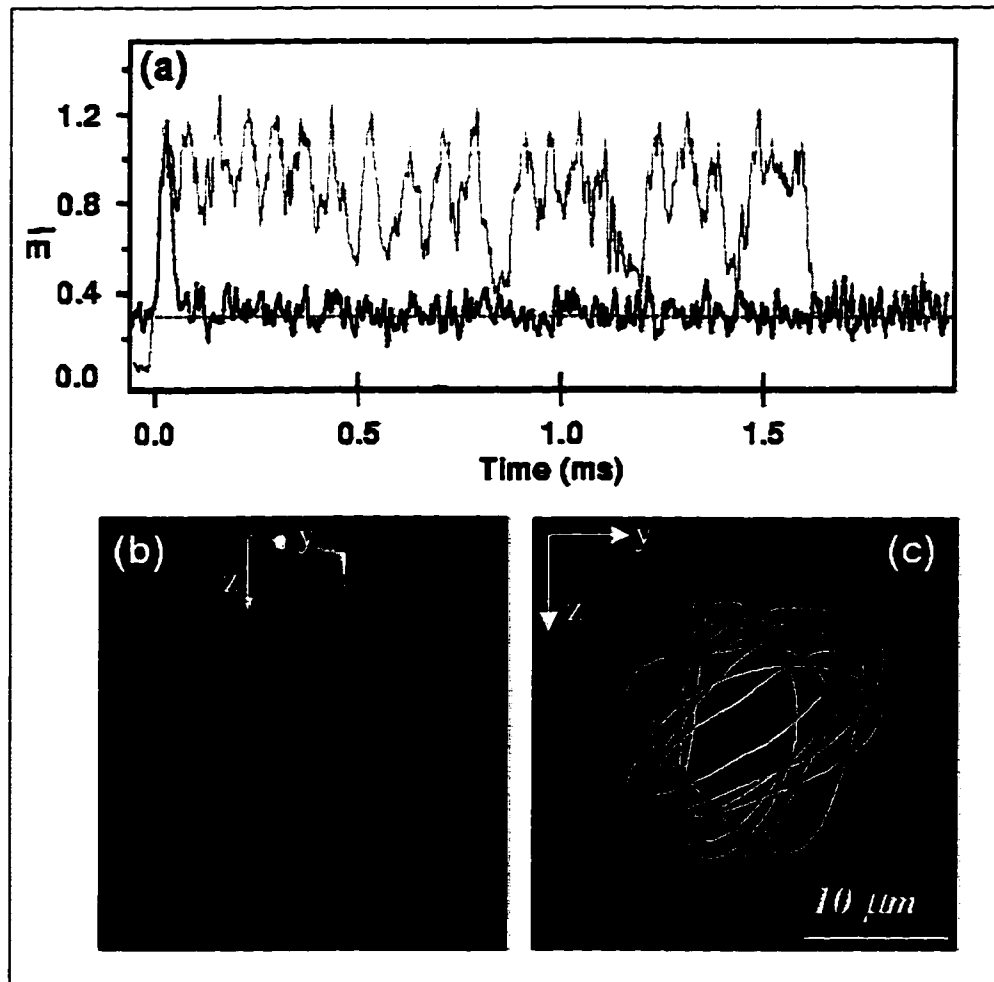


Figure 1.4: (a) Transmission of the atom-cavity for two single atom transits, with no triggering (black trace) and with the probe triggered to trap the atom (grey trace). The grey trace shows an atom trapped by an intracavity field of $\bar{m} \simeq 1$ photon mean amplitude for 1.6ms. (b) The motion of the atom lies in a plane at an anti-node of the standing-wave field. (c) The grey transmission trace can be used to reconstruct the trajectory of this trapped atom, in the plane indicated in (b).

cavity, single atoms have low enough energy to be confined in this bound state. The procedure used was first proposed and analyzed by A. S. Parkins in 1995 [42], and consists of allowing the atom to fall into the cavity with a weak probing field (which creates a shallow confining potential), then when the atom is near the center to switch up the intensity to create the deep potential and trap the atom.

Figure 1.4 shows an example of a single atom trapped using this method. The probing/trapping laser is detuned to the red, as was the case in Figure 1.3(b). The black curve of Figure 1.4(a) shows a typical transmission trace for an atom transit through the cavity when no effort to trap is made; this is the same type of signal as in Figure 1.3(b). When we trigger on the presence of an atom in the cavity and switch UP the intensity of the trapping field, traces like the grey curve of Figure 1.4(a) are seen. This example shows a single atom trapped in the cavity for $\simeq 1.6\text{ms}$, with the wiggles in transmission corresponding to the atom's motion within the trap. The nature of the atomic motion is indicated by Figure 1.4(b); single atoms are trapped at a single standing-wave antinode of the field, moving about the center of the cavity in elongated orbits, giving rise to the oscillating transmission signal of Figure 1.4(a).

These transmission oscillations can in fact be used to reconstruct the actual trajectories of single atoms. The data trace of Figure 1.4(a) yields the trajectory of Figure 1.4(c), where the plane of the atomic motion is indicated in Figure 1.4(b). This ability to track the motion of the single atom demonstrates a new form of microscopy, which we call the atom-cavity microscope (ACM).

1.5.3 Publications from graduate work

C. J. Hood, T. W. Lynn, A. C. Doherty, A. S. Parkins and H. J. Kimble, *The Atom Cavity Microscope, Single atoms bound in orbit by single photons*, Science 287, 1447 (Feb 25, 2000).

J. Ye, C. J. Hood, T. W. Lynn, H. Mabuchi, D. W. Vernooy, and H. J. Kimble, *Quantum manipulation and measurement of single atoms in optical cavity QED*, IEEE Trans. Instru. & Meas. 48, 608 (1999).

C. J. Hood, T. W. Lynn, M. S. Chapman, H. Mabuchi, J. Ye, and H. J. Kimble, *Cavity QED, where's the Q?* in Confined Photon Systems, ed. Benisty et al., Springer (1998).

C. J. Hood, M. S. Chapman, T. W. Lynn, and H. J. Kimble, *Real-time cavity QED with single atoms*, Phys. Rev. Lett. **80**, 4157 (1998).

Q. A. Turchette, N. Ph. Georgiades, C. J. Hood, H. J. Kimble and A. S. Parkins, *Squeezed Excitation in Cavity QED: experiment and theory*, Phys. Rev. A **58**, 4056 (1998).

Q. A. Turchette, C. J. Hood, W. Lange, H. Mabuchi, H. J. Kimble, *Measurement of conditional phase shifts for quantum logic*, Phys. Rev. Lett. **75**, 4710 (1995).

Chapter 2 Tools for CQED with single, strongly coupled atoms

2.1 Theoretical treatment of the atom-cavity system

We initially consider the ideal cavity QED system of a single atom (in this case cesium) coupled to the TEM₀₀ longitudinal mode of a high finesse optical cavity, shown schematically in Figure 2.1, with curved mirrors providing transverse confinement of the mode. The coherent atom-field coupling rate g_0 is given by

$$g_0 = d \cdot E = d \sqrt{\frac{\hbar\omega}{2\varepsilon_0 V_m}}, \quad (2.1)$$

where d is the atomic dipole matrix element, ω the atomic transition frequency, V_m the cavity mode volume, and $2g_0$ is the single-photon Rabi frequency. The single-photon electric field strength $\sqrt{\frac{\hbar\omega}{2\varepsilon_0 V_m}}$ is found by considering the Maxwell energy density of the electromagnetic field

$$\hbar\omega = \int \left(\frac{\varepsilon_0}{2} |E|^2 + \frac{1}{2\mu_0} |B|^2 \right) dV = \int \varepsilon_0 |E|^2 dV \quad (2.2)$$

for a single photon excitation (of energy $\hbar\omega$) confined to a volume V_m , and averaging over the optical cycle of the field. If the cavity mode volume V_m is made small, the magnitude of E for a single photon, and hence g_0 , can become large. Experimentally this is achieved both by making the cavity length short, and by using mirrors with a small radius of curvature.

The rate of dissipation is set by γ_L , the atomic dipole decay rate into modes other than the single cavity mode, and κ , the rate of decay of the cavity field. As the atomic

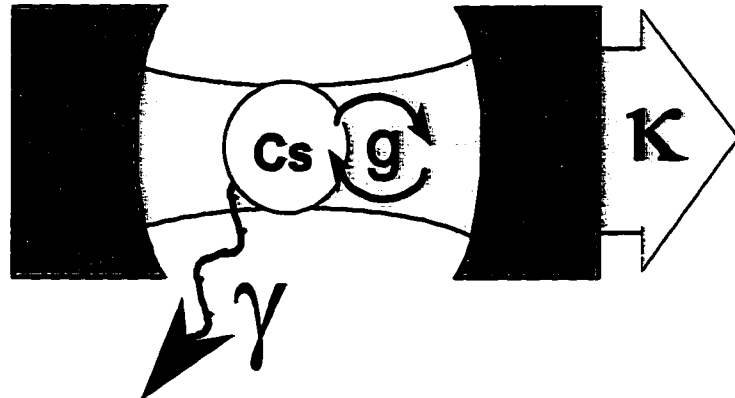


Figure 2.1: Schematic: Single-atom cavity QED.

decay is purely radiative, the rate for decay of atomic inversion $\gamma_{\parallel} = 2\gamma_{\perp}$. Also, γ_{\parallel} is essentially the same as for an atom in free space, since the solid angle subtended by our cavity mode is small ($\simeq 10^{-5}$). It should be noted that photon decay via κ does not necessarily lead to decoherence in the system, as these output photons can be measured, processed, or even used as the input to another cavity system, maintaining coherences with the atom-cavity [9, 10, 52]. Additionally, in experiments to date the atom is not indefinitely fixed within the resonator, so another important parameter is the transit time T of an atom through the cavity mode.

We can describe the atom-cavity system by two dimensionless parameters: the critical atom number, $N_0 = (2\kappa\gamma_{\perp})/g_0^2$ and critical photon number $m_0 = \gamma_{\perp}^2/2g_0^2$; the number of quanta (atoms or photons) required to significantly alter the atom-cavity response. A critical atom number of N_0 indicates that the insertion of N_0 atoms into the cavity mode has a significant effect on the transmission of a probe field through the cavity. Conversely, for a single atom in the cavity, as we turn up the power \bar{m} of a driving field while measuring the atom-cavity transmission, $\bar{m} = m_0$ indicates the intracavity photon number at which the system response to this probe becomes nonlinear.

The regime of cavity QED explored in the experiments of this thesis is that of *strong coupling*, for which the coherent evolution rate of these single quanta dominates

any dissipation in the system. That is, $g_0 > \max[\Gamma, T^{-1}]$, where g_0 is the rate of coherent, reversible, evolution for the single atom, T is the interaction time and $\Gamma = \{\gamma_\perp, \kappa\}$ is the set of decoherence rates for the system, so that for strong coupling we require

$$g_0 > (\gamma_\perp, \kappa, T^{-1}). \quad (2.3)$$

This condition also ensures that the critical parameters $(N_0, m_0) \ll 1$, that is, the atom-cavity response becomes nonlinear for a mean intracavity field of $m_0 \ll 1$ photon, and the presence of $N_0 \ll 1$ atoms in the cavity has a significant effect. As we will only ever be dealing with whole atoms, the condition $N_0 \ll 1$ means in practice that a single atom has a significant effect on the system even when it is at a position of reduced coupling strength $g(r) \ll g_0$ far from the center of the cavity mode.

In the limit of negligible dissipation and no detunings, the ideal cavity QED system of a single stationary two-level atom in an electromagnetic field is described by the Jaynes-Cummings Hamiltonian [22],

$$H = \hbar\omega\hat{a}^\dagger\hat{a} + \hbar\omega\frac{\hat{\sigma}_z}{2} + \hbar g_0(\hat{a}\hat{\sigma}^\dagger + \hat{a}^\dagger\hat{\sigma}), \quad (2.4)$$

where $(\hat{a}, \hat{a}^\dagger)$ are the field annihilation and creation operators, $(\hat{\sigma}, \hat{\sigma}^\dagger)$ the atomic lowering and raising operators (and hence $\hat{\sigma}_z$ the atomic inversion), ω the coincident frequency of the atomic transition and cavity field. This Hamiltonian can be simply diagonalized at n system excitations to find eigenstates

$$|\pm\rangle = 1/\sqrt{2}(|g, n\rangle \pm |e, n-1\rangle), \quad (2.5)$$

with (g, e) here denoting the atomic ground and excited states. These states (the Jaynes-Cummings ladder of states) represent the atom and cavity equally sharing an excitation, and have corresponding energy eigenvalues $n\hbar\omega \pm \sqrt{n}\hbar g_0$.

The *anharmonicity* of the level splittings of the Jaynes-Cummings ladder reflects the fact that quantization of the field is important in this physical system, since for a semiclassical nonlinearity the energy eigenvalues scale linearly as $n\hbar\omega \pm n\hbar g_0$. Note

that at a single excitation $n = 1$, the semiclassical and Jaynes-Cummings predictions are indistinguishable, so no conclusions about the quantum nature of the system can be drawn from a weak coherent-field measurement of the system eigenvalues.

When discussing the measurable response of the atom-cavity system we refer to *structure*, which relates to the eigenvalue spectrum discussed above and is reflected in steady-state measurements such as the atom-cavity transmission spectrum, and *dynamics*, which relates to the time-dependent behavior of the system as it makes transitions between these levels, reflected for example in a photon statistics measurement of the output cavity field.

In the regime of strong coupling $g_0 \gg (\kappa, \gamma)$, the atom-cavity must be considered as a composite coupled system, with structure and dynamics approaching those predicted by the Jaynes-Cummings Hamiltonian. Arising from this simple Hamiltonian, a rich array of quantum effects have been predicted theoretically over the last 35 years, since the first work by Jaynes and Cummings [22]. However, conditions in which they can be experimentally observed have proved difficult to achieve: we are required to be dealing with *single quanta* (atoms and photons) in the regime of *strong coupling*, both of which are experimental challenges. Many quantum optics experiments have been carried out at the single atom level [23, 53, 54, 55, 56], but these have required measurements over ensembles of atoms in a thermal beam. By contrast, the new technique of using laser-cooled atoms in cavity QED has recently enabled individual atoms to be measured one at a time, in a setting of strong coupling [24, 25, 26, 44, 45, 46, 28, 27, 47].

The *dynamical* properties of strongly coupled cavity QED systems have been explored via measurements of nonclassical photon statistics for an ensemble of atoms in an atomic beam [57, 58, 59, 12, 60] or a MOT [61]. Measurements of the *structural* properties for weak excitation yields the familiar double-peaked vacuum-Rabi transmission spectrum, arising from the splitting $\pm \hbar g_0$ in the system eigenstates for a single excitation, as was first observed for a single atom in Ref. [23]. However, as Jaynes-Cummings and semi-classical theory give rise to this same structure for weak excitation, to see a distinction between these theories (and thereby confirm

that field quantization is of critical importance to this system) we are required to be in a regime of strong driving. For stronger driving fields the nonlinear response follows from the higher lying states of the Jaynes-Cummings ladder, directly observed in the microwave domain of cavity QED [53] and reflected in nonlinear transmission measurements in optical cavity QED [25, 46], to be described in Chapter 3.

In the presence of dissipation and allowing for detunings, the Jaynes Cummings theory is extended to give a master equation for the evolution of ρ , the density operator for the joint state of the atom and cavity, given in the electric dipole and rotating-wave approximations by:

$$\begin{aligned}\dot{\rho} &= -\frac{i}{\hbar} [\hat{H}_0, \rho] + \gamma_{\perp}(2\hat{\sigma}\rho\hat{\sigma}^{\dagger} - \hat{\sigma}^{\dagger}\hat{\sigma}\rho - \rho\hat{\sigma}^{\dagger}\hat{\sigma}) + \kappa(2\hat{a}\rho\hat{a}^{\dagger} - \hat{a}^{\dagger}\hat{a}\rho - \rho\hat{a}^{\dagger}\hat{a}), \\ \hat{H}_0 &= \hbar\Theta\hat{a}^{\dagger}\hat{a} + \hbar\Delta\hat{\sigma}^{\dagger}\hat{\sigma} + \hbar g(\vec{r})[\hat{a}\hat{\sigma}^{\dagger} + \hat{a}^{\dagger}\hat{\sigma}] + \varepsilon(\hat{a} + \hat{a}^{\dagger}).\end{aligned}\quad (2.6)$$

Here ε is a driving (probe) field of frequency ω_p , $\Theta = (\omega_c - \omega_p)$ is the cavity detuning and $\Delta = (\omega_a - \omega_p)$ the atomic detuning from the probe frequency ω_p which defines the rotating frame for these equations. The coupling strength g_0 has been replaced by $g(\vec{r}) = g_0 \cos(2\pi x/\lambda) \exp[-(y^2 + z^2)/w_0^2] = g_0\psi(\vec{r})$, which reflects the position dependence of the atom-field coupling strength for an atom at position \vec{r} within the cavity mode, which varies as a standing wave in the x (cavity axis) direction and a Gaussian in the y, z directions. The full quantum theory treats \vec{r} as an operator. For these experiments the atomic kinetic energy is significantly larger than the level spacing for quantized atomic motion, and there is in addition atomic localization due to spontaneous and cavity photon emissions. This means that the atomic motion can be treated semiclassically as a wavepacket, with mean position given by the vector $\vec{r}(t)$ [62]. If spontaneous emission were to be minimized (for example by moving to a dispersive atom-cavity regime, or using Raman transitions), and the atomic motion cooled, a full account of quantized motion would need to be incorporated into the theoretical treatment, as is explored in Ref. [63].

In the strong coupling regime, numerical solution of Eq. 2.6 gives the result shown in Figure 2.2 for the frequency response of the atom-cavity as a function of

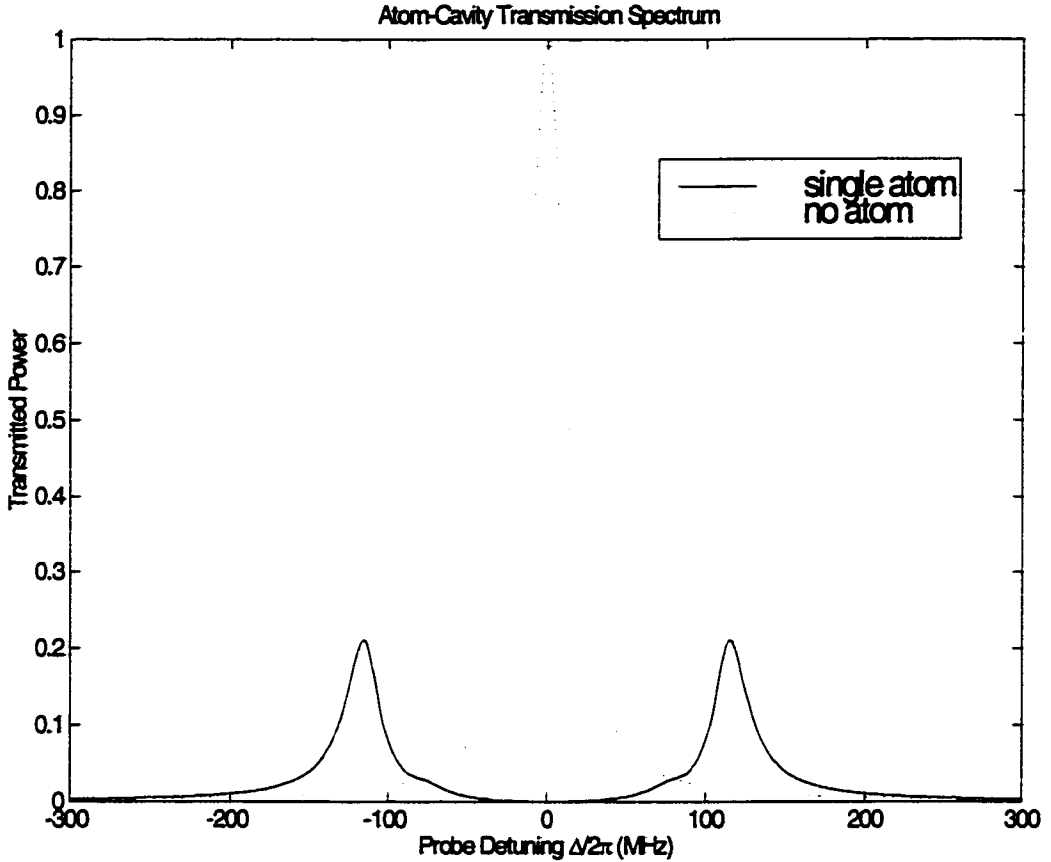


Figure 2.2: The presence of a single atom in the cavity radically changes the atom-cavity transmission spectrum, resulting in the double peaked vacuum-Rabi spectrum. Parameters are $\{g_0, \kappa, \gamma_{\perp}\}/2\pi = \{110, 14.2, 2.6\}$ MHz with $\omega_a = \omega_c$, and drive strength $\bar{n}_0 = 0.5$ photons.

probe detuning Δ . Here there is no cavity detuning ($\omega_a = \omega_c$), the cavity parameters are for the experiment of Chapter 4, $\{g_0, \kappa, \gamma_{\perp}\}/2\pi = \{110, 14.2, 2.6\}$ MHz, and the empty-cavity Lorentzian response is shown as a dotted line for comparison. The two peaks in the transmission spectrum (the vacuum-Rabi spectrum) at $\Delta = \pm g_0$ simply reflect the splittings of the Jaynes-Cummings ladder of states resulting from the coupling g_0 , and the reduction in height of these peaks from an amplitude of 1 is because the drive strength $\bar{n}_0 = 0.5$ photons $\gg m_0$, and we are therefore driving in a regime of nonlinear saturation.

By varying the cavity parameters κ and g_0 the response of the atom-cavity system to a probe field can be changed qualitatively. For example, if the cavity decay κ is

large, we find that the atom and cavity retain their distinct identities, with decay rates *modified* by their coupling. In particular, in contrast to the strong coupling regime, we can define a “1-D atom” regime by $\kappa > g_0^2/\kappa > \gamma$, in which the atomic decay to the cavity mode is at rate g_0^2/κ and we have an effectively “1-D atom” interacting preferentially with the cavity mode [31]. This was the parameter regime used in the quantum phase gate [6], and squeezed-light cavity QED [34] experiments, both of which employed the cavity as a means of enhancing an atomic interaction via the 1-D nature of the system. In these experiments, the enhancement in spontaneous emission into the cavity mode corresponds to a Purcell factor of 0.67 [6]. A more thorough discussion of the various regimes of cavity QED can be found in Ref. [38].

2.1.1 Semiclassical theoretical treatment of the atom-cavity system

Equation 2.6 for the evolution of the system density matrix can in general only be solved numerically. However, in certain restricted circumstances a semiclassical approximation can be made, which consists of factoring joint operator moments, so that for example $\langle \hat{a} \hat{\sigma}^\dagger \rangle \rightarrow \langle \hat{a} \rangle \langle \hat{\sigma}^\dagger \rangle$, and we thereby describe the field by an amplitude $\langle \hat{a} \rangle = \alpha$ rather than a quantum mechanical operator. In this approximation, the optical bistability state equation [64, 65] gives an expression for the driving field y in terms of the intracavity field x , where both y and x are scaled by the square root of the saturation parameter $\sqrt{m_0}$:

$$y = x \left[\left(1 + \frac{2C}{1 + \delta^2 + x^2} \right) + i \left(\phi - \frac{2C\delta}{1 + \delta^2 + x^2} \right) \right]. \quad (2.7)$$

Here $\delta = (\omega_c - \omega_p)/\gamma_\perp$, $\phi = (\omega_c - \omega_p)/\kappa$, and $C = NC_1$ is the N-atom cooperativity parameter, with the single atom cooperativity parameter $C_1 = g_0^2/(2\kappa\gamma_\perp)$. To relate x and y to the quantities of Eq. 2.6, the classical external driving field ε is given by $\varepsilon \equiv \kappa\sqrt{m_0}y$, and the intracavity field $\langle \hat{a} \rangle \leftrightarrow \sqrt{m_0}x$, where this correspondence for the intracavity field is not exact, because $\langle \hat{a} \rangle$ is a quantum expectation value

calculated from Eq. 2.6 while x and y are semiclassical quantities. Experimentally our detection generates a photocurrent that scales proportionally with the amplitude $\langle \hat{a} \rangle$ of a transmitted probe through the atom-cavity, which we then square to end up with a signal that scales as the amplitude squared. Consequently, for comparison with semiclassical theory, the scaled powers $X = |x|^2$ and $Y = |y|^2$ will generally be the quantities we calculate from the bistability state equation. These are scaled by m_0 from the corresponding intracavity and drive photon numbers. It should be noted that the bistability state equation gives only a steady-state solution for the system mean values ($m_0 X \leftrightarrow \langle \hat{a} \rangle$), so that it can be used to study the *structural* properties of the atom-cavity, but the *dynamical* aspects are determined by a quantum treatment of noise, expanded about the semiclassical mean values.

This semiclassical approximation is valid for large values of the critical parameters $(N_0, m_0) \gg 1$, in which case quantities obtained from Eq. 2.6 can be expanded in the small parameters $(1/N_0, 1/m_0)$ to yield Eq. 2.7; this “system-size” expansion detailed in Ref. [66] (The significance of critical parameters $N_0 = 1/C_1$ and m_0 which will be discussed in more detail in Section 2.1.1). In this regime, a collection of atoms acts as a classical nonlinear intracavity medium, and Eq. 2.7 is valid for any value of C or driving field power Y .

Even for the case of strong coupling, for which $(N_0, m_0) \ll 1$ and the above semiclassical approximation is clearly not valid, in the very restricted case of *weak excitation* (parametrization of what defines “weak” will be discussed in Section 2.1.1), we can solve for the system eigenvalues simply by noting that there is never more than one excitation in the system, so that $\langle \hat{a} \hat{\sigma}_z \rangle = -\langle \hat{a} \rangle$ and $\langle \hat{\sigma}_z \rangle = -1$, formally equivalent to a semiclassical approximation. That is, for measurements probing the *structure* of the system (such as measurement of transmission or fluorescence spectra), a semiclassical approximation is valid for weak excitation, and we therefore only expect to be able to distinguish intrinsically quantum effects in these structural measurements at higher excitation strengths.

That a semiclassical formalism correctly predicts the atom-cavity level structure for weak driving fields should not be taken as a statement that the system contains no

interesting quantum mechanics: studying the *dynamics* of a weakly driven, strongly coupled system reveals nonclassicality, such as photon antibunching of the output cavity field [59]. In fact, such photon statistics measurements such as those detailed in Chapter 6 give the largest degree of nonclassicality with weak driving fields.

Delineating parameter regions: Critical atom and photon numbers

To better parametrize exactly where semiclassical theory is valid we return to the critical atom number, $N_0 = (2\kappa\gamma_{\perp})/g_0^2$ and critical photon number $m_0 = \gamma_{\perp}^2/2g_0^2$. Most quantum systems have large critical parameters; for example a typical laser has a threshold photon number $\sqrt{m_0} \simeq 10^3 - 10^4$, indicating that adding or removing one photon has a negligible effect. Similarly, for cavity QED systems with large critical atom numbers, many atoms are required to have an effect on the intracavity light intensity, and accordingly the effect of a single atom is small. In these situations, the quantum equations (the multi-atom extensions of Eq. 2.6) governing the system can be expanded in the small parameters (m_0^{-1}, N_0^{-1}) , and the description of the system reduces again to a semiclassical prediction of the structure, with quantum noise fluctuations about these values [66]. Note that this expansion is valid for any field strength, and provides the more precise definition of the semiclassical regime, that is $(m_0, N_0) \gg 1$.

As the critical parameters are reduced, we move toward a regime where individual quanta have a profound effect on the system, so the semiclassical approximation above is no longer valid. We can expect to see uniquely quantum effects appearing in the system structure. Kimble group experiments in optical cavity QED have marked a steady progression from the semiclassical to the quantum regime: from $(m_0, N_0) \simeq 10,000$ in 1981 to recent experiments with $(m_0, N_0) \simeq 0.001$ [27].

In the intermediate regime of $(m_0, N_0) \simeq 1$ there is some disparity between the quantum and semiclassical theories; however, even for one experiment with $(m_0, N_0) = (0.02, 0.9)$, this difference could not be resolved experimentally [31, 38]. In contrast, for systems with *small* critical parameters $(m_0, N_0) \ll 1$, marked differences between the theories can readily be observed. One experiment with $(m_0, N_0) = (0.0002, 0.015)$,

described in Chapter 3, clearly demonstrates such a difference [25].

Finally, we note that the “weak” excitation regime, for which the system response is linear and a semiclassical approximation is valid, can now be parametrized by referencing the intracavity photon number \bar{m} to the saturation photon number m_0 , with “weak-field” meaning $\bar{m} \ll m_0$. Note that for our current parameters of $m_0 \simeq 10^{-4}$, we are not experimentally in the limit of weak excitation, as field strengths of $10^{-2} < \bar{m} < 1$ are required for acceptable signal-to-noise ratio.

2.1.2 Quantum theoretical treatment of the atom-cavity system

In regimes where semiclassical theory is not valid, the transmission of the atom-cavity system (for a single atom) can be found by numerical solution of the quantum master equation (Eq. 2.6) for the steady-state value of ρ [67]. In this formalism, we express decay of the system via cavity decay or atomic spontaneous emission respectively by the “jump” operators,

$$L_c = \sqrt{2\kappa a} \quad (2.8)$$

$$L_a = \sqrt{2\gamma_\perp}\sigma, \quad (2.9)$$

and re-express the master equation in terms of the superoperator \mathcal{L} , where (with $\hbar = 1$)

$$i\dot{\rho} = \mathcal{L}\rho = [H_0, \rho] - \sum_j \frac{i}{2}(L_j^\dagger L_j \rho + \rho L_j^\dagger L_j - 2L_j \rho L_j^\dagger). \quad (2.10)$$

To compare the results obtained by numerical solution to Eq. 2.10 and the semiclassical bistability state equation, plotted in Figure 2.3 is relative transmission versus empty cavity photon number for the quantum and semiclassical theories, that is, $m_0 X/m_0 Y$ vs. $m_0 Y$ in the semiclassical case, and \bar{m}/\bar{n} vs. \bar{n} in the quantum case, where $\bar{m} \equiv |\langle \hat{a} \rangle|^2$ with an atom present, and \bar{n} is the corresponding value in the absence of an atom. Referring back to Figure 2.2, for the quantum curve of Figure 2.3 we plot the ratio of the two curves of Figure 2.2, at the particular detuning

$\Delta = 0$, and as a function of driving strength. In Figure 2.3(a), cavity parameters are $g_0 = \kappa = 2\gamma_{\perp}$, so that $(m_0, N_0) = (0.125, 1)$, and there are no detunings ($\omega_a = \omega_c = \omega_p$). Here it can be seen that for critical parameters $(m_0, N_0) \lesssim 1$, the semiclassical theory predicts well the nonlinear saturation behavior of the system, even though this theory is only strictly valid for $(m_0, N_0) \gg 1$. In contrast, the experimental parameters of Chapter 3 $\{g_0, \kappa, \gamma_{\perp}\}/2\pi = \{117, 45, 2.6\}$ MHz, with $(m_0, N_0) = (2.5 \times 10^{-4}, 0.017)$ yield the curves shown in Figure 2.3(b), which show a clear distinction between the theories. The data of Chapter 3 explore this quantum/semitclassical distinction, and show agreement with the quantum predictions. Finally, Figure 2.3(c) shows the same calculation for the “dream” cavity with $\{g_0, \kappa, \gamma_{\perp}\}/2\pi = \{647, 56, 2.6\}$ MHz with $(m_0, N_0) = (8 \times 10^{-6}, 7 \times 10^{-4})$ described in Chapter 5, showing an even larger distinction between quantum and semiclassical theories.

While the weak-field agreement of the quantum and semiclassical theories remains valid in Figure 2.3(c), it can be seen that the saturation characteristics of the quantum and classical theories are becoming increasingly divergent as (m_0, N_0) become smaller, with the general trend that the quantum theory starts to saturate sooner, then takes longer for the signal contrast to finally disappear, as was investigated in Ref. [38]. In Figure 2.3(c), the quantum theory has begun to saturate a factor of 10 lower than the semiclassical turning point m_0 , and it can be seen that as we push the technical edge of making (m_0, N_0) increasingly smaller, the semiclassical theory will become increasingly irrelevant to describing the nonlinear behavior of the system.

Another interesting point to consider is that the final saturation in signal contrast moves to *higher* empty cavity drive strengths as (m_0, N_0) decrease. This can be simply understood: the weak-field relative transmission for a single-atom cooperativity C_1 is given by $(\bar{m}/\bar{n})_{\text{weakfield}} = 1/(1 + 2C_1)^2 = \{0.11, 7 \times 10^{-5}, 1.2 \times 10^{-7}\}$ in the three cases shown in Figures 2.3. The empty cavity field \bar{n} corresponding to a with-atom field \bar{m} of strength $\bar{m} = m_0$ is then $\bar{n} = (1 + 2C_1)^2 m_0 = \{1.1, 3.5, 66\}$ photons for these 3 cases, so it takes increasingly higher driving fields to access the nonlinear regime in which the system saturates. In the strong coupling regime, $(1 + 2C_1)^2 m_0 \approx (g_0^2/\kappa\gamma_{\perp})^2 (\gamma_{\perp}^2/2g_0^2) = (g_0^2/2\kappa^2)$, so an empty cavity driving field of $\bar{n} \leq g_0^2/2\kappa^2$ gives

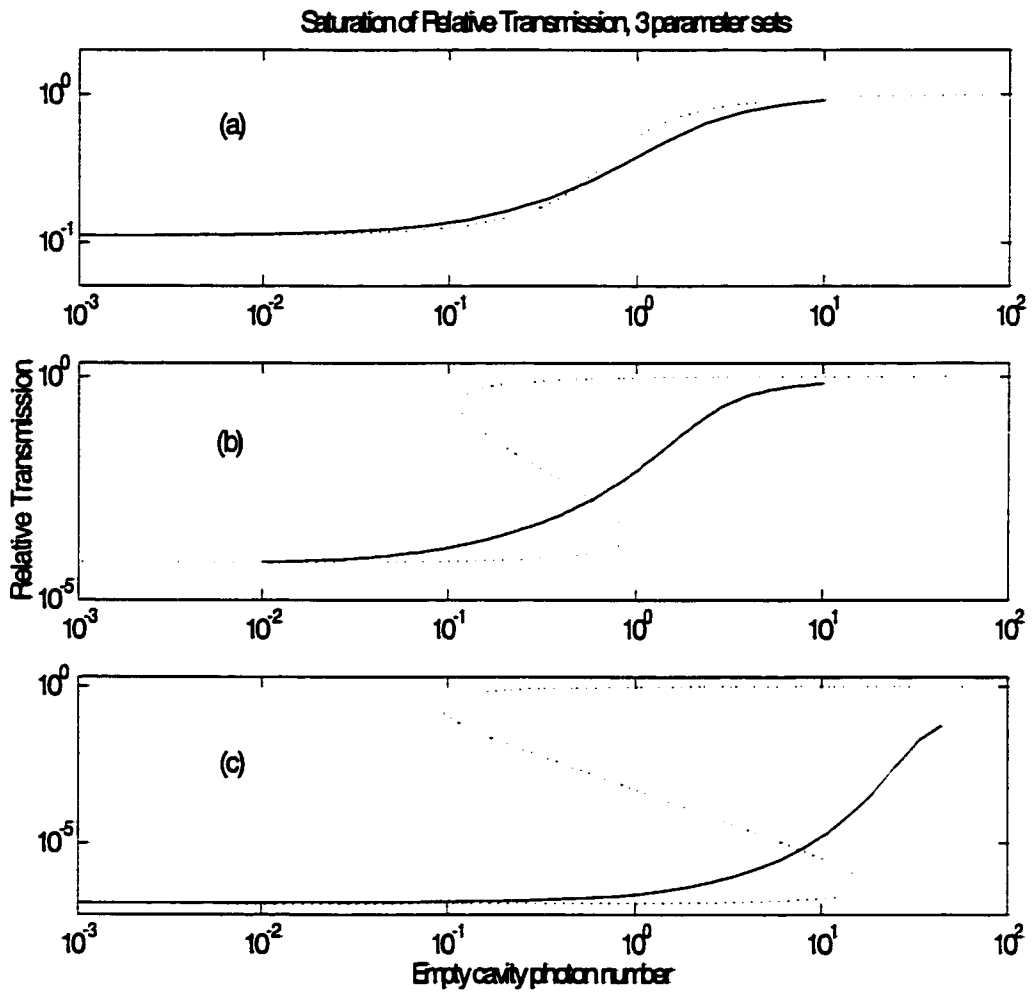


Figure 2.3: Relative transmission versus empty cavity photon number for the quantum (solid) and semiclassical (dotted) theories. Cavity parameters are (a) $\{g_0, \kappa, \gamma_{\perp}\}/2\pi = \{5.2, 5.2, 2.6\}$ MHz, (b) $\{g_0, \kappa, \gamma_{\perp}\}/2\pi = \{117, 45, 2.6\}$ MHz, and (c) $\{g_0, \kappa, \gamma_{\perp}\}/2\pi = \{647, 56, 2.6\}$ MHz, with $(\omega_a = \omega_c = \omega_p)$ for all traces.

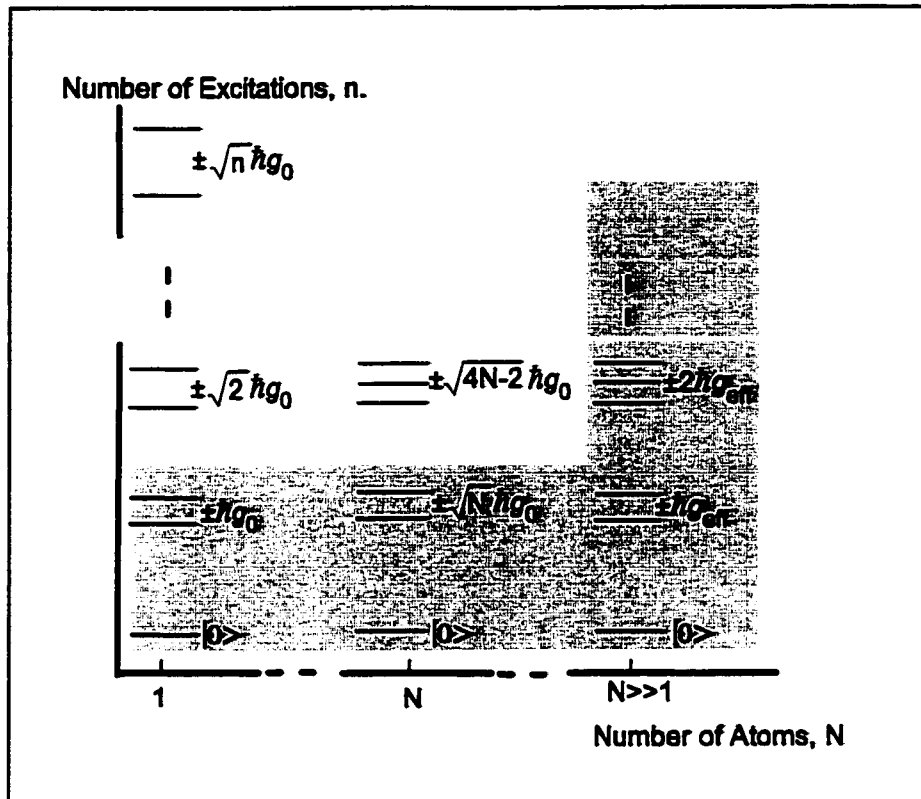


Figure 2.4: Energy eigenvalues of the atom-cavity system as a function of number of excitations, n , and number of intracavity atoms, N . In the shaded region semiclassical theory correctly predicts these eigenvalues.

a weak-field response with an atom in the cavity.

2.1.3 What's so special about a single atom?

Given that a single intracavity atom can have a profound effect on the intracavity field, the question arises as to whether this effect can be further enhanced by increasing the number of atoms. Returning to the case of a lossless interaction, the extension of the Jaynes-Cummings ladder of states to the case of N atoms [68, 69] is summarized in Figure 2.4, where the level structure of the atom-cavity system is plotted as a function of the number of interacting atoms. For one atom the structure is the familiar Jaynes-Cummings ladder, with the n -excitation levels split by $\pm \hbar g_0 \sqrt{n}$ in energy.

Moving to larger atom numbers (N), we notice that magnitude of the 1-excitation

vacuum-Rabi splitting scales as \sqrt{N} , and are hence led to define an *effective* coupling strength $g_{\text{eff}} = g_0\sqrt{N}$. Making this identification suggests that N atoms might act as one *effective* atom of coupling strength g_{eff} , following a Jaynes-Cummings Hamiltonian. Looking more closely at the higher-lying excitations shows that this is clearly *not* the case. The 2-excitation splitting is $\pm\hbar g_0\sqrt{4N - 2}$, which for $N \gg 1$ tends to the energy eigenvalues expected for *classical* coupled oscillators, $\pm 2\hbar g_{\text{eff}}$.

In the limit of large atom number $N \gg 1$, it therefore follows that semiclassical theory yields the correct values for the structure of the system irrespective of drive strength. Additionally, the quantum and semiclassical descriptions only deviate for $n \geq 2$ excitations, so it should not be surprising that semiclassical theory is also valid in the regime of weak excitation, as was already found.

Additional considerations with distributions of atoms

In cavity QED experiments which use a thermal atomic beam as an atom source, there is by nature a spatial distribution of atoms within the finite cavity mode, and a temporal variation of this distribution. Although these atoms may be collectively strongly coupled in the sense of $g_{\text{eff}} = g_0\sqrt{N}$ being large [23, 54], quantum effects are made difficult to observe by the presence of many atoms as discussed in Section 2.1.3, even when the effective atom number in the cavity mode less than one. In addition to the degradation in “quantumness” when moving from single atoms to N atoms, if the *distribution* of atoms varies spatially and temporally there are additional complications. In particular, if $\psi(r)$ is the mode function of the cavity field, then the effective atom number $N_{\text{eff}} = \sum_{i=1}^N |\psi_i|^2$ gives rise to effective coupling $g_{\text{eff}} = g_0\sqrt{N_{\text{eff}}}$ for the single photon excitation; however for excitations of 2 photons the splitting is modified to $\pm\hbar g_0\sqrt{4N_{\text{eff}} - 2M/N_{\text{eff}}}$ where $M = \sum_{i=1}^N |\psi_i|^4$ [37]. That is, various atomic distributions of the same N_{eff} will each produce different structure in the nonlinear spectrum.

Also, temporal variations in the atomic distribution lead to a time variation of g_{eff} , and a resulting averaging of output spectra over the experimental detection time. Intrinsic to thermal beams as an atom source, this effect has led to the in-

ability of optical cavity QED experiments to directly and unambiguously resolve the higher lying states of the Jaynes-Cummings ladder [37, 70], and has been a principal motivation in moving to laser cooling as a source of single atoms.

2.1.4 What do we mean by a “single photon?”

In all of our experiments, we drive the atom-cavity with weak coherent fields, but we often speak of “single photons” or “single photon fields.”

To begin with “single photon fields,” for an intracavity field characterized by moments of the operator \hat{a} , two measurable quantities are of interest to us; $|\langle \hat{a} \rangle|^2$, which is the quantity measured via our heterodyne detection, and $\langle \hat{a}^\dagger \hat{a} \rangle$, the mean photon number of the intracavity field, which would be measured via photon counting of the output cavity field. For a coherent field (as is the case in the absence of an atom), $|\langle \hat{a} \rangle|^2 = \langle \hat{a}^\dagger \hat{a} \rangle$. We often choose to work with fields of mean field amplitude $|\langle \hat{a} \rangle| \simeq 1$, in which case the mean amplitude, power, and photon number are equal, $|\langle \hat{a} \rangle| = |\langle \hat{a} \rangle|^2 = \langle \hat{a}^\dagger \hat{a} \rangle = 1$. Typically this is what is meant by a “single photon field,” although of course the actual distribution of photons is a Poisson stream, with an *average* photon number in the cavity at any time being, for example, one photon.

With an atom in the cavity the picture is more complicated. As shown in Figure 2.5, for some drive strengths the values for $|\langle \hat{a} \rangle|^2$ and $\langle \hat{a}^\dagger \hat{a} \rangle$ of the intracavity field can be different by an order of magnitude. In this regime, when discussing a measured field $\bar{m} = |\langle \hat{a} \rangle|^2 = 1$ with an atom present, we can still call this a “field with mean amplitude 1 photon,” or a “field strength of 1 photon” as these refer to the amplitude $|\langle \hat{a} \rangle|$. However, this state does not have a “mean intracavity photon number” of one. That $\langle \hat{a}^\dagger \hat{a} \rangle \gg |\langle \hat{a} \rangle|^2$ indicates that a substantial portion of the driving field is re-radiated into the incoherent part of the atom-cavity spectrum, to which our coherent heterodyne measurement is insensitive, except to add a small contribution to the noise spectrum. A photon-counting measurement would collect all photons radiated into the cavity mode, yielding $\langle \hat{a}^\dagger \hat{a} \rangle$. For a Poisson stream of photons, $|\langle \hat{a} \rangle|^2 = \langle \hat{a}^\dagger \hat{a} \rangle$, but this does not necessarily mean that $|\langle \hat{a} \rangle|^2 \neq \langle \hat{a}^\dagger \hat{a} \rangle$ signifies nonclassical (or interesting)

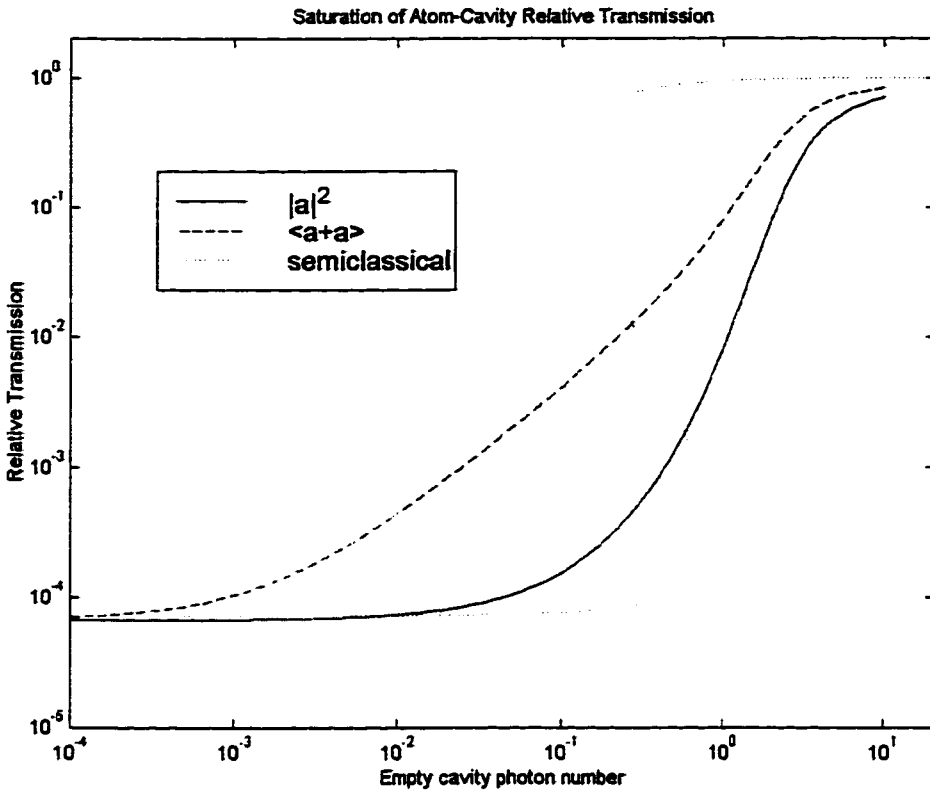


Figure 2.5: Saturation of the relative transmission of the atom-cavity system. As the system saturates, values for $|\hat{a}|^2$ and $\langle \hat{a}^\dagger \hat{a} \rangle$ are quite dissimilar. Parameters are $\{g_0, \kappa, \gamma_\perp\}/2\pi = \{117, 45, 2.6\}$ MHz with $\omega_a = \omega_c$.

photon statistics: for example, a thermal distribution and a squeezed vacuum state both have $\langle \hat{a} \rangle \equiv 0$ and $\langle \hat{a}^\dagger \hat{a} \rangle > 0$.

Having dealt with “single photon fields” we now move to discuss what we mean by a “single photon.” Quantization of the electromagnetic field inside the cavity treats the field as a quantized harmonic oscillator, of which the n-photon Fock states $|n\rangle$ are energy eigenstates. Technically then, a “single photon” is the 1-photon Fock state $|1\rangle$ of the electromagnetic field.

The question to be answered then, is when we drive the cavity with a weak coherent state, is this quantization of the intracavity field into photons significant, or should we restrict our discussion to field amplitudes $\langle \hat{a} \rangle = \alpha$ and combinations thereof?

This can be addressed by returning to the discussion of Section 2.1.2, where quantum (Eq. 2.6) and semiclassical (Eq. 2.7) theoretical descriptions of the atom-cavity were contrasted. The essence of the semiclassical approximation is that fields are treated as amplitudes $\langle \hat{a} \rangle = \alpha$ rather than operators \hat{a} , that is, in the quantum theory quantization of the cavity field into photon states is explicit, while in the semiclassical theory it is absent. Thus, if we can experimentally observe structure and dynamics in the atom-cavity system that are described only by a full quantum treatment (and are at odds with semiclassical theory), we are justified in speaking of the intracavity fields in terms of photons, and photon states. In this regime, we can think of our incident coherent field as being decomposed by the atom-cavity system into a basis of Fock states, processed in this basis, then reassembled into an emitted cavity field which is no longer a coherent state.

The measurements of Chapter 3 show such a quantum-semiclassical distinction in the system structure, justifying this picture of a quantized intracavity field.

2.1.5 Calculating mode volumes

The electric field distribution within the cavity $E(\vec{r}) = E_0\psi(\vec{r})$ is determined by a spatially varying mode function $\psi(\vec{r})$, and the corresponding energy stored in the electric field for a single photon is calculated by integrating over this mode function to obtain a mode volume V_m ;

$$\hbar\omega \propto \int |E|^2 dV = E_0^2 \int (|\psi(\vec{r})|^2 dV) = E_0^2 V_m. \quad (2.11)$$

Assuming the mode is of the form $\psi(\vec{r}) = \cos(2\pi x/\lambda) \exp[-(y^2 + z^2)/w_0^2]$, the mode volume V_m obtained (for a cavity of length L_{eff}) is

$$V_m = \int (|\psi(\vec{r})|^2 dV) = \frac{\pi}{4} w_0^2 L_{eff}. \quad (2.12)$$

This assumes that the cavity mode has hard edges at $\pm L_{eff}/2$ and of pure sinusoidal standing-wave form. However, as described in more detail in Chapter 5, the physical

mirrors that we use in the experiment are composed of a $\simeq 35$ layer dielectric stack of alternating $\lambda/4$ layers high and low index materials. The total thickness of this coating is $\simeq 5\mu\text{m}$, and penetration of the mode into this coating is not negligible for cavity lengths of less than a few tens of microns.

To calculate $\psi(\vec{r})$ and V_m including this leakage into the mirror coatings, we first note that for an electric field in a dielectric, the single-photon stored energy is modified to

$$\hbar\omega \propto \int (D \cdot E) dV = \int n^2 |E|^2 dV = E_0^2 V_m, \quad (2.13)$$

where the mode volume is now determined by the integral

$$V_m = \int n^2(\vec{r}) |\psi(\vec{r})|^2 dV, \quad (2.14)$$

with $n(\vec{r})$ is the material refractive index at position \vec{r} . Calculations for the form of $n^2(\vec{r})|\psi(\vec{r})|^2$ are made in Chapter 5 for the mirrors used in the experiment of Chapter 4, with one example shown in Figure 2.6. It can be seen that for this $3\lambda/2$ cavity, the leakage of the mode into the mirrors has a sizeable impact on the mode volume, in this case the coupling strength g_0 calculated is reduced to 80% of what would have been expected from a hard-edged cavity of length $L = 3\lambda/2$.

In the numerical integration of Eq. 2.14 over calculated field distributions such as the example of Figure 2.6, one subtlety arises - the mirrors have finite transmission, so there is a (constant amplitude) traveling-wave component to the mode which extends outside the cavity mirrors. Consequently, if the integration limits were taken to $x = \pm\infty$, the integral for V_m would also be infinite. I have chosen to truncate the mode at the outer edges of the mirror coating stack.

2.1.6 Optical Information

Over the last few years the Kimble group has pioneered the use of laser-cooled atoms in cavity QED [24, 25, 26, 46, 28, 27], enabling experiments with single atoms, one at a time. Previous experiments using atomic beams required averaging over many atom

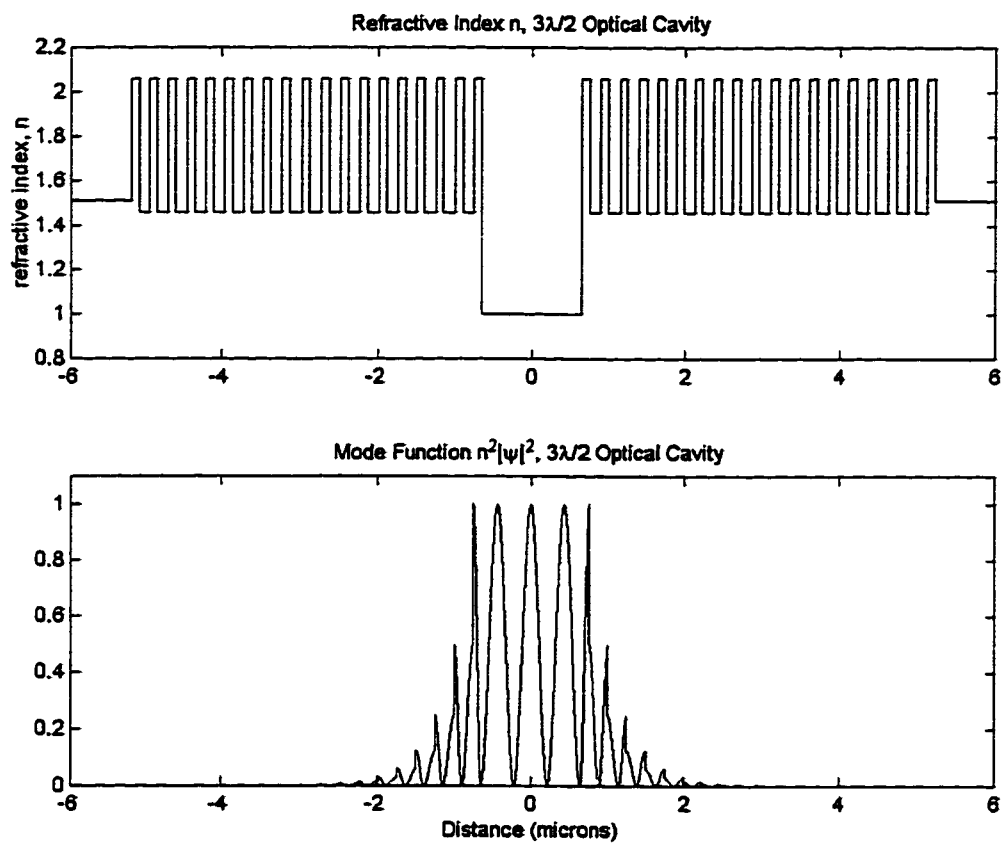


Figure 2.6: When integrating mode function $|\psi|$ to calculate the mode volume V_m , leakage of the mode into the mirror stack is a significant contribution.

transits to extract any useful data. To quantify this information rate, we derive the *optical information* I [71], which is roughly the number of photons obtained as signal for a single atom traversing the cavity in time T with photon detection efficiency α , and is given by

$$I = \frac{\alpha g_0^2 T}{\kappa}. \quad (2.15)$$

For the parameter of Chapter 3, this yields $I \simeq 54000\pi$, compared to $I \simeq \pi$ for previous atomic beam experiments. This vast increase in signal allows for the real-time monitoring and manipulation of single atoms as they traverse the cavity mode.

The optical information is derived as follows for our system with $g_0 > \kappa > \gamma$. As discussed in Section 2.1.2, when driving the atom-cavity on resonance, an intracavity field of mean photon number $\bar{n} = g_0^2/2\kappa^2$ is reduced in power to the saturation photon number m_0 when an atom enters the cavity. Photons are emitted from the cavity at rate 2κ , so the photon flux out of the cavity is reduced by $\simeq g_0^2/\kappa$ photons/sec, or a total of $I = g_0^2 T / \kappa$ photons over time T . No increase in I is obtained by further increasing the drive strength, as the signal contrast reduces. Measurement of the reflected (rather than the transmitted) cavity field would give a corresponding increase (rather than a decrease) of photon counts by I .

If the probe detuning is chosen to be $\Delta \simeq g_0$, so that the probe is tuned to one of the vacuum-Rabi sidebands (the two peaks of Figure 2.2), numerical solutions suggest that the optical information obtained for a single atom transit is of similar magnitude to the case of resonant driving, but derivation of an analytical expression is more troublesome.

2.1.7 Motivation for cold atoms in cavity QED

From the theoretical discussion above, two principal motivating factors suggest that cold, slowly moving atoms would be a better atom source for cavity QED experiments than fast thermal atomic beams.

1. With cold atoms, single atoms can be isolated one at a time, avoiding the debilitating losses discussed in Section 2.1.3 intrinsic to atomic-beam ensembles of

atoms.

2. The transit time T of a single untrapped atom falling through the cavity mode is increased by a factor of $\simeq 5000$, so the optical information obtained is large enough to monitor single atom trajectories with high bandwidth, rather than having to average over the passage of many individual atoms. The high values obtained for the optical information mean that this measurement strategy can in fact approach the standard quantum limit for the measurement of atomic position, i.e., the point at which we extract the maximum amount of information allowed by the principles of quantum mechanics [72].

In addition, there is a third important and interesting consequence of the integration of strong coupling with cold atoms. The kinetic energy E_k associated with the slow atomic motion can be smaller than the interaction energy $\hbar g_0$ of the atom-cavity coupling. This means that the strong coupling interaction between atom and cavity will then unavoidably have a significant mechanical effect on the atomic motion. In the results of Chapter 3, we see that the single photon coupling energy $\hbar g_0$ causes atoms trajectories to be channeled toward (or away from) maxima of the intracavity field, depending on probe detuning. In Chapter 4, these same quantum coupling forces are exploited to trap single atoms in the cavity with single photon fields.

2.2 Overview of experimental procedures

Many of the procedures employed and equipment used in this experiment are very similar to those of previous Kimble group cavity QED experiments. In particular, I would point to Quentin Turchette's Ph.D. thesis [38], which provides a more detailed overview of the following topics: Locking the Ti:Sapphire laser with a FM saturation lock, probe beam generation with the traveling-wave modulator, heterodyne detection, and measurement of heterodyne detection efficiency. I will focus here primarily on aspects of the experiment which are different from these earlier incarnations.

2.2.1 Atom source - Cold atoms from a MOT

From the theoretical discussion presented in Section 2.1.7, the advantages of using cold atoms rather than a fast, thermal atomic beam emerge: single atoms can be observed one at a time in real-time with high bandwidth, losses due to many-atom effects are greatly reduced, and we can expect to see interesting consequences of strong coupling on the center-of-mass atomic motion.

The setup used here to provide single atoms for the cavity QED interactions to be studied is an adaptation of apparatus used in the first cold-atom experiments by Hideo Mabuchi and collaborators [24, 73]. A cloud of $\simeq 10^4$ cesium atoms is first collected in a magneto-optical trap (MOT) [36], situated between 2mm and 5mm above the cavity mode. In the initial experiments of Chapter 3, the MOT was loaded from an atomic beam. While this helped keep the background pressure in the chamber low ($\simeq 10^{-8}$ Torr), few atoms were captured in the MOT because no beam-slowing was being employed. We soon moved to instead running the entire chamber as a Cesium vapor cell, since significantly more atoms were collected in this configuration. The edges of the MOT beams are aligned to clip on the cavity mirrors, so that a MOT can be made as close to the cavity as possible, thereby minimizing the kinetic energy of atoms entering the cavity mode. This minimum trap height is 1.5mm, the radius of the mirror substrates.

Sub-Doppler cooling

Once atoms have been collected, the MOT laser beams are reduced in intensity and detuned further to the red, and the magnetic field coils switched off, to provide sub-Doppler cooling for 5 to 15ms. The intensities and detuning are adjusted operationally to produce the coldest atom cloud, with the temperature measured by monitoring the free expansion rate of the atom cloud. Temperatures of $15\text{-}20\mu\text{K}$ are typical after sub-Doppler cooling. The MOT beams are then switched off, and the atoms allowed to fall under gravity toward the cavity mirrors. Figure 2.7 shows a time-lapse sequence of CCD images of the cloud of atoms as it falls, from an initial height of 15mm in

this series of images.

To interact with light in the cavity mode, an atom must fall through the $9\mu\text{m}$ gap between the edges of the mirrors and also through the waist $w_0 \simeq 14\mu\text{m}$ of the Gaussian mode of the resonator. As a result, even with 10^4 atoms initially, only one or two atoms are observed crossing the standing-wave mode of the cavity each time the MOT is dropped.

MOT coils

The main magnetic field coils required to form the MOT are wound directly onto the outside of the vacuum chamber. Heat generated from these coils had an unexpectedly large effect, heating the chamber which caused both an increase in chamber pressure, and undesired changes in cavity length and alignment. To counteract this heating, copper piping was wound directly over the field coils to run cooling water. With both the coils and cooling water on, several hours are required for the chamber temperature to stabilize. Additional smaller pairs of coils (trim coils) zero the magnetic field at the site of the MOT, so that when the atoms are released they expand freely, rather than feeling a force from a residual magnetic field. Good zeroing of the fields is also required for effective sub-Doppler cooling.

Finally, a single large bias coil directly above the chamber provides a field to shift the position of the MOT, from $\simeq 15\text{mm}$ above the cavity (as pictured in Figure 2.7) with this coil off, to $\simeq 3\text{mm}$ above with this bias field on. For the experiments of Chapter 4, the cavity position within the chamber was raised, and ended up slightly too high - covering the position where the MOT would form. The bias coil was used in this case to raise the MOT position to 2-3mm above the cavity.

MOT lasers and MOT beam layout

The MOT beams are provided by two home-built grating-stabilized diode lasers [74]. The trapping laser is detuned 10-30MHz to the red of the {Cs F=4→5} hyperfine component of the D2 line ($6S_{1/2} \rightarrow 6P_{3/2}$ transition). This detuning is achieved with two acousto-optic modulators (AOMs). The laser is locked directly using FM saturation

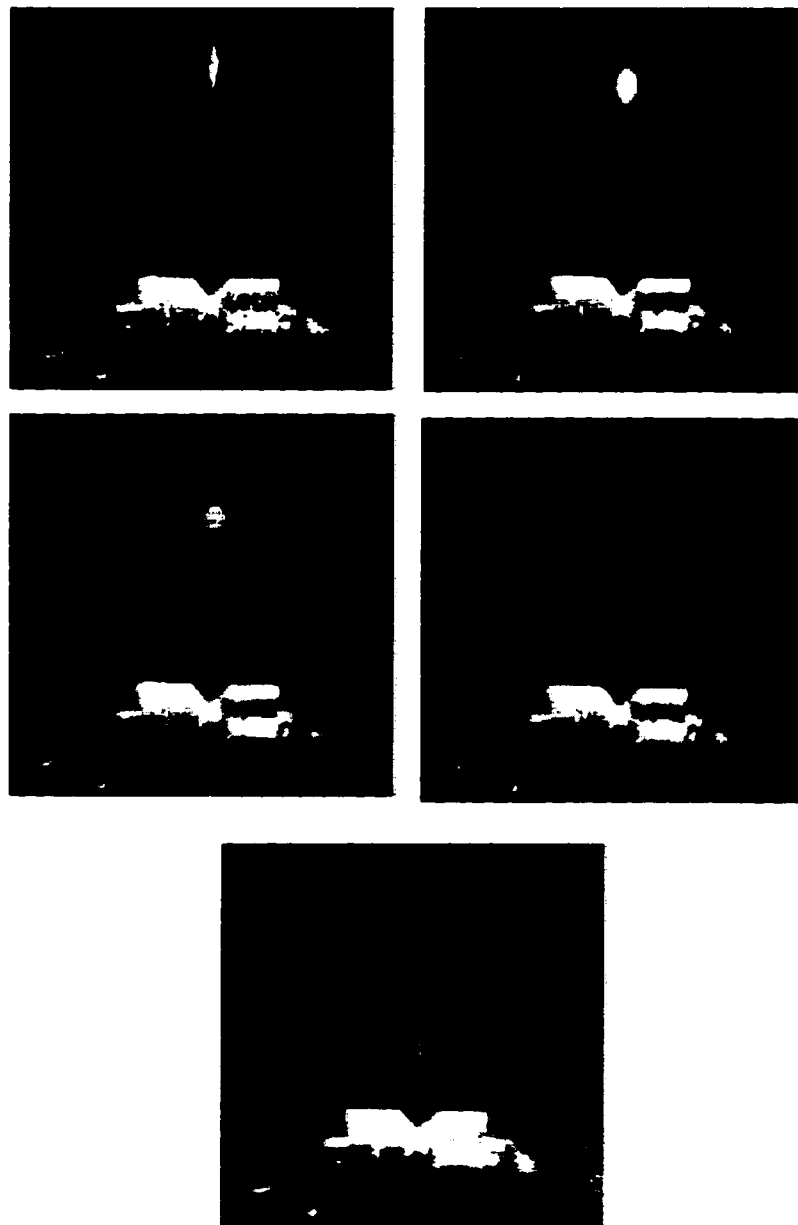


Figure 2.7: A cloud of cesium atoms falling to the cavity, 0, 10, 20, 30 and 40ms after the MOT is switched off. This expansion rate reflects a temperature of $\simeq 15\mu\text{K}$.

spectroscopy to the $F=4\rightarrow4, 4\rightarrow5$ crossover peak (126 MHz below the $F=4\rightarrow5$ transition), then is upshifted in frequency by a double-passed AOM by a total of ≈ 215 MHz, this AOM tunable to allow the laser to be detuned quickly for sub-Doppler cooling. A fixed frequency AOM then shifts the laser down by 110MHz, back to the desired frequency for trapping ≈ 10 MHz to the red of the transition, this second AOM allowing the beam to be switched on and off during the trap-drop cycle. Before passing through this second AOM, this beam is amplified by passing through the gain element of an SDL 8630 laser. This MOPA (Monolithic Optical Parametric Amplifier) chip provides a gain in power of a factor of 100, from ≈ 4 mW to ≈ 400 mW. The repumping laser, locked to the $\{Cs\ F=3\rightarrow4\}$ hyperfine level of the D2 line, addresses atoms which fall into the non-interacting $F=3$ ground state, and returns them to the $\{Cs\ F=4\rightarrow5\}$ trapping transition.

These two beams are created with opposite linear polarizations, added at a polarizing beam-splitter, then focused into a single optical fiber, which transports them across the room to the chamber where the MOT is to be formed. At the output of the fiber, the trapping beam is split evenly for the 3 axes of the MOT by using two polarizing beam-splitters with half-wave plates to rotate the polarization preceding each one. This generally gives about 15mW in each 1-inch diameter beam. The repumping laser follows the same paths, but will be split unevenly by the polarizing beam-splitters, as its initial polarization is opposite to the trapping beam. As this beam only provides optical pumping (and not radiation forces), this imbalance has negligible effect.

MOT control sequence

The data acquisition cycle, shown in Figure 2.8 is as follows: The MOT is loaded for 2s (MOT beams on, Main coils on, Bias Coil High) far from the cavity (≈ 10 mm) then lowered to ≈ 3 mm above the cavity, Since the MOT laser beams clip and are distorted at the edge of the cavity, atoms can be collected more efficiently further from the cavity. The MOT beam intensities are ≈ 10 mW per beam in a ≈ 2 cm diameter. Then, the main field coils and bias coil are switched OFF, the MOT beam intensity

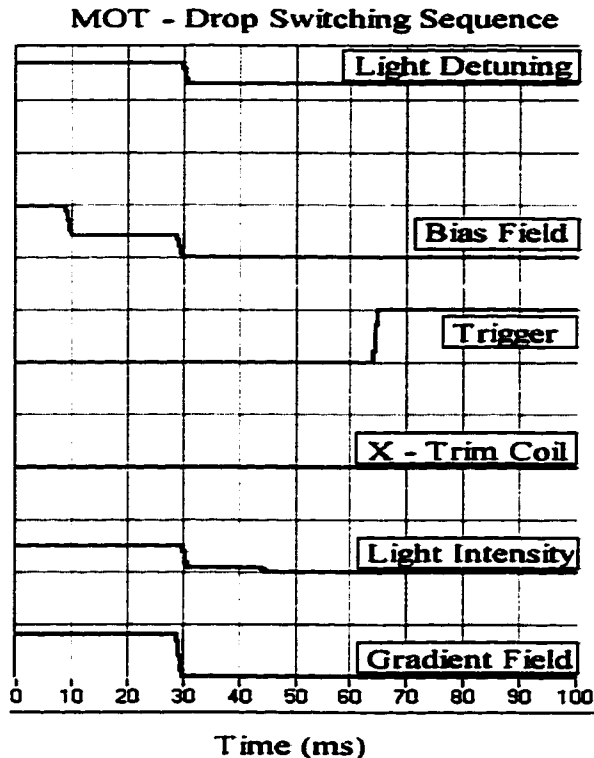


Figure 2.8: Switching sequence of optical and magnetic fields, for cooling and dropping the MOT. At 30ms, sub-Doppler cooling begins: the magnetic fields (bias field, gradient field) are switched OFF, and the MOT laser detuned and attenuated. 15ms later the MOT laser is switched OFF and the atoms fall. 20ms later, a trigger enables data acquisition. This drop sequence is repeated every 2s.

switched down to $\simeq 1\text{mW}$ and detuning increased to $\simeq 30\text{MHz}$, for $\simeq 15\text{ms}$ of sub-Doppler cooling. Finally, the MOT light is switched off and the atoms are allowed to fall toward the cavity. A trigger is sent to a separate data acquisition program $\simeq 20\text{ms}$ after the trap is dropped, to begin recording data of the atom-cavity transmission. A Labview routine controls this sequence, outputting a series of control voltages to switch the field coils, and MOT laser AOM drivers.

2.2.2 Optical layout: laser locking, frequency shifting.

The layout of optical paths for the cavity QED (rather than the MOT) part of the experiment is shown in a simplified form in Figure 2.9, and frequencies of these beams are indicated by Figure 2.10. A Ti:Sapphire laser provides 3 principal beams used in the experiment: the “lock” beam, “probe” beam and local oscillator (LO) for heterodyne detection. The Ti:Sapphire is locked $\simeq 40\text{MHz}$ above the $F=4 \rightarrow 5$ hyperfine component of the Cesium D2 line, achieved by frequency down-shifting part of the laser output with a double-passed AOM, then locking with this shifted beam directly to the $F=4 \rightarrow 4, 4 \rightarrow 5$ crossover peak in an FM saturated absorption lock. The laser lock frequency defines the LO frequency, and is adjustable by changing the frequency shift of the lock AOM.

The probe beam is a single RF sideband of a travelling-wave electro-optic modulator (TW-EOM). This probe generation method allows for rapid switching of the probe beam intensity and frequency, using RF switches. The TW-EOM does not generate sidebands very efficiently, so in order for the carrier (which is in general $\simeq 50$ times larger than the sideband) to have an insignificant effect on the intracavity physics, it must be far detuned from the cavity resonance. For our cavity of Chapter 3 with 40MHz linewidth, this led to a requirement of $\gtrsim 500\text{MHz}$ detuning. This frequency shift was achieved by double-passing a 200MHz AOM twice, to give a total shift of 800MHz. An RF frequency of $800 \pm 200\text{MHz}$ applied to the TW-EOM then generated a scannable probe beam near the Cesium resonance. With the large atom-cavity coupling strength $g \simeq 120\text{MHz}$ in this experiment, this large scan range is critical for mapping out the frequency response of the system.

The lock beam, used in the experiments of Chapter 3, was generated by taking the unshifted beam from the double-double-pass setup, and shifting it with a fixed frequency 40MHz AOM. This AOM allowed the lock beam to be chopped for use in the locking-scheme detailed in Section 2.2.4. The detuning of this beam from the Cesium resonance was adjusted by shifting the laser lock frequency. The lock and probe beams are combined on a beam-splitter, then mode-matched into the cavity

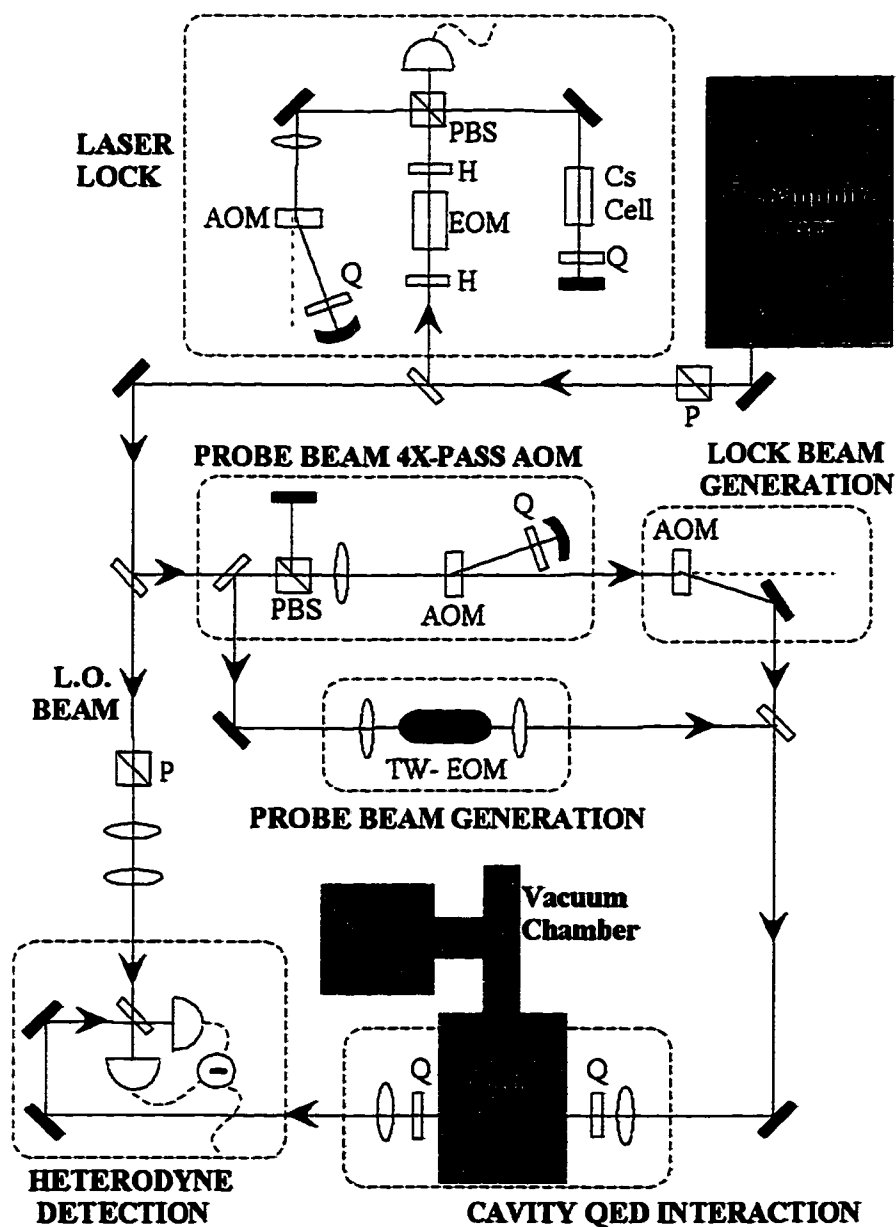


Figure 2.9: Simplified layout of the optical paths used for the cavity QED interaction and detection. Labeled elements are H=half-wave plate, Q=quarter-wave plate, PBS=polarizing beam-splitter, AOM=acousto-optic modulator, EOM=electro-optic modulator, P=polarizer. Unlabeled elements are mirrors, beam-splitters, and lenses.

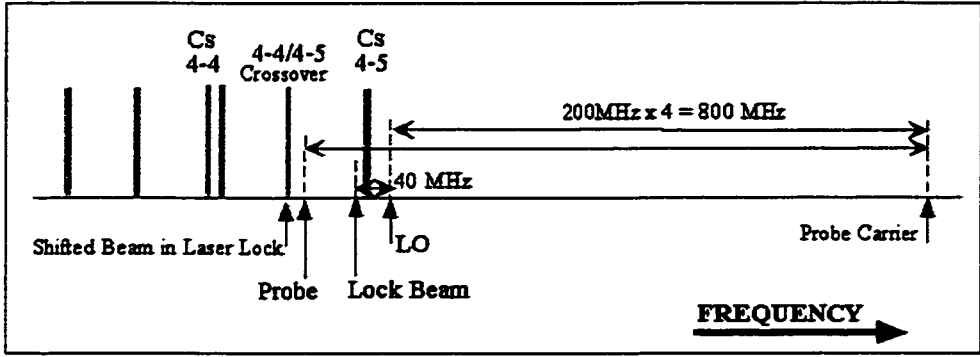


Figure 2.10: Frequencies of the LO, lock and probe laser beams.

with lenses and beam-steering mirrors.

The local oscillator beam was taken directly from the laser output, without frequency shifting, to try and keep the spatial profile of the beam as clean as possible. Lenses are used to overlap shape of this beam with the cavity output beam, the beat-note between these frequency-detuned beams detected in balanced heterodyne detection as a measurement of the cavity output beam.

2.2.3 Basic cavity design

The cavity, pictured in Figure 2.11 and shown schematically in Figure 2.12 is constructed of two mirrors, each machined down in a cone from a 3mm diameter cylindrical substrate, to leave a 1mm diameter coated surface. This machining serves two purposes. Firstly, it allows the curved mirrors to be brought more closely together than would be possible with larger diameter substrates, increasing the atom-cavity coupling strength g . Secondly, it allows clearance for the two MOT laser beams which are oriented perpendicular to the cavity axis, allowing the MOT to be formed only 1.5mm above the cavity mode. The fabrication, cleaning, and inspection and characterization of these mirrors will be discussed in more detail in Chapter 5.

In the cavity shown in Figure 2.11, the mirrors are lightly glued to aluminum v-shaped blocks, which are then glued to flat, shear-mode piezoelectric transducers (PZT's) which allow the cavity length to be scanned and actively controlled. The

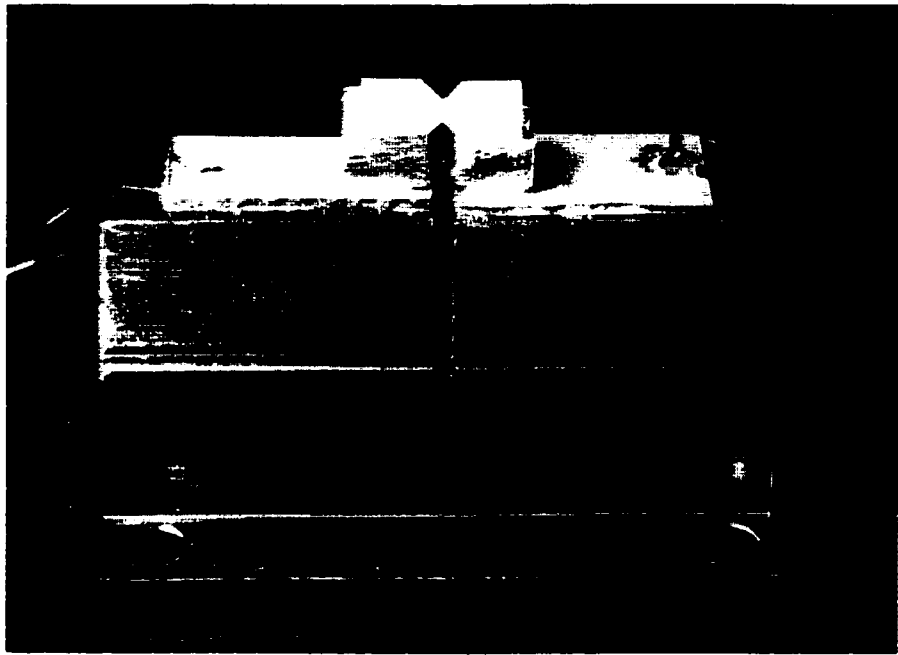


Figure 2.11: Photograph of the cavity and cavity mount used in the experiments of Chapter 4, and described in more detail in Chapter 5.

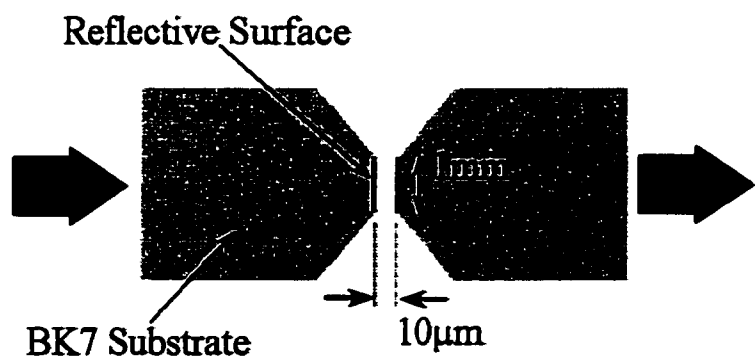


Figure 2.12: Schematic of the cavity mirrors.

PZT's are glued to a solid copper base, which gives good intrinsic cavity length stability, and forms part of the vibration-isolation stack inside the chamber. In an earlier cavity mount design, used for the experiments of Chapter 3, this base-block was made of two separate hollow sections, with an internal tube PZT providing scanning/stabilization capabilities. Mechanical resonances in this mount at low frequencies (few kHz) were eliminated by moving to the solid-block design, simplifying cavity stabilization.

2.2.4 Cavity stabilization

For cavity of finesse \mathcal{F} , the length stability required to keep the cavity resonant within its linewidth is $\Delta L \simeq (\lambda/2)/\mathcal{F}$, so for stability of 1/10 of a linewidth, which would typically be a minimum requirement for our experiments, this gives $\Delta L \simeq (\lambda/2)/10\mathcal{F} = 8.8 \times 10^{-14}\text{m}$ for a cavity with 480,000 finesse. To attain this level of length stability, the cavity needs to be isolated well from vibrations, and actively controlled.

Passive stabilization: Vibration-isolation stack

To isolate the cavity from vibrations of the chamber and table, a series of alternating heavy copper blocks and absorbing materials (viton, RTV) is used, with the specific design employed here designed by Michael Chapman. The cavity mount pictured in Figure 2.11 sits, isolated by a square of viton at each corner of the mount, on a thick copper baseplate which has a heavy copper rod extending from its base. This baseplate is then placed, with RTV underneath, onto a large copper block which is machined to fit the circular shape of the chamber. This block is composed of two heavy copper sections and a connecting crossbar, with a hole in it to allow the heavy copper rod to hang freely. Finally, the large copper piece is placed inside the vacuum chamber, supported by combination viton/RTV rubber bumpers. These pieces are shown in Figure 2.13. At each stage, there is no contact between the copper pieces, except via the rubber bumpers. The thickness of these copper pieces is chosen such

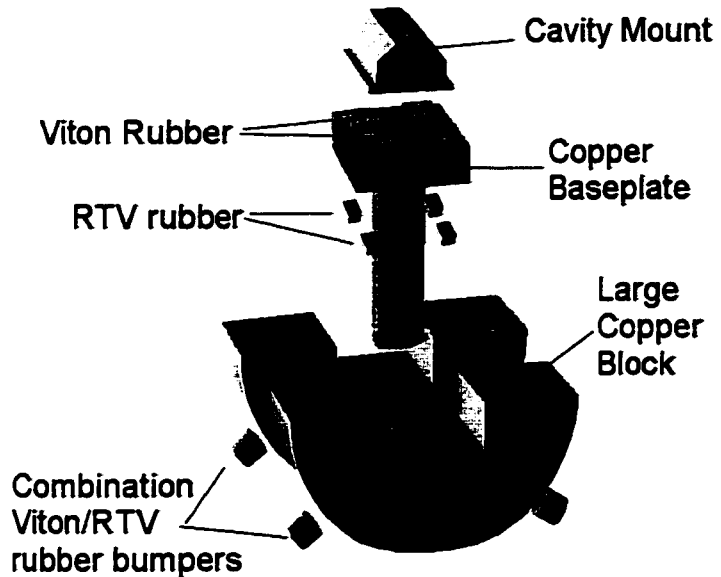


Figure 2.13: The cavity mount is isolated from vibrations by a series of copper blocks separated by rubber spacers.

that the final height of the cavity should be just below the geometric center of the vacuum chamber, where the MOT forms.

Active stabilization: Cavity locking strategies

To actively stabilize the cavity length in the first experiment, described in Chapter 3, an auxiliary locking laser beam was used in the cavity. The intensity of this beam was high enough to saturate out any atom-transit signals, so that transiting atoms had no effect on the cavity lock. This beam was chopped off in a square wave at 0.5kHz, to allow 1ms intervals of data acquisition between cavity locking. For experiments using coincident probe beams, this beam was not completely chopped off, but rather chopped to a low level suitable for probing the atom-cavity. This chopped lock has the advantage that “no-atoms” segments bracketed the atom signals which helped with normalization of the signals; however, it limits the potential dwell-time of an atom in the cavity to $\simeq 1\text{ms}$.

The lock beam was detuned from the atom-cavity resonance by κ , and the cavity locked to keep the amplitude transmission of this beam constant, thereby derived a

locking error signal directly from the slope of the side of the cavity resonance. The feedback signal came from the heterodyne detectors (via the video out port of the spectrum analyzer, log scale), this feedback filtered to $\simeq 50\text{Hz}$ bandwidth to avoid interference from the chop frequency. This direct locking was chosen after investigating chopped-locks with other methods of error signal generation: dither/lock-in, and FM reflection locking. These more complicated schemes did not improve the characteristics of the lock, primarily because the main lock excursions were cavity drifts and instabilities around or above the chop frequency of $\simeq 1\text{kHz}$, which in each case were above the lock bandwidth.

The quality of this lock is investigated in Figure 2.14, where noise variance ($\Delta\bar{n}$)² versus mean intracavity photon number \bar{n} is plotted for a laser field transmitted through the cavity, with these points taken from the data traces of Chapter 3. The cavity is locked with the chop-lock described above, and measured with an independent probe beam at a different frequency. Circles are for a probe resonant with the cavity, and triangles for a probe at 20MHz detuning ($\simeq \kappa/2$ for this cavity). The initial linear behavior (dashed line) reflects the dominance of shot noise ($\Delta\bar{n} \propto \sqrt{\bar{n}}$) at low powers, but eventually technical noise ($\Delta\bar{n} \propto \bar{n}$) introduced by cavity lock imperfections dominates, and the noise variance deviates from a linear dependence. For a probe beam resonant with the cavity, shot noise dominates up to $\bar{n} \simeq 3$ photons, whereas for a probe on the side of the cavity this limit is $\bar{n} \lesssim 1$ photon. This is expected, since a probe on the side of the cavity will be most sensitive to noise introduced by cavity vibrations.

In the data of Chapter 3, the intracavity photon number is generally $\bar{n} \lesssim 1$ photon, so the observed noise will be dominated by shot noise.

In the second series of experiments, the more stable solid-block mount (pictured in Figure 2.11) allowed a slower chop frequency. It was found that the lock was nearly as good when the independent lock beam was eliminated, and the cavity was locked directly to the probe beam. When an atom signal was observed, the lock feedback was triggered off for 2ms, to avoid interference of atom signals in the cavity lock. Due to the higher finesse of this cavity, technical noise had a greater contribution to the

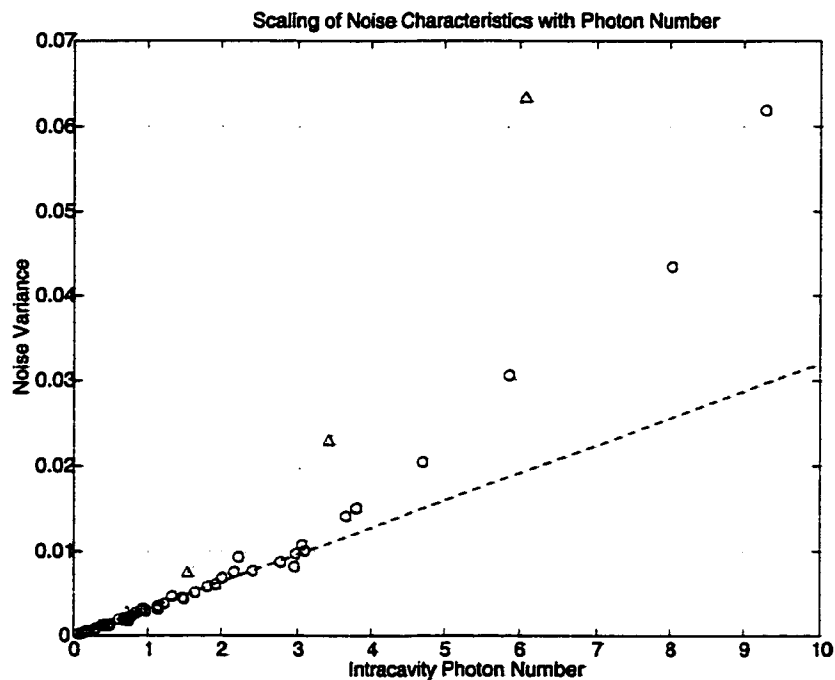


Figure 2.14: As a test of the cavity lock characteristics, we plot noise variance $(\Delta\bar{n})^2$ versus mean intracavity photon number \bar{n} in the absence of atoms. A linear dependence indicates shot-noise dominated measurement up to $\bar{n} \simeq 3$ intracavity photons for a resonant probe (circles), and up to $\bar{n} \simeq 1$ intracavity photon for a probe detuned by $\kappa/2$ (triangles).

observed noise; at 0.3 intracavity photons some contribution from was clearly visible from a mechanical resonance of the mount at 60kHz.

In both experiments, the respective cavities was estimated to be locked to $\simeq \pm 2\text{MHz}$ center frequency.

2.2.5 Heterodyne detection, data acquisition

The transmission of the probe and lock beams through the cavity are measured by balanced heterodyne detection, described in more detail in Ref. [38]. The local oscillator beam is overlapped with the cavity output on a beam-splitter, then the beat between these frequency-separated beams is measured in two detectors at each output of the beam-splitter. Subtraction of the two photocurrents yields a signal proportional to the intracavity field \hat{a} . If coherent demodulation is employed, as in Ref. [46], both quadratures of the intracavity field, and their associated noise characteristics can be obtained with this type of measurement.

In the current apparatus, we use a spectrum analyzer to provide demodulation of the beat frequency, which incoherently sums the two field quadratures to measure only the transmitted intensity $|\hat{a}|^2$ through the atom-cavity system. The video-out signal from the spectrum analyzer is digitized by our computer-controlled data acquisition. This same signal video-out signal is used for cavity lock, and in the atom-trapping experiments of Chapter 4, for triggering on atom signals. A block diagram of the electronics used in the cavity lock, data acquisition, and atom triggering is shown in Figure 2.15, for the case where the cavity is locked directly to the probe beam. With an independent lock beam the setup is more complicated; each of lock and probe has own spectrum analyzer, an additional function generator produces a square wave to chop the lock beam, this same signal used to blank OFF the lock feedback signal during data-taking phases.

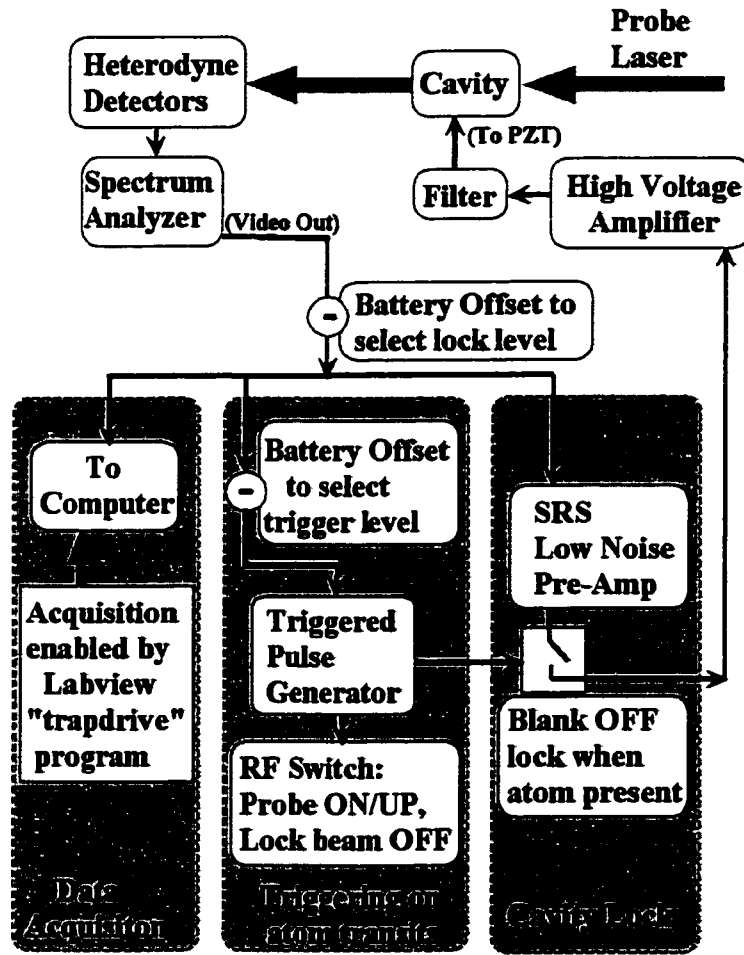


Figure 2.15: Block diagram of the electronics used in the cavity lock, data acquisition, and for triggering on single-atom events.

2.2.6 Calibration of measured signals

Over the course of these measurements, the efficiency of our heterodyne detection was 45-55%, measured independently for each data set. For a given cavity output power (typically $\simeq 20\text{nW}$ for this calibration) and a known local-oscillator beam power (typically 5mW), this efficiency can be determined by comparing the resulting beat-note size to the shot-noise level, as detailed in Ref. [38]. This is consistent with a direct measure of homodyne fringe contrast, for this experiment $\eta \simeq 0.8$, which combined with the detector quantum efficiency of $\alpha \simeq 0.8$ gives an overall heterodyne efficiency of $\alpha\eta^2 = .8 \times (.8)^2 \simeq 50\%$.

Calibration of the intracavity photon number \bar{n} is achieved by reference to a cavity output of known power; the output flux of cavity photons will be $\bar{n}(c/2L)T$, where T is the output mirror transmission, and photons strike this mirror every $c/2L$ seconds. Accounting for measured transport losses between the cavity and heterodyne setup, this allows the optical power to be related to an intracavity photon number. The corresponding spectrum analyzer beatnote level scales linearly with optical power, so the relationship between spectrum analyzer dBm level and intracavity photon number is then established.

This photon number-dBm calibration is done at a single detection frequency, so corrections need to be made for variations in detector sensitivity/gain when probing at other frequencies. These corrections were derived by measuring the shot-noise (and electronic noise) levels as a function of frequency: As the shot-noise spectrum is white, any variations will be due to detector/amplifier response. As shown in Figure 2.16, over the frequency range of 5-250MHz used in detection, variations of several dBm are seen. These variations depend on the specific detectors, cables, and spectrum analyzers used, so once the calibration was made care was taken to change nothing in the setup. In Figure 2.16, the top (dark) curve is the electronic noise (all beams blocked) and the lower (light) curve shot-noise (cavity output blocked). The shot noise trace, which is used to determine the frequency-dependent correction to the photon number calibration, has been offset downward by 6dB in this plot. Because the shot

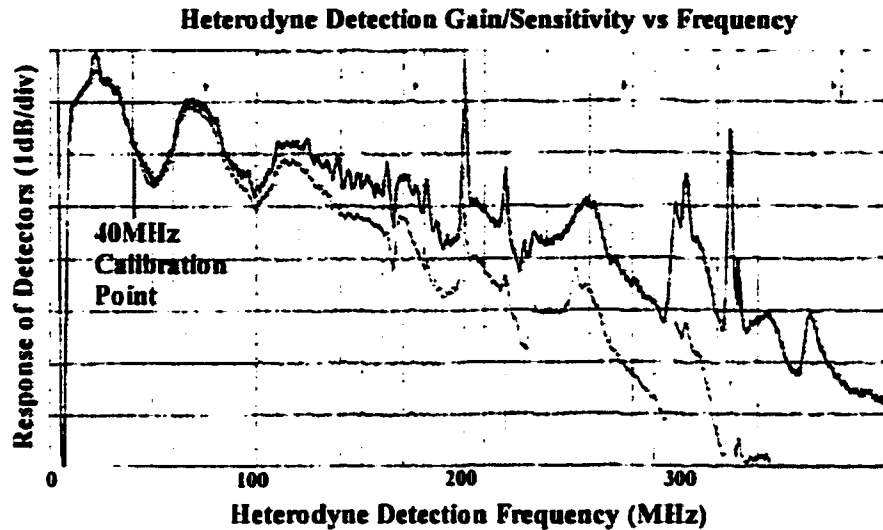


Figure 2.16: Over the frequency range 5-250MHz used in heterodyne detection, the sensitivity and gain of the detectors varies by several dB.

noise signal is ≈ 6 dB larger than the electronic noise, small spikes in the electronic noise spectrum (due to phenomena such as RF pickup in the photodetectors) are largely hidden when shot noise is added.

Finally, the signal we actually record is a voltage from the spectrum analyzer video-out port, so the calibration of this voltage to dBm needs to be measured. This varies according to which spectrum analyzer is used, and changes when auto-calibration is run on the spectrum analyzer, so again, once this calibration was determined no changes were made to the setup. The calibration relationship is non-trivial: for the data of Chapter 4, the conversion from video-out to dBm was determined by $(\text{Power in dBm}) = (\text{Vout}) \times 79.1 - 87.975 + (\text{offset due to detection frequency response})$.

Chapter 3 Real-time cavity QED with single atoms

This Chapter is largely based on “Real-Time Cavity QED with Single Atoms,” C. J. Hood, M. S. Chapman, T. W. Lynn and H. J. Kimble, Phys. Rev. Lett. **80**, 4157 (1998).

3.1 Introduction

An important trend in modern physics has been the increasing ability to isolate and manipulate the dynamical processes of individual quantum systems, with interactions studied quantum by quantum. In optical physics, examples include cavity QED with single atoms and photons [1] and trapped ions cooled to the motional zero point [11], while in condensed matter physics, an example is the Coulomb blockade with discrete electron energies [75]. An essential ingredient in these endeavors is that the components of a complex quantum system should interact in a controlled fashion with minimal decoherence. More quantitatively, if the off-diagonal elements of the system’s interaction Hamiltonian are characterized by $\langle H_{int} \rangle \sim \hbar g$, where g is the rate of coherent, reversible evolution, then a necessary requirement is to achieve *strong coupling* for which $g > \beta \equiv \max[\Gamma, T^{-1}]$ with T as the interaction time and Γ as the set of decoherence rates for the system.

Although there are many facets to investigations of such open quantum systems, our primary motivation has been to exploit strong coupling in cavity QED to enable research in quantum measurement and more generally, in the emerging field of quantum information dynamics [71]. For this system, the coherent coupling is parametrized by rate g_0 , where $2g_0$ is the single-photon Rabi frequency, and decoherence is dictated by the rates $\Gamma \equiv \{\gamma_\perp, \kappa\}$, with γ_\perp as the atomic dipole decay rate

and κ as the rate of decay of the cavity field. Several experiments in cavity QED have investigated the nonperturbative interaction of an atom with the electromagnetic field at the level of a single photon [53, 54, 58, 59]. However, without exception these experiments have employed atomic beams in settings for which the information per atomic transit (of duration T) is $I \equiv \frac{g_0^2 T}{\beta} \sim 1$, that is, little information is obtained from the passage of a single atom through the apparatus, and measurements over an ensemble of atoms are required. For example, the passage of a Rydberg atom through a microwave cavity and its subsequent measurement provides a single bit of information [53, 58].

By contrast, an exciting recent development in cavity QED has been the ability to observe single-atom trajectories in *real-time* with $I \gg 1$, pioneered by the results of Ref. [24], and explored in several subsequent experiments [25, 26, 44, 45, 46, 28, 27, 47]. In this method the transmitted power of a probe beam is monitored as cold atoms fall between the mirrors of a high-finesse optical resonator, with the probe transmission significantly altered by the position-dependent interaction between atom and cavity field [49, 50].

Similarly enabled by the use of cold atoms, the research reported in this Chapter exploits the largest coupling g_0 achieved to date to explore a new regime in cavity QED, for which single-atom trajectories can be used to infer the nature of the underlying one-atom master equation. More specifically, for atoms taken one by one, we map the frequency response of the atom-cavity system, and thereby directly determine g_0 from the vacuum-Rabi splitting. In this measurement, we observe a marked asymmetry in the vacuum-Rabi spectrum; when the probe laser is tuned to the red of the coincident atom-cavity resonance the characteristics of atom signals are in accord with the single-atom master equation, whereas for a blue-detuned probe few trajectories achieve optimal coupling, reflected in a diminution of both the peak amplitude and abundance of atom signals. We attribute this effect to light forces, which due to the strongly coupled nature of the system have a significant effect even for photon numbers < 1 . Notably, this is the first experiment for which the interaction energy $\hbar g_0$ is greater than the atomic kinetic energy.

For probe excitation frequencies near the coincident atom-cavity resonance, the nonlinear saturation behavior of the atom-cavity system is explored, and found to be in accord with the single-atom master equation (for a red-detuned probe field) but at variance with semiclassical theory.

3.2 Experimental apparatus

Our apparatus is shown schematically in Figure 3.1. The Fabry-Perot cavity consists of two superpolished spherical mirrors of radius of curvature 10 cm, forming a cavity of effective length 10.1 μm and finesse $\mathcal{F}=1.8 \times 10^5$. In this cavity $(g_0, \kappa, \gamma_{\perp}, T^{-1})/2\pi = (120, 40, 2.6, 0.002)$ MHz, where the atom-field coupling coefficient g_0 is determined by the cavity geometry (and the known transition dipole moment [76]), κ is the measured linewidth of the TEM₀₀ mode of the cavity, γ_{\perp} is the dipole decay rate for the Cs (6S_{1/2}, F=4, m_F=4) \rightarrow (6P_{3/2}, F'=5, m'_F=5) transition ($\lambda = 852.36$ nm)[76], and typical transit times for atoms through the cavity mode (waist $w_0 \simeq 15\mu\text{m}$) are $T \simeq 75\mu\text{s}$. These rates correspond to critical photon and atom numbers ($m_0 \equiv \gamma_{\perp}^2/2g_0^2$, $N_0 \equiv 2\kappa\gamma_{\perp}/g_0^2 = (2.3 \times 10^{-4}, 0.015)$), and to optical information per atomic transit $I \sim 5.4 \times 10^4\pi$ [71]. This large value of $I \gg 1$ enables not only detection of single atoms, but monitoring of the motion of these atoms in real-time with high signal-to-noise ratio. The probe transmission (typical power 10 pW) is measured using balanced heterodyne detection with overall efficiency 40%. The length of the cavity is actively stabilized by chopping an auxiliary locking beam [59].

Our experimental procedure consists of loading the MOT for 0.5s, performing sub-Doppler cooling to 20 μK and then dropping the atoms, all the while monitoring transmission of a circularly polarized probe beam with fixed detuning $\Delta \equiv \omega_p - \omega_{AC}$ (where $\omega_{atom} = \omega_{cavity} \equiv \omega_{AC}$). The circularly polarized probe beam drives the cycling transition m_F=4 \rightarrow m'_F=5 and provides optical pumping to this sublevel as an atom enters the cavity mode. The magnetic field is zeroed at the site of the MOT to allow sub-Doppler cooling and from the coil geometry, should also be well zeroed at the cavity mode. Explicit spatial quantization obtained by switching a magnetic field

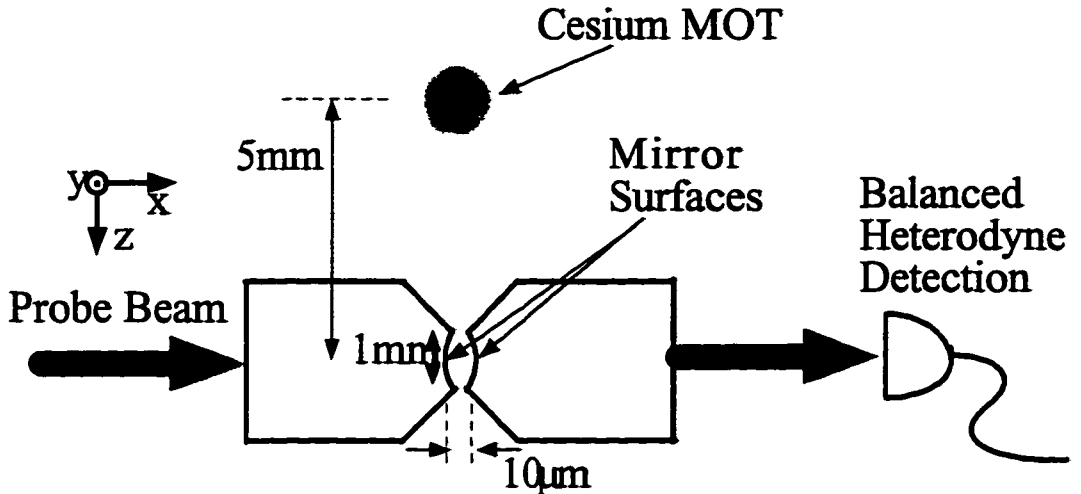


Figure 3.1: Schematic of the experimental apparatus.

“on” along the cavity axis as the atom transits produced no significant impact on the transit signals. Note that transit signals from atoms that are incorrectly optically pumped and driven on transitions other than $m_F=4 \rightarrow m'_F=5$ will be eliminated by our selection of optimal events detailed in Section 3.4.1.

3.3 Single atom transit signals

As an atom falls into the cavity, it encounters a spatially dependent coupling coefficient $g(\vec{r}) \simeq g_0 \cos(2\pi x/\lambda) \exp[-(y^2 + z^2)/w_0^2] \equiv g_0 \psi(\vec{r})$, arising from the standing-wave structure of the cavity mode. As an atom enters, and $g(\vec{r})$ increases from zero, this coupling causes the otherwise coincident atomic and cavity resonances ($\omega_{atom} = \omega_{cavity} \equiv \omega_{AC}$) to map to dressed states for the atom-cavity system, which are split in frequency by $\pm g(\vec{r})$. The probe spectrum thus evolves from a simple Lorentzian to a “vacuum-Rabi” spectrum with two peaks at $\omega_{AC} \pm g(\vec{r})$, as illustrated in Figure 3.2. Displayed is a series of theoretical transmission spectra $\bar{m}(\Delta) \equiv |\langle a \rangle|^2$. That is, $\bar{m}(\Delta)$ indicates the transmission through the atom-cavity for a probe of detuning Δ . Here $\langle a \rangle$ is the mean intracavity field amplitude calculated from the steady-state solution of the master equation for a single atom (of infinite mass). In

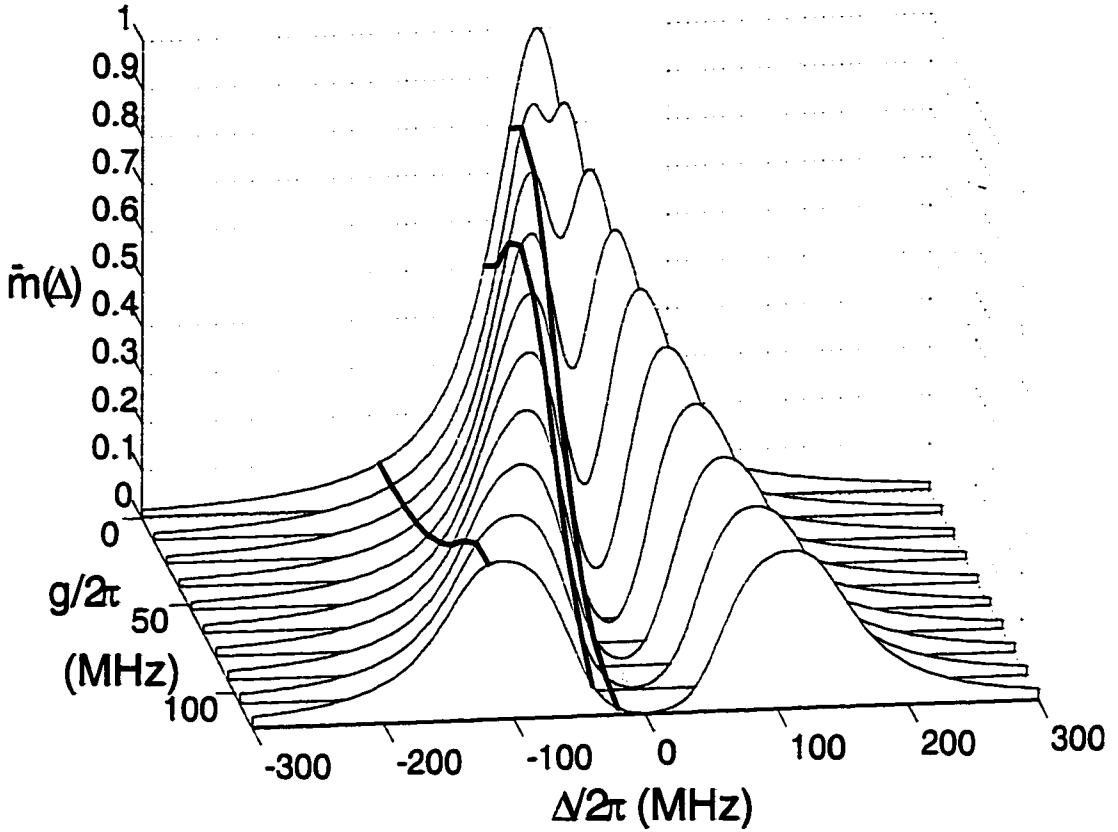


Figure 3.2: $\bar{m}(\Delta) \equiv |\langle a \rangle|^2$ as a function of probe detuning Δ for atomic positions \vec{r}_i such that $g(\vec{r}_i) = \{0, g_0/9, \dots, g_0\}$, with probe intensity fixed at $\bar{n}_0 = 1$, and $\omega_{cavity} = \omega_{atom}$. For an atom transiting the cavity, this *position dependent coupling* yields a *time dependent transmission*, indicated by the **bold** curves for fixed probe detunings $\Delta/2\pi = \{-20, -40, -120\}$ MHz.

Figure 3.2, the atom's position \vec{r}_i is stepped such that its coupling strength $g(\vec{r}_i)$ increases from $g(\vec{r}_i) = 0$ to $g(\vec{r}_i) = 2\pi \times 120\text{MHz} = g_0$.[50] Of course, the spectrum at $g(\vec{r}_i) = 0$ is simply the Lorentzian response of the cavity with no atom present, hereafter denoted by $\bar{n}(\Delta) = \bar{n}_0/[1+(\Delta/\kappa)^2]$, while the spectrum at $g(\vec{r}_i) = g_0$ corresponds to an optimally coupled atom.

Although in the actual experiment most atoms never reach a region of optimal coupling, some do enter in the desired $m_F=4$ sublevel and fall through antinodes of the field. These atoms encounter an increasing $g(\vec{r})$ which sweeps the vacuum-Rabi

sidebands of the spectrum outward in frequency to the maximal splitting of $\pm g_0/2\pi = \pm 120\text{MHz}$. (For atoms which only reach a coupling of $g_{\max} < g_0$, the sidebands will sweep out to the smaller separation of $\pm g_{\max}/2\pi$, indicated by the intermediate curves of Figure 3.2.)

Instead of measuring this entire spectrum simultaneously, we will be using a single probe field at a fixed frequency. For this probe, the *position dependent coupling* of the atom leads to a *time dependent transmission*. That is, the atom's position changes in time thereby changing its coupling strength, the spectrum shifts correspondingly, and so the probe transmission at a specific frequency changes as a result the atomic motion. The bold traces in Figure 3.2 illustrate this evolution of \bar{m} for three probe detunings Δ relevant to our observations, as an atom enters the cavity. At a probe detuning $\Delta \approx 0$, transmission *drops* as an atom enters the cavity, whereas for $\Delta/2\pi \approx g_0/2\pi = 120\text{MHz}$, the transmission increases. The process reverses as the atom leaves the cavity and the coupling returns to $g(\vec{r}) = 0$.

Turning to our measurements, we present in Figure 3.3(a)-(c) examples of the time-dependent transmission $T(t) \equiv \bar{m}(t)/\bar{n}$ of the atom-cavity system at the probe detunings of Figure 3.2. With $\omega_P \approx \omega_{AC}$ ($\Delta \approx 0$), as in Figure 3.3(a), we first observe a decreasing probe transmission (due to increasing $g(\vec{r})$ as the atom enters the mode volume), then a minimum in transmission (when $g(\vec{r}) \approx g_0$), and finally transmission increasing to its original value (as the atom exits the cavity), resulting in what we call a “downgoing” atom transit signal. $T_{\min} \approx 10^{-2}$ is regularly observed for single atom transits. Conversely, for $\Delta/2\pi = -120\text{ MHz} \approx g_0/2\pi$ (Figure 3.3(c)), the transmission increases as the atom enters the cavity mode, peaking at $T_{\max} \approx 3.5$ when $g(\vec{r}) \approx g_0$, and then falls again as the atom exits, which we call an “upgoing” transit. Finally, an intermediate regime $\Delta/2\pi = -40\text{ MHz} \approx \frac{1}{3}g_0/2\pi$ exhibits more complicated behavior (Figure 3.3(b)). Here, as the atom enters the cavity, the transmission first increases as the lower Rabi peak sweeps past ω_P , then decreases to a minimum when $g(\vec{r}) \approx g_0$, and finally passes through a second maximum as $g(\vec{r})$ decreases with the atom's departure.

The transit signals of Figure 3.3 are smoothly varying without the rapid oscillations

tions recorded in Ref. [24], which were tentatively attributed to motion along the standing wave. Here we suspect that the tenfold increase in g leads to mechanical forces which inhibit this motion.

To confirm the qualitative characteristics of the vacuum-Rabi spectrum during a single atom transit we simultaneously record the transmission of two probe beams, as in Figure 3.3(d,e). For probes with detunings $\Delta_{1,2} \approx \mp g_0$, the cavity transmission increases simultaneously for each probe during the atom transit (Figure 3.3(d)). For one probe near resonance ($\Delta_1 \approx 0$) and the other red-detuned ($\Delta_2 \approx -g_0$), there is a simultaneous reduction in the transmission at Δ_1 , and an increase in the transmission at Δ_2 (Figure 3.3(e)). Note that the signal-to-noise for these traces is less than that for single-probe measurements due to saturation, reflecting a limitation *in principle* to the rate at which information can be extracted from this quantum system.

3.4 Vacuum-Rabi splitting from single atom transits

Next, by sequentially stepping our probe laser over a range of detunings $\frac{|\Delta|}{2\pi} \leq 200\text{MHz}$, we map the frequency response of the atom-cavity system (Figure 3.4). Clearly evidenced is a double-peaked structure reminiscent of the “vacuum-Rabi” splitting, with peaks near $\pm g_0/2\pi$, as was first observed for a single atom in Ref. [23]. In contrast to previous work with atomic beams, here atoms are observed one by one with negligible effect from background atoms in the tails of the cavity-mode function[34] (in Figure 3.4, such “spectator” atoms contribute in aggregate an effective atom number $\bar{N}_e < 0.04$).

At each value of probe detuning Δ , a series of about 50 trap drops is made, yielding up to 800 single-atom events, from which the data points shown in Figure 3.4 are determined. At each frequency, the maximum (circles) and/or minimum (squares) relative transmissions are shown. Note that at small detunings, decreases in transmission are observed as an atom transits the cavity (cf. Figure 3.3a), so a minimum

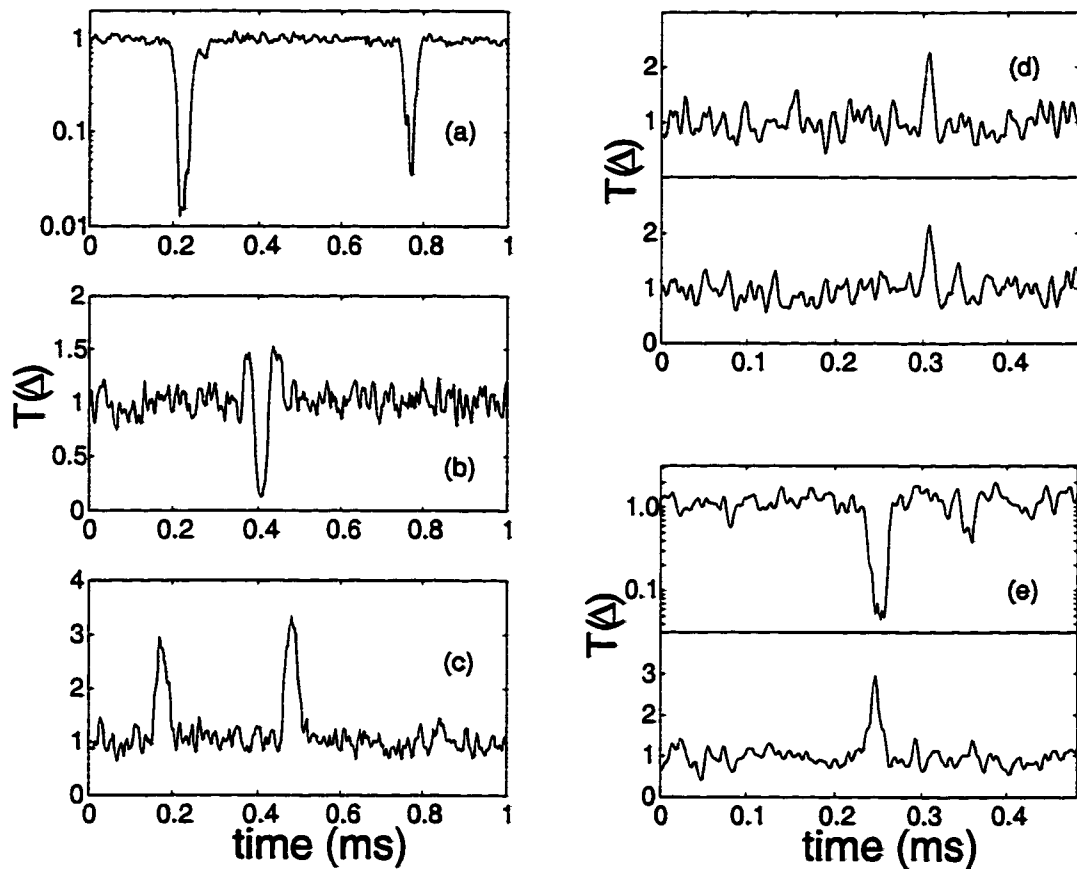


Figure 3.3: Measured cavity transmission $T(t) = \bar{m}(t)/\bar{n}$ as a function of time for individual atom transits. Traces (a)-(c) are for $\Delta/2\pi = \{-20, -40, -120\}$ MHz with $\bar{n}_0 = \{0.7, 0.6, 1.0\}$. (d) $\Delta_{1,2}/2\pi = \{-100, +100\}$ MHz with $\bar{n}_{01,02} = \{0.38, 0.22\}$. (e) $\Delta_{1,2}/2\pi = \{-20, -100\}$ MHz with $\bar{n}_{01,02} = \{0.05, 0.3\}$. All traces are with zero cavity detuning ($\omega_{atom} = \omega_{cavity}$) and are acquired with 100 kHz resolution bandwidth and digitized at 500 kHz sampling rate.

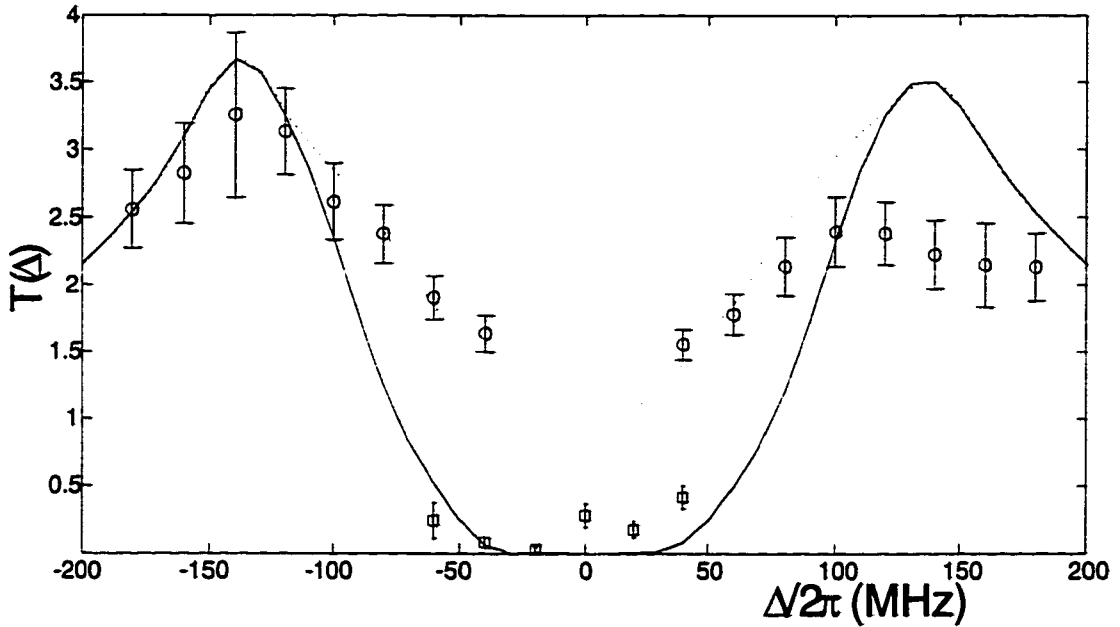


Figure 3.4: Maximum (o) and minimum (□) normalized transmission $T(\Delta)$ versus detuning Δ measured via single atom events. The solid curve gives $T(\Delta)$ for an atom with $g(\vec{r}) = g_0$ (the vacuum-Rabi spectrum), while the dashed line is the maximum transmission for any coupling $g(\vec{r}) \leq g_0$.

value for the relative transmission is shown in Figure 3.4. Conversely, at large detunings (cf. Figure 3.3c,d) increases in transmission are observed, so the maximum relative transmission is shown. For detunings $40\text{MHz} \leq |\Delta|/2\pi \leq 60\text{MHz}$ both increases and decreases are observed (cf. Figure 3.3b), hence we record and display both the maximum *and* minimum transmission. From the theoretical understanding gained from Figure 3.2, we expect that at these intermediate detunings the *minimum* relative transmission will correspond to the atom being in a position of best coupling. Again, as in Figure 3.3 the transit signals are normalized to the transmission of the empty cavity at each frequency to give $T(\Delta)$, with \bar{n}_0 varying from ≈ 0.6 photons near resonance to ≈ 1.4 photons at $\Delta/2\pi = \pm 200\text{MHz}$.

For comparison with theory, the solid curve in Figure 3.4 gives $T(\Delta)$ obtained from the steady-state solution of the master equation for a single stationary atom with optimal coupling $g(\vec{r}) = g_0$. Atoms with maximal coupling give the largest increases

in transmission for $|\Delta| \gtrsim g_0$ and similarly the deepest downgoing transits near $\Delta = 0$, so at these detunings the data points track the solid curve well. However, for intermediate detunings $40\text{MHz} \lesssim \frac{|\Delta|}{2\pi} \lesssim 100\text{MHz}$, the maximum observed transmission corresponds to a *smaller* value of coupling, $g(\vec{r}) \simeq |\Delta| < g_0$, and so these points are not expected to fall on the solid curve. We can, however, determine the maximum expected transmission at each Δ by considering all couplings $g(\vec{r}) \leq g_0$, with the result plotted as the dashed curve in Figure 3.4. Agreement between this *ideal one-atom* theory and experiment is evident for $\Delta < 0$, providing direct confirmation of the quoted value for g_0 .

One of the most striking features of the data in Figure 3.4 is the asymmetry of the spectrum between red and blue probe detunings, both in the magnitude and abundance of transits. Indeed, the number of events observed with $T(\Delta) \approx 2.5$ around $\Delta \approx +g_0$ is five times smaller than for $T(\Delta) \approx 3.3$ around $\Delta \approx -g_0$. Residual atom-cavity detunings are insufficient to explain the observed asymmetry (the cavity lock results in $\omega_{atom} \simeq \omega_{cavity}$ with systematic offsets below $\pm 2\text{MHz}$ and peak-to-peak excursions less than $\pm 5\text{MHz}$). It was also verified that none of the auxiliary laser fields present in the cavity were providing a significant AC Stark shift to the atomic transition. To check this, the strong cavity locking beam was swapped in detuning from the blue to the red side of the cavity, with no effect on the resulting asymmetry of the spectrum. The probe beam in this experiment is generated as an RF sideband of a traveling-wave electro-optic modulator. The carrier frequency of this beam is usually detuned by $+800\text{MHz}$, we switched this detuning to -800MHz , again with no effect on the atom-transit spectrum.

We attribute this asymmetry to mechanical light forces from the probe beam affecting the atom's trajectory. As analyzed in Ref.[77], weak excitation by a coherent probe tuned to $\Delta_{\pm} \approx \pm g_0$ gives rise to a pseudo-potential (for times $\gg \kappa^{-1} \sim 4\text{nsec}$), with depth $\pm \hbar g_0 p_{\pm}$, where $p_{\pm} \propto \bar{m}(\Delta_{\pm})$ is the probability of occupation of the upper (lower) dressed state. Since $\hbar g_0 / k_B \approx 7\text{mK}$, such light forces can be significant even for $\bar{m} \sim 0.5$ photons. We thus expect significant channeling of atomic trajectories into regions of high light intensity and strong coupling for a red-detuned probe ($\Delta < 0$).

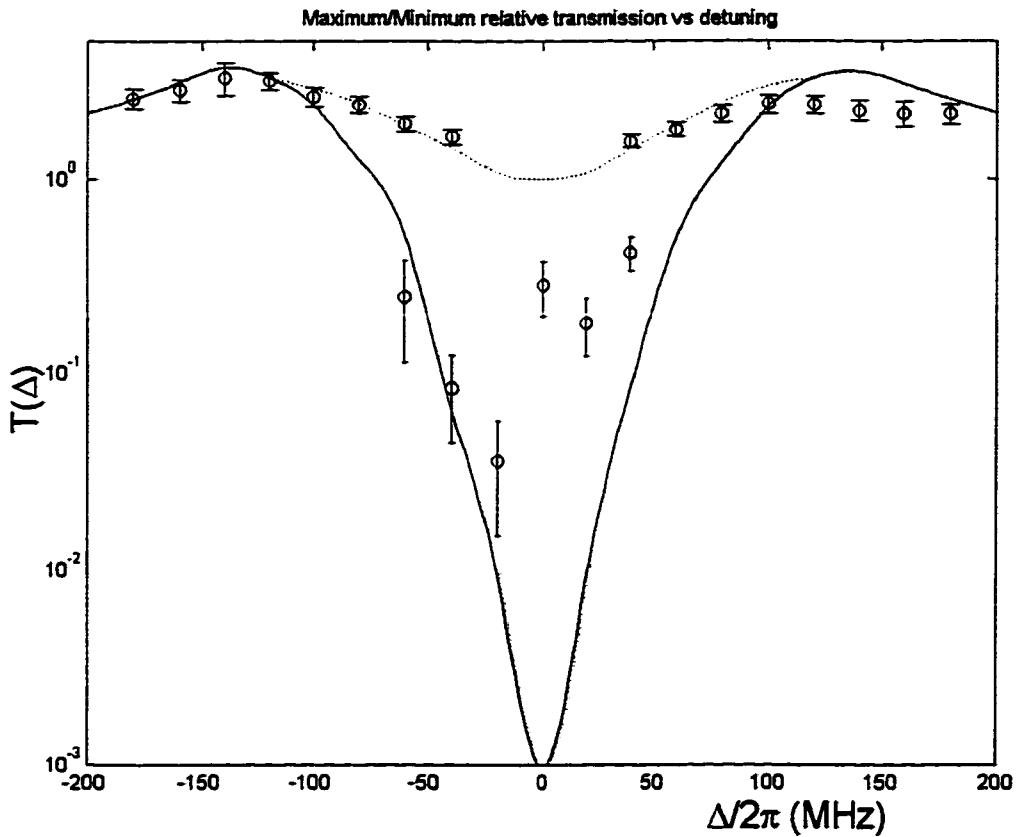


Figure 3.5: Maximum and minimum normalized transmission $T(\Delta)$ versus detuning Δ measured via single atom events. The solid curve gives $T(\Delta)$ for an atom with $g(\vec{r}) = g_0$ (the vacuum-Rabi spectrum). The asymmetry of the data points is attributed to light forces from the intracavity field of $\bar{n} \lesssim 0.5$ photons.

Conversely, a blue-detuned probe ($\Delta > 0$) creates a potential barrier and prevents an atom from reaching areas of optimal coupling. Apart from its relevance to the spectrum of Figure 3.4, this phenomenon suggests the possibility of trapping single atoms in the cavity mode with single photons.

Figure 3.5 shows the same data and traces as Figure 3.4, but with $T(\Delta)$ plotted on a logarithmic scale. It can now be seen that the asymmetry of the spectrum is present for all blue detunings, and that even in the case of resonant driving atom transits do not reach the expected depth. A probe detuning $\Delta/2\pi \lesssim -20\text{MHz}$ is apparently required to channel atoms into regions of strongest coupling, where the transit signals

will have largest amplitude. The edge of the shaded grey region indicates the shot-noise limit for determination of the depth of transits; for signals weaker than this level the observed minimum transmission will be this noise floor rather than the “true” minimum transmission. This boundary corresponds to an intracavity photon number of 6×10^{-3} photons for the 100kHz resolution bandwidth of this measurement. The driving strength \bar{n}_0 has here been chosen to be strong, so that transits do not reach this shot-noise limit, and we can therefore relate the observed value of the minimum transmission to a coupling strength $g(\vec{r})$. For a weak-field measurement, the theoretical relative transmission on resonance is $1/(1 + 2C_1)^2 = 5 \times 10^{-5}$, where $C_1 = 1/N_0 \equiv g_0^2/2\kappa\gamma_{\perp}$. For this data set the theoretical minimum is $\simeq 10^{-3}$, because for the strong driving $\bar{n}_0 \simeq 0.6$ photons we are well above the saturation photon number m_0 for the intracavity field, and the atom-cavity system is in a regime of nonlinear saturation.

3.4.1 Selection criteria for data points, generation of error-bars

The data points shown in Figures 3.4 and 3.5 are determined from a sub-selection of the up to 800 single-atom events observed at each individual probe frequency Δ .

For most atoms transiting the cavity, $g(\vec{r})$ never reaches g_0 . Referring to the bold curves of Figure 3.4, it can be seen that if the maximum coupling achieved is $g_{max} < g_0$, this will have a significant effect on the character of the transits observed. For large probe detunings ($\Delta/2\pi \approx -120\text{MHz}$), the probe transmission will not reach the same maximum value as for an optimally coupled atom, and so upgoing transits will be smaller than expected. Over an ensemble of atoms with coupling strengths $g_{max} \leq g_0$, all transit heights are possible, up to a maximum height associated with coupling g_0 . Similarly, for a probe tuned close to the atom-cavity resonance ($\Delta/2\pi \approx -0\text{MHz}$), atoms which reach coupling $g_{max} < g_0$ result in shallower downgoing transits than would be expected for an optimally coupled atom. So, for an ensemble of atoms with $g_{max} \leq g_0$, downgoing transits will be seen of all depths, down to a deepest value

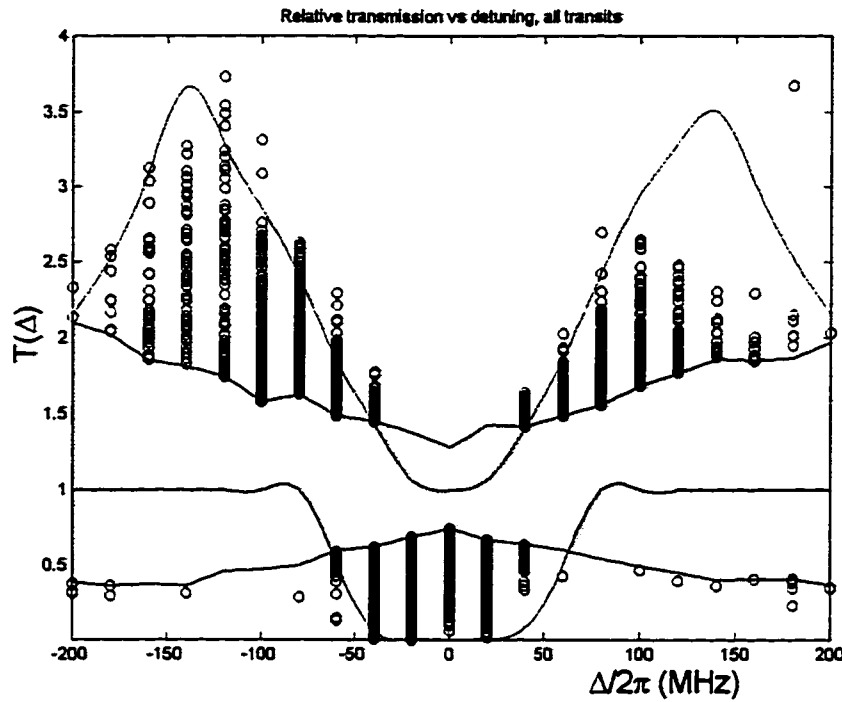


Figure 3.6: The spectrum of Figure 3.4 is generated from these individual data points. Each circle represents the height or depth of an individual atom transit.

corresponding to coupling g_0 .

This continuous distribution of transit heights/depths is shown clearly by Figure 3.6, which shows the individual transit data used to generate Figures 3.4 and 3.5. For individual signals such as those of Figure 3.3, the height of each individual upgoing signal, and depth of each downgoing signal was recorded, with each of these points displayed as a circle in Figure 3.6. Due to the inherent shot-noise of the probe laser, there is a minimum detectable size for transit signals. This is indicated by the shaded grey region: only transits extending beyond these limits are detectable with the detection bandwidth of 100kHz and drive strength of $\bar{n}_0 \approx 1$ photon used. At large detunings the intracavity field $\bar{n}(\Delta) = \bar{n}_0/[1+(\Delta/\kappa)^2]$ is weaker, so the noise is larger and transits must have larger amplitude to be detected.

We wish to use these points to extract values and uncertainties for the maximum and minimum relative transmission T observed at each Δ . Our procedure is to take a

fixed fraction f_e of the best events (maxima and/or minima) from the total data set at each Δ . The mean values of these “optimal” subsets are the points displayed for T in Figures 3.4 and 3.5.

We now must determine an appropriate value for the proportion f_e of transits to include in these “optimal” subsets. First note that in the absence of mechanical forces, we calculate that for a uniform spatial distribution of atoms dropped into the cavity, a fraction $f_t(\Delta) \sim 0.1$ of all atoms causing *detectable* transit signals reach coupling $0.9g_0 \leq g(\vec{r}) \leq g_0$. Further, for data with $\Delta/2\pi = -120\text{MHz}$ and $\Delta \sim 0$ (which have the best statistics and highest signal-to-noise ratios), as we vary the fraction f_e of the total data included in the set of optimal events (maxima or minima), both T and the sample standard deviation σ_d are found to be relatively insensitive to the choice of f_e for $f_e \lesssim 0.15$. We thus take $f = 0.15$ to determine the set of transits to be included in Figure 3.4 (and hence to fix σ_d from the associated distribution). There is an additional uncertainty σ_q arising from the shot-noise of the detected probe beam itself. We estimate this by measuring the noise for “no-atom” data bracketing the transit signals, then scaling this noise appropriately by the mean transit height/depth. The quantity $\sigma = \sqrt{\sigma_d^2 + \sigma_q^2}$ is shown in Figures 3.4 and 3.5 to estimate the error in T at each Δ . For all our data, the absolute uncertainty in the quoted photon numbers is $\simeq \pm 30\%$.

3.5 Nonlinear saturation behavior of the atom-cavity system

In the next series of measurements, we explore the nonlinear saturation behavior of the atom-cavity system. As described in Section 2.1, for measurements of structural properties of the atom-cavity system (rather than dynamical properties such as photon statistics) we expect the strongest distinction between semiclassical and quantum theories to appear in a regime of strong driving. Here, we explore this regime by vary the driving strength \bar{n}_0 , with the probe beam at fixed detuning. At each \bar{n}_0 we again

digitize the cavity transmission for a large number of transits, with a set of “optimal” single-atom events determining the value of T and its uncertainty σ . Results of such a measurement for a probe detuning $\Delta/2\pi = -20\text{MHz}$ are shown in Figure 3.7. The solid curve of Figure 3.7 is from the steady-state solution of the master equation for $T \equiv \bar{m}/\bar{n}$, for a single (stationary) atom with $g(\vec{r}) = g_0$, with reasonable agreement between the data and this ideal quantum model. By contrast, the dotted line is the semiclassical transmission function[64] evaluated for the parameters of our experiment, and exhibits bistable behavior. While shifts from the semiclassical bistability curve have also been predicted for other regimes of cavity parameters[78], this is the clearest example observed to date of a quantum/semiclassical distinction in the structural response of an optical cavity QED system. Also plotted (dashed line) is the relative transmission predicted for a photon number measurement, $\langle \hat{a}^\dagger \hat{a} \rangle / \bar{n}$, which would be the quantity measured via photon counting rather than that obtained by our heterodyne measurement of $|\hat{a}|^2$. The increase in $\langle \hat{a}^\dagger \hat{a} \rangle$ over $|\hat{a}|^2$ shows that in this driving regime there is a strong component of emission into the incoherent spectrum; $|\hat{a}|^2$ measures only the coherent transmitted field amplitude whereas $\langle \hat{a}^\dagger \hat{a} \rangle$ measures all emitted photons.

The slight red-detuning ($\Delta/2\pi = -20\text{MHz}$) of the probe beam in Figure 3.7 is required to channel atoms into regions of optimal coupling, as was the case for the spectrum measurements of Figure 3.5. The effect of this probe detuning is shown in the series of saturation curves in Figure 3.8, where transmission T is plotted versus probe drive photon number \bar{n}_0 for the series of probe detunings $\Delta/2\pi = \{-20\text{MHz}, -10\text{MHz}, 0\text{MHz}\}$, with the cavity detuning fixed at $\omega_{atom} = \omega_{cavity}$. As in Figure 3.5, across these data sets there is a progression from good agreement at red detunings ($\Delta/2\pi = -20\text{MHz}$), to clear disagreement near resonance ($\Delta/2\pi = 0\text{MHz}$), which can be understood as the mechanical effect of the red-detuned probe channeling atoms to regions of optimal coupling.

In another series of nonlinear saturation measurements, T versus \bar{n}_0 was again measured for a series of probe detunings, but this time with the atom-cavity detuning varying also, such that $\omega_{cavity} = \omega_{probe}$ for each data set, and the detuning Δ now

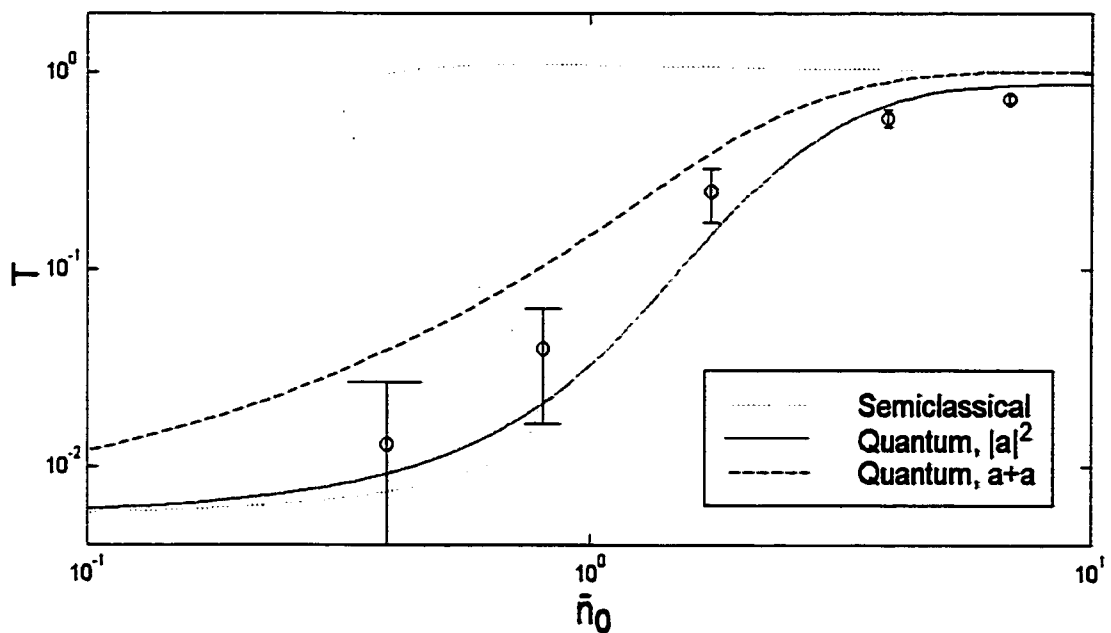


Figure 3.7: Transmission T versus probe photon number \bar{n}_0 for maximally coupled atom transits for fixed $\Delta/2\pi = -20\text{MHz}$. The solid (dashed) line results from the quantum master equation solution for the quantity $|\hat{a}|^2$ ($\langle \hat{a}^\dagger \hat{a} \rangle$) for one atom with $g(\vec{r}) = g_0$, while the dotted line is the semiclassical bistability state equation.

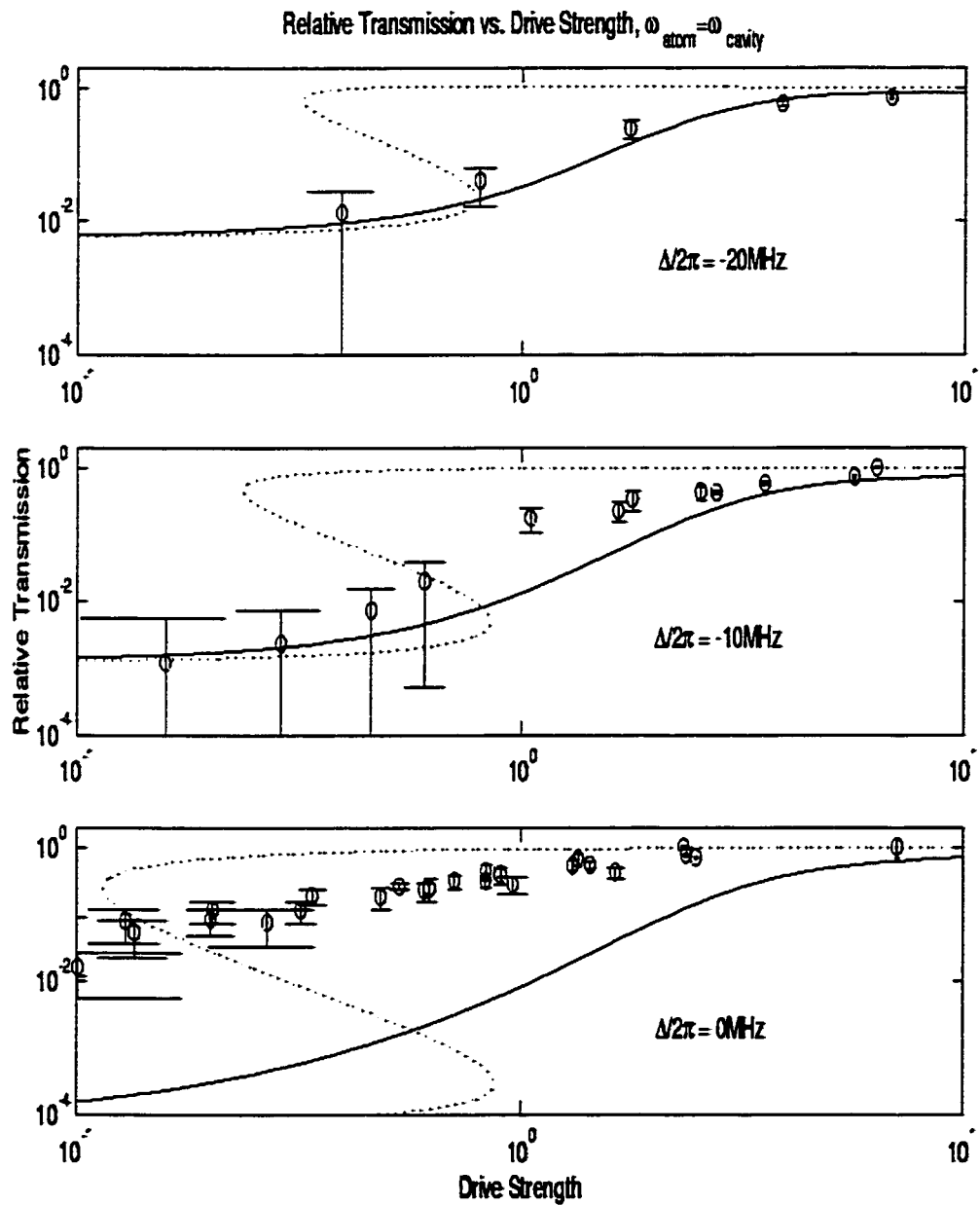


Figure 3.8: Saturation of downgoing atom transits as a function of drive strength \bar{n}_0 , for probe detunings $\Delta/2\pi = \{-20\text{MHz}, -10\text{MHz}, 0\text{MHz}\}$.

refers to $\Delta \equiv \omega_{\text{probe}} - \omega_{\text{atom}}$. For this data, shown in Figure 3.9, agreement is somewhat better for red detunings, but overall not as good as was the case in Figure 3.8. This can again be understood in terms of the channeling effect of light forces. In the data of Figure 3.8, as an atom enters the cavity the lower atom-cavity dressed state resonance (the lower peak in the vacuum-Rabi spectrum) shifts toward the probe field, meaning that this lower dressed state (which spatially forms a confining potential as discussed in Section 4.2), will be preferentially populated. However, for a probe resonant with the empty cavity, the arrival of an atom moves the dressed state resonance *away* from the probe, and no confining/channeling potential results.

We note for weak driving fields, the quantum and semiclassical theories (solid and dotted traces) yield the same results for the relative transmission, yet the data of Figure 3.9 agrees with neither. Referring back to the measurements of Figure 3.5, we see that for resonant or blue probe detunings, atoms transits do not reach their expected magnitude; a probe-cavity detuning of $\leq -20\text{MHz}$ is required to channel atoms into regions of optimal coupling. For the data of Figure 3.9 this probe-cavity detuning is zero, so we expect that atoms will not reach regions of optimal coupling and that the transit signals are therefore shallower than the ideal theory would predict.

3.6 Conclusion

In conclusion, by exploiting laser cooled atoms in cavity QED, a unique optical system has been realized which approximates the ideal situation of one atom strongly coupled to a cavity. The system's characteristics have been explored atom by atom, leading to measurements of the “vacuum-Rabi” splitting and of the nonlinear transmission for probe photon number ~ 1 . As the interaction energy $\hbar g$ is larger than even the atomic kinetic energy, the sub-photon intracavity fields have a strong mechanical effect on the atomic motion, channeling atoms toward or away from maxima of the field, depending on the detuning of the driving laser.

In these measurements, each atom signal was used to obtain only a single data point (height or depth), but as can be seen from Figure 3.3 the time-dependent

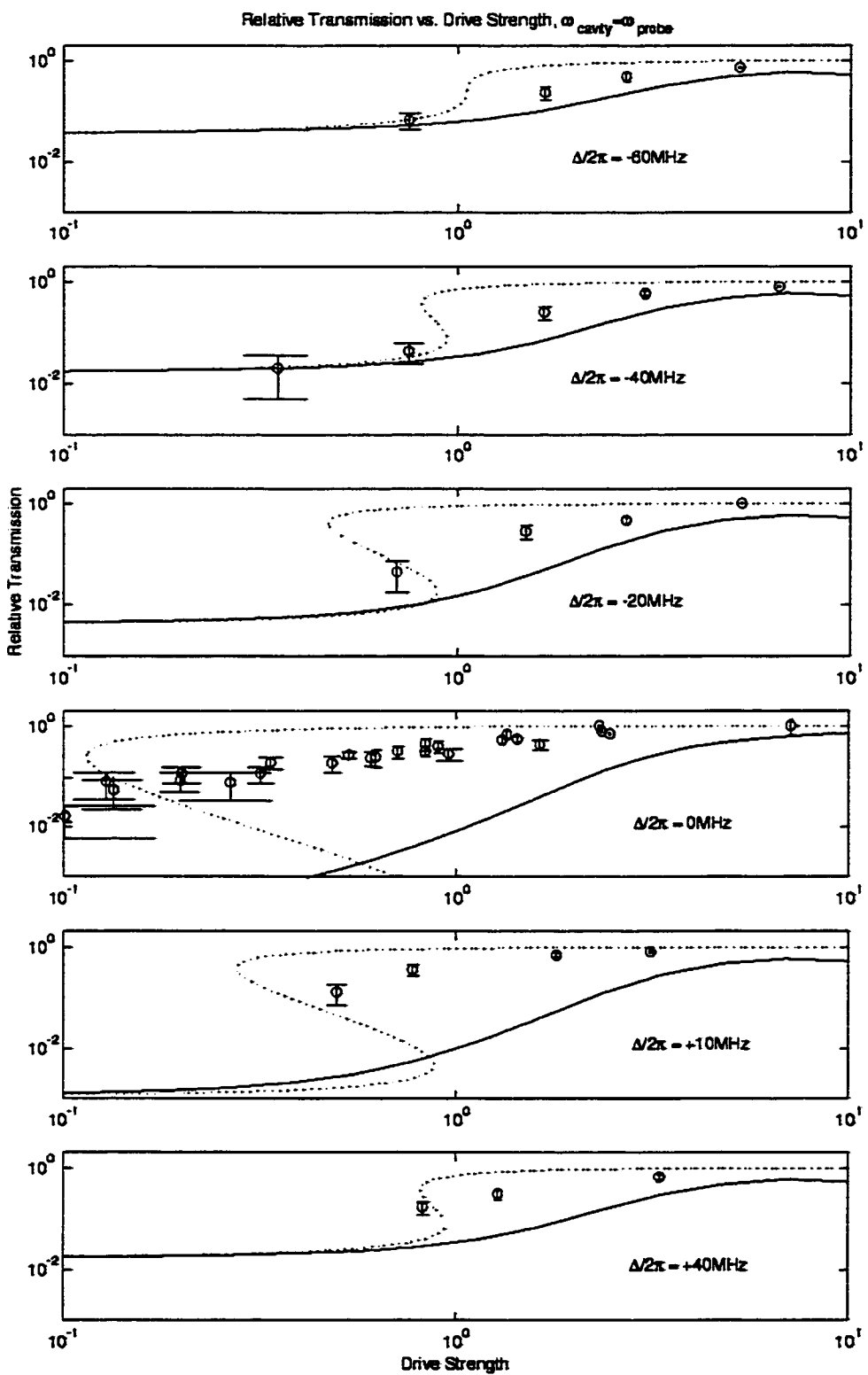


Figure 3.9: Saturation of downgoing atom transits as a function of drive strength \bar{n}_0 , for probe detunings $\Delta/2\pi = \{-20\text{MHz}, -10\text{MHz}, 0\text{MHz}\}$, and cavity detunings chosen such that $\omega_{cavity} = \omega_{probe}$.

individual atom transit signals contain far more information than just these peak values. In the next stage of this experimental effort, described in Chapter 4, we derive an explicit mapping from transmission to atomic position, and are able to reconstruct the trajectories of single atoms in the cavity.

Because $I \gg 1$, the system offers considerable opportunity for long interaction times and controlled quantum dynamics, such as to generate a bit stream containing $m \sim 10^4$ photons with a single falling atom [8] or to trap one atom in the quantized cavity field, as will be investigated in Chapter 4. Although the atomic center-of-mass motion has here been treated classically, this work sets the stage for investigations of quantum dynamics involving the quantized CM and the internal (atomic dipole+cavity field) degrees of freedom [79, 62], including trapping by way of the “well-dressed” states for single quanta [63].

Chapter 4 Experiment 2: Trapping single atoms with single-photon fields

This Chapter is partially based on “The Atom-Cavity Microscope: Single Atoms Bound in Orbit by Single Photons,” C. J. Hood, T. W. Lynn, A. C. Doherty, A. S. Parkins and H. J. Kimble, *Science* **287**, 1447 (2000).

In the experiments of Chapter 3, single atoms transits were observed, and used to map out properties of the atom-cavity system. The next stage of this experimental effort was to *trigger* the probe intensity on these atom transits, to trap individual Cesium atoms by the mechanical forces associated with single photons. The work was carried out primarily by myself and Theresa Lynn, with initial involvement by Michael Chapman, and in the final stages, by Kevin Birnbaum.

As described in Section 1.2, in addition to providing single-quantum forces able to localize single atoms, strong coupling also means that the presence of an atom can significantly modify the intracavity field [24, 25, 26, 44, 45, 46, 28, 27, 47, 49], thereby enabling real-time monitoring of an atomic trajectory by way of the light emerging from the cavity, as already observed for the atom transits of Chapter 3. In more quantitative terms, the ability to sense atomic motion within an optical cavity via the transmitted field can be characterized by the optical information $I = \frac{\alpha g^2 \tau}{\kappa}$. This indicates the number of photons that can be collected (with detection efficiency α) from this system as signal in time interval τ . When $I \simeq (5 \times 10^9 / \text{s}) \times \tau \gg 1$ as in our experiment, atomic motion through the spatially varying cavity mode leads to changes in the transmitted field that can be recorded with high signal-to-noise ratio on microsecond time scales.

In this case, for an atom *localized* within the resonator, we recover real-time information about the position of the atom as it moves within the trapping potential.

These records of the atomic motion show strong oscillations in transmission, indicative of atoms orbiting the center of the potential. The known mapping of transmission to coupling strength $g(\vec{r})$ (and hence to atomic position \vec{r}) then allows us to infer the atom's position as it moves within the potential. We can then investigate characteristics of the trapping potential in detail, including measurements of the trap oscillation frequencies and trap lifetimes of individual atoms.

Finally, an inversion algorithm developed by Theresa Lynn, which infers both atom position $\vec{r}(t)$ and angular momentum $L(t)$ from the transmission signal, allows individual atom trajectories to be reconstructed from the record of cavity transmission, and reveals single atoms bound in orbit by single photons. This reconstruction demonstrates a new measurement device, which we have called the atom-cavity microscope (ACM), which in these initial experiments yields $2\mu\text{m}$ spatial resolution in a $10\mu\text{s}$ time interval for atomic motion in free space. Over the duration of the observation, the sensitivity is near the standard quantum limit for sensing the motion of a Cesium atom.

4.1 Apparatus

The experimental setup for this work is essentially the same as for the work of Chapter 3, and is pictured in Figure 4.1. A cloud of Cesium atoms is collected in a magneto-optical trap (MOT[36]) in a vacuum chamber at 10^{-8}Torr , sub-Doppler cooled to a temperature of $\simeq 20\mu\text{K}$ then released to fall under gravity. With initial mean velocity $\bar{v} \simeq 4\frac{\text{cm}}{\text{s}}$, the cold atoms then fall 3mm toward two mirrors which form an optical resonator (cavity).

To interact with light in the cavity mode, an atom must fall through the $9\mu\text{m}$ gap between the edges of the mirrors and also through the waist $w_0 \simeq 14\mu\text{m}$ of the Gaussian mode of the resonator. As a result, even with 10^4 atoms initially, only one or two atoms are observed crossing the standing-wave mode of the cavity each time the MOT is dropped, represented by the arrow of Figure 4.1. The cavity is driven by a circularly polarized probe field $\mathcal{E}_{\text{probe}}$ of frequency $\omega_{\text{probe}} = \omega_{\text{atom}} + \Delta_{\text{probe}}$, the

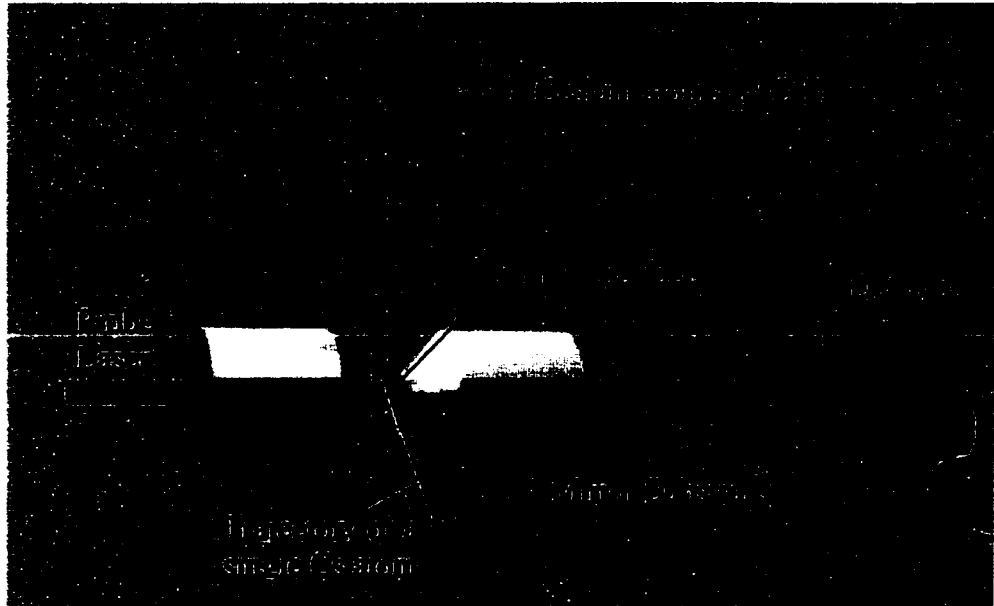


Figure 4.1: Schematic of the experimental apparatus.

transmission of which is recorded by heterodyne detection with overall efficiency for detection of an intracavity photon 25%. Three substantial changes were made to the experimental setup with respect to the earlier experiments:

4.1.1 Cavity

Since the cavity used for the experiments of Chapter 3 deteriorated unexpectedly as this next stage of experiments began, a new cavity was used for the following work. The optical cavity is formed by two 1mm diameter, 10cm radius of curvature mirrors, located on the tapered end of 4mm length x 3mm diameter glass substrates. The multi-layer dielectric mirror coatings have a transmission of 4.5×10^{-6} and absorption/scatter losses of 2.0×10^{-6} , giving rise to a cavity finesse $F = 480,000$. For the measured cavity length $l = 10.8\mu\text{m}$, we then have parameters $(g_0, \kappa, \gamma) = 2\pi(110, 14.2, 5.2)$ MHz. We ran into unexpected problems with cavity mount stability and cavity birefringence during construction of this cavity, the details of this described in Chapter 5. Our final solution was the new cavity mount design pictured in Figure 2.11.

4.1.2 Optical pumping

Once atom-trapping signals had been observed, an additional laser beam was added to the setup, tuned to the $\{6S_{1/2}, F = 3\} \rightarrow \{6P_{3/2}, F = 4\}$ transition. Without this additional field, if a trapped atom made a transition to the $\{6S_{1/2}, F = 3\}$ level it would become untrapped, and undetectable by our probe field. To optimize our trap lifetimes we therefore added this “repumping” laser to return these atoms to the $\{6P_{1/2}, F = 4\}$ ground state. The intensity of this field was adjusted operationally to give the best trap lifetimes.

The optical pumping beam is spatially overlapped with the probe and enters along the cavity axis. As this beam is 9GHz detuned from the cavity resonance, only a tiny proportion of the incident light enters the cavity. However, since the cavity FSR \gg 9GHz, and the cavity transverse-mode spacing $\simeq 60\text{GHz} \gg 9\text{GHz}$, then we expect the optical pumping light that does enter the cavity is spatially well overlapped with the probe field, and optical pumping will be fairly uniform throughout the cavity mode.

4.1.3 Locking method

For these experiments the cavity was locked directly to the transmission of the weak probe field, with the feedback signal taken from the same video-out port of the spectrum analyzer that is used to record the data. Upon triggering on an atom transit, the lock was switched off for 2ms, so as not to interfere with the atomic dynamics by moving the cavity in response to atom-dependent signals. The passive stability of our new mount design means that the cavity length does not drift significantly during this 2ms time interval (the main DC drift which limited this switch-off interval was thermal in origin, and related to heating and cooling of the chamber by our magnetic field coils and cooling water). By measuring a probe field tuned to the side of the cavity resonance, we estimate the cavity stability when locked to the weak probe in this way to be $\approx \pm 2\text{MHz}$, these being slow variations on timescales $\approx 10\text{ms}$.

4.2 Triggering trapping, the basic idea:

If an atomic dipole coupled to the quantized cavity field satisfies both the strong coupling condition (i.e., $g_0 \gg \kappa, \gamma$) for its *internal* degrees of freedom, and in addition the atom's kinetic energy E_k is small enough that $g_0 > (E_k/\hbar, \gamma, \kappa)$, then strong coupling should also have significant consequences for the *external*, center-of-mass motion of the atom. The seminal work of Refs. [51, 80] and numerous analyses since then [50, 63, 81, 82] have made it clear that a rich set of phenomena should arise from the interaction of the mechanical motion of atoms with a quantized light field in cavity QED. In this regime a single quantum is sufficient to profoundly alter the atomic center-of-mass (CM) motion, as for example in Ref. [63]. The effect of strong coupling on the atomic center-of-mass motion has only recently begun to be explored experimentally [25, 26, 45, 27, 47], but is of importance both in terms of understanding the underlying fundamental quantum processes, and also of practical concern for the use of cavity QED systems for quantum information processing protocols, for which atoms need to be strongly localized at particular locations within the cavity mode [9, 10, 6, 5].

As a significant development in this experimental effort, we have reported the first observations of a single atom trapped by an intracavity field with mean photon number $\bar{m} \simeq 1$ [26, 28, 27]. Such trapping is possible in our experiment because the coherent coupling energy $\hbar g_0 \simeq 5\text{mK}$ is larger than the atomic kinetic energy $E_k \simeq 400\mu\text{K}$.

The conceptual basis for trapping with single quanta in cavity QED is illustrated by Figure 4.2. Displayed is the spatial dependence of the energies $\hbar\beta_{\pm}(\rho)$ for the first excited states $|\pm\rangle$ of the atom-cavity system (the Jaynes-Cummings ladder of states) along the radial direction $\rho = \sqrt{y^2 + z^2}$, for optimal x (standing-wave) position and neglecting dissipation. The ground state of the atom-cavity system is $|a, 0\rangle$; the atom is in its ground state a and there are no photons in the cavity. For weak or no coupling, the first two excited states are that of one photon in the cavity and the atom in the ground state, $|a, 1\rangle$, and of the atom in the excited state e with no

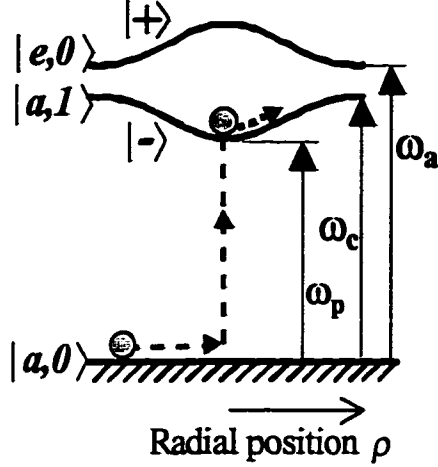


Figure 4.2: An atom entering the cavity in the ground state $|a, 0\rangle$ can be pumped into the lower dressed state $|-\rangle$, causing it to become trapped.

photons in the cavity, $|e, 0\rangle$. These two states are separated by an energy $\hbar\Delta_{ac}$, where $\Delta_{ac} \equiv \omega_{cavity} - \omega_{atom}$ is the detuning between the “bare” (uncoupled) atom and cavity resonances. As an atom enters the cavity along ρ it encounters the spatially varying mode of the cavity field, and hence a spatially varying interaction energy $\hbar g(\vec{r})$, given by $g(\vec{r}) = g_0 \cos(2\pi x/\lambda) \exp(-(y^2 + z^2)/w_0^2)$. The bare states map via this coupling to the dressed states $|\pm\rangle$, with energies $\beta_{\pm} = \frac{\omega_{atom} + \omega_{cavity}}{2} \pm [g(\vec{r})^2 + \frac{\Delta_{ac}^2}{4}]^{1/2}$. These spatially varying energies can be exploited to trap the atom via a strategy first suggested and analyzed by A. S. Parkins [42], and implemented in Ref. [26].

Consider an atom entering the cavity along ρ , with the system initially in the ground state $|a, 0\rangle$. When the atom reaches the center of the cavity mode, a laser field $\mathcal{E}_{probe}(t)$ at frequency ω_{probe} is switched on. When a photon is absorbed, the system is driven into the state $|-\rangle$, and the atom is bound by the potential well formed by spatial dependence of the energy $\hbar\beta_{-}(\vec{r})$. Photons are emitted from the system at rate κ , but continuous driving by $\mathcal{E}_{probe}(t)$ repopulates the $|-\rangle$ state. This creates a pseudo-potential $U(\vec{r})$ for times $>> \kappa$, which for weak driving fields has a depth approximately given by $p_{(-)}(\hbar\omega_{cavity} - \hbar\beta_{-}(\vec{r}))$, where $p_{(-)}$ is the steady-state population of state $|-\rangle$. For stronger driving, there will also be a contribution to

the pseudo-potential from populating higher-lying states in the Jaynes-Cummings ladder. For $\omega_{\text{probe}} \simeq \beta_-(\vec{r})$ the states populated are, like $|-\rangle$, confining, so a trapping pseudo-potential is maintained.

4.3 Simulated transits

Beyond this intuitive picture of trapping with the lower dressed state, our collaborators Andrew Doherty and Scott Parkins from the University of Auckland have carried out extensive analytical and numerical simulations of atomic motion for the parameters of our experiment, explained in more detail in Ref. [27], which I describe briefly here and will used throughout this chapter for comparison to the experimental data.

The conservative component for motion of an atom within the cavity mode can be described by an *effective potential* $U(\vec{r})$ determined by integration of the expectation value of the force operator

$$\hat{\mathbf{F}}(\vec{r}) = -\hbar \vec{\nabla} g(\vec{r}) (\hat{a}^\dagger \hat{\sigma}_- + \hat{\sigma}_+ \hat{a}), \quad (4.1)$$

with $(\hat{a}, \hat{a}^\dagger)$ as the annihilation and creation operators for photons in the cavity field and $\hat{\sigma}_\pm$ as the raising and lowering operators for atomic excitation. There are also non-conservative (velocity-dependent) and random (diffusive) forces that act on the atom. Because the time scale for internal (atomic dipole + cavity field) dynamics is much shorter than that for the atomic center of mass motion, $\langle \hat{\mathbf{F}}(\vec{r}) \rangle$ and these other forces can be calculated by solving the *steady-state* quantum master equation for the internal degrees of freedom alone [67]. The local atom-field coupling $g(\vec{r})$, probe parameters ($\mathcal{E}_{\text{probe}}, \Delta_{\text{probe}}$), detuning Δ_{ac} and cavity parameters determine the conservative force, friction, and diffusion acting on the atom at position \vec{r} . The trajectory of the atom is then calculated in a semiclassical approximation for the mean and variance of the atomic wavepacket.

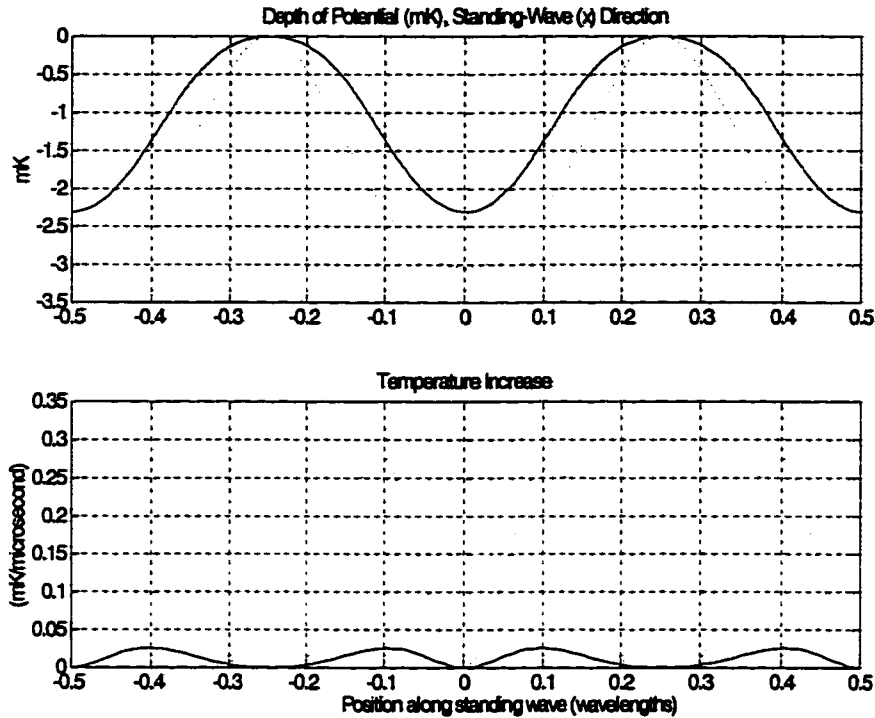


Figure 4.3: Effective Potential $U(\vec{r})$ and heating rate, along the standing-wave direction, x . Here the heating rate is predominantly due to dipole diffusion. At a field antinode (such as $x = 0$), diffusion is due to spontaneous emission only, giving a heating rate of 3×10^{-4} mK/ μ s.

4.4 Effective potentials, heating rates

Figures 4.3 and 4.4 show examples of the effective potential $U(\vec{r})$ calculated from the quantum treatment described above. Displayed are both the radial and axial dependencies $U(\rho, x_0)$ and $U(0, x)$ (that is, perpendicular to and along the cavity axis, where x_0 is an antinode of the standing wave). The depth of the potential $U_0 \simeq 2.3$ mK is greater than the initial kinetic energy of atoms in our experiment, $E_k \simeq 0.46$ mK, thereby enabling an atom to be trapped within the cavity mode. The perturbing effect of gravity on this potential is negligible.

Also shown in Figures 4.3 and 4.4 are the heating rates (mean rates of energy increase) $\frac{dE(\rho, x_0)}{dt}$ and $\frac{dE(0, x)}{dt}$ along the radial and axial directions, with $\frac{dE}{dt}$ related to the momentum diffusion coefficient D by $\frac{dE}{dt} = D/m$, where m is the atomic

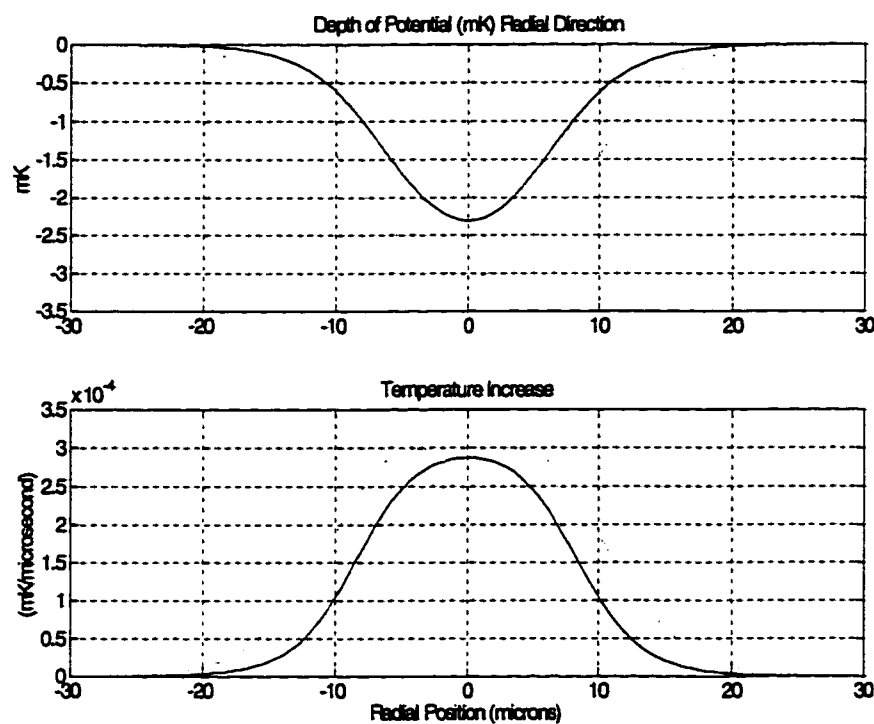


Figure 4.4: Effective Potential $U(\vec{r})$ and heating rate, along the radial direction, ρ . Here the heating rate is dominated by spontaneous emission.

mass of cesium. Near a field antinode (for example, $x = 0$), the random or diffusive component of the motion arising from $\frac{dE}{dt}$ on experimental time scales $\sim 50\mu s$ is on the whole much smaller than that associated with conservative motion in the potential U . Thus we expect a predominantly orbital motion within the cavity mode with a smaller (but non-negligible) diffusive component.

4.4.1 Comparison to a classical dipole-force trap

For comparison with the well-established theory of laser cooling and trapping in free space [36], Figures 4.3 and 4.4 also display in dotted lines the corresponding potential $V(\vec{r})$ and heating rate $\frac{dE(\vec{r})}{dt}$ derived in the absence of the cavity, but for the same beam geometry and the same peak field strength [83]. Note that although the free-space potential $V(\vec{r})$ is similar to the cavity QED potential $U(\vec{r})$, suggesting that trapping could be achieved without the cavity [as, for example, in the pioneering experiments with optical lattices [84, 85, 86]], in fact, in the axial direction the free-space heating rate $\frac{dE}{dt}$ is much greater than the corresponding cavity QED quantity $\frac{dE}{dt}$.

A simple estimate of the corresponding trap lifetimes [87] is obtained by averaging the diffusion over the spatial variation of the standing-wave (heating in the Gaussian direction is negligible by comparison). With a heating rate given by $\frac{dE}{dt} = \langle D(x) \rangle / m$ we then obtain a lifetime of $20\mu s$ for the classical dipole-force trap, and $250\mu s$ for the corresponding quantum case, for detunings and drive strength of Figures 4.7 and 4.10. However, as atoms are initially well confined to antinodes of the field where the diffusion is small, this will be an underestimate of the lifetime. A slightly better estimate (for the average distribution) is given by starting the atom initially at rest at an antinode ($x = 0$) of the field, then incrementally increasing the mean energy by steps of $(\langle D \rangle m)dt$, where $\langle D \rangle$ is the diffusion weighted by a normalized position distribution $P(x)$, that is $\langle D \rangle = \int D(x)P(x)dx$. The position distribution is here obtained at each energy step by assuming a harmonic well distribution $P(x) \propto 1/\sqrt{1 - (x/x_{\max})^2}$. This estimate gives slightly longer lifetimes of $28\mu s$ and $270\mu s$ for the classical and quantum cases. The contribution of velocity dependent forces in

the classical case was also calculated, and found to be negligible in comparison to the diffusive heating.

The trapping time for an atom in the free-space setting is tenfold less than the observations of Figure 4.7, so short that the atom would not make even one orbit before being heated out of the potential well. By contrast, this simple estimate for the quantum case within the setting of cavity QED is in reasonable agreement with the $340\mu\text{s}$ mean lifetime observed in the histogram of Figure 4.10.

We emphasize that the comparison in Figures 4.3 and 4.4 is made for the same peak electric field – the cavity is not simply a convenient means for increasing the electric field for a given incident drive strength. Rather, there are profound differences between the standard theory of laser cooling and trapping and its extension into the domain of cavity QED in a regime of strong coupling. At root is the distinction between the nonlinear response of an atom in free space and one strongly coupled to an optical cavity. In the latter case, it is the composite response of the atom-cavity system that must be considered as is described by the corresponding one-atom master equation in cavity QED. That this full quantum treatment of the atom-cavity system is required has been experimentally confirmed by way of measurements of the nonlinear susceptibility for the coupled system in a setting close to that used here [25, 26, 46].

A second and critically important point of distinction between the current work and traditional laser cooling and trapping in free space [36] relates to the ability to sense atomic motion in real time with high S/N. We stress that this is not simply a matter of a practical advantage, but a fundamental improvement beyond what is possible by way of alternate detection strategies demonstrated to date (such as absorption [88, 89] or fluorescence [90, 91, 92] for single atoms and molecules). An estimate of this enhanced capability is given by way of the optical information rate $I/\Delta t \sim 10^9/\text{s}$, which in the current work is the largest value yet achieved in optical physics.

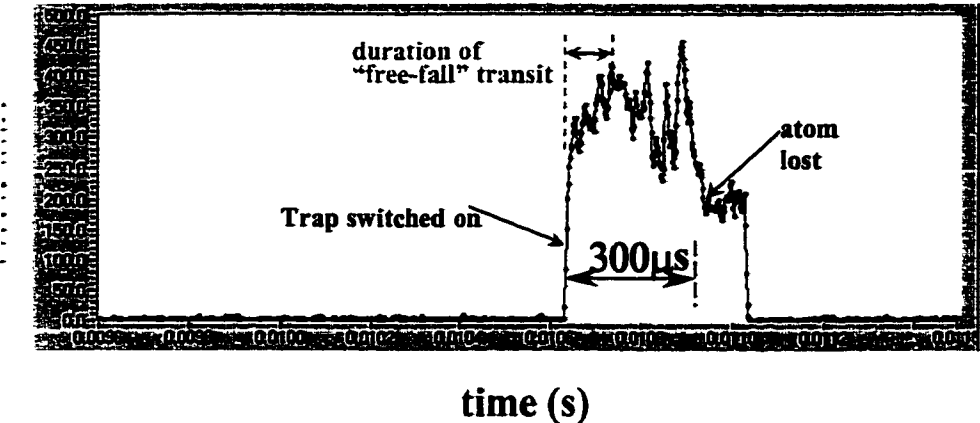


Figure 4.5: Triggered trapping with downgoing trigger signals [26].

4.5 Initial results: Triggering on resonant transits

Our first attempt at implementing this trapping scheme was carried out with the $(g_0, \kappa, \gamma) = 2\pi(120, 40, 5.2)$ MHz cavity of Chapter 3. The strategy was to (1) sense the atom entering the cavity by probing with a weak field close to the coincident atom-cavity resonance, (2) trigger this resonant field *off* (to reduce heating) and wait a fixed delay (typically $\simeq 10\mu\text{s}$) to allow the atom to move to the center of the cavity mode, then (3) trigger *on* a stronger probe field tuned to $\omega_{\text{probe}} \simeq \beta_-(0)$ (the energy of state $|-\rangle$) when the atom is at the center of the cavity mode $\vec{r} = 0$), to provide a strong potential to trap the atom.

Figure 4.5 shows an example of an atom trapped by this method. Displayed is the atom-cavity transmission for the strong trapping field (at frequency ω_{probe}). Triggered on an atom transit, this field is switched on for a total duration of $400\mu\text{s}$: the particular atom shown is trapped for $300\mu\text{s}$. While we had some limited success with this triggering strategy, with several examples observed of atoms trapped up to $300\mu\text{s}$, it was still the case that most triggers did not result in significant lengthening of the transits.

We believe that this was primarily because our triggering was not selective enough. Resonant probing gives a very sensitive meter for an atom entering the cavity mode

(the transmission drops by a factor of 10^2 for an optimally coupled atom, as discussed in Chapter 3), so that at our high trigger threshold we were detecting atoms essentially all atoms at the very edge of the cavity mode. However, very few of these atoms should be expected to end up in regions of strong coupling $g(\vec{r}) \simeq g(0)$, since many of these triggers will be for atoms with initial y position passing through the sides of the Gaussian beam with $y \gg w_0$, and others triggers are for atoms falling in the top with $y \simeq 0$ but passing through nodes of the standing-wave along x .

To try and improve this selectivity, we lowered the trigger point to select only very deep down-going transits, but this had little effect on our trapping effectiveness - presumably because heating from the resonant beam is significant in this case, limiting the trap lifetime.

4.6 Triggering on upgoing transits to trap single atoms

It was decided that a better strategy would be to tune our triggering beam to $\omega_{\text{probe}} \simeq \beta_-(0)$. This would have several positive effects:

1. Only atoms in positions of strong coupling $g(\vec{r}) \simeq g_0$ are detected and cause a triggering *on* of the trapping potential.
2. Heating from this probe beam is less than in the case of resonant probing.
3. The shallow potential formed by the weak triggering beam causes channeling of the atoms into regions of high coupling, as previously observed in the spectrum measurements of Chapter 3. This both increases the number of well-coupled atoms available for triggering, and ensures that atoms are initially located near antinodes of the standing-wave, greatly simplifying our interpretation of the atom-cavity transmission signals.

Unfortunately, as we were about to try and implement this triggering scheme our cavity finesse dropped dramatically, making further experiments impossible. A painful year of technical development (see Chapter 5) then followed before the new

cavity ($\{g_0, \kappa, \gamma\} = 2\pi\{110, 14.2, 5.2\}$ MHz) was installed in the vacuum chamber, and we were ready to resume the experiment. With the apparatus running again, we tried the new triggering scheme, and immediately saw transits lengthened to $>1\text{ms}$, with interesting internal structure (oscillations) in the single-atom transmission signals. Over the next few days, by exploring different detunings/drive strengths we operationally found regions of good trapping, with atoms trapped up to 1.9ms .

To trap an atom, we drive the cavity with a weak circularly polarized probe laser at frequency $\omega_{\text{probe}} \simeq \beta_-(0)$. This probe field initially has intracavity photon number $\bar{n}_p = 0.05$, providing a small, off-resonant excitation of the empty cavity. Because the resulting (shallow) potential $U_p(\vec{r})$ is deepest for an atom at the cavity center, an atom entering the cavity effectively sees a series of potential wells, determined by the Gaussian transverse shape of the cavity mode and the standing-wave structure of the light inside the cavity. The atom is channeled by $U_p(\vec{r})$ towards regions of high coupling, and as the energy β_- of $|-\rangle$ shifts accordingly, there is a corresponding increase in probe transmission as β_- comes into resonance with ω_{probe} [25]. By using upgoing transits, we are guarantee that the atom is at a region of high coupling strength at the time of triggering, so that when the potential is switched on the atom should be trapped. When the transit height reaches the trigger level (i.e., $g(\vec{r})$ exceeds some predetermined threshold g_t), we switch the probe power up to a level $\bar{n}_t = 0.3 \pm 0.05$ intracavity photons, creating a deep confining potential $U(\vec{r})$ around the atom to trap it.

Note that throughout we denote by \bar{n} the photon number for the *empty* cavity, with $\bar{m} \equiv |\langle \hat{a} \rangle|^2$ as the corresponding quantity with an atom present; these quantities are directly proportional to the detected transmission signal. Because we employ balanced heterodyne detection, we measure $|\langle \hat{a} \rangle|^2$ rather than the photon number $\langle \hat{a}^\dagger \hat{a} \rangle$. In the absence of an atom we have a weak coherent field within the cavity, so these two quantities are of course equal. However, with an atom present they are typically different. For the experimental parameters of the data presented in this work, this difference is calculated to be 10-20%; however, for different choices of $(\omega_{\text{cavity}}, \omega_{\text{probe}})$ the difference can be much more dramatic, as discussed in Section

4.10.2 to follow.

To demonstrate the variety of individual atom signals seen, Figure 4.6 shows a collection of individual atom transmission signals, each generated with the triggering/trapping scheme described above.

Moving now to examine these transmission signals in more detail, shown in Figure 4.7(a,b) are traces for two individual atom trajectories. At $time = 0$, the atom is detected, triggering the driving field \mathcal{E}_{probe} to switch from $\bar{n}_p \rightarrow \bar{n}_t$ to catch the atom. The cavity transmission is highest (with $\bar{m} \simeq 1$) when the atom is close to the center of the cavity, and the observed oscillations in \bar{m} result from modifications in cavity transmission as the atom moves within the cavity mode. When the atom eventually does leave the cavity mode, transmission returns to \bar{n}_t . To demonstrate the strong effect of the triggering/trapping strategy, Figure 4.7(a) also shows a typical atom transit (black trace) recorded with a drive strength of $\bar{n} = 0.3$ and no triggering. In this case, atoms fall through $U(\vec{r})$ with average transit time $74\mu s$. By contrast, the triggering protocol described above extends this average to $\tau = 340\mu s$.

Figure 4.7(c,d) show transmission calculated from the numerical simulations of individual atom transits, with experimental noise added to these traces. Also shown are the calculated positions $y(t), z(t)$ in the radial direction, and $x(t)$ in the standing-wave direction, corresponding to the transmission shown.

The simulations indicate that the motion along the cavity axis x is tightly confined (for example, to a region $\delta x \simeq \pm 50\text{nm}$ from the simulations) due to the steepness of $U(x)$ and to channeling of the incoming atoms to regions of high light intensity for the red-detuned field. However, as shown in Figure 4.7(c,d), ultimately the atom does escape due to a “burst” of heating along the cavity axis. Because the diffusion coefficient is proportional to the $|\nabla U(x)|^2$, there is a slow heating rate while the atom is well confined at the minimum of the potential, but as soon as it begins to heat and explore regions of higher curvature, the heating rate accelerates quickly and the atom is lost - this burst of heating occurring over a time less than the orbital period T . This dominant loss mechanism appears repeatedly in the simulations over a wide range of operating parameters. Once an atom is heated sufficiently to leave the antinode to

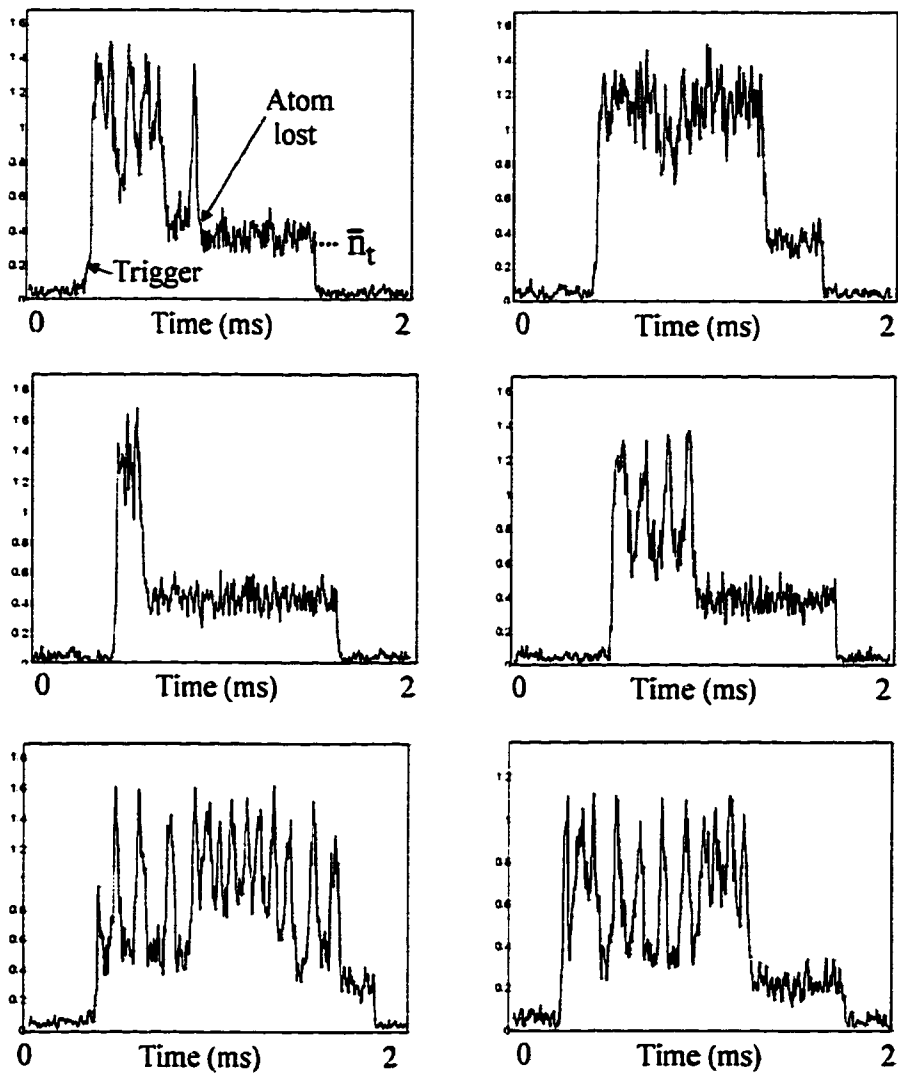


Figure 4.6: Individual trapped atoms give rise to different transmission signals $\bar{m}(t)$, depending on their individual trajectories. After the atom is lost, the intracavity intensity drops back to \bar{n}_t , then after 1.2–1.5 ms is switched back down from \bar{n}_t to \bar{n}_p . These traces are for a range of parameters near $\Delta_{ac}/2\pi \approx -100\text{MHz}$, $\Delta_{probe}/2\pi \approx -145\text{MHz}$, $\bar{n}_t \approx 0.4$ photons.

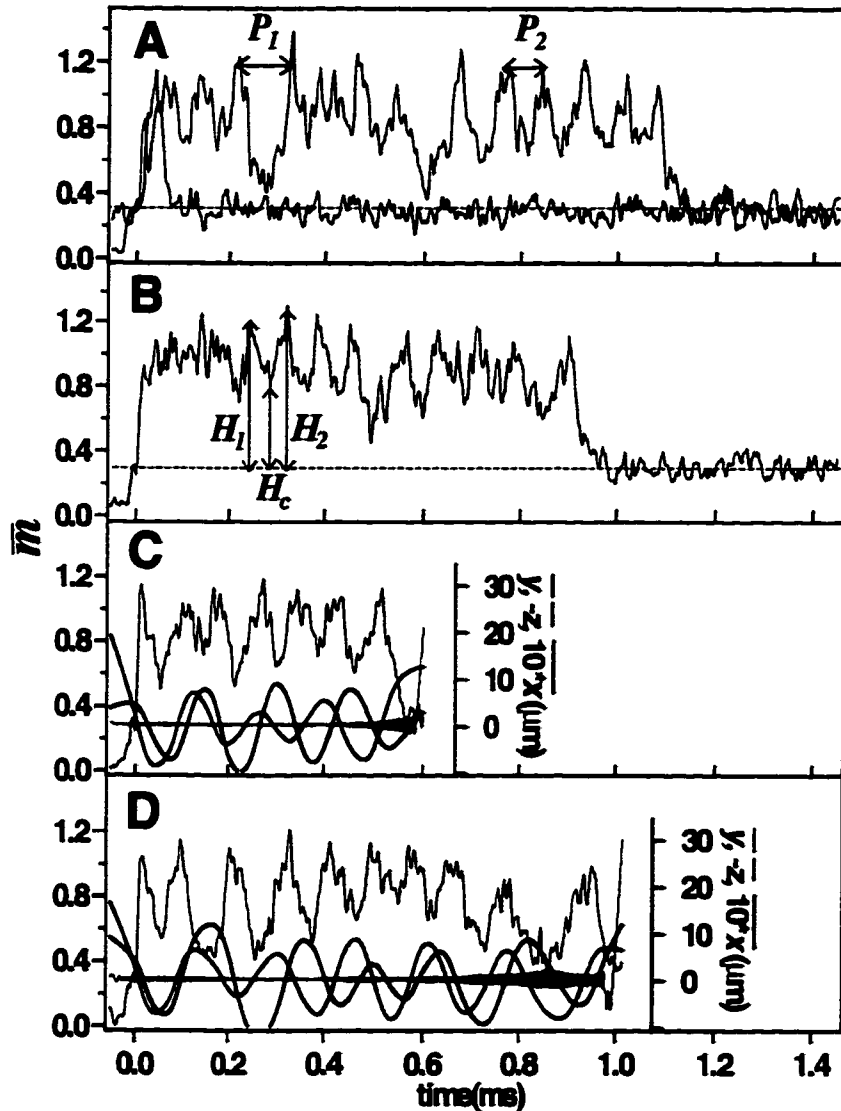


Figure 4.7: (a,b) Examples of atom transits, i.e., cavity transmission as a function of time as an atom passes through the cavity field. Red traces show atoms trapped using the triggering method described, with $\bar{m} \simeq 1$ photon mean field strength. For comparison, an untriggered (untrapped) atom transit is shown in black. For these traces, $\Delta_{\text{probe}}/2\pi = -125\text{MHz}$ and $\Delta_{\text{ac}}/2\pi = -47\text{MHz}$. The corresponding level diagram is shown in the inset, with $\omega_{(p,c,a)} = \omega_{(\text{probe},\text{cavity},\text{atom})}$ of the text. (c,d) Theoretical simulations of atom transits for the parameters $\Delta_{\text{probe}}/2\pi = -125\text{MHz}$, $\Delta_{\text{ac}}/2\pi = -47\text{MHz}$. Shot noise and technical noise have been added to the transmission signal, shown in red. Other traces show the three-dimensional motion of the atom. Motion along x , the standing-wave direction, has been multiplied by 10 to be visible on the plot. Note the atom is very tightly confined in x until rapid heating in this direction causes the atom to escape.

which it was initially confined, it is very rarely recaptured in another antinode but rather escapes the cavity altogether, because the Sisyphus-type mechanisms [82] for cooling are ineffective in the current setting (as confirmed by the simulations).

Experimentally, we can set a limit on atomic excursions along x by examining the amplitude of the observed oscillations. Since the oscillation frequency $v_x \simeq 1.5\text{MHz}$ is well above our detection bandwidth of 100kHz , large excursions in x would lead to significant reductions in amplitude for the observed oscillations in transmission, from which we deduce a bound $\delta x^e \lesssim 70\text{nm}$ for $\rho \ll w_0$. Inference of axial localization without such bandwidth limitations can be found in [46].

We emphasize that the corresponding quantum state is a *bound state* of atom and cavity. The situation is analogous to a molecule for which two atoms share an electron to form a bound state with a lower energy than two free atoms. Here a “molecule” of one atom and the cavity field is formed via the sharing of one photon excitation on average, thereby binding the atomic center-of-mass motion. Note that our atom-cavity “molecule” only exists while an excitation is present, with decay set by κ , since $\kappa > \gamma$. Photons leak out of the cavity at rate κ , but the cavity is continuously driven by the probe field which replenishes the intracavity photon number, repeatedly recreating the bound state before the atom has a chance to escape.

4.7 Characterization of transmission oscillations

A striking feature of the traces in Figure 4.7 are the oscillations in atom-cavity transmission within the transit of a single atom. As illustrated by the position traces of the simulated transits in Figure 4.7C,D, our simulations show that these oscillations arise from elongated atomic orbits in planes perpendicular to the cavity axis.

Having established that atoms are well localized in x at antinodes of the standing-wave, we can restrict our attention to motion in transverse $(y, z) \rightarrow (\rho, \theta)$ planes, and investigate the validity of our model for the effective potential $U(\rho, \theta)$ by comparing the predicted and observed oscillation frequencies of single atoms within the potential $U(\rho)$. Note that oscillations with a short period (P_1 in Figure 4.7A) have a lower

amplitude than those of longer period (P_2 in Figure 4.7A). This is due to the anharmonicity of our approximately Gaussian-shaped potential $U(\rho)$; large-amplitude oscillations are expected to have a longer period than nearly-harmonic oscillations at the bottom of the well.

The data in Figure 4.8A reveal this anharmonicity. Plotted is the period P versus the amplitude A for individual oscillations, where $A \equiv 2((H_1+H_2)/2-H_c)/(H_1+H_2)$, with parameters $\{H_1, H_2, H_c\}$ indicated in Figure 4.7B. The solid curve is calculated for motion in the effective potential $U(\rho)$ shown in the inset to Figure 4.8A; the comparison is absolute with no adjustable parameters.

We also present in Figure 4.8B similar results for A versus P from the numerical simulations (for the same parameters as Figure 4.8A, without the experimental noise added to the traces of Figure 4.7). This plot reveals the relative importance of different mechanisms that cause deviations from the one-dimensional (1D), conservative-force model. To this end, we select from the simulation points corresponding to atoms with low angular momentum about the center of the cavity, that is, those which pass close to the center of the potential ($\rho = 0$) and therefore have close to a close to 1D trajectory. As expected these points (shown in black in Figure 4.8B) fall closest to the curve given by the 1D potential $U(\rho)$. The grey points in Figure 4.8B have larger angular momentum, corresponding to atoms in more circular orbits. The presence of this separation by angular momentum in the simulation indicates that friction and momentum diffusion, which tend to invalidate the conservative-force model, have a relatively small effect on the motion. This is also evident from the discussion of potentials and heating rates $U(\vec{r})$ and $\frac{dE}{dt}$ in Section 4.4. The spread in observed angular momenta is constrained by our triggering conditions - the potential is switched up only when an atom reaches a position near the center of the cavity mode, so that the measured trajectories tend to be in a regime of tight binding. The wider spread in the data of Figure 4.8A relative to 4.8B comes from experimental noise (present in Figure 4.8A but not added to Figure 4.8B), with both shot-noise and technical noise contributing significantly. We have made comparisons as in Figure 4.8 for several data sets with varying values of $\{(\mathcal{E}_{\text{probe}}, \Delta_{\text{probe}}), \Delta_{\text{ac}}, \bar{n}_t\}$ with the same conclusions.

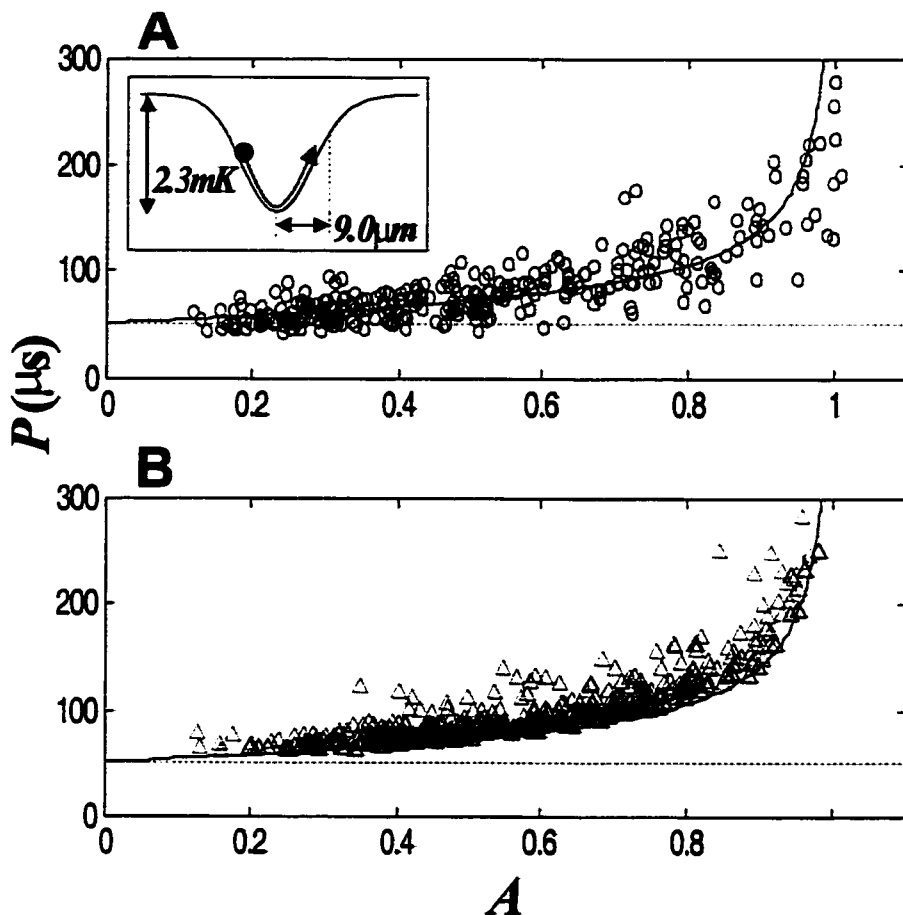


Figure 4.8: Oscillation period as a function of amplitude from experimental (a) and simulated (b) atom transits, for $\Delta_{\text{probe}}/2\pi = -145 \text{ MHz}$ and $\Delta_{\text{ac}}/2\pi = -80 \text{ MHz}$. Calculated one-dimensional oscillation in the anharmonic effective potential (inset) is shown by the solid curve, with no adjustable parameters. In simulated data, note the separation of data points by angular momentum; lowest angular momentum transits (black) most closely follow the one-dimensional model.

In Figure 4.9 are displayed a series of these anharmonicity curves, for a series of drive strengths $\bar{n}_t = \{0.08, 0.16, 0.31, 0.7\}$ photons, at detunings ($\Delta_{\text{probe}}/2\pi = -145\text{MHz}$, $\Delta_{\text{ac}}/2\pi = -80\text{MHz}$). The relative size of the atom-transit signals H/\bar{n}_t changes significantly over this range of drive strengths, and to highlight this we chose a different normalization to that of Figure 4.8, now plotting the period P versus the depth of individual oscillations, normalized by the empty cavity field \bar{n}_t . That is, we undo the previous normalization for \bar{n}_t and plot $(H_c + \bar{n}_t)/\bar{n}_t$. The solid curves are again calculated for one-dimensional conservative motion in the effective potentials $U(\rho)$ at each driving strength, derived from the quantum master equation for the measured parameters $\{(\mathcal{E}_{\text{probe}}, \Delta_{\text{probe}}), \Delta_{\text{ac}}, \bar{n}_t\}$; the comparison is absolute with no adjustable parameters. The first data set ($\bar{n}_t = 0.08$) was collected from atom transits rather than triggered/trapped atoms, this drive strength being too weak to reliably trap atoms. As a result, few oscillations were observed, with those present due to atoms which were caught in the potential well without triggering, as described in Section 4.8.1. In the final panel of Figure 4.9 the weaker driving data ($\bar{n}_t = 0.16$) of the second panel are overlaid in grey circles to highlight the difference between the data sets. The trend to smaller oscillations with higher drive strength is due primarily to saturation of the atom-cavity relative transmission as drive strength is increased, decreasing from a factor of 5 at 0.16 photons to a factor of 3 at 0.70 photons.

4.8 Experimental characterization of single-photon trapping

4.8.1 Histograms of transit lengths - triggered vs. untriggered

To explore the effect of triggering in more detail, in Figure 4.10 we plot histograms of transit lengths τ for untriggered (Figure 4.10(a)) and triggered (Figure 4.10(b)) events, for the same experimental parameters as Figure 4.7. From these histograms

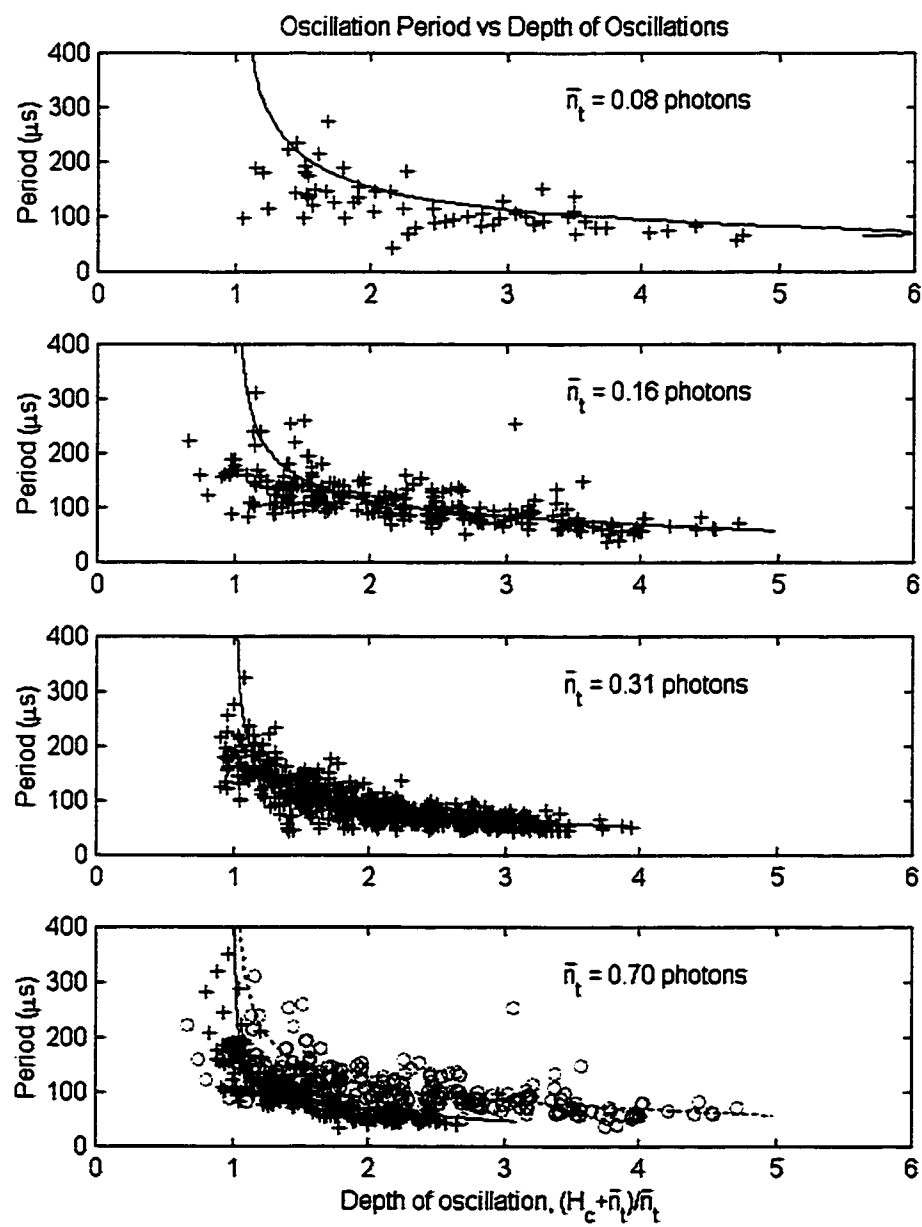


Figure 4.9: Oscillation period vs. depth of oscillations, for a series of empty cavity photon numbers $\bar{n}_t = \{0.08, 0.16, 0.31, 0.70\}$.

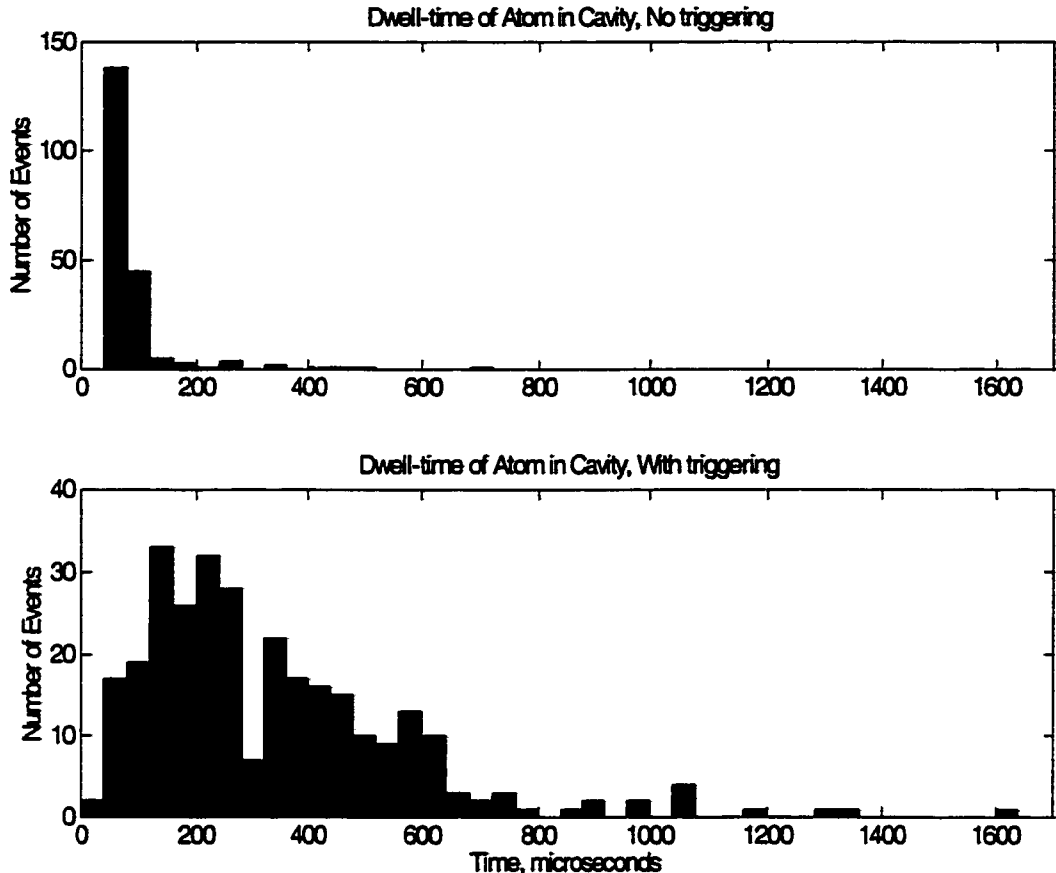


Figure 4.10: Dwell time τ of single atoms in the cavity, with and without employing the triggered trapping strategy.

it is apparent that the triggering/trapping strategy has a strong effect on extending the trap-time τ of an atom in the cavity mode, with most events lengthened from $\simeq 75\mu\text{s}$ to $> 200\mu\text{s}$, and the average trap-time extended to $\tau = 340\mu\text{s}$. The longest trap-time shown in this data set is $>1.6\text{ms}$, and times of 1.9ms have been observed in other data sets. Although single atoms have recently been trapped with lifetime 28ms in a regime of strong coupling by way of a classical dipole-force trap [28], our results are the first example of trapping using the single-photon quantum field itself.

Even in the untriggered case there are a few rare events of atoms trapped up to $\simeq 700\mu\text{s}$ duration. These can be explained by the large momentum diffusion present along the x (standing-wave) direction. As explained in more detail in Ref. [27], this diffusion is the principal cause of heating of the atomic motion, and hence limits sets

the trap lifetime. However, this strong diffusion can also occasionally lower the falling atom's energy sufficiently that it becomes trapped by the pseudo-potential even in the absence of the triggering scheme, leading to the rare long events of Figure 4.10(a). The triggering/trapping scheme is much more efficient way of loading atoms into the potential, as evidenced by the qualitatively different character of the distributions of Figure 4.10(a) and (b).

4.8.2 Histograms of traptimes - experimental vs. simulated transits

Next, we compare the histogram of experimental trap-times to the corresponding distribution obtained from the numerical simulations of single atom trajectories. These results are presented in Figure 4.11, with 4.11(a) the experimental results, and 4.11(b) the simulations.

From Figure 4.11 it can be seen that while experiment and simulation are generally in good agreement, minor differences exist, such as the slightly longer average trap-times of the simulated transits; for this simulation a mean of $\langle \tau \rangle_{sim} = 415\mu s$ compared to the $\langle \tau \rangle_{expt} = 340\mu s$ mean of the data. In the simulations, these small discrepancies were found to be highly sensitive to the initial conditions (positions and velocities) of atoms entering the cavity mode, values which are not particularly well characterized experimentally.

Additionally, the method of assigning initial conditions to the simulated atoms may cause some differences. They are set as follows: the z (vertical) position and velocity distribution are just those of the initial MOT distribution evolved forward in time. y and x are given flat position distributions (the MOT is assumed large compared to the $14\mu m$ mode waist and $9\mu m$ gap between the mirrors), the y velocity distribution is that of the initial MOT, and the x velocity is a flat distribution cut off at velocities for which the atom would hit the mirrors surfaces before reaching the mode. Each individual atom simulated is randomly assigned values for these, with each of the 6 parameters assumed uncorrelated. While this is a reasonable

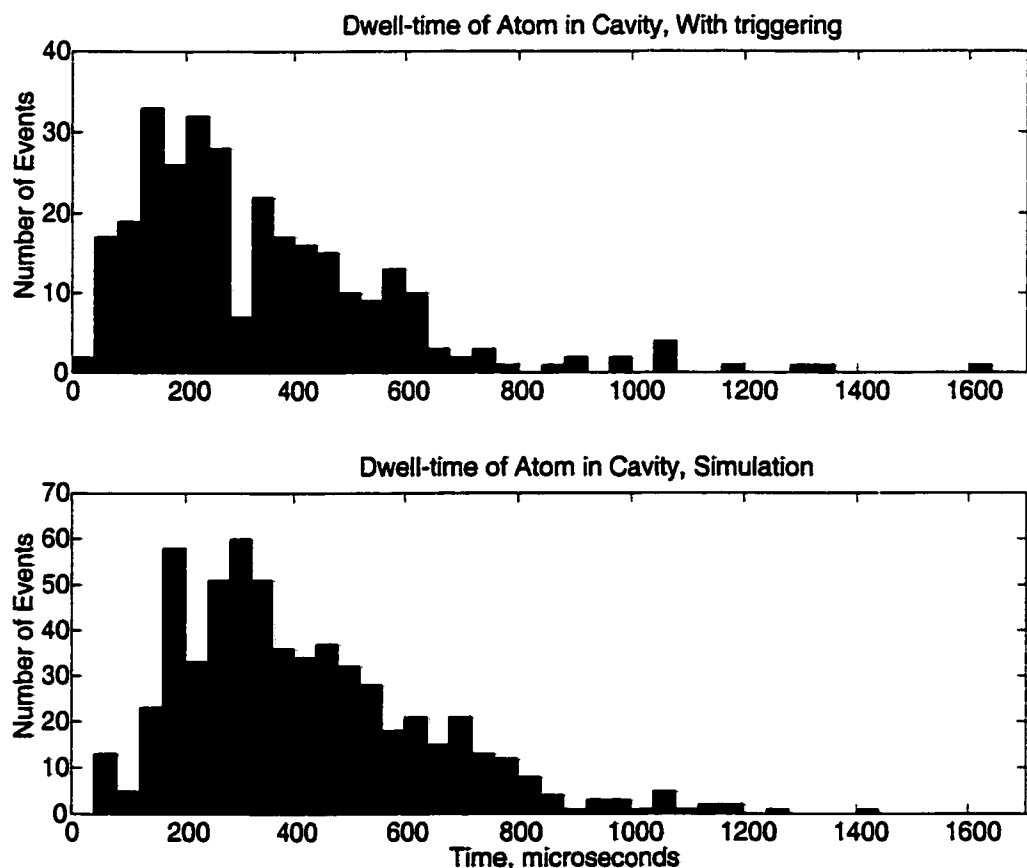


Figure 4.11: Comparison of Experimental Data and Simulated Transits - Atom dwell τ time in the cavity, for parameters $\Delta_{ac}/2\pi = -47\text{MHz}$, $\Delta_{probe} = -125\text{MHz}$, $\bar{n}_p = 0.05$ photons, and $\bar{n}_t = 0.3$ photons.

first approximation, in the actual experiment the narrow $9\mu\text{m}$ gap between the edges of the mirrors and the Gaussian waist $w_0 \simeq 14\mu\text{m}$ of the cavity mode will introduce additional correlations between position and velocity. For example, atoms which have an initial upward z -velocity will only reach the cavity mode if they have very small y and x velocities.

That there is generally a good agreement for both the mean and distribution of trap times of trapped atoms indicates that the simulations provide a good theoretical understanding of both the conservative and dissipative (heating) mechanisms in this atom trapping scheme.

4.8.3 Histograms of traptimes for different atom-cavity detunings

The data of Figures 4.7,4.10 are taken at the particular detunings $\Delta_{\text{probe}}/2\pi = -125\text{MHz}$ and $\Delta_{\text{ac}}/2\pi = -47\text{MHz}$, with drive strength $\bar{n}_p = 0.05$ before triggering, and $\bar{n}_t = 0.3 \pm 0.05$ after triggering. These values were chosen operationally - detunings and intensities were varied over a wide range, with best results for trapping achieved in the approximate range $\Delta_{\text{probe}}/2\pi = -110 \rightarrow -160\text{MHz}$, $\Delta_{\text{ac}}/2\pi = -40\text{MHz} \rightarrow -80\text{MHz}$, with drive strengths $\bar{n}_t = 0.15 \rightarrow 0.8$ intra-cavity photons.

In Figure 4.12 are shown histograms of trap times as a function of atom -cavity detuning Δ_{ac} , with the probe detuning chosen to be 10MHz above the lower dressed state resonance $\beta_-(0)$ for each data set, and with a fixed drive strength $\bar{n}_t = 0.3 \pm 0.05$. These data sets were taken before the addition of an optical pumping beam to the apparatus. The effect of optical pumping can be seen by comparing the second panel of Figure 4.12 to Figure 4.10, as these otherwise have the same experimental parameters.

This series of histograms shows that for these experimental parameters, trapping is better for intermediate detunings $\Delta_{\text{ac}}/2\pi \simeq -50 \rightarrow 100\text{MHz}$ than for near-resonant detunings $\Delta_{\text{ac}}/2\pi \simeq 0$, and larger detunings $\Delta_{\text{ac}}/2\pi \leq -150\text{MHz}$.

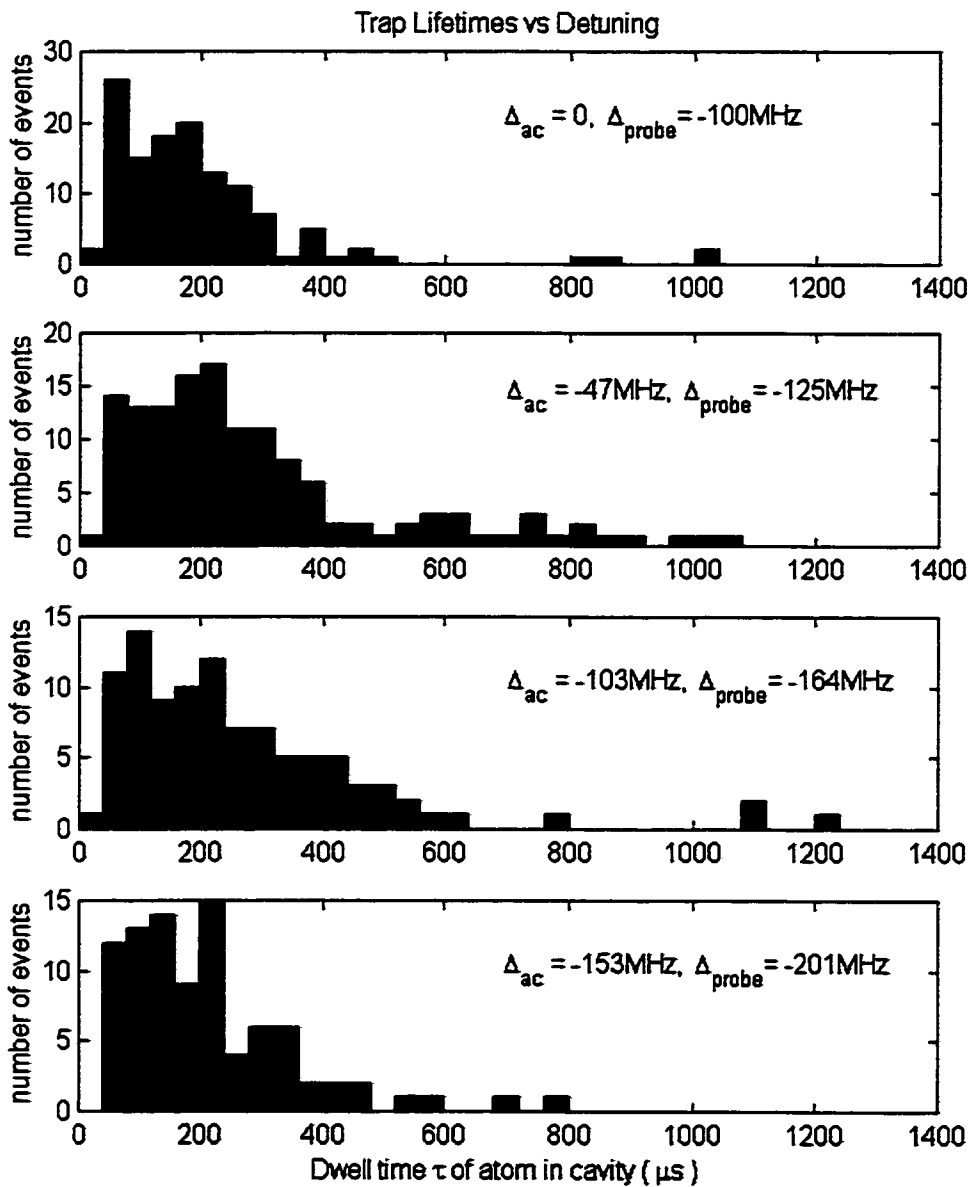


Figure 4.12: Trap lifetimes vary with atom-cavity detuning Δ_{ac} .

One further comparison that was made was to switch the role of “atom” and “cavity,” by setting the atom-cavity detuning to $\Delta_{ac}/2\pi = +102\text{MHz}$, while still probing 10MHz above the lower dressed state (now atom-like) resonance. This comparison is shown in Figure 4.13. A trapping potential is still formed by the curvature of the lower dressed state, but in this case the trapping times are shorter, evident by comparing the histograms of Figure 4.13(a,b). In Figure 4.13(c), the *untriggered* distribution corresponding to Figure 4.13(b) is shown, and it can be seen that a far larger proportion of untriggered atoms end up trapped than in the red-detuned cavity case of Figure 4.10. This figure suggests that the diffusion is larger here: larger diffusion makes it easier for untriggered atoms to randomly lose enough energy to be trapped, and also means that the trap lifetime will be shorter.

4.9 Reconstruction of atom trajectories - the ACM

The trap-time histograms together with the data of Figures 4.8 and 4.9 show that we have good agreement between experiment and theory, in terms of the depth and shape of the potential, and also in heating rates. Our understanding of atomic dynamics in the effective potential $U(\rho)$ (including confirmation that motion in the standing-wave direction is minimal) together with a knowledge of the mapping between atom position and probe beam transmission via the master equation enable accurate reconstructions of two-dimensional trajectories for the individual atom transits of Figure 4.7, extracting both radial position $\rho(t)$ and angular momentum $L(t)$ from the transmission data of Figure 4.7. This reconstruction algorithm, developed by Theresa Lynn, is discussed in detail in Ref. [27] and at the web site www.its.caltech.edu/~qoptics/atomorbits/, along with a discussion of its limitations and validity.

The single atom transmission signals of Figure 4.7(a,b) yield the trajectories of Figure 4.14(a,b), where motion is in the $y - z$ plane at optimal x position (at an antinode of the standing-wave). We now see directly that the large-amplitude transmission changes of Figure 4.7(a) relate to elongated orbits, with large excursions from the cavity center. Likewise, the smaller oscillations of Figure 4.7(b) translate to a

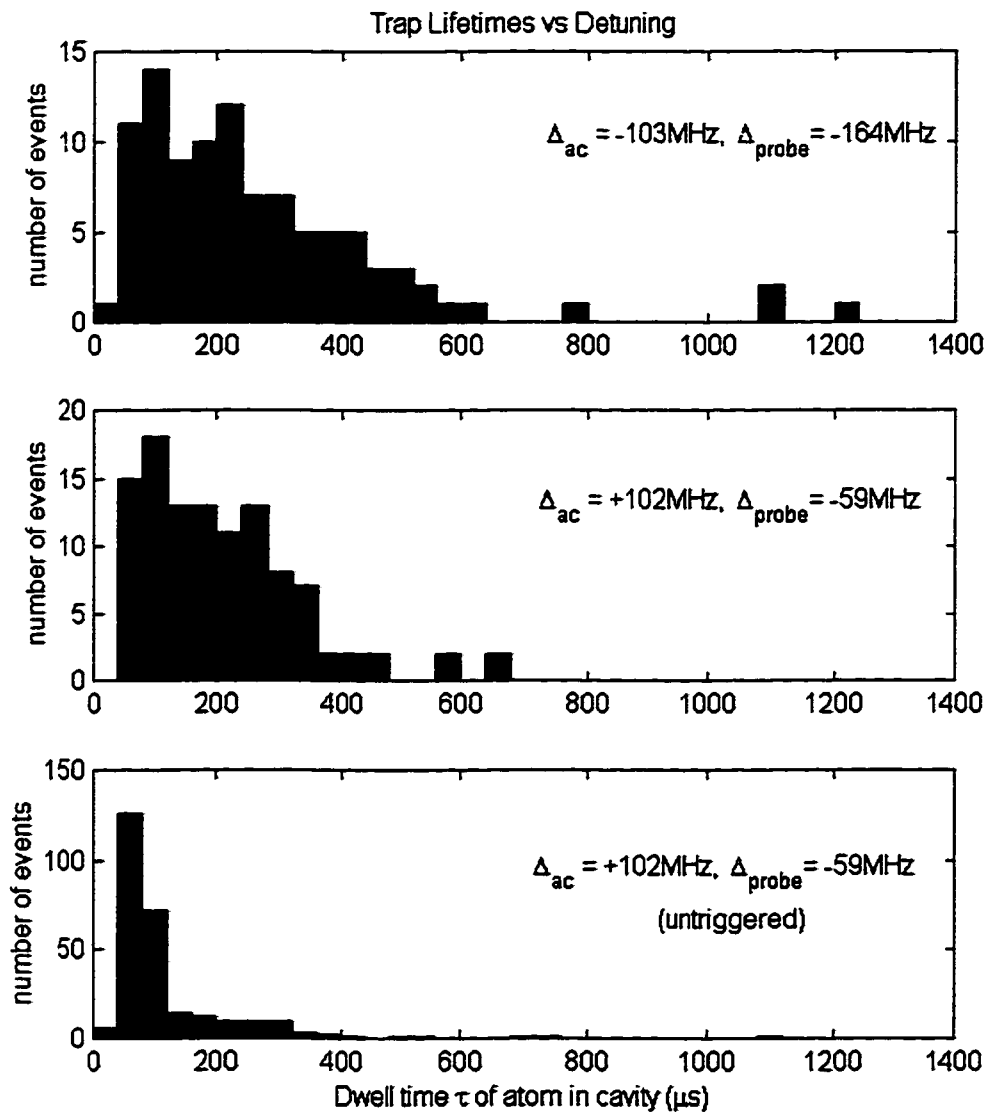


Figure 4.13: Interchanging the atom and cavity frequencies ((a) and (b)) still results in a trapping potential, but with lower trap times. (c) shows the untriggered trap time distribution for the same parameters as (b).

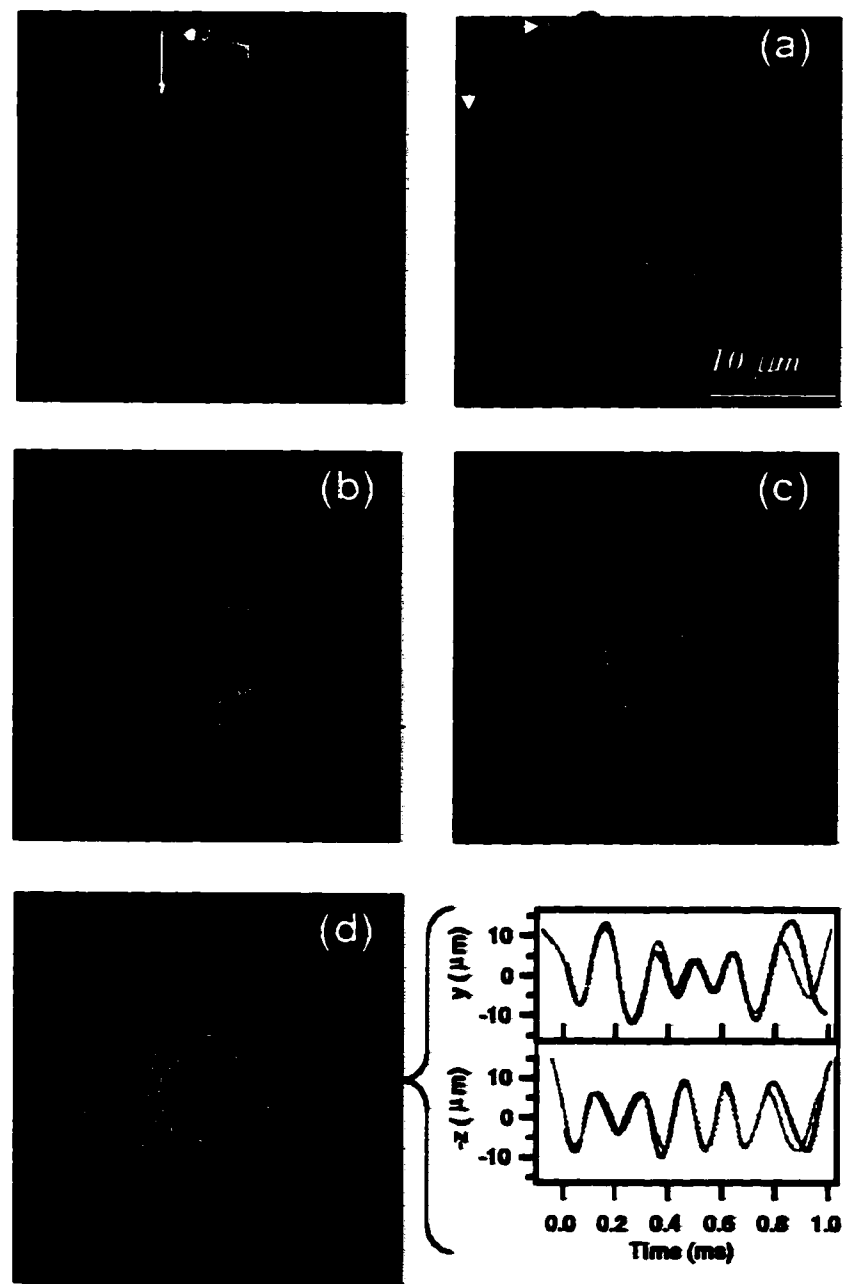


Figure 4.14: Atom trajectories lie in a plane perpendicular to the cavity axis, as illustrated by the schematic. (a)-(b) Reconstructed atomic trajectories for the transits of Figure 4.7(a,b). (c,d) Trajectories reconstructed from the simulated transits of Figure 4.7(c,d), with the actual trajectory shown in gray for comparison. Animated versions of these orbits can be viewed at <http://www.its.caltech.edu/~qoptics/atomorbits/>

more circular, tightly bound orbit of Figure 4.14(b). The size of the dot at the start of each trajectory indicates the typical error in the estimate of the atomic location, from comparisons as in Figure 4.14(c). Figure 4.14(c,d) show reconstruction from the simulated transmissions of Figure 4.7(c,d). In this case the reconstruction was made from transmission signals with noise (including fundamental shot-noise and technical noise) added to the transmission, such as is shown in Figure 4.7(c,d). For comparison, the actual trajectories provided by the simulation are shown in grey. In general we find good agreement until the very end of the trajectory, where our algorithm fails because (i) little information is known about the final angular momentum and (ii) the reconstruction ignores x -axis motion, which becomes non-negligible at the end of the trajectory (see Figure 4.7(c)).

Although modifications in cavity transmission by single atom transits were first observed in cavity QED in 1996 [24] and in several subsequent experiments [25, 26, 45, 46, 28, 27], the results of Ref. [27] represent the first time that individual trajectories for single atoms have been extractable from these signals. Moreover, beyond the scope of cavity QED *per se*, the ability to reconstruct atomic orbits demonstrates a new measurement device - the atom-cavity microscope (ACM) [27]. The position of a single atom in free space is tracked with 2 micron resolution, achieved in a 10 microsecond timescale, with extremely low levels of incident light ($\bar{m} \lesssim 1$ photon in the cavity). Over the duration of the observation, the sensitivity is near the standard quantum limit for sensing the motion of a cesium atom, that is, the limit at which the laws of quantum mechanics prohibit a better measurement without a measurement-induced backaction on the momentum of the particle. We believe that the combination of spatial and temporal resolution of ACM should be applicable beyond single-atom cavity QED, extending to include the imaging of chemical and biological processes [93].

4.10 Extensions:

4.10.1 Quantum servos

With this sensitive monitor of the atomic position, an obvious next step in this experimental effort will be to extend our triggering/trapping strategy to build a feedback system to cool the atomic motion. In response to changes in transmission, such as shown in Figure 4.7, we are free to change the depth of the effective potential well, for example by modulating the intensity or changing the frequency of our driving probe field, enabling atom cooling and manipulation by servo-control. Cooling the atomic motion so that a trapped atom has a constant coupling strength $g(\vec{r}) \simeq g_0$ will be necessary for realization of single-atom quantum computation and communications schemes [9, 10, 6, 5], measurement of the photon-statistics from a strongly coupled single-atom source, and generation of single-photon pulses [8]. In addition, at the point where our measurement efficiencies approach the standard quantum limit for detection [94], this would become a quantum servo, meaning that quantum measurement backaction must be taken into account as an integral part of the feedback loop, a system of fundamental interest to the theoretical quantum information community [29, 30]. Initial estimates based on the theoretical analysis of [72] indicate that the current experiment is perhaps a factor of five above the SQL. Straight-forward improvements to the experiment, such as enhanced detection efficiency, a single-sided versus two-sided cavity, and reduced technical noise along the lines of [46].

4.10.2 Measuring quantum/semiclassical distinctions

In the nonlinear saturation measurements described in Chapter 3, it was shown that the one-atom master equation of cavity QED was in good agreement with our transit data, whereas semiclassical theory of the optical bistability state equation predicted atom-cavity transmission markedly different from that observed, as well as predicting bistable behavior in the system saturation. Measurements made by Hideo Mabuchi and Jun Ye in similar settings show a corresponding deviation from semiclassical

theory, while quantum theory is in good agreement with the data [26, 46].

What then, are the characteristics of this quantum/semiclassical distinction for the upgoing transits of our current experiment?

Firstly, to compare the basic saturation characteristics of upgoing and downgoing transits, in Figure 4.15 I plot relative transmission versus empty cavity photon number \bar{n} , with $\omega_{cavity} = \omega_{atom}$ and for probe detunings of $\omega_{probe} = \omega_{atom}$ and $\omega_{probe} = \omega_{atom} - g_0$ on the same graph. The quantum calculations were performed using Sze Tan's quantum optics toolbox for Matlab [67], and the semiclassical by solving Eq. 2.7, the state equation of optical bistability [64, 65]. By "relative transmission," we mean the ratio of the atom-cavity transmission with an atom present to that with no atom. For the $|\langle \hat{a} \rangle|^2$ calculation the relative transmission is given by $|\langle \hat{a} \rangle|_{atom}^2 / |\langle \hat{a} \rangle|_{no_atom}^2 \equiv \bar{m}/\bar{n}$, and for the $\langle \hat{a}^\dagger \hat{a} \rangle$ calculation it is given by $\langle \hat{a}^\dagger \hat{a} \rangle_{atom} / \langle \hat{a}^\dagger \hat{a} \rangle_{no_atom} = \langle \hat{a}^\dagger \hat{a} \rangle_{atom} / \bar{n}$, since in the absence of an atom in the cavity, $|\langle \hat{a} \rangle|_{no_atom}^2 = \langle \hat{a}^\dagger \hat{a} \rangle_{no_atom} = \bar{n}$. For the semiclassical field the relative transmission is the ratio of the intracavity (and hence transmitted) power with and without the atom present.

Note that the resonant case shows the same qualitative difference between the (bistable) semiclassical theory and the quantum calculation as was evident in Chapter 3, but with the effects more pronounced here due to the increase in cooperativity C_1 . Additionally, transits persist to higher drive strengths than previously: at 10 photons empty cavity field strength downgoing transits are still present, with signal contrast still of a factor $\approx 10^2$. The separation of $|\langle \hat{a} \rangle|^2$ and $\langle \hat{a}^\dagger \hat{a} \rangle$ is also more pronounced. At a drive strength of 10 photons, measurement of $|\langle \hat{a} \rangle|^2$ (as in our experiment, by heterodyne detection) gives transmission changes of a factor of 100 as a single atom transits the cavity. If one were instead to measure $\langle \hat{a}^\dagger \hat{a} \rangle$ (by photon counting), transmission would only change by of a factor of 10 for the same atom transit. That $\langle \hat{a}^\dagger \hat{a} \rangle >> |\langle \hat{a} \rangle|^2$ means that a significant proportion of our driving field is being radiated into the incoherent part of the atom-cavity spectrum. While this difference was difficult to resolve for the data of Chapter 3, it should be easy given this order-of-magnitude separation for the current cavity parameters.

For the saturation of the upgoing transits ($\omega_{probe} = \omega_{atom} - g_0$), the differences

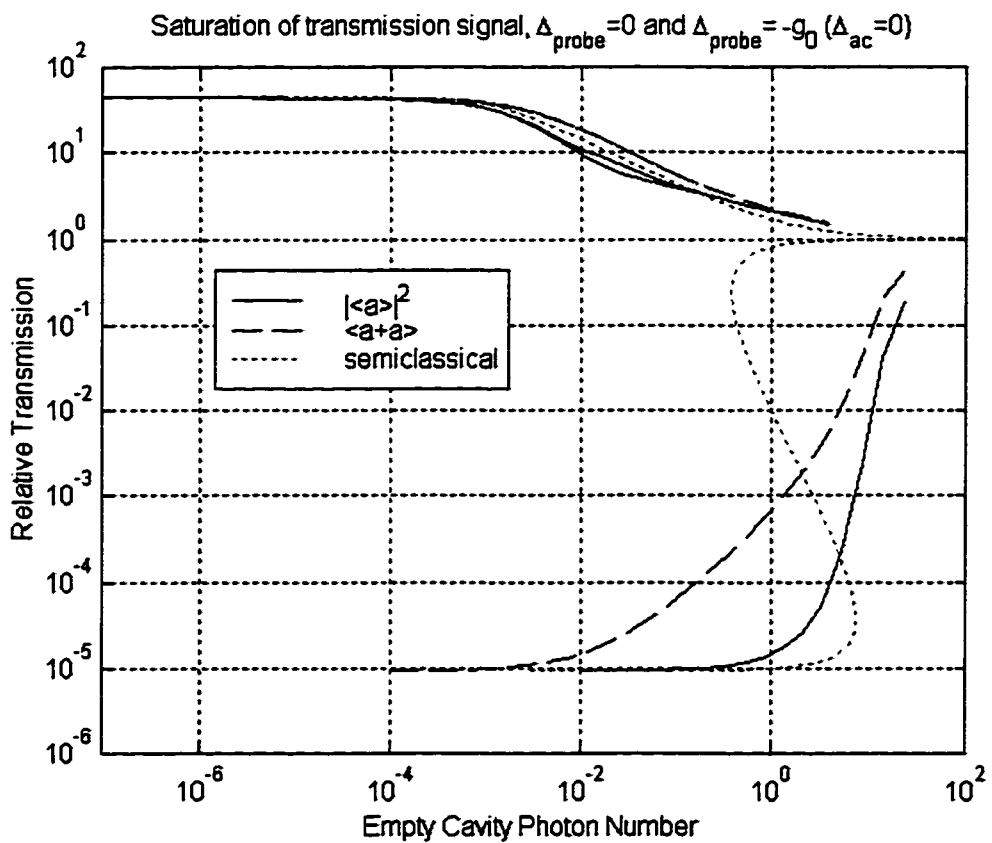


Figure 4.15: Saturation of atom transit heights/depths as the empty cavity photon number \bar{n} is increased.

between quantum and semiclassical theories are smaller, but the same basic trend is maintained: $|\langle \hat{a} \rangle|^2$ begins to saturate earlier than the semiclassical theory at low drive strengths, then at high drives it takes longer for the contrast to completely disappear. One interesting feature to note is that the trace of $|\langle \hat{a} \rangle|^2$ is double-branched in this plot. Keeping the probe frequency fixed at $\omega_{\text{probe}} = \omega_{\text{atom}} - g_0$, the *bottom* branch is \bar{n} vs. $|\langle \hat{a} \rangle|^2$ for an atom with coupling strength $g(\vec{r}) = g_0$. The top branch is \bar{n} vs. $|\langle \hat{a} \rangle|^2$ for an atom with any $g(\vec{r}) \leq g_0$. That is, when driving with a probe detuned by g_0 , higher transmission is measured for these drive strengths if the atom has coupling strength $g(\vec{r}) < g_0$.

To try and understand more quantitatively the saturation of these transits, Figure 4.16 shows the same curves, but here the relative transmission is plotted versus intracavity field strength with the atom present, that is, \bar{m}/\bar{n} vs. \bar{m} for the $|\langle \hat{a} \rangle|^2$ trace, and $\langle \hat{a}^\dagger \hat{a} \rangle_{\text{atom}}/\bar{n}$ vs. $\langle \hat{a}^\dagger \hat{a} \rangle_{\text{atom}}$ for the $\langle \hat{a}^\dagger \hat{a} \rangle$ trace. For the resonant downgoing transits, the onset of saturation is characterized by $\bar{m} = m_0 = \gamma_\perp \gamma_\parallel / 4g_0^2$, which is the drive strength at which the semiclassical (bistability state equation) transmission has saturated by a factor of 4 in intensity (a factor of 2 increase in the transmitted field amplitude). For these parameters $m_0 = 2.8 \times 10^{-4}$. The saturation photon number for the earlier experiment of Chapter 3 was very similar, at $m_0 = 2.3 \times 10^{-4}$. However, here weak-field downgoing transits have higher contrast, with the depth given by $1/(1 + 2C_1)^2 = 9.3 \times 10^{-6}$, compared to $1/(1 + 2C_1)^2 = 7.4 \times 10^{-5}$ for the previous experiment. It therefore makes some sense that transits persist to higher drive strength - approximately an extra order of magnitude in transit depth has to be saturated out, and about an order of magnitude higher drive strengths are required to achieve this.

To characterize the saturation of upgoing transits, I apply a similar semiclassical analysis, re-arranging the bistability state equation to find the intracavity photon number for which the semiclassical intensity transmission is reduced by a factor of 4. For the particular detunings chosen ($\omega_{\text{cavity}} = \omega_{\text{atom}}$, $\omega_{\text{probe}} = \omega_{\text{atom}} - g_0$), and under the assumptions of strong coupling $\gamma_\perp^2/g_0^2 \ll 1$ and $\kappa/g_0 \ll 1$, and with the additional assumption $\gamma_\perp/\kappa \ll 1$, the solution takes on the very simple form that

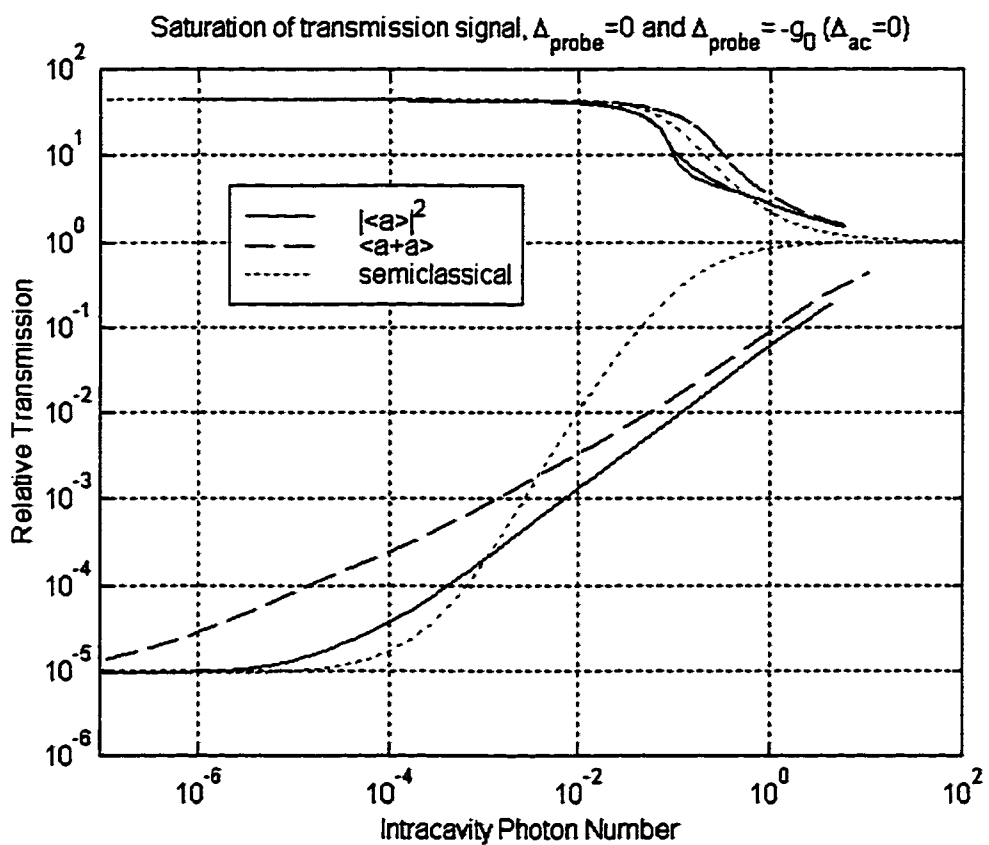


Figure 4.16: Saturation of atom transit heights/depths as a function of the mean intracavity photon number, that is, as a function of $\bar{m} = |\langle \hat{a} \rangle|^2$ for the $|\langle \hat{a} \rangle|^2$ calculation, and of $\langle \hat{a}^\dagger \hat{a} \rangle_{\text{atom}}$ for the $\langle \hat{a}^\dagger \hat{a} \rangle$ calculation.

saturation occurs for $\bar{m} = \sqrt{3}(\kappa g_0 / \gamma_{\perp}^2) m_0 = \sqrt{3}/2(\kappa/g_0)$. For our current parameters, the assumptions $\kappa/g_0 \ll 1$ and $\gamma_{\perp}/\kappa \ll 1$ are not strictly valid. Even so, this simplified formula leads to only a 15% error in estimation of the semiclassical saturation parameter, with a value of $\bar{m} = 0.11$ inferred from the simple formula and $\bar{m} = 0.13$ from the full bistability state equation. The quantum curve for $|\langle \hat{a} \rangle|^2$ saturates to this same factor of 4 change at $\bar{m} \simeq 0.07$, a factor of approximately two lower. It is apparent then, that saturation of upgoing transits onsets for a much higher intracavity photon number than for downgoing transits, in this case three orders of magnitude higher. This raises the possibility that weak-field effects associated with driving at this detuning, such as strong antibunching of photon statistics, may persist at these higher drive strengths, making this measurement a much more experimentally feasible prospect.

Moving now to the parameters of the experimental data of Figures 4.8 and 4.9 ($\Delta_{ac}/2\pi = -80\text{MHz}$, $\Delta_{probe}/2\pi = -145\text{MHz}$), I plot relative transmission as a function of empty cavity photon number \bar{n} . Each of the traces for $|\langle \hat{a} \rangle|^2$, $\langle \hat{a}^\dagger \hat{a} \rangle$ and the semiclassical result is branched: the lower branch corresponds to the saturation behavior of an atom with maximum coupling $g(\vec{r}) = g_0$, while the upper branch is the maximum transmission for any coupling $g(\vec{r}) \leq g_0$. At low drive strengths, this branching means that an atom falling through an antinode of the field (passing through a point of $g(\vec{r}) = g_0$) will produce a two-peaked transmission signal, with the dip in the center corresponding to the position of optimal coupling. It can be seen that at very low and very high photon numbers the differences between quantum and semiclassical theory are most pronounced. However, at the empty cavity values $\bar{n} = 0.1 \rightarrow 0.7$ photons of the data, we are close to the crossing-point of these two theory curves, meaning that the distinction between them is small, and would be difficult to distinguish experimentally - this was not an optimal choice of parameters if our goal were to look for a quantum/semiclassical distinction. At the detunings of the other data set ($\Delta_{ac}/2\pi = -47\text{MHz}$, $\Delta_{probe}/2\pi = -125\text{MHz}$) the behavior is very similar, and the chosen drive strength of $\bar{n} \simeq 0.3$ is once again close to the crossing-point of the quantum and semiclassical theories.

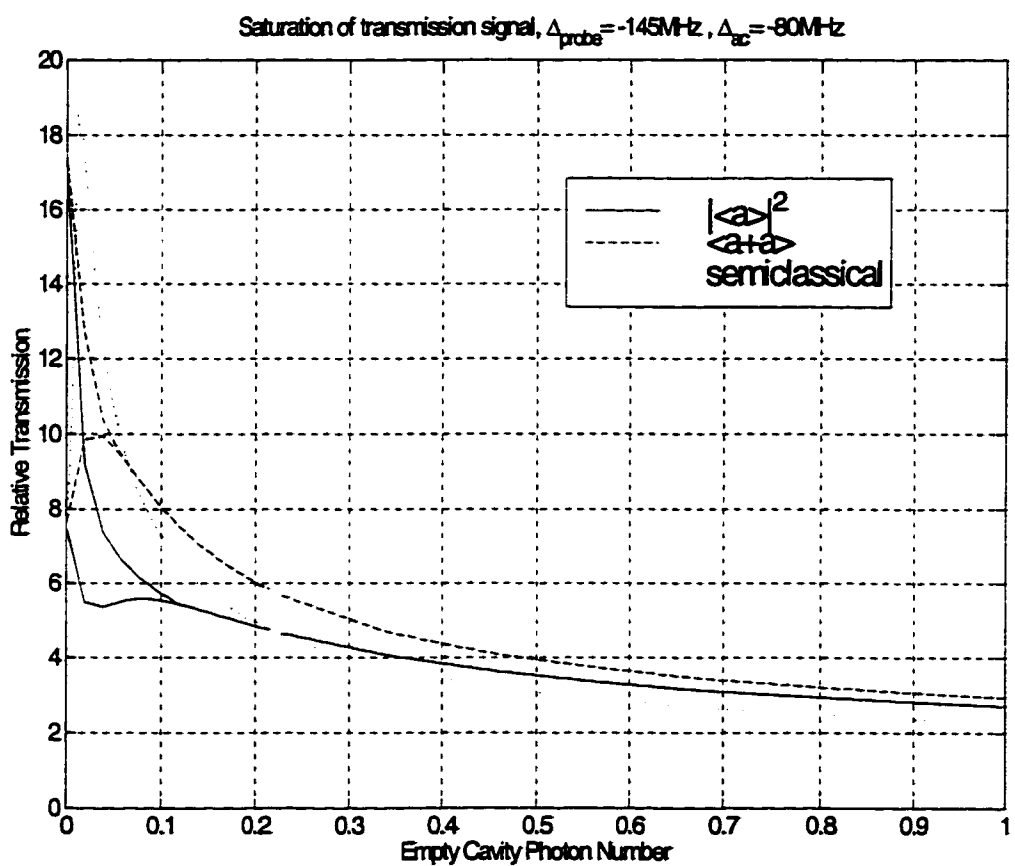


Figure 4.17: Saturation of transit heights for the detunings of the data of Figures 4.8 and 4.9.

Note however that at lower drive strengths $\bar{n} \simeq 0.05$, the $|\langle \hat{a} \rangle|^2$ calculation predicts upgoing transits with a transmission increase of a factor of $\simeq 7$, while the semiclassical prediction is for a factor of $\simeq 10$, a difference which should be experimentally distinguishable. Unfortunately, at this driving strength the potential is too shallow to trap atoms well, meaning that the measurement would have to be derived from an ensemble of transits rather than the heights of single trapped oscillating atoms. At higher drive strengths there is also a measurable difference. At $\bar{n} \simeq 1.5$ photons, quantum theory still gives transits with a factor of 2.35 intensity increase, whereas the semiclassical prediction is for only a factor of 1.9, a $\simeq 50\%$ difference in the height of transits (remembering that as this is relative transmission, the baseline is 1). As the shot-noise is reduced at this higher driving strengths, and will be approximately a factor of $\sqrt{5} = 2.2$ lower than for the data traces shown in Figure 4.7, this should be an easily distinguishable difference. Showing that the relative transmission predicted by the quantum theory is *lower* at low drive and *higher* at high drive than the semiclassical would also be a confirmation that restricts systematic offsets existing in our experimental data, which could be argued would explain a quantum-semiclassical difference observed at a single drive strength.

Given that the data taken so far in this experiment was not in a regime which demonstrates a striking quantum-semiclassical distinction, I will present here a few suggests for better experimental parameters. Firstly, by simply moving the probe beam closer to the cavity resonance, the results of Figure 4.18 are obtained for $\Delta_{ac}/2\pi = -80\text{MHz}$, $\Delta_{probe}/2\pi = -115\text{MHz}$. Here there is a qualitative change in the type of transits seen as the drive strength is increased. For a weak probe, “up-down-up” transits such as recorded in Figure 3.3(b) of Chapter 3 will be observed, since the transmission for an atom with coupling g_0 is less than that for an atom with $g(\vec{r}) < g_0$. At higher drive strengths, as the spectrum saturates simple upgoing transits are observed. In this regime of upgoing transits there is now a clear separation between $|\langle \hat{a} \rangle|^2$, $\langle \hat{a}^\dagger \hat{a} \rangle$ and the semiclassical result.

This separation can be enhanced further by moving the cavity closer to the atomic resonance, as is shown in Figure 4.19, for parameters $\Delta_{ac}/2\pi = 0\text{MHz}$, $\Delta_{probe}/2\pi =$

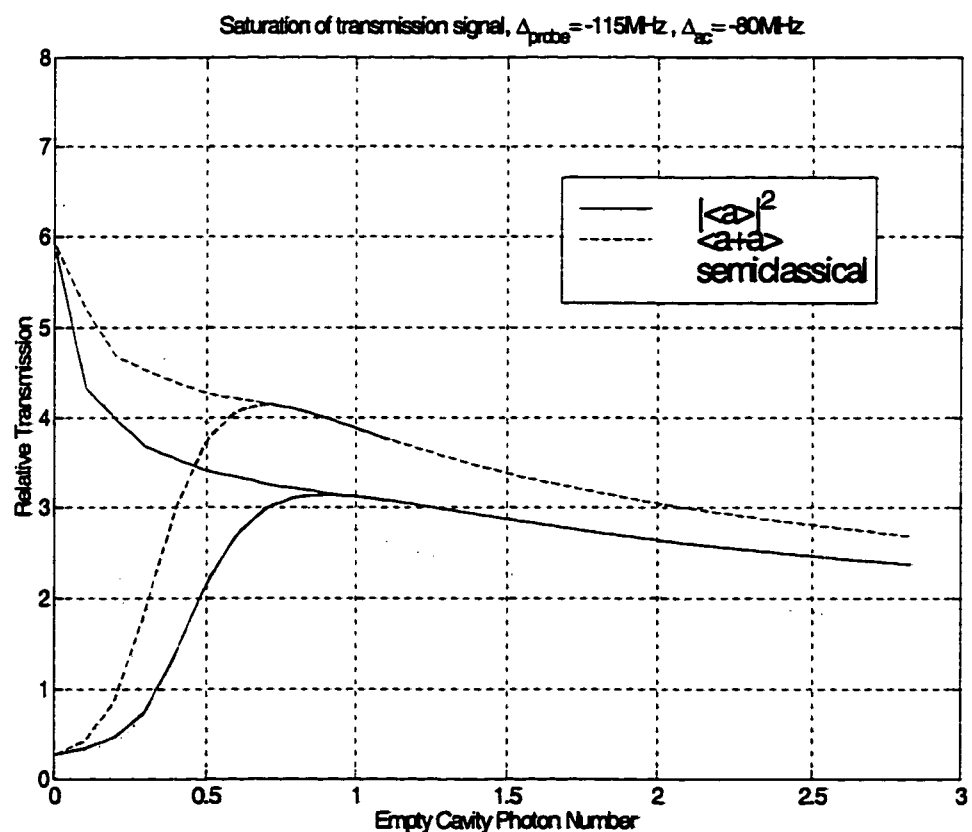


Figure 4.18: At detunings $\Delta_{\text{ac}}/2\pi = -80\text{MHz}$, $\Delta_{\text{probe}}/2\pi = -115\text{MHz}$, the distinction between quantum and semiclassical theories is more pronounced than for the parameters of the data.

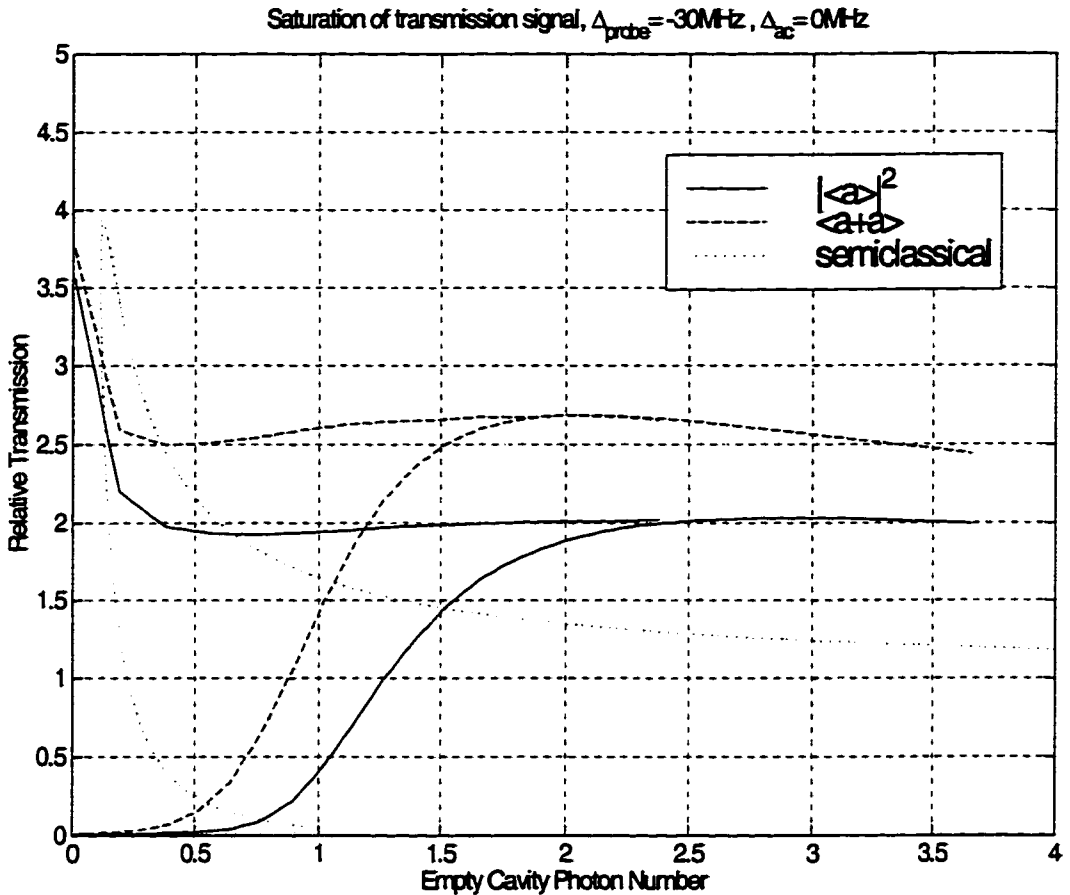


Figure 4.19: For parameters $\Delta_{\text{ac}}/2\pi = 0\text{MHz}$, $\Delta_{\text{probe}}/2\pi = -30\text{MHz}$, an even larger effect is seen at high drive strengths.

-30MHz . Our understanding of the general behavior of the quantum saturation is that it onsets sooner than the semiclassical case, then takes longer to finally saturate. Given this, it is not surprising that probing with high drive strengths is a good place to look for the quantum-semiclassical distinction. And, as the system saturates the two peaks in the spectrum move inward, so at highest drive strengths the best upgoing transits are seen for detunings close to the atom-cavity resonance, such as $\Delta_{\text{probe}}/2\pi = -30\text{MHz}$ in Figure 4.19.

Finally, as in Chapter 3, it should be pointed out that the *best* contrast is obtained for downgoing transits near the atom-cavity resonance. In Figure 4.20, a slightly red-detuned probe is chosen, with the intention of channeling atoms to regions of strong

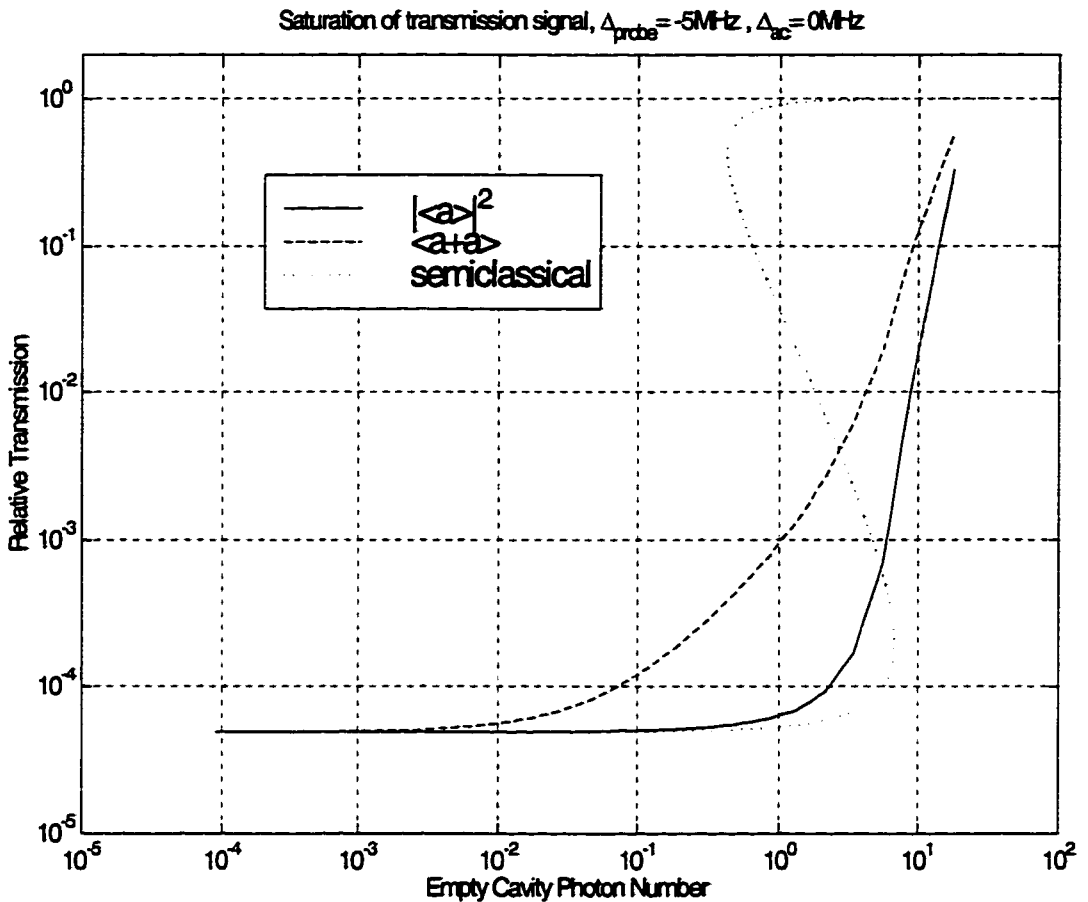


Figure 4.20: The best contrast between quantum and semiclassical theories is observed near resonance, here at detunings $\Delta_{\text{ac}} = 0$, $\Delta_{\text{probe}}/2\pi = -5\text{MHz}$.

coupling as was observed in the saturation measurements of Chapter 3. Parameters are $\Delta_{\text{ac}}/2\pi = 0\text{MHz}$, $\Delta_{\text{probe}}/2\pi = -5\text{MHz}$ for this figure. At an empty cavity field strength of 10 photons, the difference between $|\langle \hat{a} \rangle|^2$ and the semiclassical result is a factor of 100, and the difference between $|\langle \hat{a} \rangle|^2$ and $\langle \hat{a}^\dagger \hat{a} \rangle$ a factor of 10.

4.10.3 Two-atom events?

One remaining point still to be investigated are occasional anomalous signals seen such as those of Figure 4.21(b) and (f). As evidenced by the anharmonicity curves of Section 4.7, the characteristics of transits (peak amplitude, oscillation frequency) are in good agreement with quantum theory, and consistent over large data sets. The

transits of Figure 4.21 were taken from a data set with peak transit height consistently $1.5 < \bar{m} < 1.6$. Very occasionally, signals are seen extending above $\bar{m} = 2.0$, with a duration of 50-100 μ s. The timescale of these events makes them suggestive of being a second atom falling through the cavity while the first is trapped.

This could be verified experimentally by triggering on these secondary peaks and switching on a probe field at a higher detuning. The collective effect of two atoms is to give an effective coupling strength $g_{eff} = \sqrt{2}g_0$, which for the lowest dressed state determines the observed probe transmission spectrum. (For higher-lying dressed states, the dependence on atom number is more complicated, as discussed in Section 2.1.3). At a probe detuning $\simeq g_{eff}$ then, upgoing transits should be seen for two-atom coincidences in the cavity, with no signal for single atom events.

If these signals were confirmed to be 2-atom events, an obvious goal would be to trigger, and trap two atoms in the cavity. This may be achievable by first triggering to catch a single atom in the usual way, and then when a second is detected, switching to a stronger driving field at a probe detuning $\simeq g_{eff}$, which by its detuning primarily addresses the collectively coupled state of the two atoms. This second potential would need to be deeper than the first, so as to overcome the kinetic energy gained as the second atom entered the existing potential well. The lower dressed state again forms a trapping potential, this time for the collective state of 2 atoms. Interestingly, in the same sense that the state $|-\rangle = \frac{1}{\sqrt{2}}(|a1\rangle - |e0\rangle)$ (neglecting detunings) is an entangled state of a single atom and cavity mode, the lower dressed state in the two-atom case is an entanglement of two atoms and the cavity mode, so preparation of this state would in and of itself be an interesting advance.

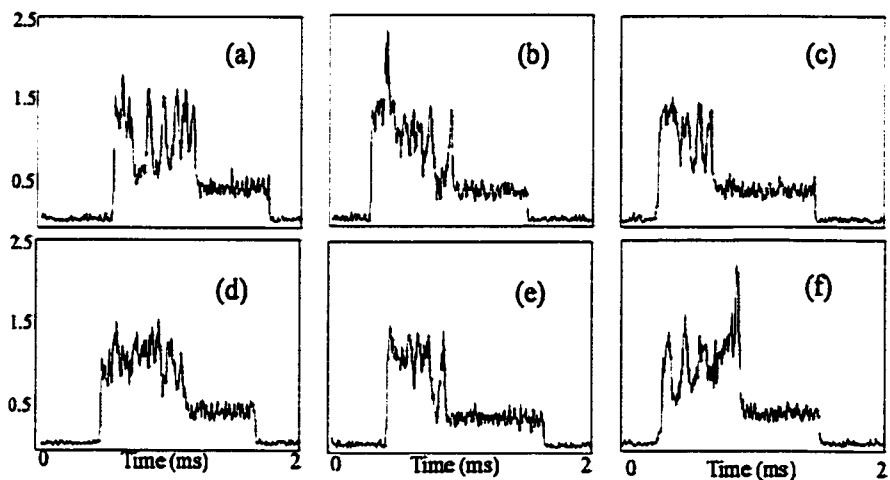


Figure 4.21: Signals (b) and (f) are suggestive of 2-atom events. These traces are for parameters $\Delta_{ac}/2\pi \approx -100\text{MHz}$, $\Delta_{probe}/2\pi \approx -145\text{MHz}$, $\bar{n}_t \approx 0.4$ photons.

Chapter 5 REO Mirrors

5.1 Fabrication, inspection and cleaning

5.1.1 Fabrication of cone-shaped mirrors by REO

The mirrors used in our current series of experiments began life as 7.75mm diameter (4mm thick) fused silica substrates, superpolished with a spherical radius of curvature to sphericity of better than $\lambda/10$ and surface microroughness less than 0.1nm[95]. A multilayer dielectric coating composed of alternating $\lambda/4$ layers of Ta_2O_5 (index of refraction $n=2.041$) and SiO_2 (index $n=1.455$) was then deposited onto these substrates by ion beam sputtering; a total of 35 layers for the first coating run (#D1306, mirror transmission 15ppm) and 37 layers for the second coating run (#T95, transmission 4.5ppm). With Jun Ye, I made a series of measurements to characterize in detail the properties of the #T95 coating run and developed a model to predict cavity properties. Details of these measurements appear in Section 5.3.

Toward the experimental goal of incorporating cold atoms and strong coupling in a cavity QED system, it became clear that the physical size of the 7.75 mm substrates was a limitation. Firstly, atoms collected in a MOT above the mirrors would have to fall $\gtrsim 4$ mm before reaching the cavity mode volume, in which time they would have acquired a substantial velocity. Minimizing this distance to reduce the initial atomic kinetic energy would have the effect of increasing the atom's interaction time inside the cavity, as well as increasing the atom's sensitivity to mechanical forces induced by the single-photon cavity field.

Secondly, the cavity length is limited by the curvature of the mirrors. To create the smallest possible cavity mode volume, and hence the strongest coupling g , it would be desirable to use short radius of curvature mirrors, resulting in a small mode waist, as well as a short cavity. To combine these requires smaller mirrors: a cavity formed

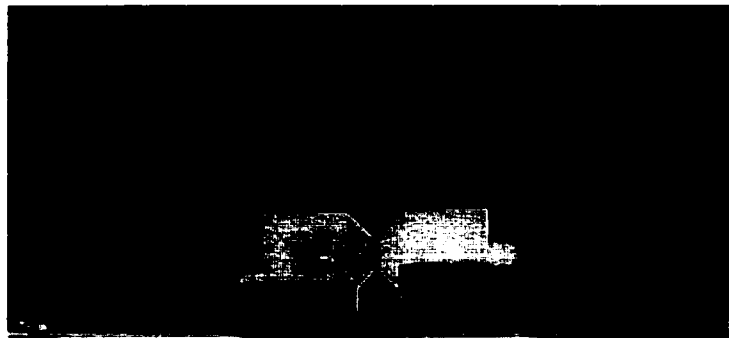


Figure 5.1: Two mirrors face one another to form an optical resonator.

with 10cm radius of curvature mirrors with 7.75mm diameter substrates can be made 150 μm short before the mirror edges touch, whereas 1mm diameter substrates of the same curvature can form a cavity of only 2.5 μm length! In practice, cavity lengths were chosen longer than this to allow a space for atoms to enter though the side of the cavity, and to allow for imperfect tilt alignment of the mirrors.

In the first experiments with cold atoms in cavity QED, Hideo Mabuchi and Quentin Turchette used mirrors reduced in diameter to a 3mm cylinder. Quentin and Michael Chapman also spent some time trying to develop 1mm cylinders, but these proved extremely difficult to clean, and alignment of a cavity with the beams passing cleanly through the narrow substrates was next to impossible. As a next-generation to the 3mm cylinder mirrors, Michael Chapman devised a design for a hybrid 3mm/1mm mirror - a 3mm cylinder which is then tapered in a cone shape down to 1mm diameter at the coated surface, as pictured in Figure 5.1.

These mirrors are fabricated at REO with the following procedure: The coated 7.75mm mirrors are glued with UV curing glue to a second 1cm mirror blank, which is then centered by eye under a microscope (to $\simeq 100\mu\text{m}$ accuracy) on the chuck of a diamond lathe and attached with wax. A drop of nail varnish is used to cover and protect the coated surface during machining. The mirror+blank are then reduced in diameter to a 3mm cylinder (programmed onto the lathe). Next, the chuck is removed and mounted on a hand-rotatable pivot, at an angle of 45° to a diamond grinding wheel. With the wheel spinning, the 3mm cylinder is gradually translated

into the grinding wheel while being slowly rotated by hand, generating a tapered cone shape at the front of the mirror. Machining stops when the final diameter reaches the specification of $1\text{mm}\pm50\mu\text{m}$, measured by removing the chuck+mirror from the grinding setup and examining the mirror under magnification. The mirror/blank is then removed from the chuck by heating the wax, and placed in a vapor degreaser to remove glue and varnish. Originally REO would perform additional cleaning which sometimes led to scratching, but we now ask that the mirrors be delivered to us uncleaned (after only this one stage of vapor degreaser cleaning).

It remains an open question as to what effect this process of machining the mirrors down from 7mm to 1mm/3mm cones has on the quality of the mirror coatings. For the coating run #T95 (which has a relatively high incidence of defects) a brief survey of the unmachined substrates suggested to me that there are *fewer* spots on the average untouched 7mm substrate than on the cone mirrors. However, defects are still present on the 7mm substrates, and are very inhomogeneously distributed, appearing in clusters, so that while most substrates looked clear a few had a high density of defects. It is possible that coincidentally the mirrors that were turned down all had higher defect densities (they were taken sequentially, and presumably therefore came from similar locations in the coating machine). Also, defects are harder to spot in the center of a 7mm substrate than on a 1mm substrate, for which the sharp edges of the mirror can be used to check focusing, so perhaps this leads to a bias in reporting defects on the cone-shaped mirrors.

A good test of the machining procedure would be to begin with 7mm substrates, clean and note any defects, then make a cavity and measure finesse. Next disassemble the cavity and coat the mirror surfaces with nail varnish. Finally re-clean the mirror surfaces to remove all traces of the varnish, look for defects, and re-measure the finesse. This test should certainly be done before considering machining higher reflectivity ($\approx 1\text{ppm}$) coatings.

5.1.2 Inspection of mirror surfaces

There are two critical elements to successfully constructing a high-finesse cavity.

1. Careful inspection of mirror surfaces - being able to identify any dust/scratches
2. Careful cleaning - being able to remove dust and solvent streaks without scratching the mirror surfaces.

Types of defects

An optical microscope with 100x, 200x, and 500x magnification is used to look for dust, glass chips, solvent streaks and scratches, with both bright-field and dark-field illumination used to examine the mirror surface. What are the characteristics of these four types of contamination?

(1) Dust/dirt spots: These appear as black spots under bright-field illumination, white spots under dark-field illumination. Some are so small as to only be visible with 500x magnification, appearing as resolution-limited dots, implying that the particles are sub-micron size. Spots are easier to see with dark field illumination, which I primarily use while cleaning mirrors. Some spots cannot be removed from the coating by cleaning - these "point defects" are probably dust contaminants embedded in the coating. I have not found a way to distinguish cleanable and uncleanable spots by visible inspection - the only way is to repeatedly try to clean the mirror and see which spots won't budge.

(2) Glass chips: generally large (visible 100x magnification), and when examined at higher magnification are transparent - looking like small sugar crystals. Be very wary of these, as they will scratch the surface easily! Often easier to identify as glass with bright-field illumination.

(3) Solvent streaks: Generally easier to see with bright-field illumination. Sometimes clearly visible as colored bands (like an oil-slick), sometimes just a patch of coating with a subtly different (darker) color. Can always be cleaned off - the trick is to do it without leaving another streak!

(4) Scratches: These are easier to see with bright-field illumination. They appear

as fine lines, slightly paler color than the coating. Also tiny pale dots are sometimes seen - I think these are pits in the coating (caused by glass chips perhaps) since they have the same optical appearance as scratches. If you see a glass chip on the coating look carefully to see if there is a scratch trailing it. Sometimes solvent streaks can masquerade as scratches, particularly during the early stages of cleaning - if the entire mirror surface is coated in an impurity (varnish in our case) then cleaned streaks look a lighter color, which can be mistaken for bad scratching.

Microscope focusing tips

To observe the defects described above requires that both the microscope, and your eye be focused precisely on the position of the defect. Often if your eye is trained slightly to the side of a defect, or is slightly defocused, the spot/scratch will be missed.

This is complicated by the fact that the field of view of the microscope (1mm diameter at 200x magnification, 400 μ m diameter at 500x magnification) is never all in focus at the same time. This is because the mirror surface is in general curved, and also because it is difficult to sit the mirror completely flat under the microscope. However, at least for our particular microscope this variation in focus provides a useful meter: the area of the substrate in focus appears slightly darker than the out-of-focus region, so that a subtle dark line across the field of view indicates the region of the substrate in focus. In addition, for 1mm diameter mirrors the sharp mirror edges can be used to check focusing.

The inspection algorithm is then to move the eyes slowly across the field of view at fixed height, while turning the focus knob of the microscope to bring the plane of focus back and forth through the mirror surface (observed as the dark line-of-focus moving back and forth across the point on which the eye is focused). Dividing the field of view into ≈ 10 such horizontal sweeps covers the surface. This "dithering" of the microscope is useful because:

- (1) Different areas of the field of view are at different focal positions as discussed above.
- (2) The eye is often more sensitive to the *change* of a tiny point flashing in and

out of view than to a static image.

- (3) It is often not obvious when viewing a very clean mirror with no visible features whether the image is in focus or not. Also my eye is sometimes defocused from the image (again, with no features it's hard to focus), so dithering the microscope in this way helps locate defects.
- (4) Defects sitting on the surface or embedded in the coating will have different focal positions.

Impact of defects on cavity finesse

Any spot/scratch which is visible is clearly having an impact on the scattering properties of the mirror surface, and hence will affect cavity finesse. The task when trying to construct a maximum-finesse cavity then becomes to try and prioritize given defects, and thereby select a pair of mirrors with the lowest total losses.

For highest finesse, ideally the central $400\mu\text{m}$ (full field of view at 500x magnification) should be completely free of defects. Guessing an uncertainty of $\simeq 100\mu\text{m}$ in how well the mode can be centered on the cavity mirrors, for a mode with waist $\omega_0 = 25\mu\text{m}$ this would give a defect free area out to at least $\simeq 4\omega_0$ radius, where the field is reduced by a factor of $e^{-16} = 10^{-7}$, meaning that scattering effects from a defect at the edge of the clean area should give sub-ppm losses.

Our first batch of coated mirrors (run #D1306, 15ppm transmission) had a very low density of point defects, so it was possible to find a pair of mirrors satisfying this criterion of a clean center. Unfortunately, at this point we were still working out how to safely clean these mirrors, so many arrived scratched from REO and others were scratched during cleaning at Caltech. As a result, only a single pair of mirrors ended up usable from the initial batch that was machined. (Subsequently, mirrors from the same coating run have been machined down without being cleaned, so scratches should no longer be a problem.) The second coating run (run #T95, 4.5ppm transmission) has a far larger number of uncleanable point defects, such that every mirror displays a few defects in the central $400\mu\text{m}$ region. When selecting mirrors to use in cavity

making, I used the following ranking of defects (from most to least serious):

thick scratches, thin scratches, spots visible bright-field and dark-field at $\geq 200\times$ magnification, spots visible dark-field only $200\times$, spots visible at $500\times$ magnification bright and dark-field, spots visible dark-field only, $500\times$ magnification only.

Weighted into this is an assessment of the position of the defect - a bad defect at the edge of the $400\mu\text{m}$ will have less impact than a small defect at the center, several small defects may be similar to one larger one...I tended to try and look for mirrors with the central $100\mu\text{m}$ completely clear. Sketches of the permanent defects of four 10cm radius of curvature substrates from the #T95 coating run are shown in Figure 5.2. Mirrors 1 and 10 are exceptionally clean for this coating run, with mirror 11 being more typical. As a test of the severity of these defects I made one test cavity with substrates 1 and 10, and another with substrates 8 and 11, with the resulting finesse measurements being $F=480,000\pm 10,000$ and $F=420,000\pm 10,000$ respectively, corresponding to total cavity losses of 13ppm and 15ppm. By the measurements detailed in Section 5.3 it was found that the mirror transmission is $\simeq 4.3\text{ppm}$, from which we can deduce absorption/scatter losses of 2.2ppm/mirror and 2.95ppm/mirror for the two cavities in question, suggesting that the few extra point defects in the central region gave rise to $\simeq 1\text{ppm}$ per mirror additional absorption/scatter losses.

Comparing this to a ring-down measurement of the unmachined 7.75mm diameter substrates, which yielded a measurement for total losses of $T + A + S = 6.2 \pm 4\text{ppm}$ ($A + S = 1.9\text{ppm}$ if $T = 4.3\text{ppm}$) and a finesse of $F = 510,000$ suggests furthermore that $\simeq 0.5\text{ppm}$ of the remaining losses may have been introduced by machining of the mirrors to $3\text{mm}/1\text{mm}$ cones.

5.1.3 Cleaning 1mm tapered cone mirrors

The task of cleaning the $3\text{mm}/1\text{mm}$ cone mirrors is a difficult one, because:

- (1) the edge of the 1mm mirror surface is surrounded by chips of ground glass, which can easily scratch the mirror surface.
- (2) residues of varnish are left on the surface and must be removed without scratch-

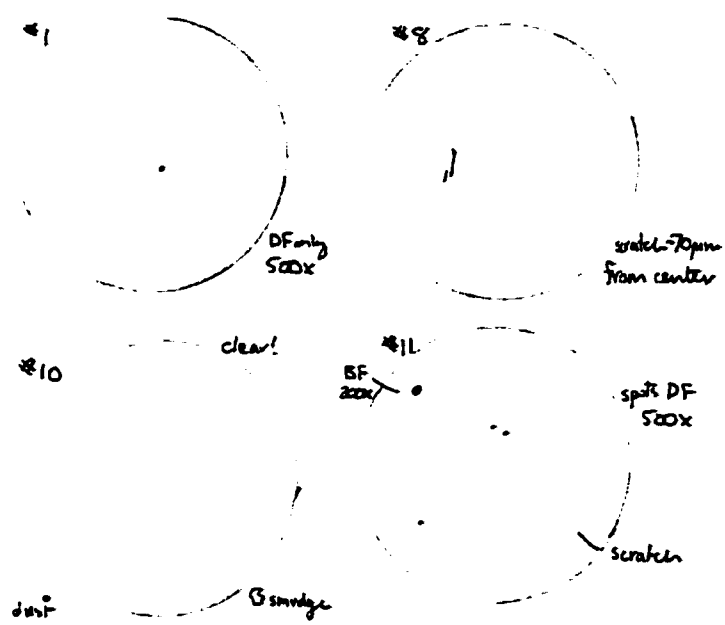


Figure 5.2: Dust and scratches observed on 4 mirrors. The circle represents the central $400\mu\text{m}$ of the coating. DF=dark-field illumination, BF=bright-field illumination.

ing the mirror.

(3) traces of glue/varnish may also be left on the tapered surfaces of the mirror or on the back surface - these must be cleaned away for the sake of eventual good vacuum pressure once the cavity is in the vacuum chamber.

This set of issues has led to the development of a cleaning/inspection procedure specifically designed for these mirrors, described below.

Throughout mirrors are handled only with teflon-coated tweezers to avoid accidental scratching, and sit only on a surface of clean lens tissue. Always sit the mirror on its back surface (coated surface up) to avoid having the mirror roll around. Gloves should be worn to prevent contamination of finger oils.

Step 1. Removal of coarse varnish/glue residues from substrate

There is a large variation in the amount of varnish left on the mirrors after the REO vapor degreaser cleaning. This residue can be softened by:

- vapor degreasing with acetone (I generally didn't do this because of the difficulty of securely mounting the small mirrors)

- boiling gently in acetone (this didn't seem to affect the resulting cavity finesse) making sure that the mirror doesn't move around in the liquid (if it grates on the side of the container then small glass fragments could scratch the surface).

- soaking in acetone

I expect that ultrasound cleaning in acetone would also be effective, if a way to hold the substrates firmly is developed.

Tweezers with folded lens tissue (see Figure 5.3) wetted with spectroscopic grade acetone can then be used to wipe away spots of varnish from around the substrate (being careful to avoid the coated surface!). Once no residue can be seen on the sides of the mirror, the back surface needs to be cleaned - hold the mirror with one set of tweezers and swipe with lens tissue/acetone held in another set of tweezers (never rest the mirror on its coated surface!), then sit the mirror coated side up on clean lens tissue.

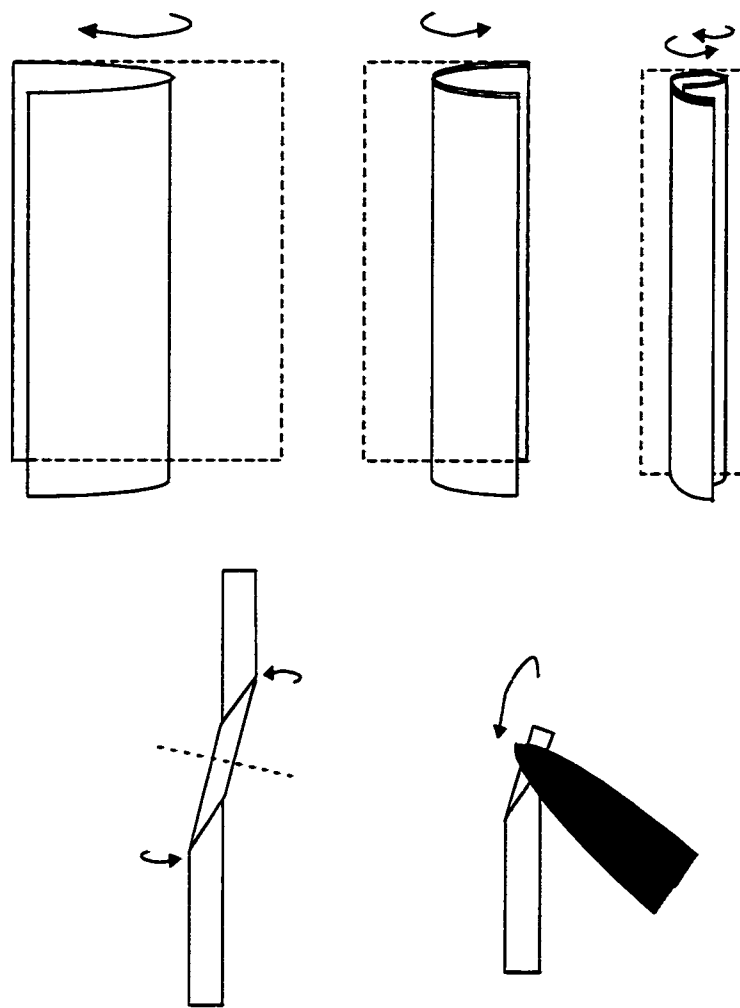


Figure 5.3: I fold lens tissue crosswise in half two times, then in three. Next I twist the tissue to reduce the diameter, then finally fold in half lengthwise. This leaves a square end $\approx 2\text{mm}$ across. Either the flat edge or a corner can be used for cleaning mirror surfaces.

Step 2. Cleaning varnish from mirror surface

Inspect the mirror under 200x magnification, bright-field illumination. There will likely be brownish globs of varnish still on the surface, and there is also likely to be a large number of glass chips sitting on the surface or embedded in the varnish.

The cleaning procedure involves wiping the surface with tightly folded acetone-soaked lens tissue held by tweezers, while grasping the sides of the mirror with another pair of tweezers for stability. The first wipe will be from the center of the substrate toward one edge. Examine the distribution of glass chips under the microscope and decide which direction is least likely to cause scratching - the goal is to gently move these chips away from the center of the mirror without bringing any toward it. Remember that the microscope field of view is spatially inverted compared to the actual mirror surface.

This first wipe should be as gentle as possible, barely touching the substrate, so as not to push down hard on the glass chips and cause scratches. After making this wipe (and after *every* wipe) inspect the mirror under the microscope again. Choose another "best" direction to minimize potential damage - this is usually in the opposite direction to the swipe just made. If there appears to be no change at all use slightly stronger pressure. Wipes need to move from the center to the edge of the mirror, because if the lens tissue catches the edge of the mirror at the beginning of a stroke it will drag glass chips across the mirror!

Repeat this cleaning/inspecting until the varnish residues are removed. Before each swipe look at the entire mirror at low magnification for any large particles (dust, glass chips, lint from lens tissue) on the surface. If an attempt to clean the mirror is made with a large particle present this could easily cause scratching of the mirror surface. These should be removed if possible by blowing with compressed air or nitrogen. If that doesn't work, always clean in the direction to take this particle away from the center of the mirror.

Step 3. Iterative cleaning/inspection to remove spots/streaks

Inspection at this stage under dark-field illumination (200x and 500x magnification) will reveal a number of small spots on the mirror surface. Also, solvent streaks are probably present near the center of the coated surface. To remove these, essentially the same cleaning technique is used as in step 2. That is, inspection (now in dark-field), a single swipe with folded lens tissue dropped with acetone in a direction to swipe defects away from the center, then repeated inspection. The difference now is that to avoid leaving solvent in the central region of the coating, the swipe needs to start closer to one edge of the mirror, but being careful still not to drag chips from the edge across the surface. After each swipe inspect at 200x, 500x to see which spots have been removed, which remain. If a spot won't shift after 3 or 4 swipes (which remove/add other spots) then it won't be cleanable. At this point I've tried switching solvents to methanol or isopropyl alcohol, but this never helped - it really seems these remaining spots are embedded in the coating.

Step 4. Final inspection

Do a careful inspection with dark-field 200x and 500x, then with bright-field to look for scratches/solvent. I find that it typically takes about 1 hour to clean a single mirror with this procedure. Once satisfied that the surface is as clean as possible, clean the back of the mirror by picking it up with tweezers and swiping the back with lens tissue/acetone. If it wasn't a clean swipe then repeat, but this surface can't be inspected at this time without dirtying the front surface. After cleaning the back place the mirror on its *side* (to keep both front and back clean). I use a v-shaped holder of two microscope slides covered in lens tissue to stop the mirror from rolling around.

5.1.4 Cleaning 7.75mm mirrors

For the ring-down measurement made with 7.75mm substrates I used basically the same cleaning procedure as above, rather than spin-cleaning as was done in previous

experiments. Obviously, the danger of scratching by glass fragments is greatly diminished in this case - but it is always possible to introduce particles on the lens tissue, so the substrate should be inspected before every swipe as before. On these substrates I looked for the central 1mm (full view 200x magnification) to be clear rather than just $400\mu\text{m}$, since it is harder to reach the same absolute accuracy in aligning the larger substrates.

5.2 Cavity construction and alignment

5.2.1 Basic design

The clean mirrors sit on small v-groove aluminum blocks to which they are glued with Torr-seal. These blocks in turn are glued to the cavity mount. For our first series of experiments this was made of two aluminum pieces surrounding a cylindrical PZT (piezo-electric transducer). With one v-block glued to each half of the mount the cavity length could be scanned and stabilized with the PZT. When moving to the higher finesse cavity of our second measurements this design wasn't stable enough, with noise at frequencies of a few kHz evident on the cavity transmission. Our eventual solution was to move to a single solid-block mount, with shear-mode, flat PZT's under each v-block to scan the cavity length - this new design developed primarily by Theresa Lynn. This design has greatly improved noise characteristics at low frequency, but still exhibits mechanical resonances at $\simeq 25\text{kHz}$ and $\simeq 60\text{kHz}$ that are evident on the cavity transmission.

5.2.2 Basic alignment

Transverse and tilt alignment of the mirrors is achieved with reflected HeNe fringes (the cavity has very low finesse at 633nm wavelength).

Starting with a collimated HeNe beam (no coupling lens), the input mirror is aligned such that the HeNe beam passes through the substrate, and hits the 1mm mirror surface in its center. With a $\lesssim 1\text{mm}$ spot size it is relatively easy to center

the HeNe beam in this way. Next the tilt of the input beam is walked so that the HeNe spot is both centered on this mirror, and the beam is backreflected (i.e., the reflection from the mirror surface is centered on the incoming beam. There will be two reflected HeNe spots - one from the mirror surface and one from the back surface of the substrate. These are easily identified because the reflection from the back of the substrate remains a collimated beam ($\approx 1\text{mm}$ size), while the beam which bounced off the curved mirror will be expanding. For a 10cm radius of curvature mirror it's about 2cm diameter at 1m distance.

Next the tilt and position of the back mirror is adjusted. Again two reflected spots result from this mirror (giving a total of 4 spots), but they are harder to identify this time because of the lensing effect of passing through the input mirror. For 10cm mirrors, two sets of circular fringes are seen within the 2cm beam (the reflection from the front mirror). At 1m distance, the large, obvious circular fringes that fill the entire spot are the *wrong* set, arising from a reflection off the back of the second substrate. The *correct* reflection off the second mirror is a very small spot ($\approx 1\text{mm}$), due to being lensed through the front mirror. Simply backreflecting this spot along the input beam path is good enough alignment. To further check the alignment the correct circular fringes can be seen by looking further back from the cavity.

The alignment procedure then consists of walking the alignment: adjusting the translation of the front mirror, the tilt of the back mirror, and the position of the input HeNe beam until:

- (1) Circular fringes from the two beams are properly back-reflected.
- (2) The mirror substrates are aligned transversely (i.e., the edges line up).

Transverse alignment of the substrates is checked with a long focal length microscope and CCD camera (looking from above), and by looking through a 5cm lens by eye (from the side).

During this alignment the front mirror/v-block is already glued to the cavity mount, which is on a translation stage. The back mirror/v-block is held by a mirror mount which gives tilt control. This translation/tilt, together with walking the alignment of the input beam allows for optimal alignment.

Once the HeNe fringes are aligned correctly, an input coupling lens is added to the setup, and a Ti:Sapphire beam (spatially overlapped with the He:Ne beam) is measured in transmission. If properly overlapped with the HeNe beam then cavity modes will be found very easily with a small adjustment of the coupling lens. Measuring resonant wavelengths of the cavity, and hence the cavity free spectral range, gives the length.

Once cavity alignment and length are correct, the translator is moved out to allow Torr-seal to be inserted between the mount and back v-block. There is then $\simeq 1/2$ hour to restore optimal alignment before the glue starts to harden. As the glue dries overnight the cavity length changes (lengthens) by $\simeq 2$ orders, then when the clamp is unscrewed the cavity gets $\simeq 1/2$ an order shorter. The back v-block should be held lightly in its clamp, so that when this is unscrewed the v-block doesn't shift and change the cavity alignment.

5.2.3 Gluing, baking and cavity birefringence

The careful alignment procedure detailed above was developed to satisfy two goals: firstly, to be able to specify cavity length precisely, and secondly to try and reduce birefringence, by aligning the mirrors well.

When a cavity has just been made both of these are correct - the cavity length can be targeted to $1\mu\text{m}$, and birefringence is low - typically birefringent axes can be found, but injected linear polarization still cancels with about a 200:1 ratio at the worst places (45° to the birefringent axes). The magnitude of the observed birefringence depends on the way in which the mirrors are glued to the v-blocks. If only small dabs of glue ($\approx 0.5\text{mm}$) at the back of the substrate are used then very low birefringence is observed (the 200:1 cancellation described above), but if a larger (several mm) gob of glue on the side or underneath the substrate is used then the birefringence will be made worse. We believe that the cone shape of the mirrors probably also has an effect in reducing birefringence: the 1mm coated surfaces are isolated better from the site of gluing than would be the case for a 3mm cylindrical mirror.

However, the birefringence got unexpectedly worse when the cavities were baked. This wasn't noticed with the cavity used in our first experiment, probably due to a combination of factors: less glue was used than in later cavities, the chamber was only baked to 50°C (mirrors would touch due to aluminum mount expansion if heated any hotter!), and this cavity had a finesse 3 times lower, making the total effect of the birefringence 3 times less apparent. When making cavities with higher finesse this became a real problem. In one typical test cavity, for which the polarization cancelled 200:1 for all polarizations before baking, after baking at 100°C for 24 hours clear birefringent axes had developed, with linear polarization now only cancelling 10:1 off-axis. The cavity length also changed during this baking, from 10.1 to 12 μm , indicating that some serious shift in the cavity alignment took place.

My belief is that this birefringence comes from shifting in the Torr-seal glue as it hardens, both changing the alignment of the cavity and adding stress to the mirrors (from the small dabs of glue on the substrates), possibly in conjunction with some shift in the PZT. This effect was seen when using both regular and shear-mode PZT's, which suggests it is more likely the glue.

As a test of whether cavity alignment alone could be responsible, one test cavity was made where the mirrors were glued to their respective v-blocks (with one glued to the cavity mount), then baked at 100°C overnight before aligning the cavity. This cavity was more birefringent than the unbaked cavities, suggesting that the birefringence is at least partly due to stresses from heat-induced changes in the small dabs of glue attaching the mirrors.

To illustrate in detail the effects seen, I present here the "baking history" of the cavity used in our second series of experiments (4.6ppm mirrors). Based on the above experience it was decided to bake the cavity and chamber as gently as possible, to try and lower the chamber pressure without destroying the cavity.

Initial cavity parameters: 852nm modes at 9.2 μm and 9.6 μm length depending on PZT voltage (20V or 200V respectively). Finesse $\mathcal{F} \approx 470,000$. Birefringence: linear polarization cancels to 1.5% in worst places. No obvious change in linewidth of 34.5MHz (at 9.2 μm length) with input polarization, so birefringent splitting $\leq 2\text{MHz}$.

The vacuum chamber with cavity inside was then baked at $\approx 38^\circ\text{C}$ for 1 week. Measurements made while the chamber was hot showed that the birefringence and finesse $\mathcal{F} \simeq 480,000$ were *unchanged* by this gentle heating, and the cavity length was now $11.4\mu\text{m}$ due to thermal expansion of the cavity mount.

When the bake was switched off the chamber slowly cooled over the course of about 1 day. With the temperature back to 22°C , a cavity length of $10.1\mu\text{m}$ at 0V PZT voltage was measured (that is, 2 orders longer than initially!), with birefringence now slightly worse (cancellation to 3% off-axis), but still with the same cavity FWHM measured along good and bad polarization axes (31MHz FWHM, $\mathcal{F} \simeq 480,000$).

Unfortunately, the chamber pressure was still too high, so we chose to do another stage of baking, expecting that if we continued the bake at the same temperature ($\approx 40^\circ\text{C}$) there would be no further changes in the cavity, since our first bake would have already made whatever changes to the glue that were going to happen. So again the chamber was raised to $\approx 38^\circ\text{C}$ for 1 week. Measurements with the chamber hot gave a cavity length of $11.8\mu\text{m}$ or $12.2\mu\text{m}$, with birefringence still small at $\approx 2.5\%$ cancellation. When the bake was turned off the birefringence again got worse - with final cavity length $10.5\mu\text{m}$ (at 120V PZT) and polarization cancellation to 7%, leading to a $\approx 1\text{MHz}$ difference in measured linewidth with polarization.

It was then decided to cool the chamber slightly by running cooling water, to bring the cavity length back to the target $10.1\mu\text{m}$ length. With the chamber temperature at 16°C and cavity length at $10.1\mu\text{m}$ (17V PZT), input polarization now only cancelled to 20% ! After the temperature had stabilized, length was $10.1\mu\text{m}$ (80V PZT), birefringence 25% cancellation, meaning that the cavity lineshape was now visibly split by about the HWHM. That is, for off-axis polarization a cavity width of 45MHz was measured, and on-axis 31MHz. When the cooling water was switched off again, the cavity returned to $10.5\mu\text{m}$, birefringence $\approx 8\%$. As a final test the cavity was cooled again and left cold for a week, to see if a gradual settling of the glue would help reduce this birefringence. The cancellation was better this time (15%) but stayed close to this value (best 13.6%). Finally the chamber was returned to room temperature.

The final length ended up being yet longer, $10.9\mu\text{m}$ (180V) at room temperature,

but with lower birefringence of 2% cancellation! Remember that this cavity gave 7% at $10.5\mu\text{m}$, and 15% at $10.1\mu\text{m}$ length.

From this series of measurements it seems to me that there is an effect due to unequal thermal expansion and contraction of the PZT/Torr-seal/glass/aluminum structure, which ends up putting a stress on the mirrors. The copper mount and aluminum v-blocks probably contract smoothly, but the Torr-seal perhaps doesn't follow this and so stresses the mirrors. Because birefringence increase seems to be associated with cooling the cavity, it also indicates that the warming and cooling the glue give different expansion/contraction rates. As for the change in cavity length, I suspect that this is because the Torr-seal is intended to be cured at high temperature and we let it set at room temperature - additional baking further hardens the glue and changes its properties.

One mystery remains: an almost identical cavity (regular not shear PZT, aluminum not copper mount, same Torr-seal gluing) was made for Jun Ye and Dave Vernooy's experiment. This cavity was baked inside their vacuum chamber to 150°C for several days, and showed no increase in birefringence. The way in which the mirrors were glued to the v-blocks was the same in both cavities. I can suggest two possible explanations, neither of which has been tested: Firstly, it may be a coincidence of where the glue was placed with respect to the birefringent axes - if the additional stresses ended up being symmetric there wouldn't be a large resulting birefringence. Secondly, it may be that their *hotter* bakeout initially introduced stresses but eventually smoothed them out, while our cooler 100°C test bake wasn't enough to remove the remaining defects.

Finally, the obvious question arises: if Torr-seal used to glue the mirrors appears to be causing this birefringence, why not use another type of glue? This raises an orthogonal problem: that of cavity mount mechanical stability. Theresa Lynn spent a considerable time testing various configurations of PZT's, v-blocks, and gluing techniques to improve the mount's isolation from mechanical excitation. This was because our first attempt at a cavity for the second experiment (4.6ppm mirrors) exhibited a strong vibration at 15kHz. This meant that looking for atom transit

signals with probe detuning on the side of the cavity would have been impossible, both because these vibrations had large amplitude ($\approx 30\%$ variation in transmission for a probe laser at the cavity half-width) and were at a frequency corresponding to expected atom signals. The 15kHz was a 'diving board' resonance of the PZT, which was not glued all the way underneath (to allow it to scan). One attempted design was to damp these oscillations by using softer RTV glue under the v-blocks, which instead introduced a large low-frequency mechanical resonance at a few kHz, corresponding to the v-blocks swaying on the RTV, of larger amplitude than the 15kHz. In the most stable design produced, the 15kHz resonance peak was pushed up to 65kHz by using shear-mode PZT's instead of regular PZT's, and by gluing everything rigidly together - this resonance probably a bending oscillation of the v-block/mirror structures. The amount of glue joining the mirrors to the v-blocks had a strong effect on this frequency: if insufficient glue was used, the resonance was around 20kHz (softer 5 minute epoxy needed more glue for the same stability than Torr-seal), and the resonance would jump to >50 kHz when a proper rigid connection was made by applying a small amount more glue.

So it seems that mirrors glued with RTV to try and avoid birefringence would probably result in an unstable cavity if the current mount were used - this problem of combining mechanical stability and low birefringence is yet to be solved.

5.3 Coating measurements and modeling

5.3.1 Introduction

For many contemporary physics experiments, measurement enhancement via an optical cavity is a useful tool. In such situations, a better understanding of cavity and mirror properties will be useful for achieving improved sensitivity and elimination of systematic errors. For example, in cavity QED, one needs to know the mode structure of intracavity fields in order to develop the optimum strategy of atom-cavity coupling; for frequency metrology, accurate determination of phase shifts of the resonant fields

can provide precision frequency markers. Additionally, the knowledge gained from such an understanding could provide guidelines for the optic coating community to develop in situ measurement and control capabilities of the coating process.

The work described in this section uses precise length measurements of short optical cavities to determine mirror coating characteristics. These cavities have length of the order of $10\mu\text{m}$, leading to a free-spectral-range (FSR) of 15 THz, or a wavelength difference of a few tens of nanometers (for example, it is 36 nm for a center wavelength of 852 nm) for neighboring cavity modes. Therefore, a 6-digit measurement of the wavelengths (Burleigh wavemeter) of the cavity modes acquires a precision of the order of 5×10^{-5} for accurate determination of the cavity length, from which details of the index of refraction and layer thickness of materials in the mirror stack can be inferred.

The cavity finesse and overall cavity transmission can also be measured directly to measure the mirror losses, l , and transmission, T . This information can be combined with the FSR measurement in two useful ways:

Firstly, the FSR measurement is sensitive to the difference in refractive index $n_H - n_L$ of the materials making up the multilayer mirror stack, whereas the transmission T depends on the ratio n_H/n_L . As a result, a precise measurement of both the FSR and T can be used to determine the values of n_H and n_L independently. Moreover, by mapping out the wavelength dependence of the FSR, the thickness of layers in the mirror stack can be determined.

Secondly, if one of the refractive indices (here n_L) is well known, then the FSR measurement determines n_H , and an independent value for the mirror transmission T can then be calculated from n_H and n_L , and compared to the experimentally measured result. In this work the values obtained by the two methods agree well.

Knowledge of the cavity properties is of importance to our current experiments in two particular ways:

1. Mirror absorption/scatter losses are a critical limiting factor in the loss rate from our cavity QED system - for our current cavities the loss rate from photon scattering due to mirror imperfections is similar in size to the atomic spontaneous

emission rate. To build robust quantum computing/communications devices from cavity QED components, it will therefore be necessary to improve the ratio of mirror transmission to mirror losses.

2. The standing-wave light field inside the cavity penetrates into the mirror coatings, giving a larger mode-volume than would be expected naively from the physical distance between the mirror surfaces. As our microcavities are pushed to shorter lengths, this leakage field will have a non-negligible effect on the achievable coupling strength g .

5.3.2 Direct transmission and loss measurements

The #T95 coating run had a design transmission of $T^{th}=7\text{ppm}$ at a center wavelength of 852nm, from which a cavity finesse of $\mathcal{F}=370,000$ was expected. It was somewhat surprising therefore to measure a finesse of $\mathcal{F}=480,000$, and this prompted me to make a more detailed measurements of the mirror properties, and design a model to match these measurements.

Firstly, losses were measured directly by Jun Ye (for a $40\mu\text{m}$ length cavity with 20cm radius of curvature mirrors) in the usual way by recording resonant cavity transmission, reflection and finesse. If we denote the transmission of mirrors 1 and 2 by T_1 and T_2 respectively, and the absorption+scatter loss per mirror as $l_i = (A+S)_i$, then the total cavity losses $T_1 + T_2 + l_1 + l_2$ can be determined from the cavity finesse \mathcal{F} (ringdown or linewidth measurement + length measurement). The cavity transmission $I_{trans} = \frac{4T_1T_2}{(T_1+T_2+l_1+l_2)^2}$ can then be used to determine $l_1 + l_2$, if T_1 and T_2 are known independently. In practice this is a difficult measurement to make, because the overall transmission I_{trans} depends on the mode-matching into the cavity being perfect. A version of this which does not require perfect mode-matching can be derived, by comparing the reflection and transmission values with the cavity locked on resonance and off resonance.

First of all, the total loss $(T_1 + T_2 + l_1 + l_2)$ is always measured first, with a cavity ringdown or linewidth measurement. Now let us denote the input power as P_{in} , the

reflected power P_r , and the transmitted power P_t . There is also a mode matching factor ϵ , meaning that of the input power of P_{in} , only ϵP_{in} is useful for coupling to the cavity TEM₀₀ mode, $(1 - \epsilon)P_{in}$ is wasted. We have the following equations:

$$\mathcal{F} = \frac{2\pi}{T_1 + T_2 + l_1 + l_2} = \frac{\pi}{l + T} \text{ assuming two equal mirrors} \quad (5.1)$$

$$\frac{P_t}{\epsilon P_{in}} = 4T_1 T_2 \left(\frac{\mathcal{F}}{2\pi}\right)^2 = T^2 \left(\frac{\mathcal{F}}{\pi}\right)^2 \quad (5.2)$$

$$\frac{P_r - (1 - \epsilon)P_{in}}{\epsilon P_{in}} = (l_1 + l_2 + T_1 - T_2)^2 \left(\frac{\mathcal{F}}{2\pi}\right)^2 = l^2 \left(\frac{\mathcal{F}}{\pi}\right)^2 \quad (5.3)$$

(Remember $(1 - \epsilon)P_{in}$ is the useless power that is reflected directly off of the input mirror, and must be subtracted from P_r to leave the reflected power we wish to measure, that is, the sum of the field leaked from the cavity storage and the field (mode-matched) directly reflected off the input mirror. This cavity contrast is a direct result of the mirror properties.)

Division of Eq. 5.2 by 5.3 gives

$$\frac{P_t}{P_r - P_{in}} = \frac{T^2 \left(\frac{\mathcal{F}}{\pi}\right)^2}{l^2 \left(\frac{\mathcal{F}}{\pi}\right)^2 - 1} \quad (5.4)$$

Eq. 5.4, combined with 5.1, will determine completely T and l .

In the experiment, Jun's direct measurement gave (from finesse we have $l + T = 7.2ppm$) $P_{in} = 54\mu W$, $P_r = 42.6\mu W$ and $P_t = 4.82\mu W$ therefore $l = 2.9$ and $T = 4.3ppm$.

Another way to measure the (T, l) is by sweeping out all the high order spatial modes and carefully noting the transmission and reflection at each of them. One measures the total input power and then sums together the powers of matched modes. That measurement produced $l = 3ppm$, and $T = 4.2ppm$. The value of T should be a bit lower in this case because it is not possible to include all higher order modes in the measurement, some of them are simply not measured due to their weakness.

Other cavities measured had higher finesse, thought to be due to a lower density of surface defects. The highest achieved with cone-shaped mirrors was $\mathcal{F}=480,000\pm10,000$,

corresponding to losses $l = 2.2\text{ppm}$ if mirror transmission $T = 4.3\text{ppm}$.

5.3.3 Technical details of the model

Next, a model for the coating was derived. A transfer-matrix formalism was used to calculate the input-output propagation of a plane-wave field through the 37 layer stack of alternating high index (Ta_2O_5 , $n_H=2.0411$) and low index (SiO_2 , $n_L=1.455$) dielectric layers (these dielectric constants are assumed to be constant with wavelength). The substrate refractive index (supplied by REO) used was $n_{sub}=1.5098$. That is, the transfer of the field through each $\lambda/4$ layer is represented by a matrix, and the response of the entire mirror (or cavity) is determined by the product of these individual matrices.

Following the treatment of Hecht [96], for normal incidence the matrix representing layer j is given by $M_j = \begin{bmatrix} \cos(kh_j) & (i \sin(kh_j))/Y_j \\ iY_j \sin(kh_j) & \cos(kh_j) \end{bmatrix}$. Here $k = 2\pi/\lambda$ is the free-space wavevector of the incident light, $h_j = n_j \times$ (layer thickness) with n_j the refractive index, and $Y_j = \sqrt{\frac{\epsilon_0}{\mu_0}}n_j$ with (ϵ_0, μ_0) the electric and magnetic constants in SI units. For an exact $\lambda/4$ layer (and for light at the design wavelength of the coating), this simplifies to $M_j = \begin{bmatrix} 0 & i/Y_j \\ iY_j & 0 \end{bmatrix}$. A multilayer stack is represented by multiplying the matrices of the individual layers: For light incident on layer 1, the matrix for the entire structure of q layers is defined as the product $M = M_1 M_2 \dots M_q$. For our mirror stack, this gives $M = (M_{\text{Ta}_2\text{O}_5} M_{\text{SiO}_2})^{18} M_{\text{Ta}_2\text{O}_5}$. Note that at the coating center (where there is an exact $\lambda/4$ layer), $M_{\text{Ta}_2\text{O}_5} M_{\text{SiO}_2} = \begin{bmatrix} -\frac{n_L}{n_H} & 0 \\ 0 & -\frac{n_H}{n_L} \end{bmatrix}$, so the system matrix has the simple form $M = \begin{bmatrix} 0 & \frac{i}{Y_H} \left(\frac{n_L}{n_H}\right)^{18} \\ iY_H \left(\frac{n_H}{n_L}\right)^{18} & 0 \end{bmatrix}$.

For a field incident from material with index n_0 and exiting into material with index n_s , the resulting transmission coefficient is given by

$$t = 2Y_0/(Y_0 M_{11} + Y_0 Y_S M_{12} + M_{21} + Y_S M_{22}), \quad (5.5)$$

with transmission $T = \frac{n_s}{n_0} |t|^2$ (the factor of $\frac{n_s}{n_0}$ re-expresses the intensity in free-space units, by accounting for the change in field amplitude in the dielectric). At the center wavelength of the coating then,

$$T = \frac{n_s}{n_0} \left| -2i/[(n_S/n_H)(n_L/n_H)^{18} + (n_H/n_0)(n_H/n_L)^{18}] \right|^2. \quad (5.6)$$

But we can make a further simplification: since $(n_L/n_H)^{18} = 0.0018$ and $(n_H/n_L)^{18} = 557$ the first term in the denominator is only a 10^{-6} correction, so the final result for at the coating center becomes

$$T = 4n_S n_0 (n_L)^{36} / (n_H)^{38}, \quad (5.7)$$

and the transmission is determined by the *ratio* of the refractive indices.

This calculation reproduced the design reflectivity of $T^{th}=7.3\text{ppm}$ for the #T95, and $T^{th}=14.6\text{ppm}$ for # D1306 coating run, for which the number of layers was reduced to 35. The model and measured (REO spectrophotometer data) “coating curves” are shown in Figure 5.4 for the D1306 coating run.

For a fixed cavity length the resonance wavelengths of the cavity can be calculated simply with the same transfer-matrix formalism, using a matrix for the entire system, $M_{total} = MM_{gap}M$, (a product of two mirrors plus a fixed length vacuum gap between). The calculation steps through a series of wavelengths calculating the cavity transmission T at each, and by finding places of maximum transmission finds the wavelengths of the cavity resonances.

Conversely, for a given set of measured cavity resonance wavelengths it is possible to determine the cavity length very precisely - and the parameters of the model (index contrast, layer thickness) are set by comparison to such measurements. Finally then, with the detailed knowledge of the mirrors provided from the model, if the cavity is locked to a laser of known frequency (in our case a cesium transition at 852.359nm) the cavity length is determined precisely. Close to the coating design wavelength it is roughly $L_{eff} = L + 1.63\lambda/2$ with L (the physical distance between the mirror

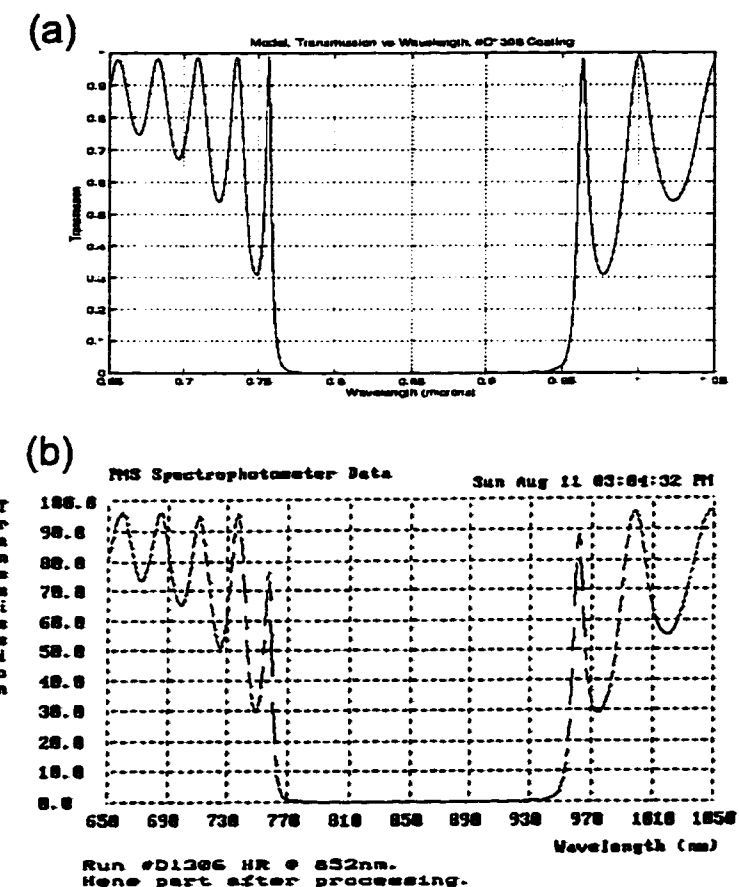


Figure 5.4: (a) Calculated and (b) Measured transmission of coating as a function of wavelength, for a 35 layer $\lambda/4$ stack with $n_H=2.0411$, $n_L=1.455$, and center wavelength 850nm.

surfaces) an integer number of $\lambda/2$. Further details of the wavelength-dependence are provided by reference to the model.

5.3.4 FSR measurements

To determine the parameters of the model (index contrast, layer thickness), a series of precise measurements of the cavity free-spectral range (frequency between successive cavity resonances) was made[97, 98, 99]. At fixed cavity length a Ti-Sapphire laser was tuned to find successive resonant wavelengths (λ_1, λ_2) of the cavity, and an experimentally determined length was then defined by $L_{\text{expt}} = \lambda_1 \lambda_2 / 2(\lambda_1 - \lambda_2)$.

This length comprises the actual physical length between the two mirror surfaces, L , plus a contribution from leakage of the mode into the mirror stack, which gives rise to an additional phase shift at the coatings, to give a length $L_{\text{eff}} > L$. In addition, the leakage into the coatings increases with wavelength as (λ_1, λ_2) move away from the coating design wavelength, so this gives another additional contribution to the round-trip phase and hence to the measured length L_{expt} .

As discussed in Ref. [97], if λ_1 and λ_2 were closely spaced compared to the scale on which the coating properties vary (so that coating dispersion could be neglected) then near the design wavelength of the coating we would have $L_{\text{expt}} = L_{\text{eff}} = L + (\frac{1}{n_H - n_L}) \times \lambda/2$ where n_H and n_L are the high and low index materials of the stack, and $\lambda = 2\lambda_1\lambda_2/(\lambda_1 + \lambda_2)$ is the average (in frequency) of wavelengths λ_1 and λ_2 . We thereby have a dependence of the free spectral range on $(\frac{1}{n_H - n_L})$, which combined with the transmission (which depends on n_L/n_H) can fix n_H and n_L . For these materials, this gives $L_{\text{eff}} = L + 1.633\lambda/2$. However, for our measurements below with short cavities, λ_1 and λ_2 are separated by $\simeq 30\text{nm}$, so $L_{\text{expt}} > L_{\text{eff}}$. But we can still use the complete model to fit to the measured values (λ_1, λ_2) and determine parameters of the coating. Finally, by mapping out this wavelength dependence of the free-spectral range to find $\min(L_{\text{expt}})$ we find the center wavelength of the coating.

In the model, the refractive indices used are adjusted to obtain the same pairs (λ_1, λ_2) as measured. Then, the layer thickness in the model adjusted to agree with

the measured coating center wavelength. By using the additional information of the measured mirror transmission T from Section 5.3.2, we can now either:

1. Derive independent values for the refractive indices and layer thickness, or
2. Assuming one index is known, use the refractive indices and layer thickness information to give an independent value for the mirror transmission, which can be compared to the measurement of Section 5.3.2.

That the dispersion (FSR) measurement alone is sufficient to determine the lossless part of the mirror properties represents some useful information for the mirror coating technicians: the index difference $n_H - n_L$ and the optical thickness of the coating layers can be simply measured in this way without interference from absorption/scatter losses. And, if n_L is known, this also gives a simple way of finding the mirror transmission. Adding in a direct measurement of mirror transmission yields values for n_H and n_L separately.

Data obtained from these measurements are shown in Figure 5.5, where L_{expt} is plotted as a function of wavelength, for a $10\mu\text{m}$ cavity with 10cm radius of curvature mirrors. The circles are measured data, and the curves the calculation from the model, with parameters chosen to best fit the data. This data was taken by setting the cavity to a series of different lengths, and recording a pair of resonant wavelengths (λ_1, λ_2) at each length. The x axis is center wavelength $\lambda_c = 2\lambda_1\lambda_2/(\lambda_1 + \lambda_2)$, the y axis the measured cavity length $L_{\text{expt}} = \lambda_1\lambda_2/2(\lambda_1 - \lambda_2)$ shown in units of $\lambda_1/2$: for each pair (λ_1, λ_2) , the length is such that $L_{\text{expt}}/(\lambda_1/2) = 24.\text{xx}$. Dividing by λ_2 instead would exactly give $23.\text{xx}$, since by rearranging the formula for L_{expt} we see that $L_{\text{expt}}/(\lambda_1/2) \equiv L_{\text{expt}}/(\lambda_2/2) + 1$. Due to a finite drift in the cavity length, each measurement of λ was made to only 5 digits resolution (e.g., $852.59 \pm 0.01\text{nm}$), leading to the uncertainty in L_{expt} shown. Uncertainty in λ_c is $\pm 0.03\text{nm}$ and cannot be seen on this scale.

Two theory curves are shown. The solid curve shows a model with n_L assumed to be fixed at its nominal value of $n_L=1.455$. To best fit the data, n_H was increased to $n_H=2.0676$ (a factor of 1.3%). In addition, the center wavelength was shifted to 847nm (by reducing the thickness of each $\lambda/4$ layer by 0.6%). Discussions with

REO confirmed that 1.3% is a known offset for the particular coating machine which produced this run, and also that a few nm uncertainty in the center wavelength is typical. With these parameters, the inferred mirror transmission is $T_{\text{inf}} = 4.6 \pm 0.2 \text{ ppm}$, agreeing well with the measured value from Section 5.3.2. The dotted curve (which overlaps the solid curve) shows the model when both n_L and n_H are allowed to vary. Their values are chosen to match both the FSR measurement shown, and to give a mirror transmission to match exactly the experimentally determined value $T = 4.3 \text{ ppm}$. Parameters which satisfy these criteria are $n_H = 2.0564$ (0.75% increase) and $n_L = 1.4440$ (0.76% decrease). Our direct measurement of T in Section 5.3.2 had a large uncertainty, which limits the absolute determination of n_H and n_L to about this 1% level; however, a more precise measurement could in principle determine the indices at the 0.1% level. One application might be to measure T and the FSR as a function of position across a mirror substrate, thereby mapping out stress induced variations in the refractive indices at the 0.1% level.

In this data set the correction for the Gaussian phase difference between the actual resonator mode and the plane-wave of the model has been neglected. After the propagation distance from the mode waist to the mirror surfaces, a Gaussian beam will have acquired less phase than a plane wave travelling the same distance. For a $10\mu\text{m}$ cavity with 10cm radius of curvature mirrors, this gives a 2% correction, corresponding to a shift in L_{expt} by $\simeq 0.0045$ cavity orders. Lowering the refractive index contrast of the model to shift the calculated curve by this amount would increase the inferred mirror transmission by $\lesssim 0.1 \text{ ppm}$. For our second cavity ($44\mu\text{m}$, 20cm radius of curvature mirrors), the correction is 0.0066 cavity orders.

The mirror phase shift (FSR measurement) is only sensitive to the transmission (index contrast) and center wavelength (layer thickness). Therefore, if absorption/scatter losses are added to the model (by introducing an imaginary component to the refractive index) the cavity resonance wavelengths do not change. More precisely, adding a scattering loss at the mirror surfaces has exactly zero effect on the FSR and mirror transmission. Adding losses *within* the coatings has a small effect: increasing the mirror absorption from 0.5ppm to 2ppm (an experimentally reasonable

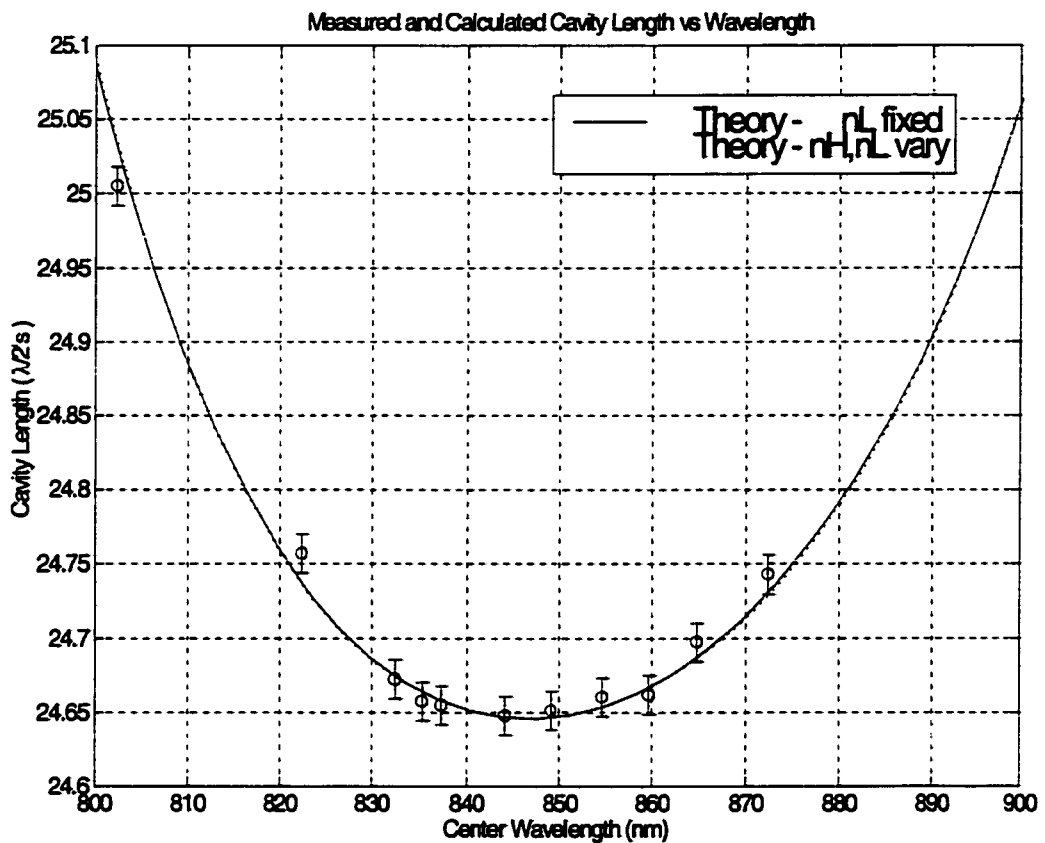


Figure 5.5: The cavity length L_{expt} measured from the Free-Spectral Range (FSR) varies about the design wavelength of the coating. Fitting a model to these data points gives a measure of mirror transmission (from fitting of the difference $n_H - n_L$) and center wavelength (from fitting layer thickness).

range) changes the mirror transmission by a factor of $\simeq 10^{-5}T$, clearly negligible, and again there is no effect on the FSR measurement. As a result, this measurement (with n_L assumed fixed) provided a very simple and sensitive inference of the mirror transmission of $T_{\text{inf}} = 4.6 \pm 0.2 \text{ ppm}$, which is *unaffected* by absorption/scatter losses.

The same measurement and fitting procedure was used on another cavity with mirrors from the same coating run. This $44\mu\text{m}$ cavity made from 20cm radius of curvature mirrors gave a transmission of $T_{\text{inf}} = 4.5 \pm 0.2 \text{ ppm}$, with a center wavelength of 848nm (This was the cavity used for the direct measurements of Section 5.3.2 which gave $T=4.3 \text{ ppm}$.)

One other factor which has been ignored so far is the effect of fluctuations in the $\lambda/4$ layer thickness. Discussions with REO suggested that a 1% variation in thickness was reasonable, so a Gaussian-distributed variation (of standard deviation 1%) was added to the layer thicknesses of the model. For cavity calculations, identical mirrors were used for both sides of the cavity. The principal effect of this variation is to shift the center wavelength of the coating - over several realizations of random coatings, this resulted in an rms shift of the center wavelength by $\pm 1.2 \text{ nm}$. So, the measured shift of center wavelength in the coating (from 852nm to 847nm) is probably due partly to a systematic offset, and partly to fluctuations. The mirror transmission is also affected: the value of the transmission is on average *increased* slightly, by 0.6% in the case studied, from 4.55ppm to 4.58ppm at the center of the coating. At the level of our current measurements this is another negligible effect, but with a more precise measurement aimed at determining n_H and n_L , the possibility of a systematic offset from this mechanism should be considered. Lastly, the FSR measurement is mostly effected via the change in center wavelength of the coating - the value of $\min(L_{\text{erpt(simulated)}})$ has a mean the same as without the added fluctuations, and varies by only 0.0014 mode orders rms, again negligible for our purposes.

Another useful result of these calculations is that the free spectral range of the cavity is well known, so that resonant wavelengths of the cavity can be accurately predicted. This is important for choosing a diode laser of correct center wavelength to match the mode, for applications such as cavity locking or dipole-force traps. With the

idea of using a laser of $>920\text{nm}$ wavelength to form an intracavity dipole-force trap, this knowledge was particularly important: our Ti:Sapphire laser tuned only as high as 890nm so cavity resonances in this wavelength range could not be measured, only predicted. With the parameters chosen above for the model, the following theoretical and experimental resonance wavelengths resulted:

theory	787.208nm	818.659	853.255	890.798	930.683
experiment	787.170nm	818.651	853.255	890.80	?

Table 5.1: Measured and predicted values for the cavity free spectral range (FSR).

The experimental value for the cavity resonance can then confidently be predicted to be $930.7 \pm 0.05\text{nm}$, and a diode laser chosen accordingly.

5.3.5 Limitations to mode volume

In a similar calculation to one above, it is possible to calculate the field distribution of light inside the resonant cavity, by describing each layer separately with a left and right travelling plane wave, then matching electromagnetic boundary conditions between layers. An example of this kind of calculation is shown in Figure 5.6, where refractive index and field distribution (Electric-field) are plotted as a function of distance for a $3\lambda/2$ cavity. The coupling strength g of an atom placed in the center of the cavity mode is proportional to $\frac{1}{\sqrt{V_m}}$, where V_m the cavity mode volume is found by integrating the field ($D \cdot E$) over the standing wave and Gaussian transverse mode profile. Large coupling is achieved by making a short cavity with a small mode waist (short radius of curvature mirrors).

For a cavity of physical length L , the “leakage” of the mode into the $\lambda/4$ mirror stack (look at the tails of the mode in Figure 5.6) that increases L to L_{eff} also increases the cavity mode volume. For our materials at 852nm , $L_{eff} = L + 1.63\lambda/2$, so for a cavity with physical distance between mirror surfaces $L = \lambda/2$, the cavity mode volume ends up being 2.63 times larger than you might expect, and hence the atom-cavity coupling g is 0.6 times smaller than the naive estimate based on the physical separation of the mirror surfaces.

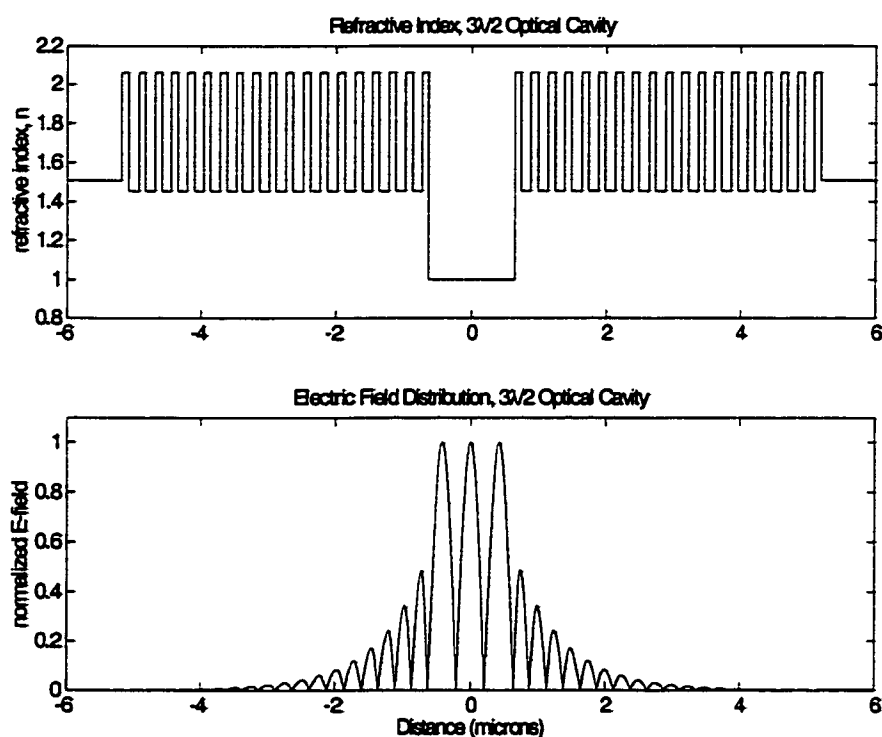


Figure 5.6: Mirror refractive index stack design, and resulting electric field distribution for a resonant $3\lambda/2$ cavity made from dielectric mirrors.

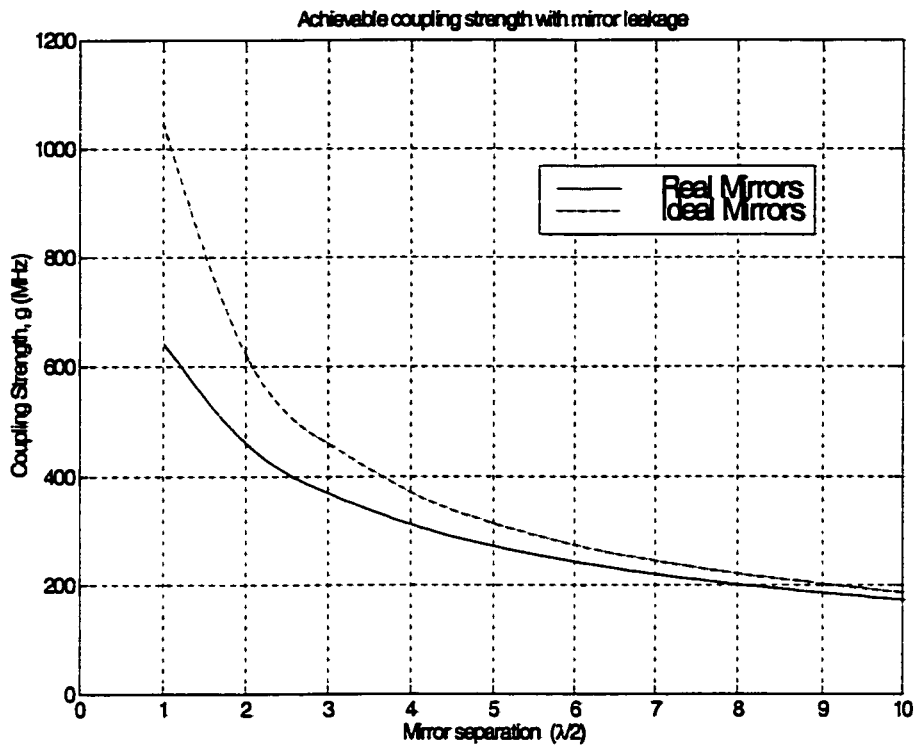


Figure 5.7: Due to penetration of the standing-wave mode into the mirror coatings, the cavity mode volume achieved with real mirrors is larger (and hence the coupling strength smaller) than for an ideal mirror with the same spacing between mirror surfaces but no penetration.

This effect is proportionately larger as the cavity length gets shorter. In Figure 5.7, the expected g is plotted for a cavity formed with two 20cm radius of curvature mirrors, as a function of the physical distance L between the mirrors. The two curves show a real mirror (with g reduced by leakage into the coatings) and an idealized mirror with no leakage (perfect reflectors at $\pm L/2$). The transverse (Gaussian waist) dimension is calculated by simple Gaussian beam propagation, which is not strictly accurate for length scales less than a few microns; however any error in this should be roughly the same for both the ideal and actual mirror cases, so the ratio of these remains correct. The cavity is assumed resonant at an integer number of half-wavelengths of light at the 852nm Cs D2 transition; that is, each $\lambda/2$ is a distance of 0.426 microns.

The discrepancy between the expected and achieved coupling g is large even for

our longer cavities - 5% for a $10\mu\text{m}$ cavity. However, in the lab this is largely compensated by the fact that we never measure the actual physical distance L between mirror surfaces, but instead $L_{\text{expt}} = \lambda_1\lambda_2/2(\lambda_1 - \lambda_2)$, which is close to L_{eff} , and so incorporates the same offset of mirror penetration that determines g . This method of length measurement breaks down eventually due to the dispersion of the mirror coatings: Eventually if λ_1 is at the center of the coating, λ_2 will be so far separated in wavelength that it reaches the edges of the mirror coating stopband, and the observed phase has then more to do with the coating than the cavity length. That is to say, our measured L_{expt} becomes increasingly different from L_{eff} and introduces an offset in estimating the mode volume.

At $L = 20\lambda/2$ physical length (the regime of our present cavities) the difference between the g inferred from L_{expt} and that found by integrating $D \cdot E$ over the mode volume is $<0.1\%$. At $L = 10\lambda/2$ ($4.26\mu\text{m}$) it would be a 1% error, at $5\lambda/2$ an 8% error. Note however that knowledge of these offsets means that when calculating g from L_{expt} we can compensate for this error. Measurements of L_{expt} for cavities any shorter than $5\lambda/2$ would be impossible since λ_2 has reached the edge of the mirror stopband. To align shorter cavities a new method for length measurement will need to be developed, such as measuring the frequency spacing of transverse modes.

We are now in a position to estimate parameters for the best Fabry-Perot cavity that will be experimentally feasible in the near future using this type of mirrors. First consider a $L = \lambda/2$ cavity with 20cm radius of curvature mirrors. If the mirror transmission and losses were each reduced to $T = l = 0.5\text{ppm}$ to yield a cavity finesse of $\mathcal{F} = 3.14 \times 10^6$, then this cavity has parameters $(g, \kappa, \gamma)/2\pi = (647, 56, 2.5)\text{MHz}$, which gives critical photon number $n_0 = \gamma^2/2g^2 = 7.5 \times 10^{-6}$ and critical atom number $N_0 = 2\kappa\gamma/g^2 = 6.7 \times 10^{-4}$. To make a cavity of this length the 20cm mirrors would have to be reduced to a diameter of 0.5mm rather than 1mm. At this size there would still be a $0.11\mu\text{m}$ gap between the mirror edges for the $L = \lambda/2$ (0.426 micron) cavity length, which should make it possible to still get atoms in and out, and align the mirrors.

If the mirror diameter could be reduced to $350\mu\text{m}$, then 10cm radius of curvature

mirrors could be used, with a $0.12\mu\text{m}$ gap at the edges. Due to the tighter radius of curvature, $g/2\pi$ would be increased to 770MHz in this case. Now speculating that “dream” mirrors of $T = 0.2\text{ppm}$ transmission, $l = 0.2\text{ppm}$ loss might be possible ($\mathcal{F} = 7.85 \times 10^6$), we could aim for the ultimate goal of $(g, \kappa, \gamma)/2\pi = (770, 22, 2.5)\text{MHz}$, in which case $n_0 = 5.3 \times 10^{-6}$ photons, and $N_0 = 1.9 \times 10^{-4}$ atoms.

Chapter 6 Ideas for future directions

6.1 Manipulation of AC Stark shifts in optical traps by utilizing multiple excited states

A scheme is presented which allows AC Stark shifts (light shifts) in optical dipole force traps[100] to be manipulated by choosing a trapping laser wavelength that couples (off-resonantly) to several excited states. This idea was proposed by Chris Wood (NIST, now at Lightwave in Boulder, CO), and I have adapted this to the specific example of a trap for cesium, and added an analysis of the polarization dependence of the light shifts. By varying the trapping wavelength around 920-950nm, the excited state Stark shift is strongly affected because it couples to another, higher-lying excited state while the ground state shift remains essentially constant. In addition, for atoms prepared in a particular hyperfine magnetic sublevel, polarization of the trapping laser can be exploited to control the characteristics of the excited-state AC Stark shift. This is similar conceptually to the proposal of Ref. [101], in which the AC Stark shifts of hyperfine ground states are manipulated by tuning the trapping laser between the D1 and D2 excited states; this scheme recently experimentally realized in Ref. [102].

Spatial variations of the AC Stark shift are necessary for optical trapping, but lead to problems for spectroscopy experiments, since the ground and excited states of the transition are differentially shifted, leading to a change in the atomic transition frequency that is position dependent. In addition, in a trap designed for ground-state atoms, atoms in the excited state experience the opposite AC Stark shift, so are repelled from the desired trapping region. In the solution proposed here, the ground and excited state shifts can be individually controlled. It is thereby possible to give ground and excited states the same confining potential, and hence an unshifted atomic

transition frequency. Alternatively, the excited state can be made more tightly confining, which Taieb et al. [103] show enables an efficient Sisyphus cooling mechanism with the added benefit of reduced heating rates and diffusion.

To achieve this manipulation of the differential AC Stark shift for a particular transition, it is necessary to choose the trapping wavelength carefully. Specifically, the trapping laser wavelength must be selected such that a third energy level gives rise to an important, or even dominant, contribution to the differential AC Stark shift of the transition of interest. Wavelengths for optical traps are usually chosen to be either near an atomic transition, or at a wavelength where high optical power is available. While such choices simplify experimental requirements, a higher degree of control can be achieved if the trapping laser wavelength is selected with respect to spectroscopic implications rather than experimental convenience.

6.1.1 Multi-level dipole traps - the basic idea

Consider the three-level (ladder) system $\{|a\rangle, |b\rangle, |c\rangle\}$ shown in Figure 6.1. For the current purposes, $|a\rangle$ is the ground state of an atomic transition of interest, $|b\rangle$ the excited state, and $|c\rangle$ an auxiliary level which will be used to modify the AC Stark shift of level $|b\rangle$.

Applying a laser field detuned from the $|a\rangle \rightarrow |b\rangle$ transition generates AC Stark shifts (in the limit of large detunings) $U_a \propto -\Gamma_b I / \Delta_{ab}$, $U_{b1} = -U_a$ on levels $|a\rangle$ and $|b\rangle$, where Γ_b is the spontaneous decay rate of $|b\rangle$, I the intensity of the applied laser field, and Δ_{ab} the frequency detuning of the applied field from the $|a\rangle \rightarrow |b\rangle$ transition. Since for Δ_{ab} is positive for a red-detuned ($\lambda > \lambda_{ab}$) field, the resulting potential is confining for ground state atoms, and repulsive for excited state atoms.

Similarly, the same laser field generates shifts $U_{b2} \propto -\Gamma_c I / \Delta_{bc}$, $U_c = -U_{b2}$ on levels $|b\rangle$ and $|c\rangle$ arising from its coupling to the $|b\rangle \rightarrow |c\rangle$ transition. The resulting *total* shift on level $|b\rangle$ is then $U_b \sim I(\Gamma_b / \Delta_{ab} - \Gamma_c / \Delta_{bc})$, which can be manipulated by choice of the detunings (Δ_{ab}, Δ_{bc}) by changing the wavelength λ of the driving laser.

In the case of a red-detuned laser field ($\lambda > \lambda_{ab}, \lambda_{bc}$), to make $U_b < 0$ and the

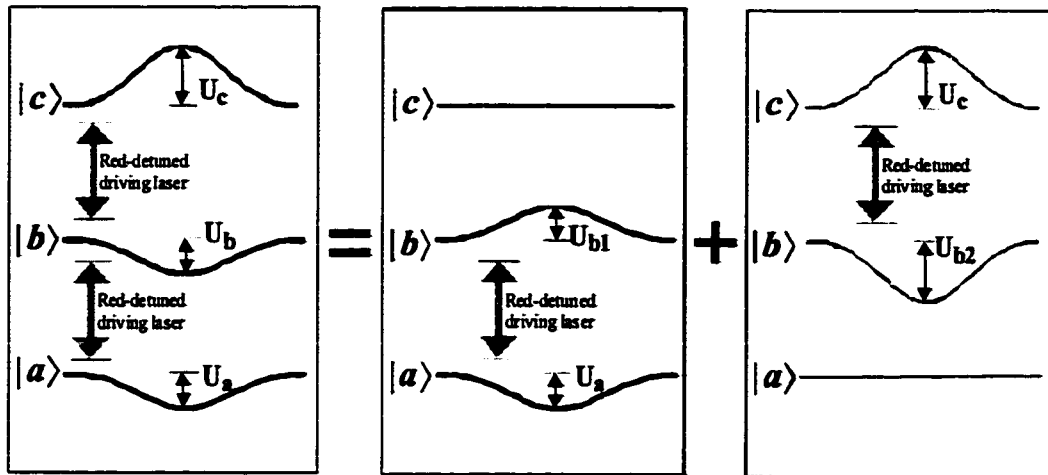


Figure 6.1: By utilizing an additional level $|c\rangle$, the AC Stark shifts of ground state $|a\rangle$ and excited state $|b\rangle$ can be made the same.

potential *confining*, it is required that $\Delta_{ab} > \Delta_{bc}$ (since $\Gamma_b \simeq \Gamma_c$), which leads to the requirement that $\lambda > \lambda_{bc} > \lambda_{ab}$ for a red-detuned trap in which levels $|a\rangle$ and $|b\rangle$ are both *confining* potentials. Conversely, to construct a blue-detuned trap in which $|a\rangle$ and $|b\rangle$ both feel repulsive potentials, the analogous requirement is $\lambda < \lambda_{bc} < \lambda_{ab}$. From here forward, I will only consider the case of a red-detuned driving field, as this will be the case applicable to our Cesium system.

One particular choice of the driving wavelength λ will balance the light shifts, such that $U_a = U_b$. This will be the case of interest for spectroscopic applications - since the transition frequency ω_{ab} is then unchanged by the presence of the trapping laser, which now confines atoms in both the ground and excited states. It should be noted that for a given atom (with fixed the Γ 's and transition wavelengths) this cancellation depends only on the driving wavelength λ , and is independent of driving intensity, so that an arbitrarily deep trap can be made while still inducing no shift to the atomic transition frequency. (Errors in finding the correct wavelength λ to balance the light shifts will have a larger effect at high intensity, which could be used as a “fine-tuning” of the choice of λ).

Other choices of driving wavelength can make the potential of the upper state more

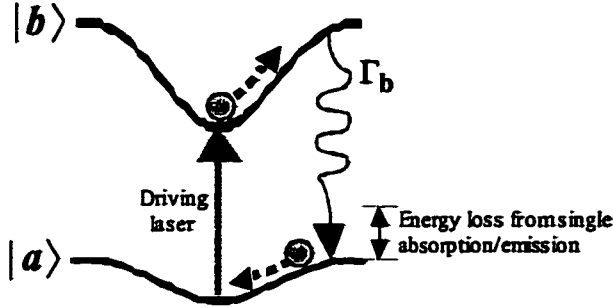


Figure 6.2: Sisyphus cooling scheme.

tightly confining than that of the lower state. In this case, a very efficient Sisyphus cooling mechanism [103] can be realized, the basic idea of which is illustrated in Figure 6.2. An additional laser is tuned to the $|a\rangle \rightarrow |b\rangle$ transition when the atom is at the center of the trap. If the secular frequency of oscillation in the trap is similar to the atomic spontaneous emission rate Γ_b , then the atom will tend to absorb at the center of the trap, then emit when at the edges of the potential. The energy loss per emission event is then given by the difference in potentials at this spatial position, which could be as large as $\sim 1\text{GHz}$. With secular frequencies on the order of MHz, this will provide very fast cooling.

6.1.2 Theory with polarizations and hyperfine sublevels

To implement this scheme in a real atom (such as Cesium in our case), we wish to extend this simple treatment to include effects of polarization, and to allow for fine and hyperfine structure within the atomic levels [101].

To calculate the polarization dependent light shifts for individual $|F m_F\rangle$ sublevels, I follow the treatment of Deutsch & Jessen [104], which gives a very formal derivation of light shifts and coherences between magnetic sublevels, with particular regard to optical lattices. The light shifts now have an additional contribution due to the strength of angular momentum coupling between different $|F m_F\rangle$ sublevels.

In the absence of magnetic fields, the potential for atoms in the ground state is

determined by the operator $\hat{U}(x) = -\mathbf{E}_L^*(x) \cdot \hat{\alpha} \cdot \mathbf{E}_L(x)$, where $\mathbf{E}_L(x)$ is the spatially varying electric field, and $\hat{\alpha}$ the atomic polarizability tensor operator. The light shift of a particular $|F, m\rangle$ sublevel will then be given by the expectation value $U(x) = \langle F, m | \hat{U}(x) | F, m \rangle$. In a spherical basis for the electric field, we can write $\hat{U}(x) = E_q^*(x) \mathbf{e}_{q'}^* \cdot \hat{\alpha} \cdot \mathbf{e}_q E_q(x)$. Deutsch & Jessen [104] show that for an atom having a multiplet of hyperfine excited states, the components of the atomic polarizability tensor in this spherical basis are given (in the limit of detunings \gg hyperfine splitting) by

$$\hat{\alpha}_{q,q'} = \mathbf{e}_{q'}^* \cdot \hat{\alpha} \cdot \mathbf{e}_q = \bar{\alpha} \sum_{F'} f_{F'F} \sum_m c_{F,m+q-q'}^{F',m+q} c_{F,m}^{F',m+q} \times |F, m + q - q'\rangle \langle F, m| . \quad (6.1)$$

This expresses couplings between ground states within the same F manifold, that is, between $|F, m\rangle$ and $|F, m + q - q'\rangle$, via intermediate excited states $|F', m + q\rangle$. Here, $f_{F'F}$ are the oscillator strengths for decay $F' \rightarrow F$, given in terms of 6J symbols by

$$f_{F'F} = (2J' + 1)(2F + 1) \left| \left\{ \begin{array}{ccc} F' & I & J' \\ J & 1 & F \end{array} \right\} \right|^2 , \quad (6.2)$$

$c_{F,m}^{F',m'}$ is the Clebsch-Gordan coefficient for the $|F, m\rangle$ to $|F', m'\rangle$ transition, and $\bar{\alpha}$ is a reduced (scalar) polarizability given by

$$\bar{\alpha} = \frac{|\langle J' \| d \| J \rangle|^2}{\hbar \Delta} , \quad (6.3)$$

with $\langle J' \| d \| J \rangle$ the reduced matrix element for the $J \rightarrow J'$ transition.

As we only wish to calculate level shifts (and not coherences between sublevels), we only need the $q' = q$ components, so Eq. 6.1 simplifies to

$$\hat{\alpha}_{q,q} = \bar{\alpha} \sum_{F'} f_{F'F} \sum_m (c_{F,m}^{F',m+q})^2 \times |F, m\rangle \langle F, m| . \quad (6.4)$$

Finally, calculating the light shift on a particular $|F, m\rangle$ ground state sublevel for a particular polarization q , the result is then a sum of coupling probabilities to all possible $|J', F', m+q\rangle$ excited states, scaled by their detunings Δ and reduced matrix

elements $|\langle J' \| d \| J \rangle|^2$. That is,

$$U(x) = |E_L(x)|^2 \sum_{J'} \frac{|\langle J' \| d \| J \rangle|^2}{\hbar \Delta_{J'J}} \sum_{F'} (2J'+1)(2F+1) \left| \begin{Bmatrix} F' & I & J' \\ J & 1 & F \end{Bmatrix} \right|^2 (c_{F,m}^{F',m+q})^2. \quad (6.5)$$

When calculating this sum for a particular *excited* state $|F m\rangle$ (this would be state $|b\rangle$ in Section 6.1.1), remember that shifts due to coupling to ground states $|a\rangle$ get an additional minus sign, while shifts due to coupling to higher lying states $|c\rangle$ follow Eq. 6.5.

6.1.3 Cesium parameters

In atomic cesium, the $\{|a\rangle, |b\rangle, |c\rangle\}$ ladder can be realized using the $\{6S_{1/2}, 6P_{3/2}, 6D_{5/2}\}$ set of atomic levels. As $\lambda(6S_{1/2} \rightarrow 6P_{3/2})=852\text{nm}$ and $\lambda(6P_{3/2} \rightarrow 6D_{5/2})=917\text{nm}$, then for some choice of $\lambda > 917\text{nm}$ we will be able to construct a red-detuned trap in which the light shift of the $6P_{3/2}$ level cancels, as this set of wavelengths satisfies the condition $\lambda > \lambda_{bc} > \lambda_{ab}$. For the general case of arbitrary polarization and initial magnetic sublevel, other transitions also need to be taken into account. The ground state $|a\rangle = 6S_{1/2}$ can couple to the $6P_{1/2}$ state (894.6nm), and the excited state $|b\rangle = 6P_{3/2}$ can couple to the $6D_{3/2}$ (921.1nm) and $8S_{1/2}$ (794.6nm) levels. Figure 6.3 shows a level diagram for Cesium, marking these transitions. For the red-detuned traps explored here with $\lambda > 917\text{nm}$, coupling to the $8S_{1/2}$ has a negligible effect.

In order to apply this formalism to the particular case of Cesium one critical element was to track down the best known numbers for the oscillator strengths of the relevant Cesium transitions. The $6P_{1/2}$ and $6P_{3/2}$ levels are extensively measured and calculated, largely motivated by precision measurements of parity non-conservation using these transitions [105]. Many other quantities are not measured at all but have been calculated - below are the best values I could locate.

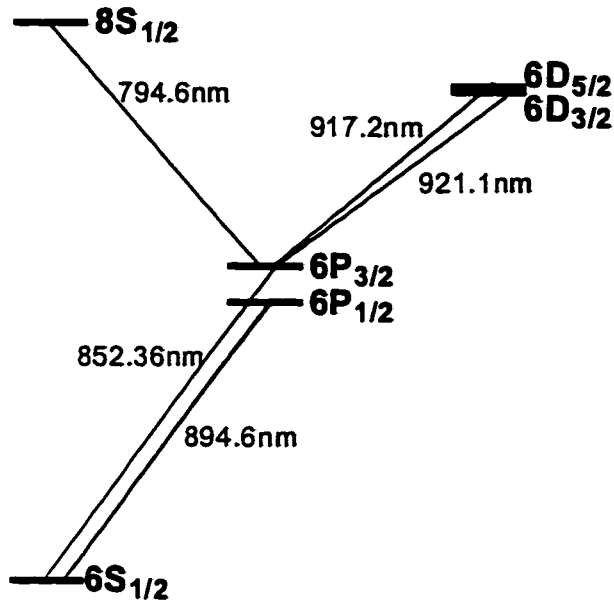


Figure 6.3: Transitions in atom Cesium. We consider light shifts to the $6S_{1/2}$ and $6P_{3/2}$ levels, so only transitions involving these particular levels are shown.

Lifetimes:

Rafac, Tanner et al.[106][107] measured the Cesium $6P_{1/2}$ and $6P_{3/2}$ lifetimes as $35.07(0.1)$ ns and $30.57(0.07)$ ns respectively, motivated to such accuracy by PNC experiments. Unfortunately, the D levels haven't been measured as accurately, with the only result by Georgiades et al., which gave 51.3 ± 3 ns for the $6D_{5/2}$ level [108]. As a result, for the D levels I decided to use some very good theory work by Theodosiou [109] instead. I presume this theory is good for the 6D levels, because in 1998 Berardino, Tanner and Sieradzan [110] made accurate measurements of the 5D levels, and Theodosiou's theory agreed very well (better than 0.5%) with these values. Theodosiou gives 58.14 ns for the $6D_{3/2}$ and 58.38 ns for the $6D_{5/2}$.

6P _{1/2}	35.07ns (expt)
6P _{3/2}	30.57ns (expt)
6D _{3/2}	58.14ns (theory)
6D _{5/2}	58.38ns (theory)

Table 6.1: Lifetimes of relevant atomic Cesium levels used in the dipole-trap calculations.

Reduced matrix elements:

The reduced matrix elements for each of the transitions can be derived from the above lifetimes. First note that for a single decay channel, the relationship is given by

$$\gamma_{J'J} = \frac{4\hbar}{3} \left(\frac{2\pi}{\lambda} \right)^3 \left[\frac{\langle J' | d | J \rangle}{\sqrt{2J'+1}} a_0 \frac{q}{4\pi\epsilon_0} \right]^2 , \quad (6.6)$$

where a_0 is the Bohr radius, J' is the spin of the *upper* state, and the lifetime = $1/\gamma$. This directly gives the 6P_{1/2}, 6P_{3/2} and 6D_{5/2} matrix elements to be 4.498, 6.331 and 6.24. The 6D_{3/2} has decays to both the 6P_{1/2} and 6P_{3/2}, so

$$\frac{1}{\text{lifetime}} = \frac{4\hbar}{3} \left(\frac{2\pi}{\lambda_1} \right)^3 \left[\frac{\langle J' | d | J \rangle_1}{\sqrt{2J'+1}} a_0 \frac{q}{4\pi\epsilon_0} \right]^2 + \frac{4\hbar}{3} \left(\frac{2\pi}{\lambda_2} \right)^3 \left[\frac{\langle J' | d | J \rangle_2}{\sqrt{2J'+1}} a_0 \frac{q}{4\pi\epsilon_0} \right]^2 . \quad (6.7)$$

Unfortunately, the actual matrix elements used in Theodosiou's calculations are not presented - so I have derived a guess at them from the oscillator strengths quoted in the next section.

Oscillator strengths:

The "oscillator strength" of a transition is the ratio of the transition rate to that of the corresponding classical electron oscillator, and is just a convenient dimensionless way of characterizing transitions. From Cohen-Tannoudji *Atom – Photon Interactions* [111], and Siegman *Lasers* [112] we see that:

$$f_{J'J} = \frac{2m\omega_0}{\hbar} \left[\frac{\langle J' | d | J \rangle}{\sqrt{2J'+1}} a_0 \right]^2 \text{ defined for a downgoing transition, and}$$

$$f_{J,J'} = \frac{2m\omega_0}{\hbar} \left[\frac{\langle J' | d | J \rangle}{\sqrt{2J'+1}} a_0 \right]^2 \frac{2J'+1}{2J+1} \text{ defined for an upgoing transition.}$$

Often the degeneracy factor is omitted in definitions, which can be confusing.

Laplanche et al. [113] calculated these oscillator strengths for Cesium. Comparing the matrix elements derived from these oscillator strengths to those obtained from the lifetimes, they're the same to better than 5%, but the Laplanche matrix elements are consistently smaller (see Table below).

Working out the $D_{3/2}$ lifetime from Laplanche's matrix elements gives 62ns, higher than the 58ns of Theodosiou's theory. That is, the Laplanche matrix elements are also too small for the $6P_{3/2} \rightarrow 6D_{3/2}$ transition, by a similar factor to those of the $6P_{3/2} \rightarrow 6D_{5/2}$ transition, a factor of $6.24/6.08=1.026$ (see Table 6.2).

So, I chose to scale Laplanche's matrix element values for the $D_{3/2}$ transitions up by 1.026. These new matrix elements give a $D_{3/2}$ lifetime of 59ns, more consistent but somewhat arbitrary. These numbers for the $D_{3/2}$ should be treated as around 5% accurate.

Note that Liaw's calculations [114] give very good agreement with experiment for the S→P transitions.

Transition:	λ	$\langle J' \ d \ J \rangle$	used:	Laplanche osc. str.
$6S_{1/2}$ to $6P_{1/2}$	894.6nm	4.498 (from lifetime)	.335 → m.el.=4.44	
$6S_{1/2}$ to $6P_{3/2}$	852.36nm	6.331 (from lifetime)	.700 → m.el.=6.27	
$6P_{1/2}$ to $6D_{3/2}$	876.4nm	4.31 (from osc. str.)	.306 → m.el.=4.2	
$6P_{3/2}$ to $6D_{3/2}$	921.1nm	2.11 (from osc. str.)	.035 → m.el.=2.06	
$6P_{3/2}$ to $6D_{5/2}$	917.2nm	6.24 (from lifetime)	.306 → m.el.=6.08	

Table 6.2: Summary of Matrix Elements used in the dipole-trap calculation.

Clebsch Gordan coefficients:

Clebsch-Gordan coefficients and 6J symbols are most easily found using the built-in functions "ClebschGordan" and "SixJSymbol" in Mathematica.

6.1.4 Results for a cesium trap in an optical resonator

To examine the potential use of this idea in our cavity QED experiments, I next calculate the magnitude of light shift obtained for an experimentally realizable system - a standing wave trap inside an optical cavity.

In our recent cavity QED experiments we have chosen to drive the atom-cavity system with circularly polarized light, optically pumping the atom into the cycling $6S_{1/2}, F=4, m_F=4 \rightarrow 6P_{3/2}, F=5, m_F=5$ transition at 852nm. All of the calculations to follow will be for these particular magnetic sublevels. That is, we chose the “ground state” $|a\rangle = |6S_{1/2}, F=4, m_F=4\rangle$ and the “excited state” $|b\rangle = |6P_{3/2}, F=5, m_F=5\rangle$, and calculate modifications to the AC Stark shift of these levels when coupling to other transitions is considered.

Fields inside an optical resonator

Returning to Eq. 6.5, it remains to express the laser field $|E_L(x)|^2$ in a more experimentally useful form. As the dipole trap in question is going to be made inside an optical cavity, the cavity finesse can be used to build up a high peak intensity (and hence deep trap) with a fairly weak input laser.

One way to express the field is in terms of a Rabi frequency associated with the intracavity photon number. This gives an obvious link to our cavity QED parameters, as $2g$ is the Rabi frequency corresponding to 1 photon. For N intracavity photons, there is an intracavity energy $Energy_{in} = N\hbar\omega_0$, and a corresponding Rabi frequency

$$\Omega_{J'} = d \cdot E = \left(\frac{\langle J' | d | J \rangle}{\sqrt{2J'+1}} * a_0 * q \right) * \frac{2}{\hbar} \sqrt{\frac{Energy_{in}}{2\varepsilon_0 V_m}}, \quad (6.8)$$

for a transition $J \rightarrow J'$ with Clebsch-Gordan coefficient = 1. The electric field E has been incorporated via the intracavity energy density $\frac{Energy_{in}}{V_m} \propto |E|^2$, with V_m the cavity mode volume. For a symmetric cavity driven on resonance, $Energy_{in}$ is determined by the input power P_{in} , cavity decay rate κ and mirror losses. For a known cavity, we can then express Ω entirely by means of the power of an input beam to the cavity. Allowing for saturation behavior (with large Ω), the AC Stark shift of level $|J F m\rangle$ is given by:

$$U = \sum_{J'} \frac{\hbar\Delta_{J'J}}{2} \ln \left[1 + \frac{\Omega_{J'}^2/2}{\Delta_{J'J}^2 + (\gamma_{J'J}/2)^2} \right] \quad (6.9)$$

$$\times \sum_{F'} (2J' + 1)(2F + 1) \left| \begin{Bmatrix} F' & I & J' \\ J & 1 & F \end{Bmatrix} \right|^2 (c_{F,m}^{F',m+q})^2 ,$$

where all possible couplings to states $|J' F' m + q\rangle$ are summed. Here $\Delta_{J',J}$ is the detuning of the driving laser from the $J \rightarrow J'$ atomic resonance, $\gamma_{J',J}$ the linewidth of this transition, and the angular momentum couplings have been taken directly from Eq. 6.5. If the driving field is weak this reduces to: $U = \frac{\hbar\Omega^2}{4} \frac{\Delta}{\Delta^2 + (\gamma/2)^2}$, and for large detunings this becomes the familiar $U = \frac{\hbar\Omega^2}{4\Delta}$.

The magnitude of the shifts depends on the peak intracavity intensity, that is, the power of the input laser field and the cavity Finesse (which determines κ). From the calculations of Chapter 5, I estimate that our cavity mirrors (transmission 4.6ppm at 852nm, finesse $\mathcal{F}=480,000$) have $\mathcal{F} \approx 3000$ at 920nm, and $\mathcal{F} \approx 1000$ at 950nm. The calculated level shifts below do not take into account this variation of finesse with drive wavelength, assuming a fixed finesse.

Resulting level shifts for σ^+ circular polarization

For a σ^+ polarized driving laser, the $|S_{1/2}44\rangle$ ground state can only couple to $m_F=5$ sublevels, so coupling to $|P_{3/2}55\rangle$ (the excited state) is the only contribution, and the level shift is as for a 2-level system. The $|P_{3/2}55\rangle$ excited state can couple both to $|S_{1/2}44\rangle$ and $|D_{5/2}66\rangle$ however, so it experiences modification in its light shift. Figures 6.4,6.5 show the ground state shift (dotted) and excited state shift (solid) as a function of wavelength of the dipole-trap laser, with Figure 6.5 zoomed in to the region 930–960nm to show the wavelength (≈ 952 nm) at which the level shifts are equal.

In the calculation shown, a 1mW laser resonant with a 1000 finesse cavity gives a trapping potential 40MHz deep at the balancing point of 952nm. The potential could be made deeper by increasing the input laser power, or using mirrors that give a higher finesse at this wavelength.

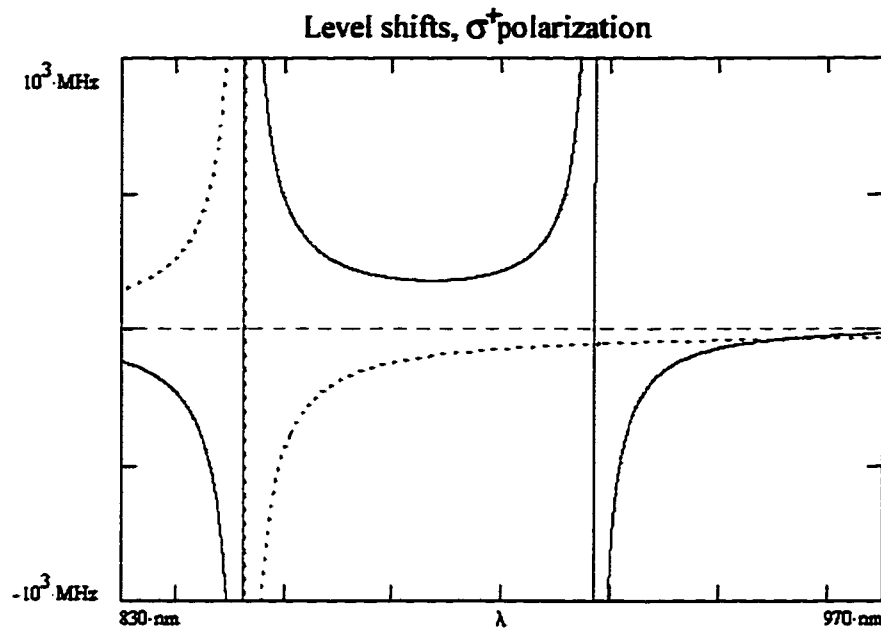


Figure 6.4: Shifts of the Cs $6S_{1/2}$, $F = 4, M = 4$ (dotted) and $6P_{3/2}$, $F = 5, M = 5$ (solid) levels, as a function of wavelength of an applied σ^+ polarized laser field.

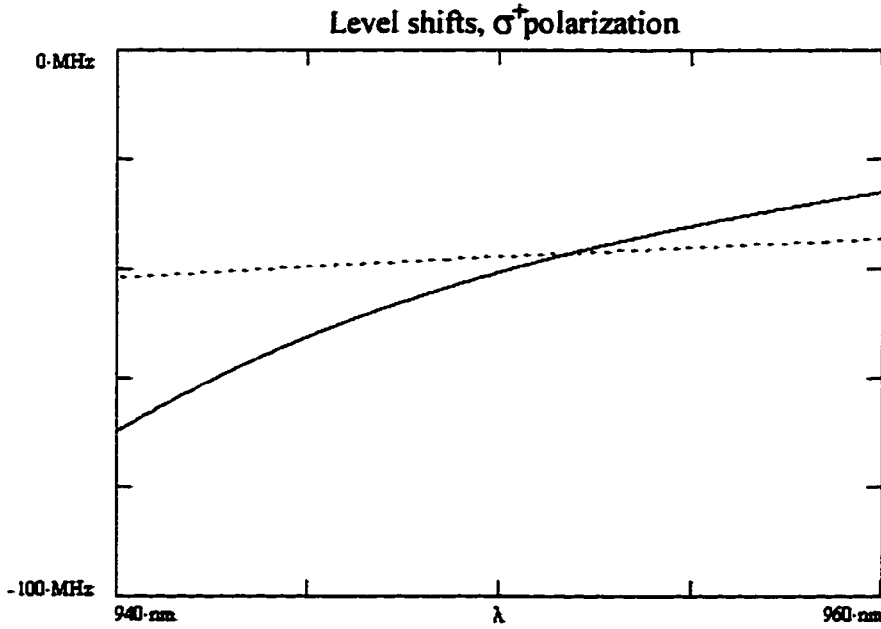


Figure 6.5: Shifts of the Cs $6S_{1/2}$, $F = 4, M = 4$ (dotted) and $6P_{3/2}$, $F = 5, M = 5$ (solid) levels, as a function of wavelength of an applied σ^+ polarized laser field (Expanded View).

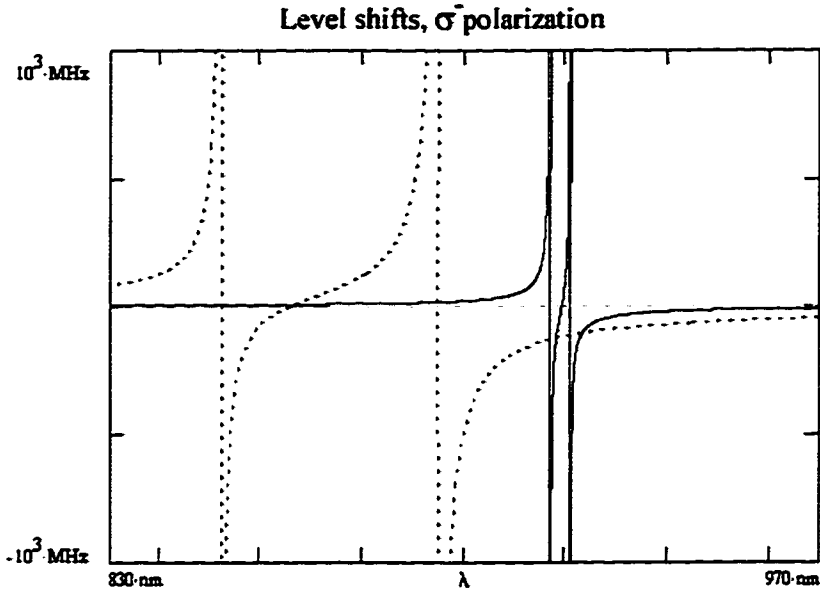


Figure 6.6: Shifts of the Cs $6S_{1/2}$, $F = 4, M = 4$ (dotted) and $6P_{3/2}$, $F = 5, M = 5$ (solid) levels, as a function of wavelength of an applied σ^- polarized laser field.

Resulting level shifts for σ^- polarization

For σ^- polarization, the $|S_{1/2}44\rangle$ ground state can now couple to $m_F=3$ sublevels, so contributions arise from coupling to levels $|P_{3/2}53\rangle, |P_{3/2}43\rangle, |P_{3/2}33\rangle$ at 852nm, and $|P_{1/2}43\rangle, |P_{1/2}33\rangle$ at 894nm. The excited state $|P_{3/2}55\rangle$ cannot couple to the ground state with this polarization, but does couple to $|D_{5/2}64\rangle, |D_{5/2}54\rangle, |D_{5/2}44\rangle$ at 917nm and $|D_{3/2}54\rangle, |D_{3/2}44\rangle$ at 921nm. Since a completely new set of wavelengths have been introduced to the coupling scheme, the level shifts are now qualitatively different, shown for σ^- polarization in Figures 6.6 and 6.7. Again, the ground state shift (dotted) and excited state shift (solid) are equal at some wavelength - here it is $\approx 923\text{nm}$. This calculation is for a 1mW laser resonant with a 1000 finesse cavity, and gives a trapping potential 100MHz deep at the balancing point of 923nm.

Tuning the potential with polarization

Given the marked differences in the potentials for σ^+ and σ^- polarizations, it should be possible to *tune* the potential by applying an intermediate (elliptical or linear)

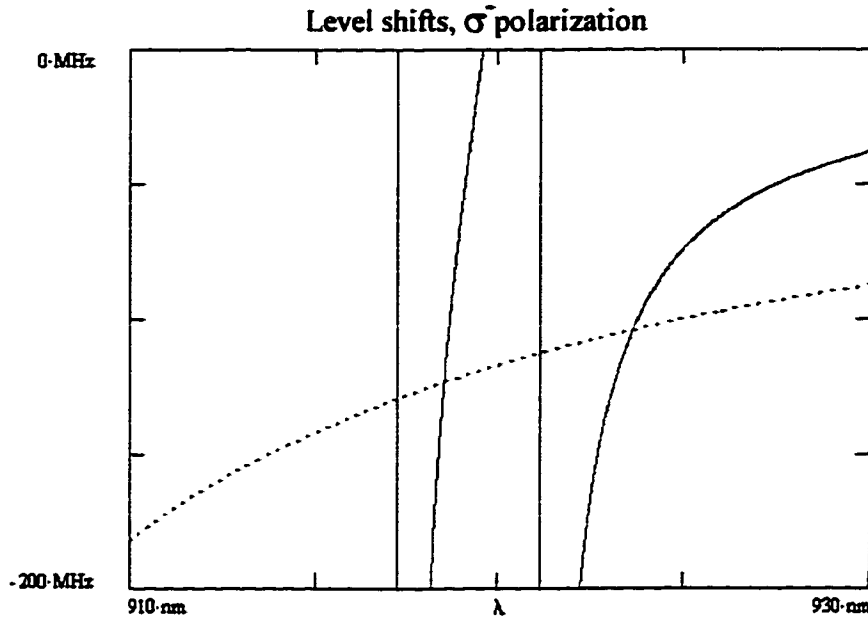


Figure 6.7: Shifts of the Cs $6S_{1/2}$, $F = 4, M = 4$ (dotted) and $6P_{3/2}$, $F = 5, M = 5$ (solid) levels, as a function of wavelength of an applied σ^- polarized laser field (Expanded View).

polarization which can be written as a sum of σ^+ and σ^- . This will be particularly important when integrating this trap into a cavity QED setup, where the cavity length is locked to be resonant with the 852nm transition. Given that the free-spectral range of our cavities is large (up to 30 nm), typically only one or two cavity resonances fall in the 920-960nm range, and, to provide good overlap between the dipole-trap and cavity QED field at the center of the cavity mode, the wavelength chosen must be an even number of cavity orders detuned from the 852nm laser. While the wavelength of the dipole-trap will therefore be fixed by the cavity length, tuning of the potentials to balance the AC Stark shifts could be accomplished by changing the input polarization of the dipole-trap laser.

Note that this introduces a new constraint on the trapping laser: fluctuations in polarization will lead to strong changes in the trapping potential, so for a stable trap both intensity and polarization will need to be controlled precisely.

Spin polarization lifetimes and trap heating rates

For a simple two-level system, the photon scattering rate is related to the optical potential by the relation

$$\Gamma_{sc} = \frac{\Gamma}{\Delta} \frac{U}{\hbar}. \quad (6.10)$$

Considering only the $6S_{1/2}, F=4, m_F=4 \rightarrow 6P_{3/2}, F=5, m_F=5$ transition at 852nm, and a dipole-trap laser at 950nm, a well depth of 40MHz gives a photon scattering rate $\Gamma_{sc} \simeq 2\pi \times 5.7\text{Hz}$, or a single photon scatter every 28ms. When driving with σ^- polarization, these single photon scattering events can optically pump the atom out of its initial $|S_{1/2}44\rangle$ magnetic sublevel, at which point the polarization-dependent potentials derived above would no longer apply. Additionally, this optical pumping between potentials of different depths would cause additional heating of the atomic motion, as observed in Ref. [102].

That this spin polarization lifetime is much shorter than the trap lifetime would seriously degrade the usefulness of this polarization-dependent trapping scheme. However, fortunately when multiple atomic levels are again considered, there is a cancellation which greatly enhances the spin polarization lifetime [115]. For a laser detuning comparable with or larger than the splitting between D1 ($P_{1/2}$) and D2 ($P_{3/2}$) lines, any particular photon scattering event between ground state sublevels $|Fm\rangle$ and $|F''m''\rangle$ can occur through the $P_{1/2}$ or $P_{3/2}$ lines, so the amplitudes for these need to be added, which from [115] gives

$$\Gamma_{sc} = \frac{3\pi c^2 \omega_L^3 I(r)}{2\hbar} \left| \frac{\Gamma_{1/2}}{\omega_{1/2}^3 \Delta_{1/2}} \alpha_{FM \rightarrow F''M''}^{(1/2)} + \frac{\Gamma_{3/2}}{\omega_{3/2}^3 \Delta_{3/2}} \alpha_{FM \rightarrow F''M''}^{(3/2)} \right|^2. \quad (6.11)$$

For $FM \neq F''M''$ (Raman scattering) it can be shown that $\alpha_{FM \rightarrow F''M''}^{(3/2)} = -\alpha_{FM \rightarrow F''M''}^{(1/2)}$, so that except for the difference in detunings there would be an exact cancellation, and including detunings Raman scattering will be suppressed by a factor of

$$\frac{\left| \frac{\Gamma_{1/2}}{\omega_{1/2}^3 \Delta_{1/2}} - \frac{\Gamma_{3/2}}{\omega_{3/2}^3 \Delta_{3/2}} \right|^2}{\left| \frac{\Gamma_{1/2}}{\omega_{1/2}^3 \Delta_{1/2}} \right|^2}. \quad (6.12)$$

For $FM = F''M''$ (Rayleigh scattering) $\alpha_{FM \rightarrow F''M''}^{(3/2)} = \alpha_{FM \rightarrow F''M''}^{(1/2)}$, so that the predominant scattering (at rate $\sim 1/\Delta^2$) will be Rayleigh scattering which returns the atom to the same magnetic sublevel and maintains the spin polarization.

At laser wavelengths of 920nm-950nm the detunings $\Delta_{1/2}$ and $\Delta_{3/2}$ are quite different, so that there is only a partial cancellation, giving a suppression of scattering by a factor of 0.22 at 950nm, and 0.43 at 920nm. This means that the spin polarization lifetime will be slightly enhanced in our experiment to $\sim 127\text{ms}$ at 950nm and $\sim 65\text{ms}$ at 920nm.

6.2 Photon statistics of a single, strongly coupled atom.

In a regime of strong coupling $g_0 > (\gamma, \kappa)$, for which single quanta (atoms or photons) play an important role in the *dynamics* of the cavity QED system, it is not surprising that the output cavity field can have interesting quantum statistical properties. In this section, we consider the correlation function $g^{(2)}(\tau) = \langle : \hat{I}(t)\hat{I}(t+\tau) : \rangle / \langle \hat{I} \rangle^2 = \langle \hat{a}(t)^\dagger \hat{a}(t+\tau)^\dagger \hat{a}(t+\tau) \hat{a} \rangle / \langle \hat{a}^\dagger \hat{a} \rangle^2$ for the intensity \hat{I} of the output cavity field.

For a Poisson stream of photons (a coherent state) $g^{(2)}(\tau) \equiv 1$, that is, there is no correlation in the arrival times of detected pairs of photons. In our strongly coupled atom-cavity system both sub-Poissonian statistics ($g^{(2)}(0) < 1$) and photon antibunching ($g^{(2)}(0) < g^{(2)}(\tau)$) are present. A value of $g^{(2)}(0) < 1$ is manifestly non-classical, and is a signature that the field is interacting with a two-level system. One example is resonance fluorescence from a single closed atomic transition: having absorbed a photon the atom can only re-emit on timescale γ^{-1} , thus a second photon cannot also be emitted within this time window, so the fluorescence photons gener-

ated are antibunched and sub-Poissonian. In the cavity QED system, the transition between the system ground state $|0, 0\rangle$ and lower dressed state $|-\rangle$ can be employed to form an effective two-level system in a similar way [116]. For certain choices of driving/detunings of the atom-cavity the field can also be “bunched,” characterized by $g^{(2)}(0) > 1$.

Nonclassical photon statistics have been observed experimentally in cavity QED for an ensemble of atoms in an atomic beam [58, 59, 12, 60] or a MOT [61], but to date photon statistics from an individual atom in a cavity have not been measured, primarily because single atoms have not been trapped in cavities until recently [28, 27]. In this section I calculate $g^{(2)}(\tau)$ for our current experimental parameters.

In the weak-field limit, the master equation can be solved exactly to find a solution for the atom-cavity density matrix ρ , and hence an analytic expression found for $g^{(2)}(\tau)$ [117]. This derivation is based on the assumption that the field is weak enough that only $|atom, field\rangle = \{|0, 0\rangle, |1, 0\rangle, |0, 1\rangle, |1, 1\rangle, |0, 2\rangle, |2, 0\rangle\}$ contribute to ρ . Of course, the last term $|2, 0\rangle$ is only possible in the case $N>1$ atoms. In this restricted basis, the master equation can be solved exactly.

This derivation can be modified to account for detunings[118], in which case atom and cavity parameters become $\tilde{\kappa} \equiv \kappa(1 + i\theta)$ and $\tilde{\gamma}_{||} = \gamma_{||}(1 + i\Delta)$, where $\theta = (\omega_a - \omega_0)/\kappa$, $\Delta = 2(\omega_a - \omega_0)/\gamma_{||}$, and $\{\omega_a, \omega_c, \omega_0\}$ are the atomic, cavity and probe frequencies respectively. The solution for the second order intensity correlation function (for N atoms in the weak-field limit) is then:

$$g^{(2)}(\tau) = [1 + \frac{\Delta\tilde{\alpha}}{\tilde{\alpha}} \exp[-\frac{1}{2}(\tilde{\kappa} + \tilde{\gamma}_{||}/2)\tau] \times [\cosh\tilde{\Omega}\tau + \frac{(\tilde{\kappa} + \tilde{\gamma}_{||}/2)}{2\tilde{\Omega}} \sinh\tilde{\Omega}\tau]]^2, \quad (6.13)$$

where

$$\frac{\Delta\tilde{\alpha}}{\tilde{\alpha}} = -2\tilde{C}'_1[2\tilde{C}/(1 + 2\tilde{C} - 2\tilde{C}'_1)], \quad (6.14)$$

and

$$\tilde{\Omega} = \sqrt{(1/4)(\tilde{\kappa} - \tilde{\gamma}_{||}/2)^2 - Ng^2}. \quad (6.15)$$

with $\tilde{C}_1 = g_0^2/\bar{\kappa}\bar{\gamma}_{\parallel}$, $\tilde{C}'_1 = \tilde{C}_1/(1 + \bar{\gamma}_{\parallel}/2\bar{\kappa})$, and $\bar{C} = N\tilde{C}_1$.

Firstly, in the case $\omega_a = \omega_0 = \omega_c$, the result for $g^{(2)}(\tau)$ for $N=1$ atom is shown in Figure 6.8, where τ is shown in units of nanoseconds, and the calculation is for the experimental parameters $\{g_0, \kappa, \gamma_{\parallel}\}/2\pi = \{110, 14.2, 5.2\}$ MHz. The large value of $g^{(2)}(0) = 3 \times 10^6$ and subsequent strong oscillations at timescale g_0^{-1} can be understood in terms of an interference between the driving field, and the emitted field of the atomic dipole which is out of phase with the driving field. This cancellation of driving and emitted fields gives rise to the strong contrast $1/(1 + 2C)^2$ in transmission on resonance: an intracavity intensity of strength n corresponds to a driving intensity of strength $(1 + 2C)^2n$.

The trace of $g^{(2)}(\tau)$ in Figure 6.8 represents the probability of detecting a second photon at time delay τ conditioned on the detection of a first photon. At $\tau = 0$ a photon has just been detected, so the system's state is the corresponding collapsed state (by a quantum jumps formalism [117, 119]), and the associated “switching off” of the induced dipole field allows the driving field to pass through the cavity uncanceled, giving a huge increase in photon count rate and hence $g^{(2)}(0) \gg 1$.

While this argument is correct for the bad cavity limit ($\kappa \gg g_0 \gg \gamma$) in which the cavity field switches faster than g_0^{-1} , in the case of strong coupling the interference of fields is actually an infinite sum over successive emission and re-absorption events as the atom-cavity Rabi-flops at rate g_0 . The time evolution of this sum after a collapse (photon measurement) gives rise to the pronounced oscillations in $g^{(2)}(\tau)$.

The lower panel of Figure 6.8 shows the same curve with the axes zoomed in to show the first minimum, in the region $0 < g^{(2)}(\tau) < 2$. While strong sub-Poissonian statistics are exhibited at the minima, experimentally this would be prohibitively difficult to resolve for two reasons. Firstly, given the fast timescale of g_0^{-1} and sharp contrast in the signals, a time resolution of $\simeq 200$ fs would be required. Secondly, any tiny variation in coupling strength will change the position of the minima: If the atom were moving around the field antinode such that $g(\vec{r}) = g_0 \pm 1\%$, then averaging over the resulting time dependences means this first minimum would have a value of $g^{(2)}(\tau) \simeq 175$. A stability of $g(\vec{r}) \simeq g_0 \pm 0.05\%$ would be required to recover $g^{(2)}(\tau) < 1$

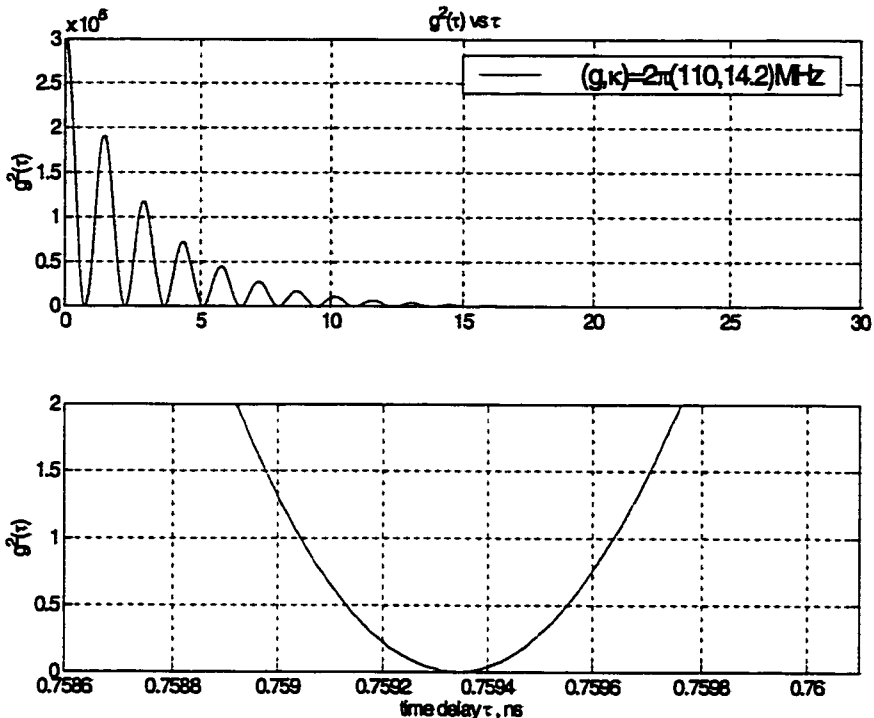


Figure 6.8: Second order intensity correlation function $g^{(2)}(\tau)$, calculated in the weak-field approximation for parameters $\{g_0, \kappa, \gamma_{||}\}/2\pi = \{110, 14.2, 5.2\}$ MHz, and no detunings ($\omega_a = \omega_0 = \omega_c$).

at the first minimum, which presently does not seem experimentally feasible.

Next, we switch the probe detuning to be tuned to the state $|-\rangle$, by choosing $\omega_c - \omega_0 = \omega_a - \omega_0 = g_0$. This situation is shown schematically by the black arrows of Figure 6.9. Because of the anharmonicity of the Jaynes-Cummings ladder of states, once the system has absorbed a single photon and been driven into the state $|-\rangle$, then a second photon cannot easily be absorbed because the transition from $|-\rangle$ to the $|2-\rangle$ (the lower dressed state of the 2-excitation manifold) is detuned from the driving frequency ω_0 . If the level anharmonicity is larger than the linewidths of the $|-\rangle$ and $|2-\rangle$ levels, then the $|2-\rangle$ state is rarely populated and the systems acts as an effective two-level system [116].

This detuning leads to strong antibunching $g^{(2)}(0) < 1$ of the output cavity field, as calculated in Figures 6.10 and 6.11. In Figure 6.10, the solid curve is for the experimental parameters $\{g_0, \kappa, \gamma_{||}\}/2\pi = \{110, 14.2, 5.2\}$ MHz, and the dotted curve

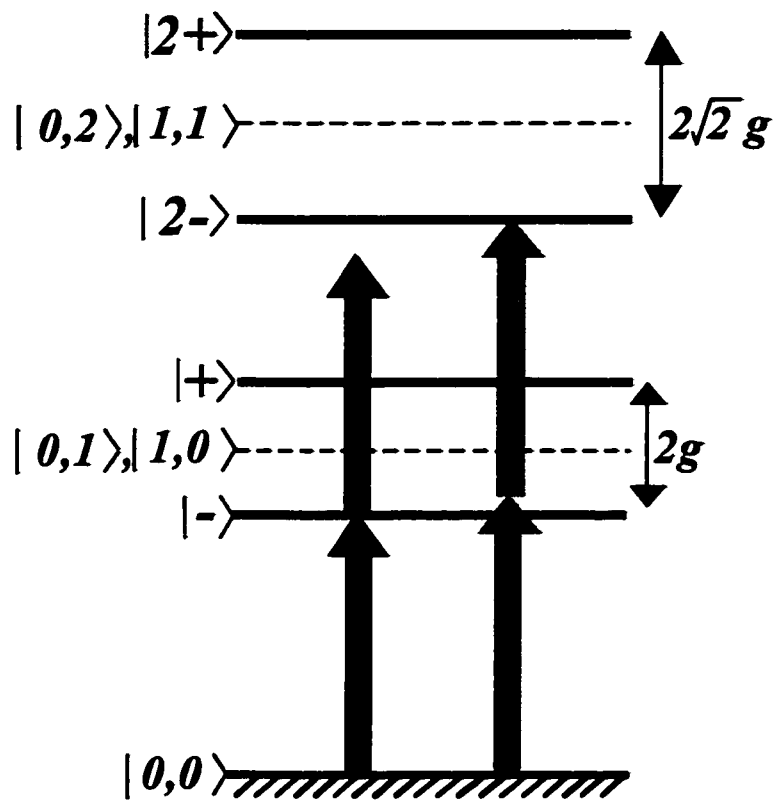


Figure 6.9: Level diagram showing the lowest states of the Jaynes-Cummings ladder for the atom-cavity system. When the probe frequency is tuned to the state $|-\rangle$ (black arrows) two-photon absorption is suppressed, and $g^{(2)}(0) < 1$. Conversely, for the probe frequency shown by the grey arrows, two-photon absorption is favored and $g^{(2)}(0) \gg 1$.

for a longer cavity constructed from the same mirrors, which at $80\mu\text{m}$ length has parameters $\{g_0, \kappa, \gamma_{||}\}/2\pi = \{25.3, 1.94, 5.2\}\text{MHz}$. The dashed curve is for the experimental parameters of Ref. [28], $\{g_0, \kappa, \gamma_{||}\}/2\pi = \{32, 4, 5.2\}\text{MHz}$. Note that the antibunching persists over a time $((\kappa + \gamma_{||})/2)^{-1}$. This is simply because once one photon is absorbed, it is difficult for a second to be absorbed until the first leaves, which happens in the characteristic decay time given by the inverse of the linewidth of the state $|-\rangle$, this linewidth being $((\kappa + \gamma_{||})/2)$ since $|-\rangle$ is an equal superposition of $|1, 0\rangle$ and $|0, 1\rangle$. This situation represents a “photon blockade” [120, 121]; that is, the presence of one photon in the cavity reduces the probability of admission of a second within this time window.

That $g^{(2)}(0) > 0$ indicates that there is some population of the $|2-\rangle$ state, since for our experimental parameters the linewidths of the states are not negligible. The ripples in $g^{(2)}(\tau)$ on timescale g_0^{-1} arise from Rabi oscillations between states $|+\rangle$ and $|-\rangle$; for the experimental linewidths, there is still a small probability of off-resonantly populating the state $|+\rangle$.

In Figure 6.11, the solid curve is calculated for the proposed $\lambda/2$ cavity with $\{g_0, \kappa, \gamma_{||}\}/2\pi = \{647, 56, 5.2\}\text{MHz}$ described in Section 5.3.5. A calculation for a longer ($30\lambda/2$) cavity constructed from the same mirrors is shown also by the dotted line. This longer cavity would have parameters $\{g_0, \kappa, \gamma_{||}\}/2\pi = \{79.7, 1.86, 5.2\}\text{MHz}$. These proposed cavities have smaller $g^{(2)}(0)$ since the single atom cooperativity C_1 is larger, and they also show fewer ripples on timescale g_0^{-1} as the ratio g_0/κ is higher giving better isolation from off-resonant driving of the state $|+\rangle$.

For the cavity detuning $\omega_a = \omega_c$ chosen here, the Jaynes-Cummings ladder of states is symmetric around a probe detuning of $\omega_0 = \omega_a = \omega_c$, so the same result of antibunching would be obtained by tuning the probe laser to the upper dressed state $|+\rangle$. Experimentally, driving state $|+\rangle$ would lead to heating of atoms, as this state spatially forms a repulsive potential. Conversely, the state $|-\rangle$ is trapping [25, 27], so driving at this frequency would help confine atoms while measuring photon statistics.

Turning now to a different set of detunings, we set the probe frequency to $\omega_c - \omega_0 = \omega_a - \omega_0 = g_0/\sqrt{2}$. As shown by the grey arrows of Figure 6.9, the one-photon transition

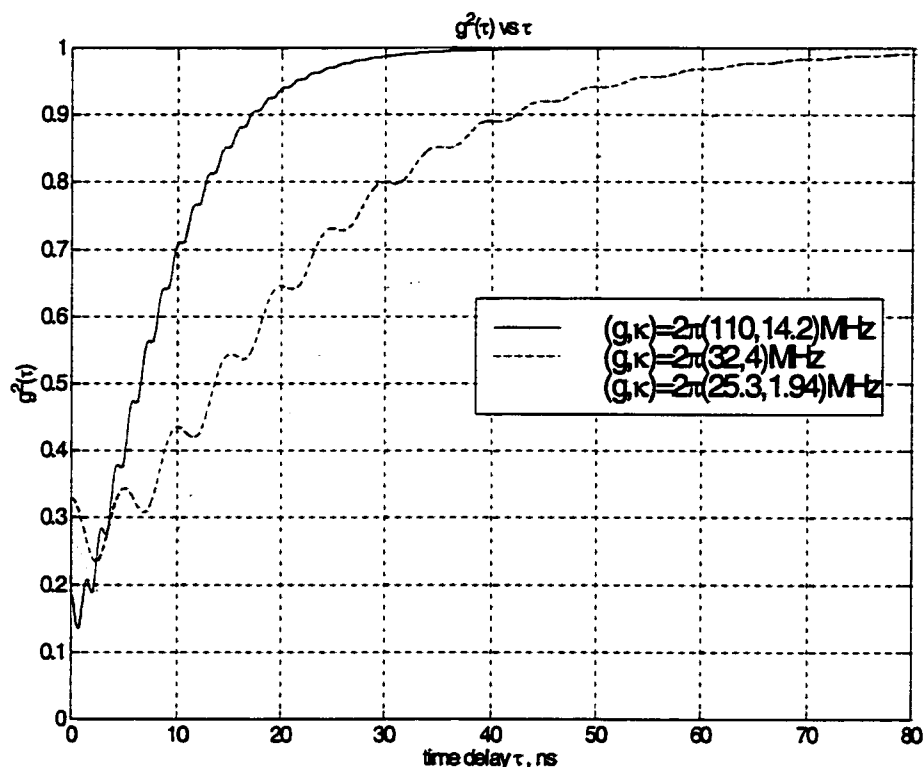


Figure 6.10: Second order intensity correlation function $g^{(2)}(\tau)$, calculated in the weak-field approximation for parameters $\{g_0, \kappa, \gamma_{||}\}/2\pi = \{110, 14.2, 5.2\}$ MHz (solid curve), $\{g_0, \kappa, \gamma_{||}\}/2\pi = \{32, 4, 5.2\}$ MHz (dashed curve) and $\{g_0, \kappa, \gamma_{||}\}/2\pi = \{25.3, 1.94, 5.2\}$ MHz (dotted curve), with the probe beam tuned to state $|-\rangle$, that is $\omega_c - \omega_0 = \omega_a - \omega_0 = g_0$.

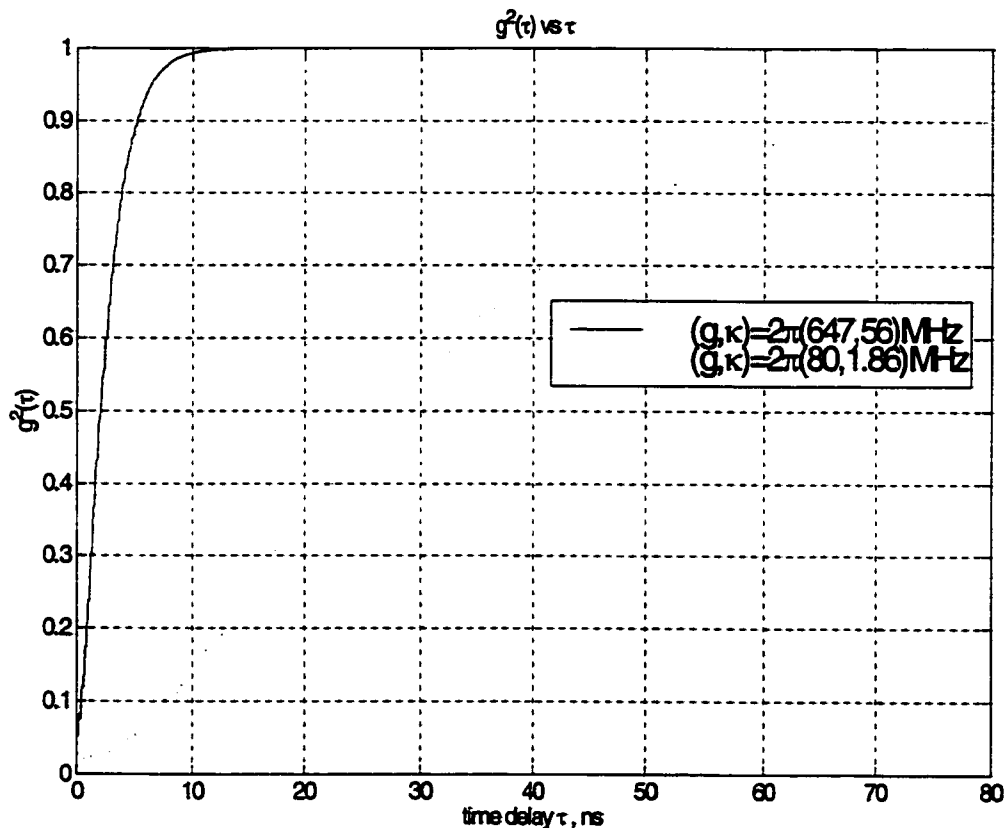


Figure 6.11: Second order intensity correlation function $g^{(2)}(\tau)$, calculated in the weak-field approximation, with the probe beam tuned to state $|-\rangle$, that is $\omega_c - \omega_0 = \omega_a - \omega_0 = g_0$. Ideal cavity parameters.

is now detuned from the state $|-\rangle$, suggesting that the probability of a $|0,0\rangle \rightarrow |-\rangle$ transition will be suppressed. However, the two-photon transition to the state $|2-\rangle$ is resonant, so when pairs of photons are incident on the cavity from the weak driving coherent field, it is likely that they will be absorbed. We would therefore expect the cavity output field to show strong *bunching* $g^{(2)}(\tau) >> 1$. This is borne out by the calculations shown in Figure 6.12, where again the solid curve is for the experimental parameters $\{g_0, \kappa, \gamma_{||}\}/2\pi = \{110, 14.2, 5.2\}$ MHz, and the dotted curve for a longer cavity with $\{g_0, \kappa, \gamma_{||}\}/2\pi = \{25.3, 1.94, 5.2\}$ MHz. Since at this detuning the probe field is closer to the state $|+\rangle$, Rabi oscillations due to population of this level are more pronounced here.

Summarizing these weak-field results is Figure 6.13, which shows $g^{(2)}(\tau)$ represented by a color scale, plotted vs probe detuning $\omega_a - \omega_0$ (scaled by g_0), for a fixed cavity detuning $\omega_c = \omega_a$, and the experimental parameters $\{g_0, \kappa, \gamma_{||}\}/2\pi = \{110, 14.2, 5.2\}$ MHz. Blue areas indicate $g^{(2)}(\tau) < 1$. Note that for easier display the red side of the color scale (where $g^{(2)}(\tau) > 0$) is drastically scaled logarithmically, while the blue side (where $g^{(2)}(\tau) < 0$) has a linear color scale. The time axis τ is scaled by $(\gamma_{||}/2)^{-1}$.

Several experimentally interesting features can be gleaned from this plot. Firstly, it can be seen that the level of antibunching for detunings $\simeq g_0$ is present over a large range of probe detunings. This means that in a realistic experiment (without an auxiliary locking laser as in Refs. [46, 28]), for which it is challenging to lock the laser and cavity frequencies to better than $\simeq 1$ MHz, the antibunching will still be observable. Secondly, there is a wide contrast between timescales of the on-resonant oscillations (at rate g_0), and antibunching (over timescale $((\kappa + \gamma_{||})/2)^{-1}$). For a photon counting experiment, detector dead-times limit time resolution to a few ns, so measurements at $((\kappa + \gamma_{||})/2)^{-1} \simeq 17$ ns are on the edge of being possible with a single detector, whereas measurements at $g_0^{-1} \simeq 1.4$ ns would be unfeasible without cascading several detectors. Improvements in mirror reflectivity to reduce κ , or alternatively to use longer cavities (sacrificing coupling strength g , but also decreasing κ) would clearly make this an easier experiment to perform. A broad region of antibunching can also

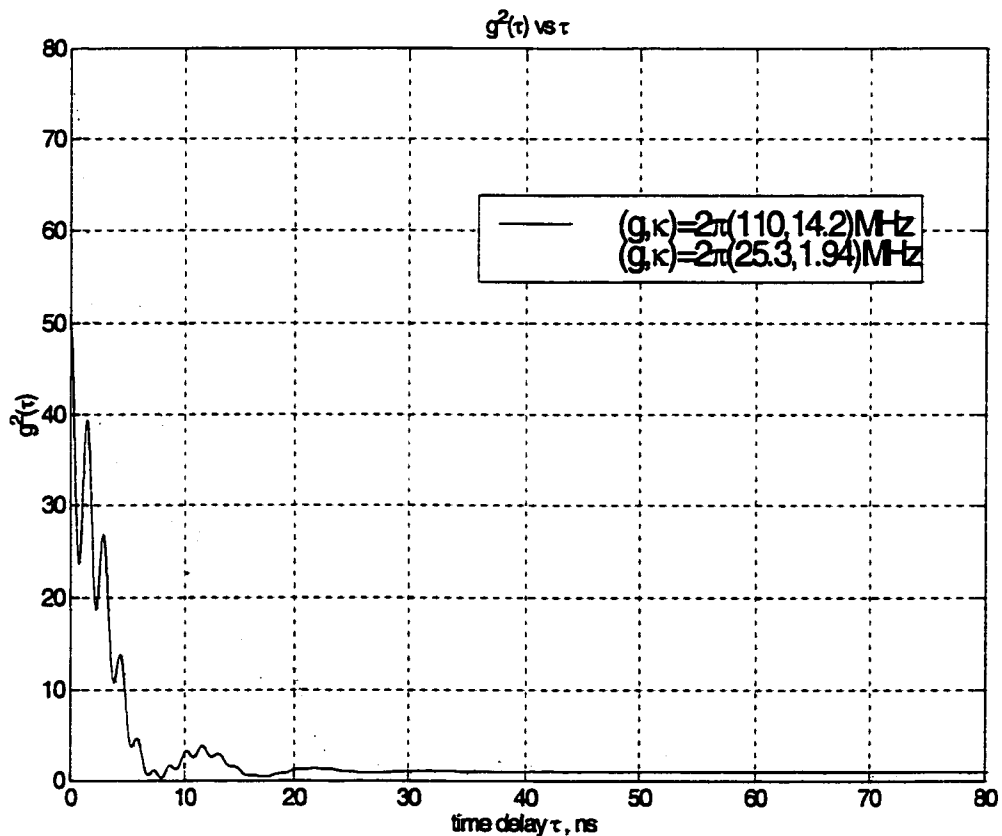


Figure 6.12: Second order intensity correlation function $g^{(2)}(\tau)$, calculated in the weak-field approximation, with the probe field tuned to be resonant with the two-photon transition to the state $|2-\rangle$, that is, $\omega_c - \omega_0 = \omega_a - \omega_0 = g_0/\sqrt{2}$. The solid curve is for $\{g_0, \kappa, \gamma_{\parallel}\}/2\pi = \{110, 14.2, 5.2\}$ MHz and the dotted for $\{g_0, \kappa, \gamma_{\parallel}\}/2\pi = \{25.3, 1.94, 5.2\}$ MHz.

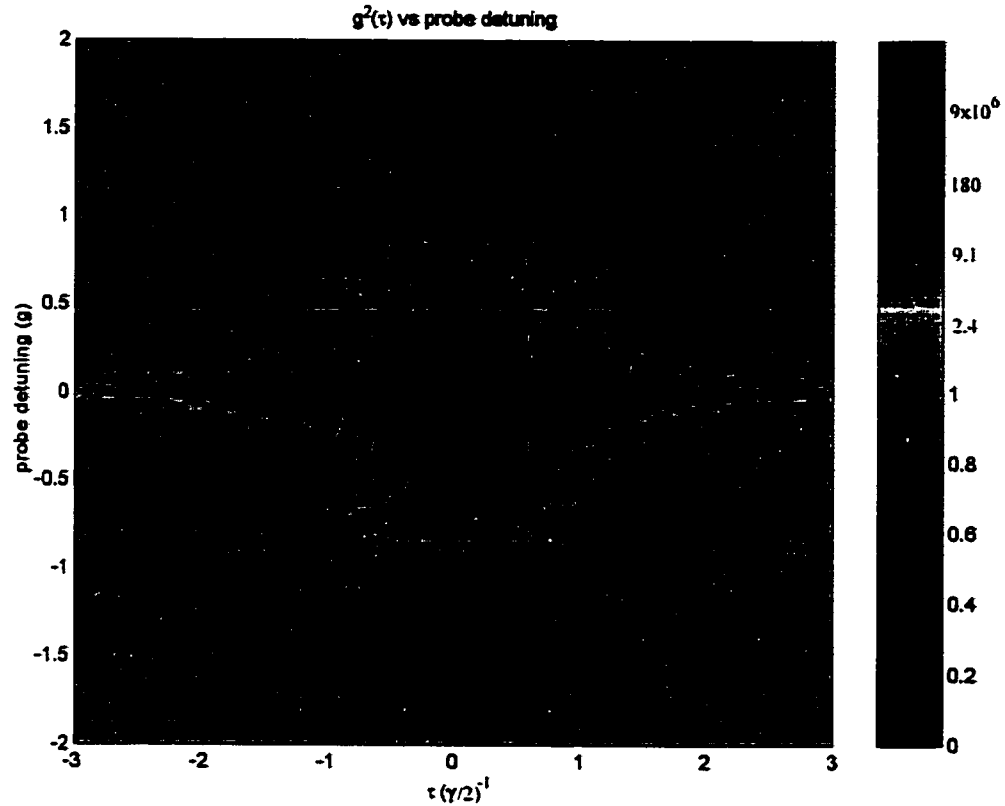


Figure 6.13: Second order intensity correlation function $g^{(2)}(\tau)$, calculated in the weak-field approximation, shown by the color scale is plotted as a function of time delay τ (x axis) and probe detuning from the atom-cavity resonance (y axis). Parameters are $\{g_0, \kappa, \gamma_{\parallel}\}/2\pi = \{110, 14.2, 5.2\}$ MHz. Note the logarithmic scaling of the $g^{(2)}(\tau) > 1$ part of the color scale.

be seen around detunings $g_0/\sqrt{2}$, again persisting for timescale $((\kappa+\gamma_{\parallel})/2)^{-1}$. Thirdly, since $\omega_c = \omega_a$, $g^{(2)}(\tau)$ is symmetric about $\omega_0 = \omega_c = \omega_a$, and strong antibunching is seen for detunings $\omega_a - \omega_0 = \pm g_0$. The symmetry that $g^{(2)}(-\tau) = g^{(2)}(\tau)$ is also apparent from Figure 6.13.

Another interesting proposal for reducing the cavity linewidth, and hence lengthening (and enhancing) the duration of the photon blockade is to use a cavity EIT effect on a single atom [122, 123]. In these schemes, an second laser field and multiple internal states of the atom are employed to generate a quantum interference effect which reduces the linewidth of the 1-excitation levels of the manifold, and in addition

greatly reduces atomic spontaneous emission, while maintaining the anharmonicity of the 2-excitation levels which allows the atom-cavity to act as an effective two-level system. This effect is the one-atom equivalent of schemes which have been used in dense atomic clouds to enhance the refractive index without increasing spontaneous emission [124]. It has been shown that such a multi-atom EIT scheme will not work in the cavity QED context [120, 125, 126], but the case of a single (or few) atoms in a cavity will still produce a strong effect. It is yet to be seen how easy it will be to incorporate into our experiment the additional complexities required by the EIT scheme, including additional locked laser fields and optical pumping.

It should be pointed out that the strong antibunching $g^{(2)}(\tau) < 1$ is a fundamentally single-atom effect. It arises because of the anharmonicity of the Jaynes-Cummings ladder of states, and as discussed in Section 2.1.3 this anharmonicity decreases (for the same overall coupling strength) as the number of atoms increases. To demonstrate this deterioration, in Figure 6.14 is plotted $g^{(2)}(\tau)$ from Eq. 6.13, for probe detuning $-g_0$, with 1 atom (solid), 2 atoms (dashed) and 10 atoms (dotted), each with the single atom coupling strength g_0 adjusted to give the same coupling strength $g = g_0\sqrt{N}$. As can be seen, the anharmonicity, and hence the degree of antibunching, are quickly reduced.

Finally, a few words on the practicalities of a weak-field photon statistics measurement in our experimental apparatus, where atoms are currently trapped only for $\simeq 1\text{ms}$. To be truly “weak-field” requires the intracavity photon number $n < n_0$. For an intracavity coherent state, this would give an average photon count rate of $n_0 \times$ cavity linewidth \times branching ratio for cavity decay, which gives $n_0((\kappa + \gamma_{||})/2) \times \kappa / (\kappa + \gamma_{||}) = n_0\kappa/2$ photons per second, or alternatively 1 photon per $2/n_0\kappa$ seconds. For the current experimental values $\{g_0, \kappa, \gamma_{||}\}/2\pi = \{110, 14.2, 5.2\}\text{MHz}$ ($n_0 = 2.8 \times 10^{-4}$), this would give 1 photon every $80\mu\text{s}$, which leads to a total of only 12 photons counted over a 1ms trap lifetime. However, for the photon statistics measurement of $g^{(2)}(\tau)$ considered here, the relevant count rate is the *conditional* count rate $(n_0\kappa/2)g^{(2)}(\tau)$, which can be very different to $(n_0\kappa/2)$.

The question arises then as to whether n_0 is an appropriate measure of “goodness”

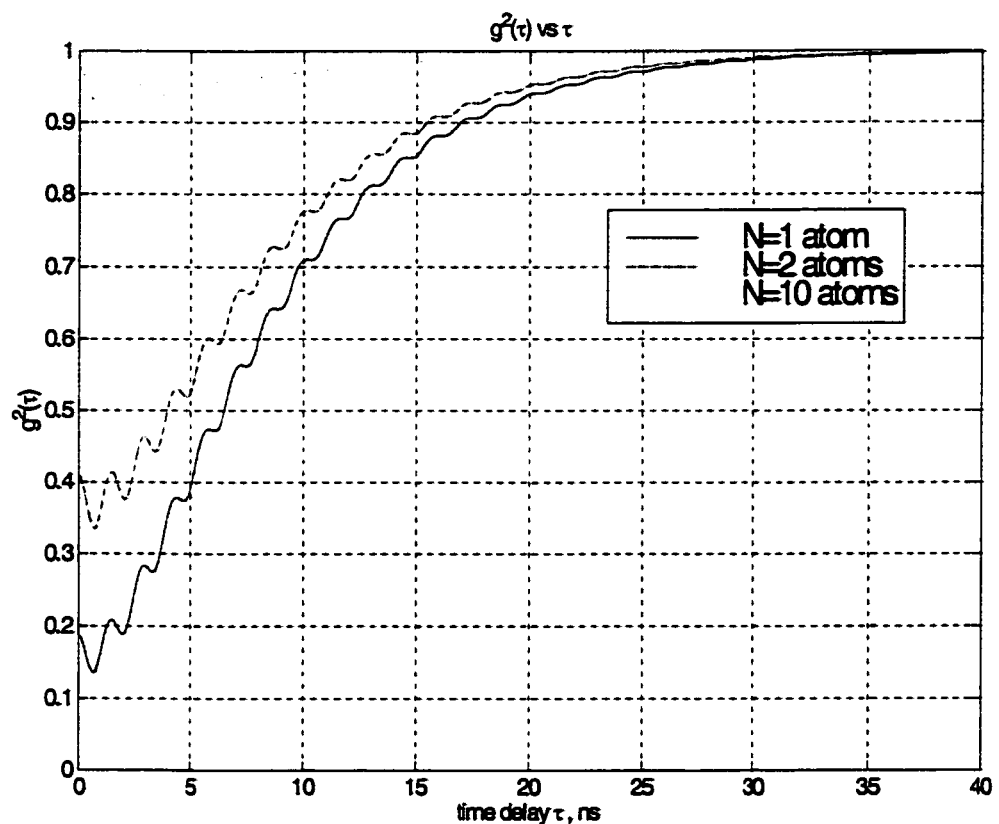


Figure 6.14: Second order intensity correlation function $g^{(2)}(\tau)$, calculated in the weak-field approximation, for increasing atom number, but the same effective coupling strength $g = g_0/\sqrt{N}$, for experimental parameters $\{g, \kappa, \gamma_{\parallel}\}/2\pi = \{110, 14.2, 5.2\}$ MHz.

of photon statistics, or whether a stronger field could be employed.

For the resonant case ($\omega_a = \omega_0 = \omega_c$), the large value of $g^{(2)}(0)$ leads to a conditional count rate closer to the drive strength ($(1+2C)^2 n_0$) than the steady-state value n_0 , so that collecting a reasonable number of photons is not so much of a problem.

When the driving field is detuned by g_0 however, there is only a suppression of the conditional count rate, to $\simeq 0.2(n_0\kappa/2)$ at $\tau = 0$. However, in this case it is not obvious that n_0 is the relevant parameter for describing saturation of the system. From Figure 4.16 it can be seen that for parameters $\{g_0, \kappa, \gamma_{||}\}/2\pi = \{110, 14.2, 5.2\}$ MHz, signals at a probe detuning of g_0 saturate fairly abruptly at $n \simeq 0.1$ intracavity photons (a semiclassical analysis gives $\sqrt{3}\kappa/2g_0$ for this saturation value), and at $n \simeq 0.01$ the signal contrast is degraded by < 10% from the weak-field case. This suggests that an intracavity field of $n \simeq 0.05$ may still have large quantum statistical variations, while still providing a larger number of conditional photon counts ($\simeq 0.2 \times 2000$ photons in 1ms).

At even stronger driving, the nonclassicality of $g^{(2)}(\tau)$ deteriorates as the field strength is increased - at an intracavity field strength of $|a|^2 \simeq 1$ as in the experiments of Chapter 4, the photon count rate over 1ms would be increased to a respectable 40,000 in 1ms, however the value of $g^{(2)}(0)$ is suppressed to $g^{(2)}(0) \simeq 0.95$ [127]. [The weak-field equations given above no longer apply here, but $g^{(2)}(\tau)$ can still be calculated by numerical integration of the master equation.]

It looks like it should be possible then to find a regime of driving and detuning for which $g^{(2)}(0)$ is significantly < 1, while still maintaining a count rate of $\gtrsim 1000$ photons in a 1ms interval, so that a measurement of photon statistics from an individual trapped atom should be possible.

Bibliography

- [1] *Cavity Quantum Electrodynamics*, ed. P. Berman (Academic Press, San Diego, 1994).
- [2] The lecture notes to J. Preskill's Caltech quantum information class provide a good introduction, available at <http://theory.caltech.edu/~preskill/ph229/> .
- [3] P. Shor, Phys. Rev. A **52**, 2493 (1995).
- [4] A. M. Steane, Phys. Rev. Lett. **77**, 793 (1996).
- [5] T. Pellizzari, S. Gardiner, J. I. Cirac, P. Zoller, Phys. Rev. Lett. **75**, 3788 (1995).
- [6] Q. A. Turchette, C. J. Hood, W. Lange, H. Mabuchi, H. J. Kimble, Phys. Rev. Lett. **75**, 4710 (1995).
- [7] A. S. Parkins, P. Marte, P. Zoller, H. J. Kimble, Phys. Rev. Lett. **71**, 3095 (1993).
- [8] C. K. Law, H. J. Kimble, Quantum Semiclass. Opt. **44**, 2067 (1997).
- [9] J. I. Cirac, P. Zoller, H. J. Kimble, H. Mabuchi, Phys. Rev. Lett. **78**, 3221 (1997).
- [10] S. J. van Enk, J. I. Cirac, P. Zoller, H. J. Kimble, H. Mabuchi, J. Mod Opt **44**, 1727 (1997).
- [11] C. Monroe et al., Phys. Rev. Lett. **75**, 4011 (1995).
- [12] M. Brune, E. Hagley, J. Dreyer, X. Maitre, A. Maali, C. Wunderlich, J. M. Raimond, S. Haroche, Phys. Rev. Lett. **77**, 4887 (1996).
- [13] G. K. Brennen, C.M. Caves, P. S. Jessen, I. H. Deutsch, Phys. Rev. Lett. **82**, 1060 (1999).

- [14] Y. Nakamura, Y. A. Pashkin, J. S. Tsai, *Nature* **398**, 786 (1999).
- [15] N. Gershenfeld, I. Chuang, *Science* **275**, 350 (1997); D. Cory, A. Fahmy, and T. Havel, *Proc. Nat. Acad. Sci.* **94**, 1634 (1997).
- [16] D. Loss, D. P. DiVincenzo, *Phys. Rev. A* **57**, 120 (1998).
- [17] T. Tanamoto, *Phys. Rev. A* **61**, 022305 (2000).
- [18] B. Kane, *Nature* **393**, 133 (1998).
- [19] A. Imamoglu, D. D. Awschalom, G. Burkard, D. P. Divincenzo, D. Loss, M. Sherwin, A. Small, *Phys. Rev. Lett.* **83**, 4204 (1999).
- [20] M. Sherwin, A. Imamoglu, T. Montroy, *Phys. Rev. A* **60**, 3508 (1999).
- [21] T. A. Brun, H. Wang, *Phys. Rev. A* **61**, 032307 (2000).
- [22] E. T. Jaynes, F. W. Cummings, *Proc. IEEE* **51**, 89 (1963).
- [23] R. J. Thompson, G. Rempe, H. J. Kimble, *Phys. Rev. Lett.* **68**, 1132 (1992).
- [24] H. Mabuchi, Q. A. Turchette, M. S. Chapman, H. J. Kimble, *Opt. Lett.* **21**, 1393 (1996).
- [25] C. J. Hood, M. S. Chapman, T. W. Lynn, H. J. Kimble, *Phys. Rev. Lett.* **80**, 4157 (1998).
- [26] J. Ye, C. J. Hood, T. W. Lynn, H. Mabuchi, D. W. Vernooy, H. J. Kimble, *IEEE Trans. Instru. & Meas.* **48**, 608 (1999).
- [27] C. J. Hood, T. W. Lynn, A. C. Doherty, A. S. Parkins H. J. Kimble, *Science* **287**, 1447 (2000).
- [28] J. Ye, D. W. Vernooy, H. J. Kimble, *Phys. Rev. Lett.* **83**, 4987 (1999).
- [29] J. A. Dunningham, H. M. Wiseman, D. F. Walls, *Phys. Rev. A* **55**, 1398 (1997).
- [30] A. C. Doherty, K. Jacobs, *Phys. Rev. A* **60**, 2700 (1999).

- [31] Q. A. Turchette, R. J. Thompson, H. J. Kimble, App. Phys. B **60**, S1-S10 (1995).
- [32] P. R. Rice, L. M. Pedrotti, J. Opt. Soc. Am. B **9**, 2008 (1992).
- [33] N. Ph. Georgiades, *Nonclassical Excitation and Quantum Interference in a Three Level Atom*, California Institute of Technology doctoral dissertation (1997).
- [34] Q. A. Turchette, N. Ph. Georgiades, C. J. Hood, H. J. Kimble, A. S. Parkins, Phys. Rev. A **58**, 4056 (1998).
- [35] A. Furusawa, J. L. Sorensen, S. L. Braunstein, C. A. Fuchs, H. J. Kimble, E. S. Polzik, Science **282**, 706 (1998).
- [36] For an overview of atom cooling and trapping techniques, see the Nobel lectures by S. Chu [Rev. Mod. Phys. **70**, 685 (1998)], C. Cohen-Tannoudji [Rev. Mod. Phys. **70**, 707 (1998)], and W. D. Phillips [Rev. Mod. Phys. **70**, 721 (1998)].
- [37] R. J. Thompson, Q. A. Turchette, O. Carnal, H. J. Kimble, Phys. Rev. A **57**, 3084 (1998).
- [38] Q. A. Turchette, *Quantum Optics with single atoms and single photons*, California Institute of Technology doctoral dissertation (1997).
- [39] R. J. Thompson, *Cavity Quantum Electrodynamics in the Optical Domain: Structure and Dynamics in the Strong Coupling Regime*, University of Texas at Austin doctoral dissertation (1994).
- [40] Z. Hu, *Quantum Optics with Cold Atoms - Nonlinear Spectroscopy and Road toward Single-Atom Trap*, California Institute of Technology doctoral dissertation (1995).
- [41] H. Mabuchi, H. J. Kimble, Opt. Lett. **19**, 749 (1994).

- [42] *Stopping and “Trapping” and Atom in a Few-Photon Optical Cavity Field*, research seminar, Caltech, Sept. 1995.
- [43] D. W. Vernooy, A. Furusawa, N. Ph. Georgiades, V. S. Ilchenko, H. J. Kimble, Phys. Rev. A **57** R2293 (1998).
- [44] P. Munstermann, T. Fischer, P. W. H. Pinkse, G. Rempe, Opt. Comm. **159**, 63 (1999).
- [45] P. Münstermann et al., Phys. Rev. Lett. **82**, 3791 (1999).
- [46] H. Mabuchi, J. Ye, H. J. Kimble, Appl. Phys. B**68**, 1095 (1999).
- [47] P. W. H. Pineske, T. Fischer, P. Maunz, G. Rempe, Nature **404**, 365 (2000).
- [48] A. C. Doherty, T. W. Lynn, C. J. Hood, H. J. Kimble, in preparation.
- [49] G. Rempe, Appl. Phys. B**60**, 233(1995).
- [50] A. C. Doherty, A. S. Parkins, S. M. Tan, D. F. Walls, Phys. Rev. A **56**, 833(1997).
- [51] S. Haroche, M. Brune, J. M. Raimond, Europhys. Lett. **14**, 19 (1991).
- [52] H. Mabuchi, P. Zoller, Phys. Rev. Lett. **76**, 3108 (1996).
- [53] M. Brune, F. Schmidt-Kaler, A. Maali, J. Dreyer, E. Hagley, J. M. Raimond, S. Haroche, Phys. Rev. Lett. **76**, 1800 (1996).
- [54] J. J. Childs, K. An, M. S. Otteson, R. R. Dasari, M. S. Feld, Phys. Rev. Lett. **77**, 2901 (1996).
- [55] H. Walther, P. Roy. Soc. A **454**, 431 (1998).
- [56] H. Walther, Phys. Scr. T**76**, 138 (1998).
- [57] M. G. Raizen, L. A. Orozco, X. Min, T. L. Boyd, H. J. Kimble, Phys. Rev. Lett. **59**, 198 (1987).

- [58] G. Rempe, F. Schmidt-Kaler, H. Walther, Phys. Rev. Lett. **64**, 2783 (1990).
- [59] G. Rempe, R. J. Thompson, R. J. Brecha, W. D. Lee, H. J. Kimble, Phys. Rev. Lett. **67**, 1727 (1991).
- [60] S. L. Mielke, G. T. Forster, L. A. Orozco, Phys. Rev. Lett. **80**, 3948 (1998).
- [61] A. Lambrecht, T. Coudreau, A. M. Steinberg, E. Giacobino, Europhys. Lett. **36**, 93 (1996).
- [62] A. C. Doherty, A. S. Parkins, S. M. Tan, D. F. Walls, Phys. Rev. A **57**, 4804 (1998).
- [63] D. W. Verwoerd, H. J. Kimble, Phys. Rev. A **56**, 4207 (1997).
- [64] L. A. Lugiato, *Progress in Optics, Vol. XXI*, ed. E. Wolf (Elsevier Science Publishers B. V., Amsterdam, 1984).
- [65] H. M. Gibbs, *Optical Bistability: Controlling Light with Light* (Academic Press, Inc., Orlando, Florida (1995)).
- [66] H. J. Carmichael, *Quantum Statistical Techniques in Quantum Optics*, Springer (1993).
- [67] This part of the calculation was performed using code based on Sze Tan's 'Quantum Optics Toolbox', <http://www.phy.auckland.ac.nz/Staff/smt/qotoolbox/download.html>.
- [68] M. Tavis, F. W. Cummings, Phys. Rev. **170**, 379 (1968).
- [69] G. V. Varada, M. S. Kumar, G. S. Agarwal, Opt. Comm **62**, 328 (1987).
- [70] H. J. Carmichael, B. C. Sanders, Phys. Rev. A **60**, 2497 (1999).
- [71] H. J. Kimble, Phil. Trans. A **355**, 2327 (1997).
- [72] H. Mabuchi, Phys. Rev. A **58**, 123 (1998).

- [73] H. Mabuchi, *Continuous Observation of Quantum Variables*, California Institute of Technology doctoral dissertation (1998).
- [74] K. G. Libbrecht, J. L. Hall, Rev. Sci. Instr. **64**, 2133 (1993); K. G. Libbrecht et al, Am. J. Phys. **63** (8), 729 (1995).
- [75] D. C. Ralph, C. T. Black, M. Tinkham, Phys. Rev. Lett. **78**, 4087 (1997).
- [76] C. E. Tanner et al., Nucl. Inst. **B99**, 117(1995).
- [77] A. S. Parkins, unpublished notes (1995); P. Horak et al., Phys. Rev. Lett. **79**, 4974 (1997).
- [78] C. M. Savage, H. J. Carmichael, IEEE J. Quantum Electron. **24**, 1495 (1988).
- [79] R. Quadt, M. Collett, D. F. Walls, Phys. Rev. Lett. **74**, 351(1995).
- [80] B. G. Englert, J. Schwinger, A. O. Barut, M. O. Scully, Europhys. Lett. **14**, 25 (1991).
- [81] M. O. Scully et. al., Phys. Rev. Lett. **76**, 4144 (1996); W. Ren, H. J. Carmichael, Phys. Rev. **A51**, 752 (1995).
- [82] P. Horak et al., Phys. Rev. Lett. **79**, 4974 (1997).
- [83] C. Cohen-Tannoudji, in *Fundamental Systems in Quantum Optics, Les Houches, Session LIII, 1990*, eds. J. Dalibard, J. M. Raimond, J. Zinn-Justin (Elsevier Science Publishers, Amsterdam, 1992), pp. 21-52.
- [84] P. Verkerk, B. Lounis, C. Salomon, C. Cohen-Tannoudji, J.-Y. Courtois, G. Grynberg, Phys. Rev. Lett. **68**, 3861 (1992).
- [85] P. S. Jessen, C. Gerz, P. D. Lett, W. D. Phillips, S. L. Rolston, R. J. C. Spreeuw, C. I. Westbrook, Phys. Rev. Lett. **69**, 49 (1992).
- [86] P. Marte, R. Dum, R. Taieb, P. D. Lett, P. Zoller, Phys. Rev. Lett. **71**, 1335 (1993).

- [87] J. P. Gordon, A. Ashkin, Phys. Rev. A **21**, 1616 (1980).
- [88] D. J. Wineland, W. M. Itano, J. C. Bergquist, Opt. Lett. **12**, 389 (1987).
- [89] W. E. Moerner, L. Kador, Phys. Rev. Lett. **62**, 2535 (1989).
- [90] R. J. Cook, in *Progress in Optics, Vol. XXVIII*, ed. E. Wolf (North Holland, Elsevier Science Publishers B. V., Amsterdam, 1990), 361.
- [91] M. Ortiz, J. Bernard, R. Personov, Phys. Rev. Lett. **65**, 2716 (1990).
- [92] W. P. Ambrose, W. E. Moerner, Nature **349**, 225 (1991).
- [93] E. Betzig, R. J. Chichester, Science **262**, 1422 (1993); X.S. Xie, J.K. Trautman, Ann. Rev. Phys. Chem. **49**, 441 (1998) ; W.E. Moerner, M. Orrit, Science **283**, 1670 (1999); S. Weiss, Science **283**, 1676 (1999).
- [94] V. B. Braginsky, F. Ya. Khalili, *Quantum Measurement* (Cambridge University Press, 1992).
- [95] G. Rempe, R. J. Thompson, H. J. Kimble, R. Lalezari, Opt. Lett. **17** (5) 363, (1992).
- [96] E. Hecht, *Optics*, (pp.373-375), Addison-Wesley Publishing (1987).
- [97] For a derivation of the $(\frac{1}{n_H - n_L})$ effective length correction, see R.G. DeVoe, C. Fabre, K. Jungmann, J. Hoffnagle, R.G. Brewer, Phys. Rev. A. **37**, 1802 (1988).
- [98] W. Lichten, J. Opt. Soc. Am. A **2**, 1869 (1985).
- [99] H. P. Layer, R. D. Deslattes, W.G. Schewietzer, Jr., Applied Optics **15**, 734 (1976).
- [100] R. Grimm, M. Weidemuller, Y. B. Ovchinnikov, Adv. At. Mol. Opt. Phys. **42**, 95 (2000).
- [101] D. Cho, J. Korean Phys. Soc., **30**(2), 373 (1997).

- [102] K. L. Corwin, S. J. M. Kuppens, D. Cho, C. E. Wieman, Phys. Rev. Lett. **83**, 1311 (1999).
- [103] R. Taïeb, R. Dum, J. I. Cirac, P. Marte, P. Zoller, Phys. Rev. A **49**, 4876 (1994).
- [104] I. H. Deutsch, P. S. Jessen, Phys. Rev. A **57**, 1972 (1998).
- [105] C. S. Wood, S. C. Bennett, D. Cho, B. P. Masterson, J. L. Roberts, C. E. Tanner, C. E. Wieman, Science **275**, 1759 (1997).
- [106] R. J. Rafac, C. E. Tanner, A. E. Livingston, K. W. Kukla, H. G. Berry, C. A. Kurtz, Phys. Rev. A **50** (3), 1976 (1994).
- [107] R. J. Rafac, C. E. Tanner, A. E. Livingston, H. G. Berry, Phys. Rev. A **60**(5), 3648 (1999).
- [108] N. Ph. Georgiades, E. S. Polzik, H. J. Kimble, Opt. Lett. **19**(18), 1474 (1994).
- [109] C. E. Theodosiou, Phys. Rev. A **30**, 2881 (1984).
- [110] D. DiBerardino, C. E. Tanner, A. Sieradzan, Phys. Rev. A **57**, 4204 (1998).
- [111] C. Cohen-Tannoudji, *Atom – Photon Interactions* pg. 518 (John Wiley & Sons, Inc. 1992).
- [112] A. E. Siegman, *Lasers* pg. 123, (University Science Books, Mill Valley 1986).
- [113] G. Laplanche, M Jaouen, A. Rachman, J. Phys. B. At. Mol. Phys **16**, 415 (1983).
- [114] S. S. Liaw, Can. J. Phys. **70**, 1279 (1992).
- [115] R. A. Cline, J. D. Miller, M. R. Matthews, D. J. Heinzen, Opt. Lett. **19** (3), 207 (1994).
- [116] L. Tian, H. J. Carmichael, Phys. Rev. A **46**, R6801 (1992).
- [117] H. J. Carmichael, R. J. Brecha, P. R. Rice, Opt. Comm. **82**, 73 (1991).

- [118] R. J. Brecha, P. R. Rice, M. Xiao, Phys. Rev. A **59**, 2392 (1999).
- [119] H. J. Carmichael, S. Singh, R. Vyas, P. R. Rice, Phys. Rev. A **39**, 1200 (1989).
- [120] A. Imamoglu, H. Schmidt, G. Woods, M. Deutsch, Phys. Rev. Lett. **79**, 1467 (1997).
- [121] J. Kim, O. Benson, H. Kan, Y. Yamamoto, Nature **397**, 500 (1999).
- [122] S. Rebic, S. M. Tan, A. S. Parkins, D. F. Walls, J. Opt. B - Quant. Semimiclass. Opt. **1**(4), 490 (1999).
- [123] M. J. Werner, A. Imamoglu, Phys. Rev. A **61**, 011801(R) (2000).
- [124] S. E. Harris, J. E. Field, A Kasapi, Phys. Rev. A **46**, R29 (1992); M. Xiao, Y. Q. Li, S. Z. Jin, J. Geabanacloche, Phys. Rev. Lett. **74**, 666 (1995); L. V. Hau, S. E. Harris, Z. Dutton and C. H. Behroozi, Nature **397**, 594 (1999).
- [125] P. Grangier, D. F. Walls, K. M. Gheri, Phys. Rev. Lett. **81**, 2833 (1998).
- [126] K. M. Gheri, W. Alge, P. Grangier, Phys. Rev. A **60**, R2673 (1999).
- [127] This value was provided by Andrew Doherty as part of calculations for the experiment of Chapter 4.